TECHNISCHE UNIVERSITÄT WIEN

HEPHY INSTITUT FÜR HOCHENERGIEPHYSIK

Sub-GeV Dark Matter Studies and Universal Bound States Exploration with CRESST-III

DISSERTATION

zur Erlangung des akademischen Grades

Doktor der Technischen Wissenschaften

eingereicht von

Shubham Gupta, M.Sc.

Matrikelnummer 12102621

ausgeführt am Atominstitut
der Fakultät für Physik der Technischen Universität Wien
in Zusammenarbeit mit dem Institut für Hochenergiephysik
der Österreichischen Akademie der Wissenschaften

Betreuung: Univ.-Prof. Dipl.-Phys. Dr. Jochen Schieck
Zweitbetreuung: Assist.-Prof. Dipl.-Phys. Dr. Florian Reindl

Wien, 13. Dezember 2023

Shubham Gupta	Jochen Schieck

Technische Universität Wien
A-1040 Wien ▪ Karlsplatz 13 ▪ Tel. +43-1-58801-0 ▪ www.tuwien.at

"We can judge our progress by the courage of our questions and the depth of our answers, our willingness to embrace what is true rather than what feels good."

- Prof. Carl Segan

Contents

Abstract

The mystery of Dark matter (DM) has eluded us for about a century and has been one of the biggest open questions in modern-day physics. Numerous efforts have gone into understanding its nature, origin, and properties. Despite a huge number of attempts, there has been no convincing evidence of its detection or production. Many different models have been proposed to date that aims at explaining the underlying nature of the elusive substance, although none have been completely confirmed experimentally or observationally.

Λ-CDM has been a prevalent cosmological model in describing the large-scale structures in the universe and their cosmic evolution. Although Λ-CDM has been successful at larger scales, it faces severe issues on smaller scales when compared to the observations. Introducing self-interactions between dark matter (SIDM) particles claims to solve the small-scale issues in Λ-CDM simulations while also being consistent with the large-scale observations. One of such SIDM theories considers some (or all) of the dark matter particles in the universe today to be a bound state of two or more dark particles called as a Darkonium. If such bound states exist, then the form factor of such bound states and the possibility of breakup of such states would impart a different signature on the direct detection experiments, that can be smoking gun evidence for its existence.

CRESST is one of the leading experiments for the direct detection of DM in the sub-GeV DM mass range, and it provides the most stringent exclusion limits in the said mass region. CRESST is able to achieve this sensitivity as it employs bolometers operating at cryogenic temperatures and is able to achieve nuclear recoil thresholds of $\mathcal{O}(10\text{ eV})$. Sensitivity to go even lower in threshold is restricted by the presence of an unknown background at low energies called as Low Energy Excess (LEE).

This thesis has two main parts where the first part aims to present the data analysis chain in CRESST and show the results obtained with the latest run (*Run36*) of CRESST-III. In this run, different detector materials, modules, and holding designs were operated with the aim of understanding the origin of the LEE. During the run, the detectors were warmed up multiple times to high temperatures in order to study the effect of this warm-up on the rate of LEE. The results obtained with these warm-ups for different detector modules are discussed, and the possible origins of the LEE are narrowed down further.

A new method of calibration at sub-keV energies was recently proposed where a radiative neutron capture on ^{182}W would be followed by a de-excitation with a single γ-emission that gives a nuclear recoil peak at 112.4 eV. This method would be useful for calibration at low energies, and more accurate than conventionally used X-ray sources, which generally lie in $\mathcal{O}$(keV) energy regime. With the data obtained by irradiating an AmBe neutron source in Run36, the observation of this expected peak at 112 eV in the $CaWO_4$ detectors will also be shown.

With the blind data obtained from February 2021 - August 2021 in the same run, exclusion limits were extracted for different detector modules, and huge improvements in limits were obtained for the spin-dependent DM-nuclei interaction scenario using lithium aluminate targets. The analysis of these modules, results obtained, and implications are also discussed.

The second main part of the thesis focuses on the direct detection results of the SIDM model described above using CRESST-III. The study focuses on self-interactions at non-relativistic velocities necessary to explain small-scale structures. Assuming an energy region where the self-interaction cross-section approaches the S-wave unitarity bound, low-energy scattering properties rely on the large scattering length γ, specifically the self-interacting scattering cross-section $\sigma_{\chi-\chi}$. Estimating γ from CRESST data establishes exclusion limits on its value, converted to exclusion limits on $\sigma_{\chi-\chi}/m_\chi$, dependent on the relative momentum between dark matter particles. Results reveal the first exclusion limits on the self-interaction cross-section from the direct detection window under the given physics model for various dark matter masses and their interaction cross-sections with the detector nucleus. Enhanced sensitivity of the experiments in the future enables a deeper study of self-interactions in the given physics case.

Kurzfassung

Das Geheimnis der Dunklen Materie (DM) ist seit etwa einem Jahrhundert ein Rätsel und eine der größten offenen Fragen der modernen Physik. Zahlreiche Anstrengungen wurden unternommen, um ihre Natur, ihren Ursprung und ihre Eigenschaften zu verstehen. Trotz zahlreicher Versuche, gibt es weder einen directe Nachweis, noch einen Nachweis der Produktion von Dunkle Matarie. Bis heute wurden viele verschiedene Modelle vorgeschlagen, die darauf abzielen, die zugrundeliegende Natur dieser schwer fassbaren Substanz zu erklären, obwohl keines davon experimentell oder durch Beobachtungen bestätigt wurde.

Λ-CDM ist ein weit verbreitetes kosmologisches Modell zur Beschreibung der großen Strukturen im Universum und ihrer kosmischen Entwicklung. Obwohl Λ-CDM in größeren Maßstäben erfolgreich war, hat bei Beobachtungen in kleineren Maßstäben große Probleme. Die Einführung von Selbstwechselwirkungen zwischen Teilchen der Dunklen Materie (SIDM) soll die Probleme auf kleiner Skala in Λ-CDM-Simulationen lösen und gleichzeitig mit den Beobachtungen auf großen Skala vereinbar machen. Eine dieser SIDM-Theorien geht davon aus, dass einige (oder alle) der Dunklen Materieteilchen im heutigen Universum ein gebundener Zustand von zwei oder mehr Teilchen sind, der als Darkonium bezeichnet wird. Wenn solche gebundenen Zustände existieren, dann würden der Formfaktor solcher gebundenen Zustände und die Möglichkeit des Aufbrechens solcher Zustände den direkten Nachweisexperimenten eine andere Signatur verleihen, die ein entscheidender Beweis für ihre Existenz sein könnte.

CRESST ist eines der führenden Experimente für den direkten Nachweis von DM im Sub-GeV-Massenbereich und bietet die strengsten Ausschlussgrenzen in diesem Massenbereich. CRESST ist in der Lage diese Empfindlichkeit zu erreichen, da es Bolometer einsetzt, die bei kryogenen Temperaturen arbeiten und in der Lage sind, Kernrückstoßschwellen von $\mathcal{O}(10\text{ eV})$ zu erreichen. Die Empfindlichkeit für noch niedrigere Schwellenwerte wird durch einen unbekannten Untergrund bei niedrigen Energien eingeschränkt, der als Low Energy Excess (LEE) bezeichnet wird.

Vorliegende Arbeit besteht aus zwei Hauptteilen, wobei der erste Teil darauf abzielt, die Datenanalysekette in CRESST vorzustellen und die mit dem letzten Run (*Run36*) von CRESST-III erzielten Ergebnisse zu zeigen. In diesem Run wurden verschiedene Detektormaterialien, Module und Haltevorrichtungen eingesetzt, um den Ursprung des LEE zu verstehen. Während des wurden die Detektoren mehrmals auf höhere Temperaturen

erwärmt, um die Auswirkungen dieser Erwärmung auf die LEE-Rate zu untersuchen. Die Ergebnisse, die mit diesen Aufwärmvorgängen für verschiedene Detektormodule erzielt wurden, werden erörtert, und die möglichen Ursachen für den LEE werden weiter eingegrenzt.

Kürzlich wurde eine neue Kalibrierungsmethode für Energien im Sub-keV-Bereich vorgeschlagen, bei der auf einen neutroneneinfang an ^{182}W eine Abregung mit einer einzigen γ-Emission folgt, die einen Kernrückstoßpeak bei 112,4 eV ergibt. Diese Methode wäre für die Kalibrierung bei niedrigen Energien nützlich und genauer als die herkömmlich verwendeten Röntgenquellen, die im Allgemeinen im $\mathcal{O}$(keV)-Energiebereich liegen. Mit den Daten, die durch die Bestrahlung einer AmBe-Neutronenquelle in Run36 gewonnen wurden, wird auch die Beobachtung dieses erwarteten Peaks bei 112 eV in den $CaWO_4$-Detektoren gezeigt.

Mit den Blinddaten, die im selben Run von Februar 2021 bis August 2021 gewonnen wurden, wurden Ausschlussgrenzen für verschiedene Detektormodule extrahiert und enorme Verbesserungen der Grenzen für das spinabhängige DM-Kern-Wechselwirkungsszenario unter Verwendung von Lithiumaluminat-Targets erzielt. Die Analyse dieser Module, die erzielten Ergebnisse und die Implikationen werden ebenfalls diskutiert.

Der zweite Hauptteil der Arbeit konzentriert sich auf die Ergebnisse des direkten Nachweises des oben beschriebenen SIDM-Modells mit CRESST-III. Die Studie konzentriert sich auf Selbstwechselwirkungen bei nichtrelativistischen Geschwindigkeiten, die zur Erklärung von Strukturen auf kleiner Skala erforderlich sind. Unter der Annahme eines Energiebereichs, in dem sich der Selbstwechselwirkungsquerschnitt der S-Wellen-Einheitlichkeitsgrenze nähert, hängen die Eigenschaften der Streuung bei niedriger Energie von der großen Streulänge γ ab, insbesondere vom Selbstwechselwirkungs-Streuquerschnitt $\sigma_{\chi-\chi}$. Durch die Abschätzung von γ aus CRESST-Daten werden Ausschlussgrenzen für diesen Wert festgelegt, die in Ausschlussgrenzen für $\sigma_{\chi-\chi}/m_\chi$ umgewandelt werden und vom relativen Impuls zwischen den Teilchen der Dunklen Materie abhängen. Die Ergebnisse zeigen die ersten Ausschlussgrenzen für den Selbstwechselwirkungsquerschnitt aus dem direkten Nachweisfenster unter dem gegebenen physikalischen Modell für verschiedene Massen der Dunklen Materie und ihre Wechselwirkungsquerschnitte mit dem Detektorkern. Eine verbesserte Empfindlichkeit der Experimente in der Zukunft ermöglicht ein genauers Studium der Selbstwechselwirkungen im gegebenen physikalischen Fall.

List of Figures

List of Tables

Preamble

This thesis is the culmination of research funded by the FWF-FG1 grant. While the collaborative efforts of the entire CRESST collaboration shaped the results presented here, my focus centered on the detailed analysis of the *Comm2* module in Run36. I contributed as the primary analyst for the *Comm2* module and any results produced by this module. Chapter 5 outlines the specifics of this module, presenting a deep dive into the intricacies of the data.

Beyond *Comm2*, I also acted as a secondary analyst for other modules, including *Li1* and *Si2*. Chapter 5 also discusses my involvement in the high-level analysis of the *Li1* detector, where I applied bandfit techniques to produce the spin-dependent dark matter results with the analyzed raw data and also conducted cross-check analysis of the raw data to reproduce the results, adding layers of reliability to our findings.

In Chapter 6, the spotlight turns to self-interacting dark matter. My role involves synthesizing all the results with the resonant dark matter using the CRESST data. The findings in this chapter will also be published in the months following this thesis.

I extend my gratitude to the FWF grant FG1 for their financial support, a vital enabler of this journey into dark matter physics. This thesis stands as a testament to the collective dedication, collaboration, and exploration within the CRESST community.

CHAPTER 1

Introduction to Dark Matter

The mystery of "dark matter" has engaged humankind's contemplation for centuries. One of the earliest discussions on the topic can be traced back to 1877 in a memoir written by Father Angelo Secchi, who was then the director of the Roman College Observatory. The topic was discussed in the form of dark clouds or dark "nebulae" [1, 2]:

"Among these studies, there is the interesting probable discovery of dark masses scattered in space, whose existence was revealed thanks to the bright background on which they are projected. Until now, they were classified as black cavities, but this explanation is highly improbable, especially after the discovery of the gaseous nature of the nebular masses."

In 1904, Lord Kelvin was one of the first ones to give the dynamic estimation of dark matter in the Milky Way galaxy. Considering the stars in the galaxy as a gas of particles moving under the influence of gravity, a relation between the velocity dispersion and the size of the system could be established. He was able to conclude that nine-tenths of the stellar bodies in the galaxy might not be bright enough to be seen at their actual distances from Earth. [3]

1.1 Observational Evidences

Then, in 1933, working on the redshifts of different galaxy clusters, Fritz Zwicky noticed a huge amount of velocity dispersion in the Coma Cluster. While working on 800 galaxies in the cluster, using 10^9 $M_\odot$ as the average mass of each galaxy as suggested by Hubble and assuming 10^6 light-years to be the size of the system, he calculated that the galaxies in the cluster should exhibit a velocity dispersion of 80 km/s. However, 1000 km/s velocity dispersion was observed along the line-of-sight [4]. He concluded:

"If this would be confirmed, we would get the surprising result that dark matter is present in much greater amounts than luminous matter"

A similar calculation was done by Sinclair Smith in 1936 on the Virgo cluster, where he concluded the average gravitational mass per galaxy to be $2 \times 10^{11} M_{\odot}$ compared to $10^{9} M_{\odot}$ as suggested by Hubble (which was based only on the observed luminosity). Zwicky published a new article in 1937 where he refined his analysis of the coma cluster (Fig: 1.1) and was able to calculate an unexpectedly high light-to-mass ratio for the cluster of around 500 [5].

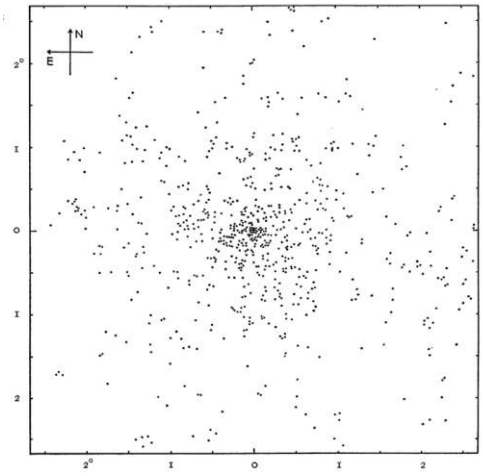

Figure 1.1: The coma cluster of nebulae as shown in Ref. [5]

In 1954, Martin Schwarzschild applied this similar methodology to various galaxies and clusters of galaxies and compiled the results as shown in Fig. 1.2.

Objects	Distance (in kpc)	Luminosity (in sol. lum.)	Mass (in sol. mass)	Mass/Lum. f
Solar Neighborhood	—	—	—	4
Triangulum Nebula, M33	480	1.4×10^{9}	5×10^{9}	4
Large Magellanic Cloud	44	1.2×10^{9}	2×10^{9}	2
Andromeda Nebula	460	9×10^{9}	1.4×10^{11}	16
Globular Cluster, M92	11	1.7×10^{5}	$<8 \times 10^{5}$	<5
Elliptical Galaxy, NGC 3115	2100	9×10^{8}	9×10^{10}	100
Elliptical Galaxy, M32	460	1.1×10^{8}	2.5×10^{10}	200
Average S in Double Gal.	—	1.3×10^{9}	7×10^{10}	50
Average E in Double Gal.	—	8×10^{8}	2.6×10^{11}	300
Average in Coma Cluster	25000	5×10^{8}	4×10^{11}	800

Figure 1.2: The distance, luminosity, mass, and mass-luminosity ratio of various galaxies and galaxy clusters compiled by M. Schwarzschild in [6]

1.1.1 Galactic Rotation Curves

In the decades following the work of Zwicky and Smith, there wasn't complete agreement on the existence of dark matter in the community, and many alternate theories were suggested to explain this high mass-to-light ratios in the galaxy clusters. A consensus started to appear in the 1970s with the increased work on galactic rotation curves. Working on the optical data, Rubin et al. [7–9] published extended rotation curves from individual galaxies with varying luminosities and morphologies (Fig. 1.3).

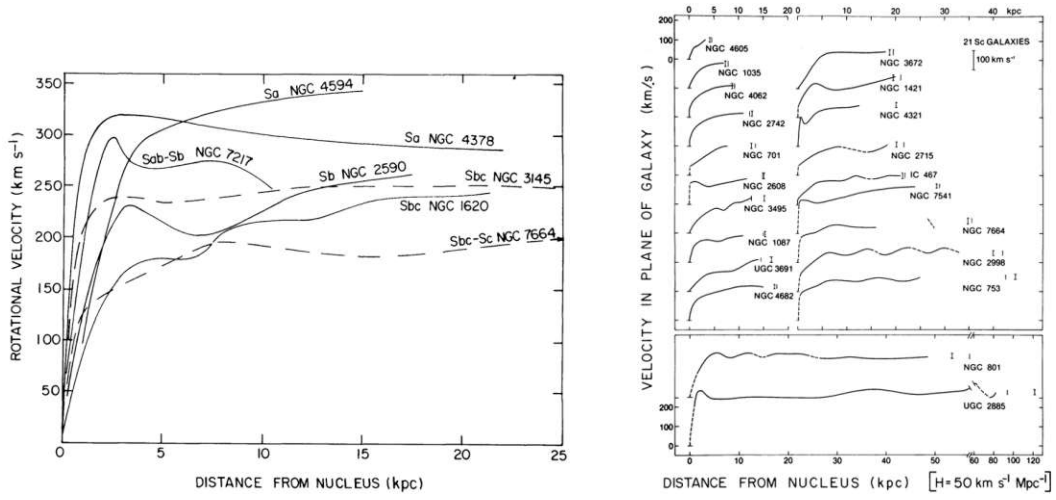

(a) (b)

Figure 1.3: (a) Rotational velocities for 7 high-luminosity galaxies as a function of their radial distance from the galactic center. Image taken from Ref. [8]. (b) Rotational velocities of 21 different Sc-type galaxies as a function of their radial distance from the galactic center. Image taken from Ref. [9]

If Newtonian mechanics is assumed to be correct on the galactic scales, the orbital velocity of the gravitationally orbiting stars around the galactic center can be given by:

$$v = \sqrt{\frac{GM(r)}{r}} \tag{1.1}$$

where all the symbols have their usual meanings. The observations by Rubin et al. showed that the orbital velocity of the stars in the individual galaxies stays almost constant at higher radial distances instead of following the $v \sim \sqrt{1/r}$ relation as one would expect. This would imply the presence of a *halo* of dark matter around every individual galaxy distributed quite differently than its exponentially distributed optical part. The expected rotation curve plotted along with the observed motion of the stars for the M33 galaxy can be seen in Fig. 1.4. The halo contribution is seen clearly, as the observed rotation curve is seen to be rising out to 50000 light-years (~ 15 *kpc*). Further precise observations

have since been made for many other galaxies where a "flat" rotation curve is seen to be almost ubiquitous.

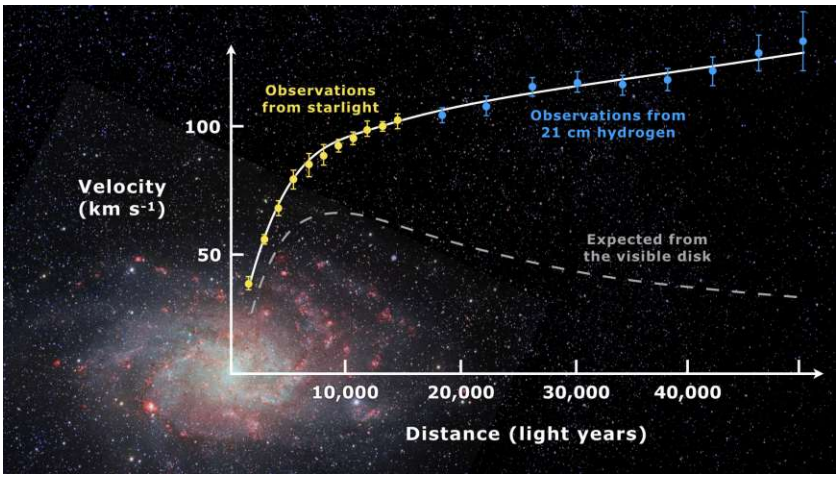

Figure 1.4: The galactic rotation curve of M33 with yellow points taken with starlight observation and blue points with 21 cm hydrogen line along with error bars. The data is taken from [10] and the image is taken from Ref. [11]

1.1.2 Cosmic Microwave Background

More conclusive evidence for the existence of additional non-baryonic matter came after the discovery of cosmic microwave background radiation by Panzias and Wilson in 1965 [12]. While working with the horn antenna, Panzias and Wilson discovered a persistent background noise in their data with a wavelength of 7.35 cm that corresponded to a 3.5 K blackbody radiation. This background noise was present irrespective of the direction they pointed their antenna to. They concluded that the noise was coming from outside our galaxy and later realized that what they were observing were signatures from the beginning of the universe known as the *Cosmic Microwave Background* (CMB).

As per our current understanding of the universe, the CMB is the remnant photons from around 380,000 years ($z \sim 1100$) after the Big Bang. As the universe expanded and cooled down after the Big Bang, at around 380,000 years, the temperature of the universe was cold enough for protons and electrons to combine and form neutral atoms (also known as *recombination*). This decreased the number of free electrons and protons in the universe by a huge amount, and the universe became transparent to the remnant photons as their mean free path became larger than ct, where c is the speed of light and t is the age of the universe. These photons have since been traveling through space in the universe and have vastly red-shifted to microwaves. The spectrum of CMB is seen to exhibit an almost perfect blackbody spectrum with a temperature of 2.725 K (Fig. 1.5).

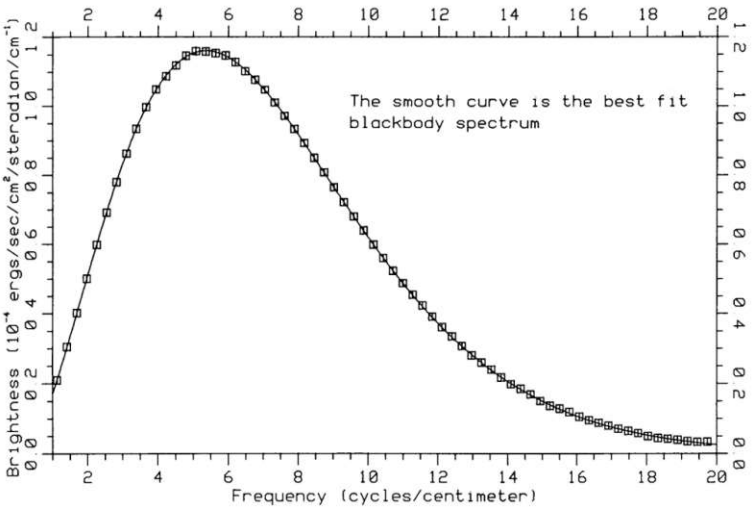

Figure 1.5: The CMB spectrum measured by the FIRAS instrument on COBE satellite (empty squares) with a 2.725 K blackbody spectrum (black line) as shown in Ref. [13].

Since the discovery, many further precise measurements of the CMB sky map have been done. Even though the CMB is seen to be very homogeneous throughout the sky, there are observed anisotropies in the CMB of the order $\delta T/T \sim 10^{-5}$ (Fig. 1.6), where T is the corresponding blackbody temperature. These temperature variations originate due to the gravitational redshift of these photons at the time of recombination. Thus, these variations can be used as an excellent probe to study matter distribution in the universe at that time.

These temperature fluctuations can be written in the form of spherical harmonics as:

$$\frac{\delta T}{T}(\theta,\phi) = \sum_{l=0}^{\infty}\sum_{m=-l}^{l} a_{lm} Y_{lm}(\theta,\phi) \tag{1.2}$$

where, Y_{lm} are Laplace's spherical harmonics and a_{lm} are its coefficients. Now, between two points in the sky $\hat{n}$ and $\hat{n}'$, a correlation function $C(\theta)$ can be written for these fluctuations as:

$$C(\theta) = \left\langle \frac{\delta T}{T}(\hat{n}) \frac{\delta T}{T}(\hat{n}') \right\rangle_{\hat{n}\cdot\hat{n}'=cos\theta} \tag{1.3}$$

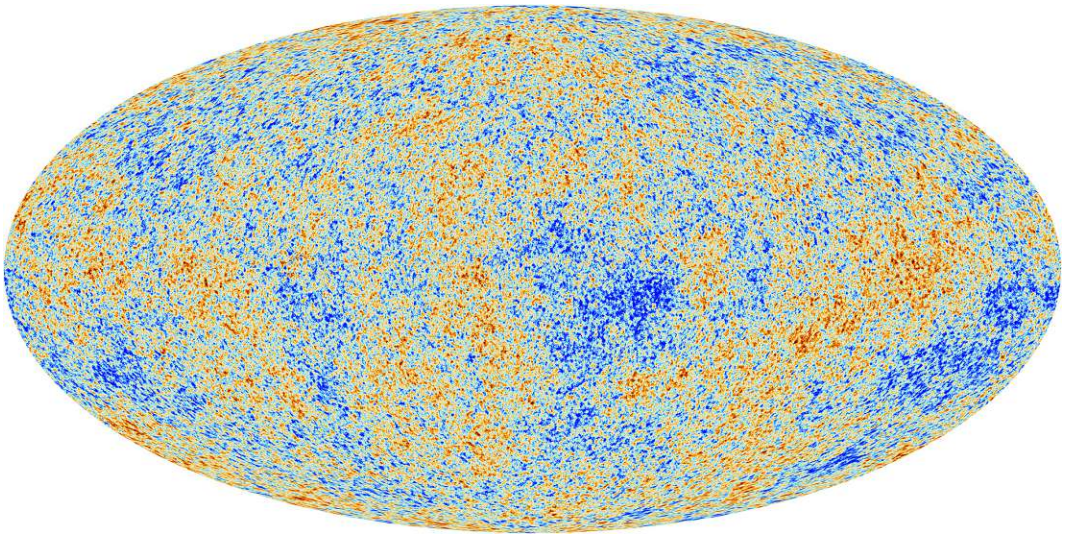

Figure 1.6: The cosmic microwave background radiation sky map as measured by Planck. The blue regions correspond to negative temperature fluctuation, and the red regions correspond to positive temperature fluctuations. Image is taken from Ref. [14].

Therefore, the correlation function can also be expanded in terms of the spherical harmonics as:

$$C(\theta) = \frac{1}{4\pi}\sum_{l=0}^{\infty}(2l+1)C_l P_l(cos\theta) \tag{1.4}$$

where C_l denotes the temperature fluctuations on an angular scale $\theta = 180°/l$ and P_l is the Legendre polynomial of degree l. Thus, these fluctuations can be plotted against the multipole l, and the spectrum is shown in Fig. 1.7.

It can be realized that the peaks observed in Fig. 1.7 are caused by baryon acoustic oscillations (BAO) in the universe that froze in at the time of recombination. The first peak seen at $l \sim 200$ that corresponds to around 0.9° (about double the size of the full moon) provides information about the largest scales and hence represents the curvature of the universe. The following peaks represent the small scales and thus give information about the matter content of the universe. As it can be shown, the ratio of the height of the third peak and the second peak reflects the size of dark matter and baryonic matter content. Since dark matter is not affected by radiation pressure, its presence boosts the height of the third peak in the CMB spectrum. The latest results on various cosmological parameters, as measured by the Planck collaboration [16], give the density of baryonic matter (Ω_{Baryons}) as 4.9% and the dark matter density ($\Omega_{\text{Dark Matter}}$) to be 26.8%, which is almost five times as much as the baryonic matter. The rest to be dark energy ($\Omega_{\text{Dark Energy}}$) as 68.3%, which is associated with the expansion of the universe. A detailed review of dark energy can be found in Ref. [17].

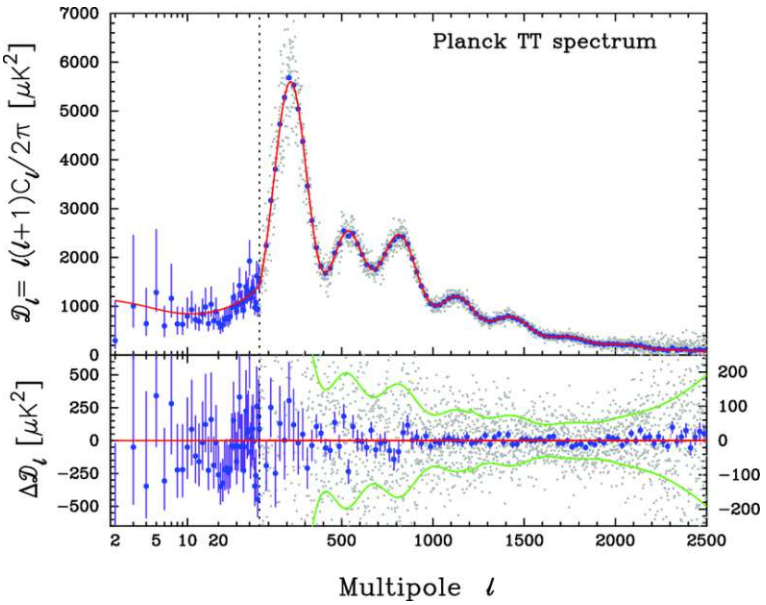

Figure 1.7: The *Planck* CMB power spectrum plotted against the multipole l. Image taken from Ref. [15].

1.1.3 Big Bang Nucleosynthesis

In the first few seconds after the Big Bang, the first composite nuclei were created by the interaction of neutrons(n) and protons(p), as the other hadrons had already decayed. The process of formation of the first light elements after the big bang is called as *Big Bang Nucleosynthesis* (BBN). Different nuclei such as ^{2}H, ^{3}He, ^{3}H, ^{4}He and ^{7}Li were produced in the process. The amount of nuclei produced depends on the density of the baryonic matter at that time. Thus, comparing the abundance of these baryons to the abundance of photons (baryon-to-photon ratio) present in the universe can be used as an independent probe to estimate the baryonic density of the universe. The current measurements by Planck collaboration [16] gives:

$$\Omega_{\text{Baryons}} h^2 = 0.0224 \pm 0.0002 \tag{1.5}$$

Here, h is the dimensionless Hubble parameter. This is in agreement with the CMB measurements and signifies that the baryonic content of the universe is not significant, and the majority of the matter in the universe is non-baryonic dark matter.

1.1.4 The Bullet Cluster

Not only was F. Zwicky the first one to hint towards the existence of non-luminous matter on the scales of galaxy clusters to explain the velocity dispersion of galaxies, but he was also the first one to propose that gravitational lensing can be used as an excellent method to measure the gravitational mass of a galaxy or a galaxy cluster in his paper in

1937 [5]. Using this method, an estimate of the distribution of gravitating matter (that would include dark matter) can be made, and it can be compared to the luminous matter distribution. One such observation and calculation was by Douglas Clowe et al. [18] for a pair of merging galaxy clusters 1E 0657-558, often referred to as the *Bullet cluster* (Fig. 1.8), in his famous article "A direct empirical proof of the existence of dark matter".

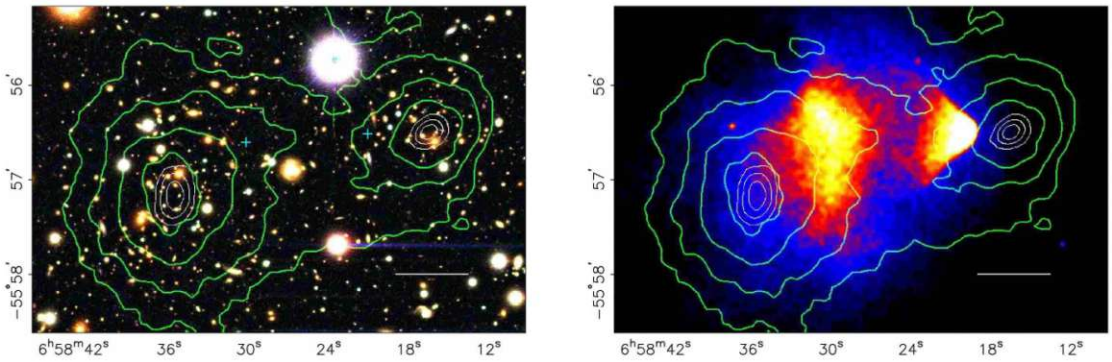

Figure 1.8: Images of the *Bullet cluster* as shown in Ref. [18]. Left: An optical image of the cluster. Right: An X-ray image of the cluster as seen by the *Chandra* observatory. Both images are overlaid with a green contour map showing the gravitational matter distribution calculated from gravitational lensing. The white bar at the bottom right represents 200 kpc at the distance of the cluster.

It is widely known that the majority of the baryonic mass of a galaxy cluster lies in the intergalactic medium (IGM) as hot, X-ray emitting gas containing primarily hydrogen and helium ions at millions of degrees of temperature. The *Bullet cluster* is a collision of two galaxy clusters that happened at some time in the past, and the signature of the penetration can be seen today with the X-ray observation shown in Fig. 1.8(right). A bullet-shaped shock wave can be seen on the right side of the image, which is caused as the right cluster (the sub-cluster) powers through the left one (the main cluster) at a speed of around 10 million km/h (∼3000 km/s) and the IGM gas is slowed down due to electromagnetic interaction. The overlaid green contour map shows the mass distribution using gravitational lensing. It can be seen that there is a clear offset between the two distributions as the majority of gravitating matter in these clusters has little-to-none interaction with the gas or with its counterpart in the other cluster and just passes through each other. This observation crucially signifies the presence of a gravitating matter in the clusters that barely has any interaction with the baryonic matter and is the direct evidence for the existence of dark matter. The observation also indicates the nature of self-interaction of dark matter at the given velocity scale of $\mathcal{O}(10^{-2}c)$, providing the best current constraints on the self-interaction cross-section of the dark matter at $\sigma/m < 1.25\ \mathrm{cm}^2/\mathrm{g}$ [19], where m is the mass of the dark matter particles. It also provides a piece of vital evidence against the theory of Modified Newtonian Dynamics (Sec. 1.3.2) that aims to provide an alternative explanation to dark matter.

Observations across various scales have consistently indicated the presence of non-baryonic

dark matter, constituting approximately five times the abundance of baryonic matter. These observations suggest that dark matter has persisted since the early universe, currently enveloping galaxies and galactic clusters. Importantly, dark matter exhibits minimal self-interaction and interacts weakly, if at all, with baryonic matter. Given its ubiquitous presence around large-scale structures, it is reasonable to infer that dark matter played a pivotal role in initiating the gravitational collapse necessary for the formation of structures in the universe as observed today. In essence, dark matter serves as the gravitational scaffolding upon which baryonic matter collapses, facilitating the development of the cosmic structures we observe.

1.2 Cosmological Description

The framework of the *General theory of relativity* developed by A. Einstein in 1915, was under the assumption of a static universe, an assumption that was a dominant paradigm at the time. Using the equivalence principle, Einstein derived his field's equations relating mass-energy distribution to the spacetime curvature given as:

$$G_{\mu\nu} = \frac{8\pi G}{c^4} T_{\mu\nu} \tag{1.6}$$

where $T_{\mu\nu}$ is called as the *stress-energy tensor*, and it parametrizes the distribution of energy and momentum in spacetime; and $G_{\mu\nu}$ is called as the *Einstein tensor* that describes the curvature of the spacetime and is given as:

$$G_{\mu\nu} = R_{\mu\nu} - \frac{1}{2} g_{\mu\nu} R \tag{1.7}$$

with $R_{\mu\nu}$ as the *Ricci tensor*; R as the *Ricci scaler*; and $g_{\mu\nu}$ as the *metric tensor*. Then, in 1929, Edwin Hubble sat out to measure the relative velocities of different galaxies at different distances using the redshift of their spectral lines [20]. To his surprise, he made a staggering observation that almost every galaxy in his survey of 46 galaxies was redshifted, and the amount of redshift was directly proportional to our radial distance to the galaxy. The expression relating the two could then be written as:

$$v = H_0 d \tag{1.8}$$

where H_0 is called the Hubble constant at the present time, d is the distance to the galaxy, and v is its relative velocity. This relation is famously known as Hubble's law. This finding proved that the universe was not static, but rather expanding. Therefore, the field's equations had to be adjusted for an expanding universe, thereby Einstein adding an extra term to his field's equation such that:

$$G_{\mu\nu} + \Lambda g_{\mu\nu} = \frac{8\pi G}{c^4} T_{\mu\nu} \tag{1.9}$$

where Λ is known as the *Cosmological constant* that acts as a negative pressure that results in the expansion of the universe. The nature of this constant is still an unresolved mystery [17].

Under the assumptions of the *Cosmological principle*, which states that the universe is isotropic and homogeneous on large scales (which can be seen in the CMB as the anisotropies are of the order 10^{-5}), a metric can be chosen that describes the spacetime in the universe. This metric is called as the *Friedmann-Lemaître-Robertson-Walker(FLRW) metric* and is given as (in natural units):

$$ds^2 = dt^2 - a(t)^2 \left[\frac{dr^2}{1 - kr^2} + r^2(d\theta^2 + sin^2\theta d\phi) \right] \tag{1.10}$$

where $k = 0$ for a flat, -1 for a negatively curved and $+1$ for a positively curved spacetime; and $a(t)$ is the *scale factor* whose value goes from 0 to 1 and by definition $a(t_0) = 1$, where t_0 is the present age of the universe. Using this metric under the assumption of the Cosmological principle in Einstein's field equation (Eq. 1.9), and solving it for $\mu = 0, \nu = 0$, we get the first *Friedmann equation* (in natural units):

$$H(t)^2 = \left(\frac{\dot{a}(t)}{a(t)} \right)^2 = \frac{8\pi G}{3}\rho + \frac{\Lambda}{3} - \frac{k}{a(t)^2} \tag{1.11}$$

Now, using the critical density ρ_c required for a "flat" universe ($\rho_c = \frac{3H_0^2}{8\pi G}$), a density parameter Ω_i can be defined for all the terms in the Eq. 1.11 as:

$$\Omega_i = \frac{\rho_i}{\rho_c} \tag{1.12}$$

which simplifies the Eq. 1.11 to:

$$\Omega_m + \Omega_\Lambda + \Omega_k = 1 \tag{1.13}$$

for $\Omega_\Lambda = \Lambda/3H_0^2$ and $\Omega_k = -k/3a(t)^2H_0^2$. Thus, all the terms are shown to contribute to the total energy density of the universe. The matter density parameter can further be expanded into:

$$\Omega_m = \Omega_{\text{Baryons}} + \Omega_{\text{Neutrinos}} + \Omega_{\text{Dark Matter}} + ... \tag{1.14}$$

Thus, Ω_m also contains the contribution of dark matter in the energy density of the universe. From various observations, it is seen that $\Omega_{\text{Dark Matter}}$ contributes to as large as five times Ω_{Baryons}, whereas $\Omega_{\text{Neutrinos}}$ has negligible contribution. The values of Ω_Λ and Ω_k can be measured from the CMB density fluctuations.

1.3 Dark Matter Models

Since its discovery, many different explanations have tried to answer the nature of dark matter. Several models, particles, scenarios, etc., have been suggested that are within and also beyond the Standard Model of Particle Physics. For the particle explanation, the candidate certainly has to satisfy some conditions, such as not having strong or electromagnetic interactions, being stable or long-lived to have survived through the age of the universe, being non-baryonic, having limited self-interaction, etc. Some of these candidate particles, other explanation attempts, and possible models of dark matter have been briefly explained in this section.

1.3.1 MACHOs

Early observations requiring additional unseen mass in galaxies and galactic clusters obviously led astronomers to suspect the compact objects that were much less luminous than stars, and hence not easy to observe, to be the possible explanation of the missing matter. This class of candidates is called as *Massive Astrophysical Compact Halo Objects* (MACHOs). However, if MACHOs were responsible for the massive halo around galaxies, one can expect to observe micro-lensing effects in some of the background stars of the galaxies. Such observations made by EROS collaboration [21] place an upper limit of 8% of halo mass fraction to be coming from MACHOs. Also, since MACHOs are intensely dense baryonic matter, the baryonic content of the universe from BBN as measured by the Planck collaboration [16](discussed in Sec. 1.1.3) also disregards MACHOs as a complete explanation.

There is also a possibility of the formation of black holes before the epoch of BBN, with mass ranges that are below the current sensitivities of microlensing surveys. These are known as the *Primordial Black Holes*(PBH) and dark matter could also consist of them. Although, a major challenge faced by PBHs is if one considers a scale-invariant primordial power spectrum, the predicted formation rate of PBHs comes out to be negligible. In order to produce such black holes, one has to introduce a large variation from the Gaussian distribution in the power spectrum [22].

1.3.2 Modified Newtonian Dynamics

The rotation curves of galaxies could also be explained by requiring a modification in Newton's second law in very low acceleration conditions, as seen in the outer parts of the galaxies. If the force due to acceleration in very low acceleration limit ($a \ll a_0$), were to be given as:

$$F_N = m\frac{a^2}{a_0} \tag{1.15}$$

where $a_0 = 1.2 \times 10^{-10}\mathrm{m/s^2}$ is another fundamental constant, then the resulting dynamics would explain the motion of stars and gasses in the outer parts of the galaxies without

requiring any dark matter. This framework is known as the *Modified Newtonian Dynamics* (MOND), and it was developed by Mordehai Milgrom in 1983 [23]. The model was later also extended as a relativistic theory by Bekenstein and is known as *tensor-vector-scaler gravity* (TeVeS) [24]. Although MOND has been able to explain the rotation curves of the galaxies, since the discovery of the Bullet cluster (Sec. 1.1.4), MOND has faced serious challenges in explaining the behavior of cluster mergers and the CMB anisotropies without the additional contribution of the dark matter.

1.3.3 Neutrinos

The first particle in the Standard model of particle physics that stood out to satisfy the conditions that an ideal candidate dark matter particle should abide was the Neutrino. Naturally, this made them a strong candidate for dark matter. Although, it is now known that neutrinos are very light thermal relics, which makes them a candidate for "hot", relativistic dark matter. From numerical simulations, the differences between the structure formation in the universe from a "hot" dark matter (HDM) scenario and from a "cold" dark matter (CDM) scenario were shown. It was seen that in the HDM scenario, the universe follows a "top-down" approach, where large-scale structures collapse first, and then galaxies and stars are formed. Whereas in the CDM scenario, the "bottom-up" approach is seen where the small-scale structures are seen to collapse first [25]. By comparing these results with the ones of the Galaxy survey [26], any HDM scenario can be ruled out as accounting for most of the dark matter in the universe. Thus, being relativistic, these observations also disregard neutrinos as a potential dark matter candidate.

1.3.4 Axions

Quantum Chromodynamics(QCD) has been incredibly successful in describing the mechanism and interactions of the strong force with exceptional precision. However, there is a problem with the theory that lies in a particular term in the QCD Lagrangian for a single massive quark, i.e.:

$$\mathcal{L}_{QCD} \supset \bar{\Theta}\frac{g^2}{32\pi^2}G^{a\mu\nu}\tilde{G}_{a\mu\nu}, \tag{1.16}$$

where $\bar{\Theta}$ is a dimensionless parameter. This term introduces a CP violation effect in the Lagrangian of the theory, although observations suggest that the theory is CP invariant to very high precision [27], restricting the value of $\bar{\Theta} < 10^{-10}$. This is known as the "Strong CP" problem.

The solution to this problem was suggested by Roberto Peccei and Helen Quinn [28, 29] via a mechanism known as the "Peccei-Quinn mechanism," where they introduced a new $U(1)$ symmetry that is spontaneously broken that brings the $\bar{\Theta}$ down. As a result of this breaking of symmetry, the existence of a new Nambu-Goldstone boson called the Axion,

is predicted. It can be shown that these axions must be very light ($m_a \approx 10^{-4} - 10^{-6} eV$) and very weakly interacting with the standard model, thus could account for the dark matter in the universe. This way, both the strong CP problem and the dark matter problem can be solved. There are dedicated experiments searching for relic dark matter axions and Solar axions like ADMX [30] and CAST [31], Although, to date, no definitive experimental confirmation supporting the existence of axions has been obtained.

1.3.5 Asymmetric Dark Matter

The observed abundance of dark matter compared to ordinary baryonic matter in the universe could also be explained by the presence of a possible asymmetry in the dark sector between dark matter particles and antiparticles, similar to the baryonic sector. These models are known as Asymmetric Dark Matter(ADM) models, and their production mechanism is analogous to baryogenesis in the early universe. Thus, the relic density of dark matter is not defined by its annihilation cross-section as in the standard dark matter scenarios (Sec. 1.3.6), but by any other process in the dark sector that produces this asymmetry. Many of the ADM models suggest the dark matter particle mass in the GeV regime which hints toward their origin to be related to visible sectors such as the QCD or electroweak scales. A detailed review of various ADM models can be found in Ref. [32].

1.3.6 WIMPs

Weakly Interacting Massive Particles (WIMPs) have long been regarded as the leading candidates for non-baryonic, cold, and non-relativistic dark matter. These particles are proposed within a compelling extension of the Standard Model, where their primary mode of interaction is gravity, along with forces comparable to or weaker than the weak force. In the framework of Supersymmetry, the lightest supersymmetric particle (LSP) is often identified as a WIMP candidate. This LSP, known as the Neutralino, is a mixture of supersymmetric partners of neutral gauge bosons (photons and Z bosons) and the Higgs boson. Extensive theoretical and experimental studies have been conducted on WIMPs, with the Neutralino being a well-studied representative. The experimental constraints on WIMPs, to date, form some of the most stringent limitations on dark matter candidates.

The idea is that one can basically consider WIMPs to be in thermal equilibrium in the early universe, where they are continuously produced from and annihilated to Standard Model particles f via scattering:

$$\chi\bar{\chi} \Longleftrightarrow f\bar{f} \tag{1.17}$$

Thus, the number density of WIMPs in the early universe can be described by writing down the Boltzmann equation:

$$\frac{dn_\chi}{dt} = -3Hn_\chi - \langle\sigma_{ann}v\rangle(n_\chi^2 - n_{\chi,eq}^2) \tag{1.18}$$

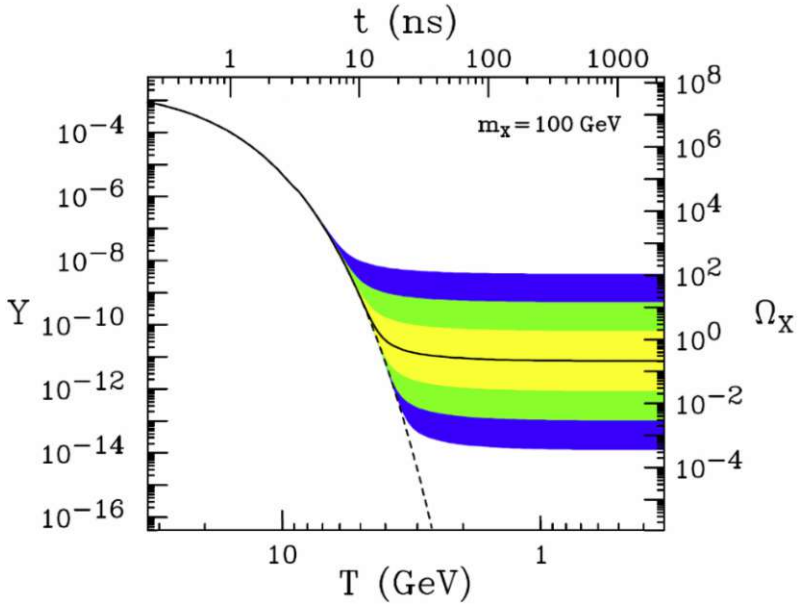

Figure 1.9: An illustration of WIMP freeze-out. At $T >> m_\chi$, the number density sustains an equilibrium value. At $T << m_\chi$, the WIMPs freeze out and maintain a constant number density. Y is dimensionless number density given by n_χ/s, where s is the entropy of the system. Image taken from Ref. [33].

where H is the Hubble's constant; σ_{ann} is the annihilation cross-section of the WIMPs; and $n_{\chi,eq}$ is the number density of WIMPs at the thermal equilibrium. Thus, we can see that with the expansion of the universe and the decrease in the temperature, the equilibrium cannot be sustained anymore, and the WIMPs number density becomes constant in the comoving coordinates (freeze-out) (Fig. 1.9).

By choosing the mass and interaction cross-section of WIMPs with the Standard Model particles in the electroweak scales, one can solve the given Boltzmann equation to calculate the constant number density in the end after freeze-out. It turns out that this matches with the relic density of the dark matter that we observe in the universe today. This remarkable consensus is often referred to as the "WIMP miracle", and provides strong support for the existence of weakly interacting dark matter particles.

A bound on the allowed mass range of WIMPs restricts them to be above ~ 3 GeV/c^2, which is known as the Lee-Weinberg-bound [34]. The idea is that the lower-mass WIMPs would have lower annihilation cross-sections as the cross-section scales by $\sim m^2/M^4$, where m is the mass of the WIMP and M is the mass of the mediator particle, which is taken to be the Z boson. Hence, with lower cross-sections, WIMPs would freeze-out earlier in the universe at relatively higher temperatures, causing it to happen at a relatively higher relic density. As it turns out, for WIMP masses lower than ~ 3 GeV/c^2, the relic density leads to an overclosure of the universe and is the primary reason for the existence of this bound. However, lighter WIMPs can also be explored if one allows for

the existence of a light mediator particle through new forces below the electroweak scale.

1.4 N-body simulations

Our major understanding of the dynamics, nature, and evolution of the galaxy structures in the universe today comes primarily from the results of the N-body simulations. Their results have played a major role in disregarding neutrinos as a dark matter candidate, as discussed in Sec. 1.3.3. Motions of masses in these simulations are considered to be influenced by the gravitational field of other masses around. Thus, structures in the universe form as a result of these gravitational collapses.

Dark matter plays an important role in these simulations as, acting under the CDM paradigm, it behaves as a pressure-less fluid that collapses more readily than the baryonic matter and thus provides the primary potential wells for the visible matter in the universe.

ΛCDM model of the universe is frequently considered as the standard model of Big Bang cosmology where it has primarily three components: 1) Λ that is the cosmological constant which is associated with the accelerated expansion of the universe, 2) CDM that is the collisionless cold dark matter and 3) the ordinary matter. The earlier numerical simulations performed by allowing for density perturbations from CMB as the initial conditions and simulating under the ΛCDM paradigm without ordinary matter showed a remarkable agreement with the observational surveys, on the large-scale structures [35, 36].

1.4.1 Limitations of ΛCDM

Although ΛCDM has been extremely successful at large scales, i.e., $\mathcal{O}$(Mpc), it faces serious challenges at small scales when compared to the observations. A few of the main challenges have been explained in the following:

1.4.1.1 Cusp-Core Problem

The density profile of the dark matter halos in the numerical simulations shows a "cuspy" profile towards the inner radii of the halo. Defining the logarithmic slope of these profiles as $\alpha = d(\ln\ \rho_{dm})/d(\ln\ r)$, it is seen that $\alpha \approx -1$ at smaller radii [37, 38]. Whereas, observation of the velocity dispersion of stars at the inner radii shows no evidence of a cusp but rather a "cored" profile where $\alpha \approx 0$ [39]. This discrepancy between the numerical simulation and the observations is known as the Cusp-Core Problem.

A very well-described parameterization of the density profiles of halos from the N-body simulations was given by J. F. Navarro, C. S. Frank, and S. D. M. White, which is also known as the Navarro-Frank-White (NFW) profile [37] and is given by:

$$\rho_{\mathrm{NFW}}(r) = \frac{\rho_0}{(r/r_s)(1 + r/r_s)^2}, \tag{1.19}$$

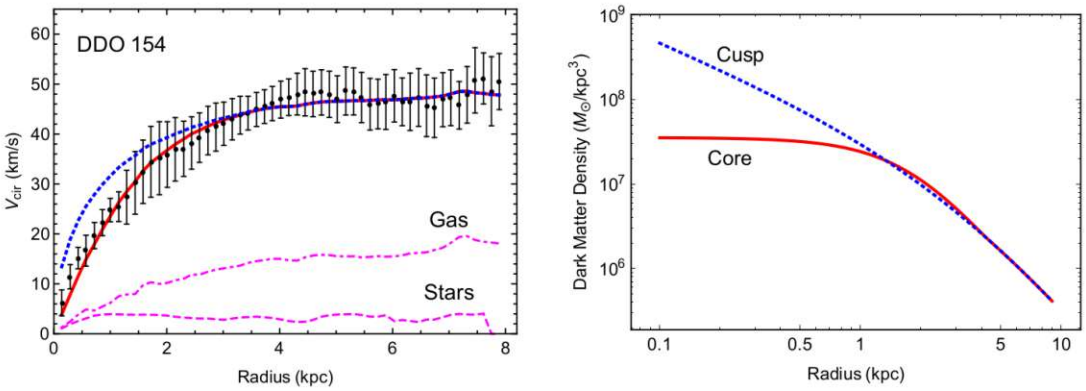

Figure 1.10: *Left:* HI rotation curve of dwarf galaxy DDO 154 with corresponding fits for the cuspy(NFW) profile(red solid) and a cored profile(blue dotted). The stellar and gas contributions are shown in pink dot-dashed lines. *Right:* Corresponding density profiles of the fits. Data is from Ref. [40] and the image is taken from Ref. [41].

where r is the radial coordinate; and r_s and ρ_0 are the scale radius and characteristic density respectively, which is specific to a halo. An example of this problem can be seen in Fig. 1.10, where the rotation curve for dwarf galaxy DDO 154 is shown in black dots with the corresponding fits with the NFW (blue dotted) and cored (red solid) profiles in the left panel. It can be seen that the NFW profile expects a steep rise in the inner radii, which is not seen in the data. The corresponding density profile of these fits can be seen on the right panel.

1.4.1.2 Missing Satellite Problem

The bottom-up scenario of the structure formation, where smaller structures collapse first, is seen to predict a large number of smaller subhalos within the CDM halos in the numerical simulations. For a Milky Way (MW) sized halo, several hundreds of subhalos are predicted with maximum circular velocity $V_{\max} \approx 10 - 30$ km/s, and each should host a dwarf galaxy within. Although, a problem was raised when this number was compared to the observations where only 11 were found at the time [42]. An illustration of this problem can also be seen in the Fig. 1.11:

As can be seen, for subhalo circular velocities $V_{circ} > 50$ km/s, the simulations agree well with the observations. Although, for lower V_{circ}, the numbers start to go off by a factor of five. Thus, the number of smaller subhalos showed a clear discrepancy between simulations and observations.

However, improved simulations, including the effect of baryonic feedback and reionization [43, 44] along with the results of the Sloan Digital Sky Survey and the Dark Energy Survey [45] have shown less severity to this problem. Although this problem remains incompletely resolved, it continues to be an active and ongoing area of research.

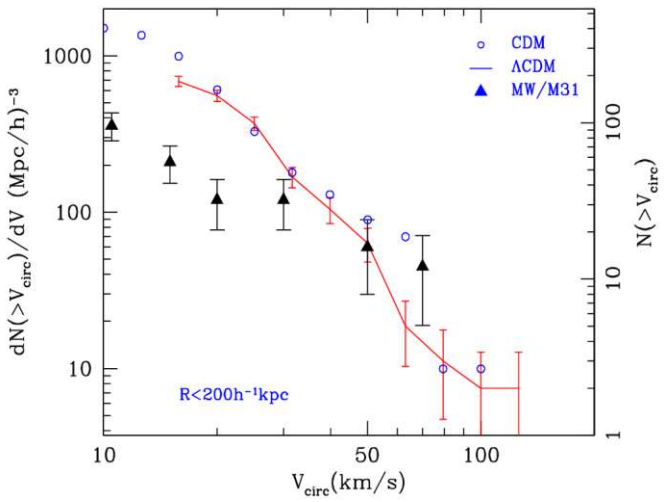

Figure 1.11: The cumulative velocity distribution function(VDF) of the satellite galaxies in the MW and M31 as a function of their circular velocities. The data is only shown for satellites within $200h^{-1}$ kpc, where h is the dimensionless Hubble constant. *Solid black triangles* are the averaged VDF of MW and M31 satellites, *Open blue circles* represent the results from the CDM only simulations, and *Solid red line* shows the averaged VDF in ΛCDM simulation. The y-axis on the right shows the corresponding number of satellites in ΛCDM simulation. Image taken from Ref. [46]

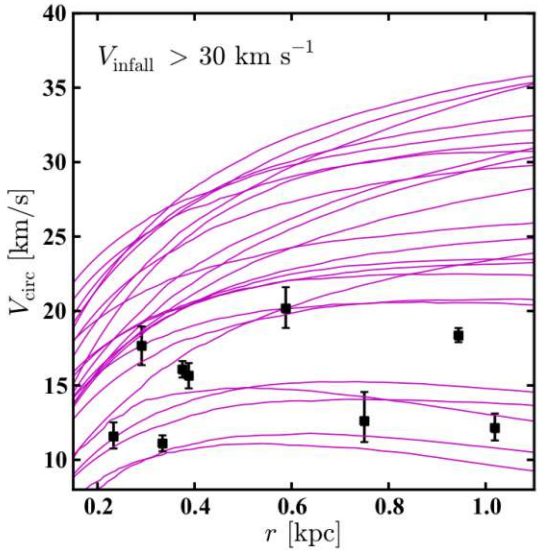

Figure 1.12: *Purple Lines* represents the circular velocity profiles of MW subhalos with maximum circular velocities $V_{\rm max} > 10$ km/s as seen in the CDM simulations. *Black points* are the circular velocities for the brightest dSphs of MW calculated at half-light radius. The data is only shown for subhalos with infall velocity towards the galaxy $V_{\rm infall} < 30$ km/s. Image and data are taken from Ref. [47].

1.4.1.3 Too-big-to-fail(TBTF) Problem

Another discrepancy was seen to arise when the Milky Way's brightest dwarf spheroidals (dSphs) were compared to the CDM simulations. In principle, these dSphs are majorly dark matter dominated and since they have high luminosity and high maximum radial velocities of stars within ($V_{\rm max}$), they are expected to reside within the most massive sub-halos. Whereas in the CDM simulations, the central densities in the most massive subhalos are seen as much larger compared to the observed galaxies.

The most massive MW subhalos are expected to have $V_{\rm max} > 30$ km/s from the simulations, whereas the brightest dSphs are seen to exhibit 12 km/s $< V_{\rm max} <$ 25 km/s (Fig. 1.12). Thus, a question arose why do the most massive subhalos not host stars as their central densities should be "too-big-to-fail" providing the potential wells for the gas to trigger the star formation?

This problem can be seen to be connected to the cusp-core problem as the central densities of the subhalos expected from the simulations seem too large, which makes the gas and stellar velocities steeper than the observations. Thus, by invoking a mechanism that reduces the central densities of these galaxies can potentially solve both of these small-scale issues.

1.4.2 Self-interacting Dark Matter as a potential solution

In order to solve these small-scale issues of ΛCDM, it has been shown in many studies that including the effect of baryonic feedback in the simulations, from supernova explosions, stellar winds, reionization, etc. can disturb the gravitational potential of the galaxies and lead to a shallower density profile [48–50]. Similarly, the cosmological hydrodynamical simulations have been performed that show the missing satellite and TBTF problem could potentially be solved [51]. However, it still remains unclear to what degree should the baryonic feedback affect the halo properties as many discrepancies still remain unsolved [52, 53]. Thus, the small-scale issues of the CDM remain under vast scrutiny and could potentially pose a strong challenge to the paradigm.

Including the effect of self-interactions within the dark matter particles in the N-body simulations has been studied rigorously in recent years as it elucidates the small-scale issues preserving the large-scale structures. The formation of the cores in the central region of the halo can be seen in the following way: For a collisionless CDM halo, the velocity profile peaks at a scale radius r_s (Eq. 1.19), and the region inside and outside r_s is relatively colder. As an effect of self-interactions, collisions start to take place, and the heat starts flowing inwards of r_s because of a huge relative temperature gradient. As the thermal contact is reached with the inner region, the heat starts to flow outwards because of the negative temperature gradient, and gravothermal collapse of the core takes place [54].

Elbert et al.[55] have shown in the simulation of a dwarf galaxy with resolution down to $\mathcal{O}(100$ pc) that the values of σ/m affect the central densities monotonically (Fig.

1.13(left)).

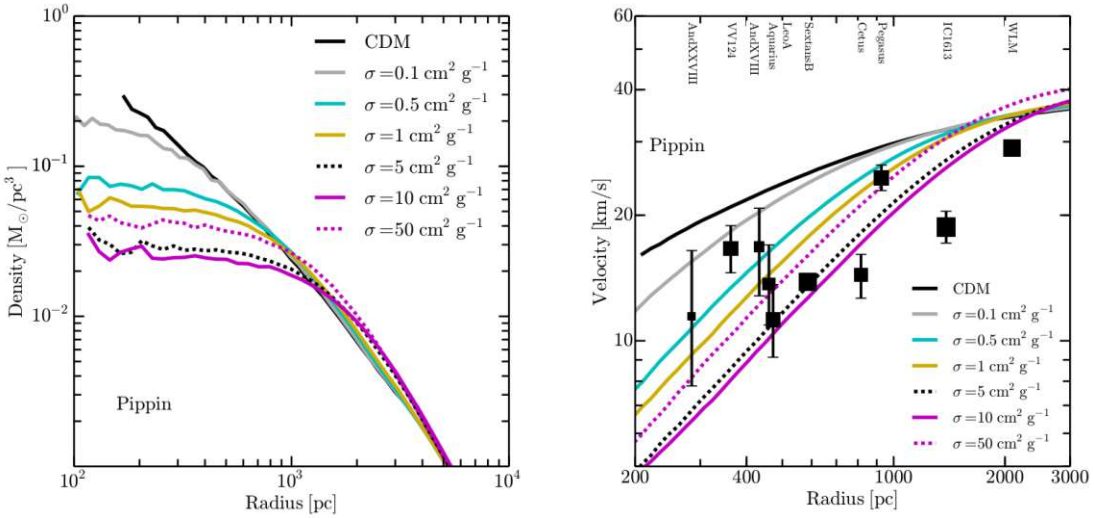

Figure 1.13: *Left*: The simulated density profile for a halo of mass $\approx 10^{10} M_\odot$ in a DM-only simulation with different values of σ/m along with the normal NFW profile from the ΛCDM simulation. *Right*: The corresponding rotation curves, along with the stellar velocity of the field dwarf galaxies in the Local Group, calculated at the half-light radius. Image taken from [55].

A comparison with the dwarf galaxies within the local group has also been shown in Fig. 1.13(right) and the rotation curves seem to be consistent with the simulations. It can be seen that self-interacting dark matter (SIDM), in this context, is able to explain the cusp-core issue by reducing the central densities of the galaxy, and σ/m need not be fine-tuned in order to achieve this. By extension, reducing central densities also poses a solution to the TBTF problem, as already discussed.

Coming to the issue of missing satellites, it was recently shown in a high-resolution SIDM simulation [56] that including a constant $\sigma/m = 1$ cm^2/g, the subhalo mass function for a MW-like halo is very similar to the collisionless CDM case. Allowing for cross-sections as large as $\sigma/m = 10$ cm^2/g, the subhalo mass function reduces by an $\mathcal{O}(30\%)$, and substructures are suppressed, although this comes at a cost that the host halo comes out to be spherical out to 50 kpc, a scenario that is excluded is excluded by ellipticity constraints (A review can be found in Sec. III.C. in Ref. [41]). Thus, it seems from the simulations that SIDM alone is unable to address the missing satellite problem properly. However, SIDM does impact the stellar mass function for subhalos forming reduced central densities, which are less tightly bound and are prone to tidal stripping. Also, as it was already discussed in Sec. 1.4.1.2, the problem in itself has been recently shown to be not as severe as it was originally thought of [43–45].

Cluster mergers: The system of merging clusters of galaxies has provided the most stringent constraints on SIDM. The main tool to study the effect of self-interactions in these systems is to examine the offset of the mass peak, which is inferred through strong

and weak lensing, and the luminosity that comes from the galactic counterparts, which act as collisionless test particle due to negligible cross-sections. After the observation of the Bullet Cluster (Sec. 1.1.4), which remains as the archetypal dissociative merger, many other cluster mergers have been observed providing various constraints on the value of σ/m, where some of them agree with collisionless nature of the DM particles and are consistent with CDM [57, 58] and others where significant offset between the mass peaks and the galactic part can be seen which could be easily explained by self-interactions [59]. A summary of these can be found in Ref. [41].

At these large scales, assuming a fixed σ/m has been unable to reproduce the observed dynamics as at these high velocities, the self-interaction cross section is boosted and thus should produce DM cores and offsets, which have been largely unobserved. Although these observations have been consistent with a low value of $\sigma/m < 0.1$ cm^2/g, thus favoring an inverse velocity dependence of SIDM cross-sections, which explains the observation at all scales.

Since SIDM is able to resolve the small-scale crisis of the ΛCDM, this has led to the development of various SIDM particle physics models. The simplest model considers the existence of a scalar field, and the self-interactions between the dark matter particles arise from the quadratic coupling of this scalar field, giving the existence of a mass scale below the weak scale [60, 61]. However, this model has a major drawback as it results in a constant SIDM cross-section having no velocity dependence, which is required to explain the structures observed on small as well as large scales. Another model predicts the self-interactions to be originating due to an exchange of a gauge boson that exists due to a $U(1)$ gauge symmetry in the dark sector, similar to the visible sector [62, 63]. For this model in the perturbative limit, it can be shown that the strength of the self-interactions depends on the dark matter particle mass, the mediator mass, and the relative velocities between the particles [63]. In the non-perturbative limit, under the existence of an S-wave resonance close to the scattering threshold between the dark matter particles, the self-interactions also allow for the existence of bound states of dark matter particles [64, 65], which are studied in Chapter 6.

CHAPTER 2

Detection techniques of dark matter

To understand the nature of dark matter, there are essentially three main detection channels that are currently employed which study the interaction of the dark matter particles with the Standard Model particles. In the direct detection searches, the potential scattering of dark matter particles with the earth-bound detectors is investigated. The aim of the indirect searches is to look for primary or secondary Standard Model particle signals of dark matter annihilation or decay, potentially coming from regions of high dark matter density in the universe. Whereas, the production of the dark matter particles in the Standard Model particle collisions is searched at the collider experiments. The three Feynman diagrams in Fig. 2.1 illustrate these different detection channels.

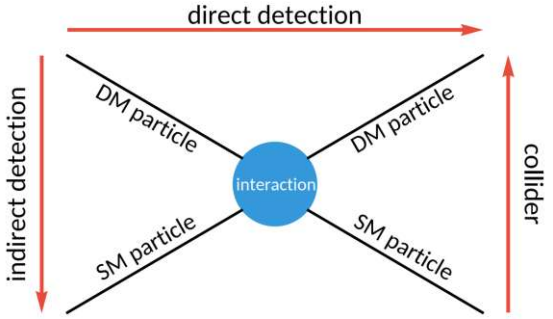

Figure 2.1: The main detection strategies for different dark matter searches[66].

Searches with colliders and indirect detection are discussed very briefly in the following sections. Thereon, different technologies used by the direct detection experiments are shown, and the chapter concludes with the current status of the direct searches.

2.1 Production

If the dark matter interacts with the Standard Model particles weakly, one could expect the production of dark matter particles in the high-energy collider experiments. Since there is no electromagnetic interaction of dark matter, a very clear signal for its production is to look for the missing energy or missing transverse momentum in the final state products. The net momentum in the plane that is perpendicular to the propagation direction of the colliding beams should also be zero in the final products. It's important to note that triggering an event necessitates either initial or final state radiation. Thus, by studying the imbalance in the transverse energy ($E_{\mathrm{T}}^{\mathrm{miss}}$) of the mono-jet events, signatures of dark matter production could be probed [67]. However, since neutrinos also follow similar behavior, they amount to an irreducible background in these searches. Moreover, collider experiments are unable to probe the lifetimes longer than it takes for collision products to transverse the detector, which is required for the dark matter particles that constitute the relic density. Nevertheless, a positive detection in the collider experiments would provide essential insights for the fine-tuning and enhancement of direct detection experiments. A comprehensive review of dark matter searches with collider experiments can be found in Ref. [67].

Currently, no hint of significant excess over the Standard Model predictions has been observed by CMS and ATLAS searches with the center-of-mass energy of $\sqrt{s} \sim 13$ TeV [68]. Under the assumption of which mediator takes part in the interaction, along with assumed coupling strengths, a comparison of the interaction cross-section could be done with the direct detection experiments as shown in Fig. 2.2.

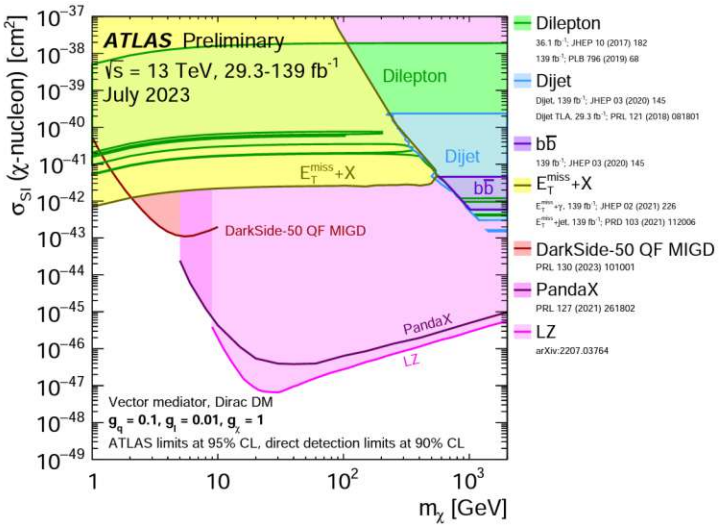

Figure 2.2: Comparison of direct detection exclusion limits of the spin-independent dark matter-nucleus cross-section with the ones inferred from ATLAS search under the leptophilic vector mediator simplified model with the coupling strength as shown in the plot. Reprinted from Ref. [69]

.

2.2 Indirect Detection

The aim of the indirect detection searches is to look for cosmic rays produced in the WIMP annihilation process that is similar to the WIMP freeze-out mechanism (Sec:1.3.6) from the regions of the universe with large dark matter density using ground-based telescopes and instruments. The galactic center and dwarf spheroidal galaxies (dSphs) become the ideal candidate targets for these searches. In principle, the annihilation could produce all the Standard Model particles, although an advantage is provided by studying the neutral particles, such as gammas and neutrinos, as they are not affected by the interstellar magnetic field. Such observation of gamma rays from the dSphs has been performed by the MAGIC collaboration, although no significant excess flux of gammas was observed [70]. Similar observation from the galactic center has shown an excess of gammas after background reduction [71]. However, millisecond pulsars have been shown recently to be a possible explanation of this signal [72]. Another signal that has been observed from the galactic center is the 511 keV gamma-ray line, which is produced when e^-- e^+ pairs annihilate [73]. The origin of this e^+ excess is under investigation, although several dark matter origins of this excess have been proposed [74]. The sun is also a potential target for the evidence of WIMP annihilation as it acts as a local potential well for the dark matter particles. As they accumulate inside the sun and start to annihilate, neutrinos could be produced that can be observed. Since the scattering with hydrogen in the core of the sun slows down the WIMPs and allows them to annihilate, observing these neutrinos also provides a comparison of DM-nucleus cross-section with the direct detection experiments (Fig.2.3) [75]. For an extensive review, the reader is referred to [76].

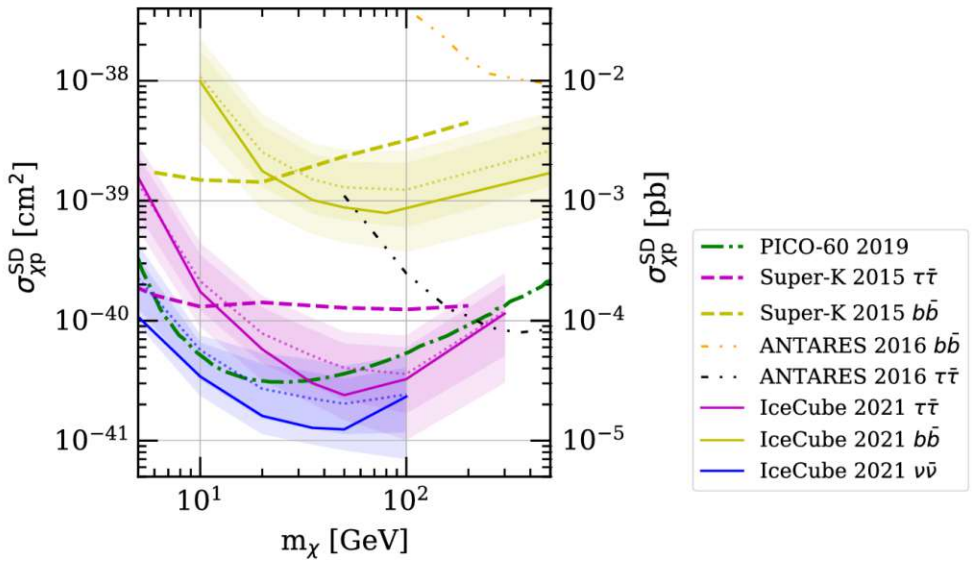

Figure 2.3: Comparison of direct detection 90% exclusion limits of the spin-dependent dark matter-proton cross-section with the ones from Neutrino observatories. Reprinted from Ref. [75]

.

2.3 Direct Detection

Envisioning a scenario where dark matter goes beyond gravitational interactions and possesses a very weak interaction with visible matter, we open up exciting possibilities. The prospect of detecting dark matter through its recoil interactions with earth-bound detector materials comes to the forefront. Ground-based direct detection experiments are diligently trying to identify dark matter particles within our solar neighborhood, presenting an opportunity to affirm the existence of the elusive stuff. These experiments aim to measure the signal that potentially comes from elastic and/or inelastic scattering of dark matter particles in the local dark matter halo with the detector nuclei. Thus, input from astrophysics, as well as nuclear physics, is required in order to understand the expected signal.

As these interactions are exceptionally rare, understanding, identifying, and reducing the background is tremendously important in order to recognize the signal. Thus, most of the direct detection experiments are located underground as rock overburden provides shielding against the cosmic and atmospheric backgrounds. Furthermore, detectors are covered with layers of other active and passive shielding materials. Irrespective of these shieldings, a very small percentage of the background still makes it to the detector, and some radio and cosmogenic background could originate from the detector itself. These backgrounds need to be vetoed or identified. Therefore, experiments use various techniques for this identification, such as pulse shape discrimination, multiple-channel readout, etc.

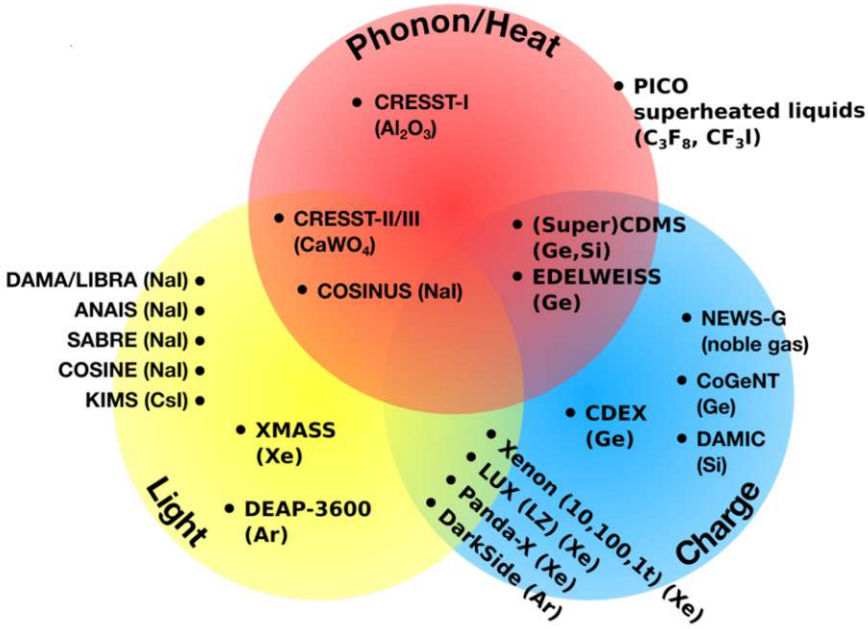

Figure 2.4: Different detection channels used in the direct detection experiments along with some of the experiments using them along with their detector materials. Image taken from [77].

Currently, three main detection channels are used in direct detection experiments that are phonon excitation, scintillation (light), and ionization (charge) (Fig. 2.4). The phonon excitation channel is used to assess the total deposited energy inside the detector. The scintillation signal is used for particle identification in multi-channel experiments via the phenomenon of *quenching* where the nuclear recoils are expected to give a lesser amount of scintillation signal when compared to electron, gamma-ray, or alpha recoil of the same energy. Quenching is seen to be material-specific, and its quantification is done by the *Quenching factor* (QF).

Various detector designs and approaches have been used in the past decades with the aim of detecting the WIMP nuclear recoils. Some of these detector designs have been discussed here. The contents described here closely follow the review in Ref. [78].

2.3.1 Liquid Nobel Gas Experiments

Nobel gasses such as Xenon and Argon are extensively used in direct detection experiments as they are excellent scintillators, chemically inert, dense, and the employed Nobel gasses are inherently low in radioactivity. In the liquid form, they can be used to massively upscale the detector volume and mass, thereby increasing the total exposure, which increases the probability of catching a rare event such as a WIMP/neutrino scattering. Hence, these experiments show leading sensitivities to high-mass dark matter particles.

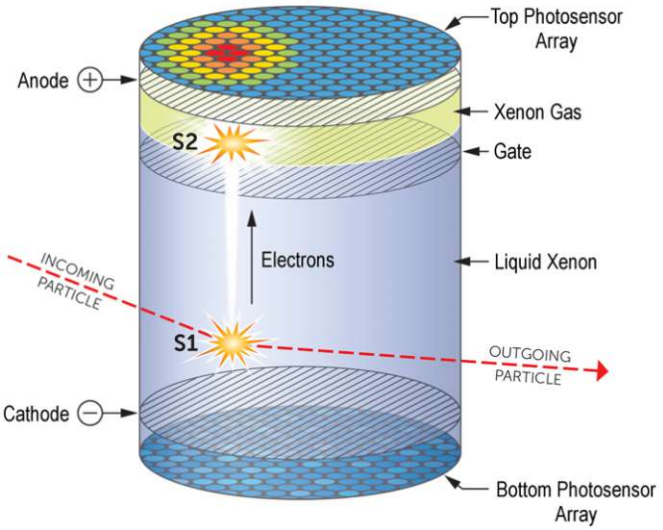

Figure 2.5: A schematic of the dual-phase time projection chamber with an illustration of detection mechanism upon a particle interaction. Image taken from Ref. [79].

Experiments such as XENONnT[80], LUX-ZEPLIN(LZ)[81], PandaX[82] and Darkside-50[83] employ the concept that is dual-phase time projection chamber(TPC) in their experiments, where both the scintillation as well as the ionization signal of the interaction are read. These TPCs are filled with huge amounts of liquid noble gasses in a cylindrical

tank. Upon an interaction, scintillation light is produced, which is detected by the photo-multiplier tubes(PMTs) installed above and below the tank. This allows reconstruction of the position of interaction in the horizontal plane of the tank and is typically known as the S1 signal. Electrons and hole pairs are also created as a result of the initial interaction. In order to accelerate them, a strong electric drift field ($\sim$ 0.1 - 1.0 kV cm^{-1}) is applied, which takes them to the gas-liquid interface where an even stronger extraction field ($\sim$ 10 kV cm^{-1}) is present. As these electrons enter the gaseous medium, they produce another burst of scintillation light, which is also read by the PMTs. The time delay between S1 and this second signal(S2) is proportional to the drift time and gives information on the position of the interaction on the vertical axis of the detector. Combining both signals allows reconstruction of the 3D position of the interaction and enables *fiducialization* i.e. ability to reject the events that occur very close to the TPC wall. This helps in significant background reduction in TPCs as the majority of the background originates from outside the walls or the walls themselves. Moreover, for liquid Xenon detectors, taking the ratio of S2/S1 allows to distinguish nuclear recoils from electron recoils as the electron recoils are expected to induce more charge, which helps in further background reduction. A schematic of the dual-phase TPCs can be seen in Fig. 2.5.

Similarly, single-phase detectors also exist where only the first scintillation light signal(S1) is read. These detectors are typically spherical and have a 4π PMT coverage in order to increase the light collection efficiency. Additionally, these detectors also use pulse shape discrimination in order to separate nuclear recoils from other backgrounds, especially for liquid argon. This is due to a large difference in the decay times of its excited ionized states between the nuclear and the electron recoils (DEAP-3600 [84]).

2.3.2 Bubble Chambers

These detectors work on the principle of nucleation, where superheated liquids are kept in a condition such that their temperature and pressure are very close to the boiling point of the liquid. Upon the interaction with an incoming particle, if the energy deposition is above the detector threshold, it can locally heat the liquid and cause a local phase transition, leading to the formation of macro bubbles. These bubbles can easily be detected via stereoscopic camera readout. Since the formation of bubbles takes place at the site of interaction, it also allows for fiducialization and thus helps in background reduction similar to liquid noble gas experiment (Sec. 2.3.1). Electron and gamma background are easily reduced in these experiments as the probability of the formation of bubbles from an electron recoil is extremely low. Thus major background in these experiments comes from neutrons and α-particles, although α recoils can be identified based on the acoustics of the bubbles [85]. Many of the target liquids used in these experiments (CF_3I, C_3F_8, etc.) contain ^{19}F, which allows them to probe the dark matter-proton spin-dependent interactions (PICO [86]). Additionally, some of the targets also contain iodine, which provides good sensitivity to spin-independent interactions and can also be compared with the other scintillating crystal detector experiments using NaI (Sec: 2.3.4).

2.3.3 Cryogenic Detectors

Cryogenic detectors work with crystals that aim to measure the phonon signals that originate upon elastic/inelastic interaction inside the target material. The operating temperatures of these materials are generally below 50 mK, and they are required to be of low heat capacity in order to reach very low energy thresholds ($\leq$ 100 eV). The created phonons cause a tiny increase in the temperature of the target, which is typically read out by either transition edge sensors (TESs) for athermal phonons or neutron transmutation doped(NTDs) germanium thermistors for the heat. Having a secondary channel readout of ionization/scintillation also allows for the discrimination of electron/gamma recoils from the nuclear recoils, which helps in background identification.

For kinematic reasons, having low energy thresholds is required in order to probe low-mass dark matter particles. Thus, these experiments lead in the low mass dark matter search regime. However, these crystals are hard to operate at the exposure of liquid noble gas experiments because of two major reasons. First is that increasing the mass of individual crystals leads to an increase in the heat capacity which decreases the sensitivity. Secondly, the growth of large radiopure crystals and their instrumentation are intensively intricate processes.

A few examples of cryogenic experiments include: EDELWEISS [87], which uses Ge as a target material, and SuperCDMS [88], which uses Ge and Si. Both of these experiments also use the ionization readout for particle discrimination. CRESST-III [89], which mainly uses $CaWO_4$ along with a scintillation light readout. As CRESST-III is the focus of this thesis, its detector design and readout will be explained in detail in the following chapter. COSINUS [90] is another upcoming cryogenic experiment that employs NaI, with the advantage of being able to discriminate between nuclear and electron recoils as the detector technology is similar to that of CRESST.

2.3.4 Scintillating Crystal Detectors

These are usually detectors with arrays of NaI(Tl) or CsI(Tl) scintillating crystals that aim to measure the quenched scintillation light upon a WIMP-nucleus recoil. The scintillation light is detected using the PMTs. Having large mass numbers for Iodine and Cesium gives high sensitivity to spin-independent dark matter interactions. Since these detectors have only single-channel scintillation readouts, background discrimination on an event-by-event basis is not possible. Hence, they typically have high intrinsic background levels. Thus, these experiments aim to measure the annually modulating dark matter signal above the non-modulating background. Annual modulation of the dark matter signal is expected as the Earth goes around the sun throughout the year. Usually, one would expect a higher event rate when the Earth is moving opposite to, and a lower event rate when the Earth is moving with the direction of the local WIMP wind.

One such signal is reported by the DAMA/LIBRA collaboration that uses an array of 25 NaI crystals (5×5) with a mass of 9.7 kg each. They have been reporting an annual modulation in their event rate with 22 annual cycles(Fig. 2.6) with 2.86 tonne-year of full

exposure and 13.7σ confidence level [91]. The modulation amplitude reported is (0.01058 $\pm$ 0.00090) and (0.01014 $\pm$ 0.00074) cpd/kg/keV for 1-6 keV$_{ee}$ and 2-6 keV$_{ee}$ energy range respectively. The energy here is given in electron equivalent(ee) units, which has been explained in Sec. 3.3.1. The phase and the amplitude are seen to be compatible with the expectation from the motion of the Earth in the galactic frame. Despite its apparent significance, the assertion made by DAMA/LIBRA lacks acceptance within the dark matter research community. This is primarily due to the fact that the calculated cross-section and dark matter mass based on DAMA's results [92] have already been ruled out by other direct detection experiments.

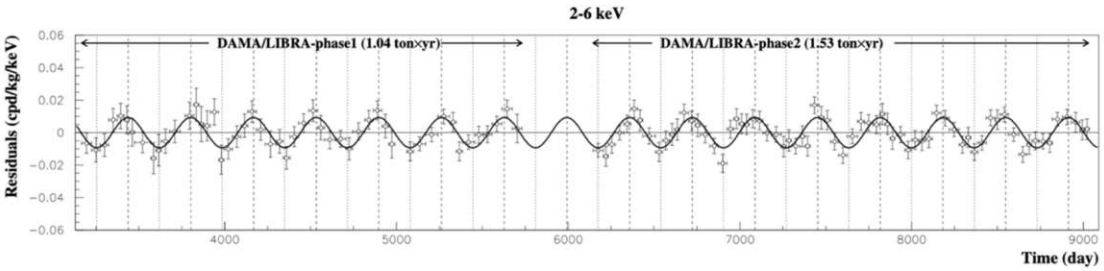

Figure 2.6: Annual modulation shown in the residual event rate in the range of 2-6 keV$_{ee}$ for the DAMA/LIBRA-phase1 and phase2 [91]. The time axis starts around 3300 days after the first measurement[93].

In order to study the material dependence of the dark matter interaction, several other NaI(Tl) have also been running and also under construction. COSINE-100 has performed a search with 2.82 years of data taking with 106 kg of NaI(Tl) and has reported the modulation amplitude to be (0.0067 $\pm$ 0.0042) and (0.0051 $\pm$ 0.0047) cpd/kg/keV in the same energy region (keeping the phase and period fixed as DAMA's), which neither confirms nor denies DAMA's claim [94]. They plan to release their new analysis with twice the exposure soon, and then upgrade to COSINE-200 with newly developed crystals with low background levels [95], which would improve their sensitivity to observe DAMA's signal. ANAIS employs 112.5 kg of NaI(Tl) crystals (or ANAIS-112) and has reported results after 3 years of running, modulation amplitudes of (–0.0034 $\pm$ 0.0042) and (0.0003 $\pm$ 0.0037) cpd/kg/keV being incompatible with DAMA results at 3.3 σ and 2.6 σ significance [96]. In order to demystify the modulation seen by DAMA as originating due to seasonal effects in the background, SABRE aims to use twin detectors in the northern and southern hemispheres, where the seasonal effect would have an opposite phase in the modulation of signal in the two detectors [97]. Lastly, COSINUS (as already explained in the previous subsection 2.3.3) would use NaI as a scintillating calorimeter with background discrimination capability [90] and is expected to deliver the first 1π physics results by the end of 2025.

2.3.5 Current Status

The current status of the direct detection searches showing the leading exclusion limits in different detection technologies can be found in Fig. 2.7. It can be shown that utilizing the Migdal effect for setting exclusion limits enables the probing of even lower dark matter masses [98]. First postulated by Arkady B. Migdal in 1956 [99], the Migdal effect involves the modification of ionization energy in a material due to interactions between the incoming particle and the surrounding atomic electrons, including their subsequent excitation. However, due to the absence of experimental confirmation for this effect, the limits derived using the Migdal effect are not presented here.

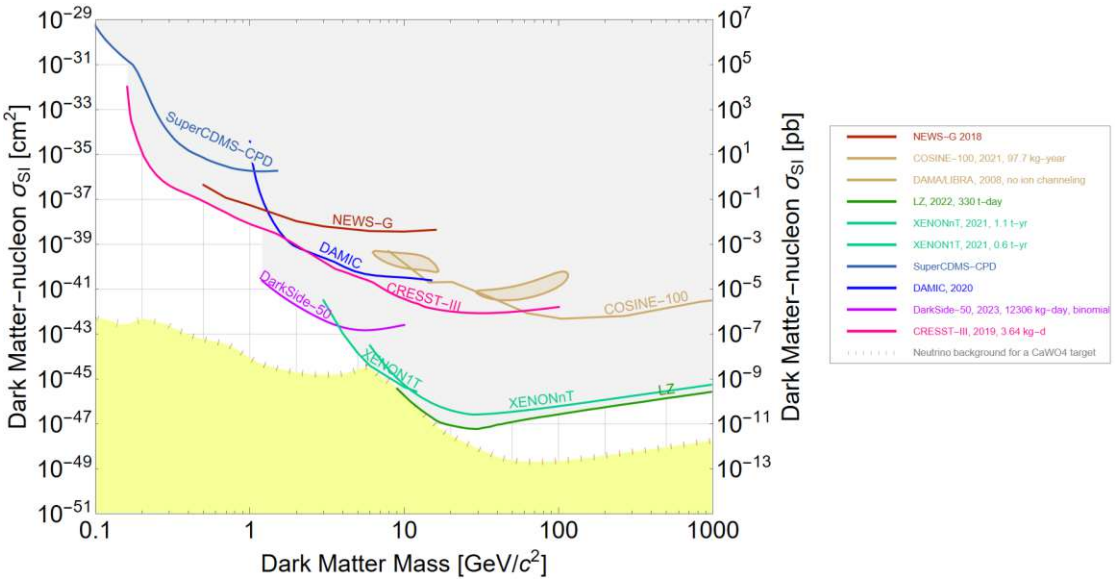

Figure 2.7: Current status of direct detection experiments searching for spin-independent WIMP-nucleus elastic scattering. Limits obtained using the Migdal effect [99] are not shown here. The plot is obtained using SuperCDMS's limit plotter [100]. Along with the ones explained in the text, exclusion limits from NEWS-G [101], DAMIC [102] and SuperCDMS-CPD [103]. The yellow region represents the coherent neutrino background for $CaWO_4$ target [104].

As expected, for high-mass WIMPs, liquid noble gas experiments provide the leading sensitivity as they can run with huge amounts of exposure due to the high-mass targets. They also employ Xenon, which has a high mass number (A = 131.29), and they run at very low background levels. The most stringent limit above 9 GeV/c^2 is provided recently by the LUX-ZEPLIN experiment with a 90% confidence level [81]. The lowest probed cross-section delivered by them is 9.3×10^{-48} cm^2 for a 36 GeV/c^2 WIMP. From 3.6 - 9.0 GeV/c^2, the XENON experiment leads the searches with XENON1T [105, 106] and XENONnT [80]. The region 1.2 - 3.6 GeV/c^2 is led by DarkSide-50 [107], with their LAr TPC experiment. The region below 1.2 GeV/c^2, until 160 MeV/c^2, is led by CRESST-III running $CaWO_4$ as cryogenic calorimeters [89]. The two islands seen around 10 and 50 GeV/c^2 are the discovery islands compatible with DAMA/LIBRA

using NaI(Tl) scintillators [92, 108]. Using the same material, COSINE-100 has its limits very close to these islands and plans to improve in the coming years [109].

With the goal of exploring the entire accessible parameter space above the neutrino fog [104], many of these various experiments are planning upgrades in the coming future. From the LXe side, a multi-ton detector target is proposed by the DARWIN collaboration, that aims to reach the cross-sections of 2×10^{-49} cm^2 at 40 GeV/c^2 WIMP mass using a 200 t×year exposure [110]. Similarly, DarkSide-20k is planned to operate a 23 t LAr target with an ultra-low background, which is expected to reach a sensitivity of around 1.2×10^{-47} cm^2 for 1 TeV/c^2 WIMPs [111]. The ultimate aim of the LAr community is to build the ARGO detector with a 300 t fiducial mass, which is expected to push the sensitivity for high-mass WIMPs where the coherent neutrino scattering of the atmospheric neutrinos becomes a limiting background [112]. A detailed review of direct detection experiments can be found in Ref. [78].

CHAPTER 3

CRESST Dark Matter Search

The work in this thesis is focused on the direct detection of dark matter using the CRESST experiment, hence, in this chapter, the CRESST dark matter search will be discussed in detail. The chapter starts with the derivation of the expected nuclear recoil spectra for the spin-independent interaction of dark matter seen by the earth-bound experiments, and then the spectra specifically for the CRESST detectors are calculated. This is followed by the description of the detector setup and its working principles. Details on the data acquisition system are discussed at the end of the chapter.

3.1 The Expected Signature

It is known that the Earth and the whole solar system move around the center of the Milky Way through a dark matter halo whose distribution and mass have been calculated using measurement of stellar velocities with the Hubble space telescope and the GAIA telescope [113]. Assuming that the halo is composed of standard WIMPs (which we denote by χ), a flux (Φ_χ) of these WIMPs on earth can be calculated using their number density (n_χ) and expected relative velocity($\langle v_\chi \rangle$):

$$\phi_\chi = n_\chi \cdot \langle v_\chi \rangle = \frac{\rho_\chi}{m_\chi} \cdot \langle v_\chi \rangle \tag{3.1}$$

where ρ_χ is the density and m_χ is the mass of the WIMPs. Given the flux of the incoming particles, the total rate of interaction R for a unit mass of the detector material depends on its interaction cross-section with the target material ($\sigma_{\chi N}$) and the total number of target nuclei N_T in the following way:

$$R = \Phi_\chi \cdot \sigma_{\chi N} \cdot N_T = \frac{\rho_\chi}{m_\chi} \langle v_\chi \rangle \cdot \sigma_{\chi N} \cdot \frac{M_T}{m_N} \tag{3.2}$$

where M_T is the mass of the target material and m_N is the mass of one nucleus inside the target material.

The expected value of the WIMP velocity can be calculated using the WIMP velocity distribution in the Milky Way, which is given by $f(\vec{v})$. Now, rather than using the total rate, a more relevant quantity used by experiments is the differential interaction rate, which is typically measured in terms of the number of events per kg of the detector material, per day, and per keV of recoil energy. This quantity can easily be derived from Eq. 3.2 by differentiating it with respect to the recoil energy E_R and calculating it for 1 kg of detector material:

$$\frac{\mathrm{d}R}{\mathrm{d}E_R} = \frac{\rho_\chi}{m_\chi m_N} \int_{v_{min}}^{v_{esc}} \mathrm{d}^3v f(\vec{v}) v \frac{\mathrm{d}\sigma_{\chi N}(\vec{v}, E_R)}{\mathrm{d}E_R} \tag{3.3}$$

where the lower limit of the velocity integral is the minimum velocity that can be probed by a specific nucleus of the detector material, which is the minimum WIMP velocity required to produce a nuclear recoil of energy, E_R. This is given by:

$$v_{min} = \sqrt{\frac{E_R m_N}{2\mu_N^2}} \tag{3.4}$$

where μ_N is the reduced mass of the WIMP-nucleus system. The upper limit of the velocity integral is truncated at the escape velocity of the Milky Way galaxy, as WIMPs with higher velocity are not expected to be bound to the halo.

Now the quantity of interest is the differential WIMP-nucleus scattering cross-section $\frac{\mathrm{d}\sigma_{\chi N}}{\mathrm{d}E_R}$, which describes the final spectral shape. This quantity, in general, has two major contributions coming from the spin-independent(SI) interactions and the spin-dependent(SD) interactions:

$$\frac{\mathrm{d}\sigma_{\chi N}}{\mathrm{d}E_R} = \left(\frac{\mathrm{d}\sigma}{\mathrm{d}E_R}\right)_{\mathrm{SI}} + \left(\frac{\mathrm{d}\sigma}{\mathrm{d}E_R}\right)_{\mathrm{SD}} \tag{3.5}$$

where the SI interaction describes all the scalar interactions with the nuclei and scales with mass number as A^2. The coupling of WIMPs to protons and neutrons is usually taken to be equal. The SD interaction describes the interaction with the net spin of the nuclei, which is determined by the single unpaired protons or neutrons and is generally zero for nuclei with an even number of nucleons. A brief description of the differential cross-section for the SD interactions can be found in Sec. 5.4. Here, we focus mainly on the SI interactions. Assuming the elastic interaction between the WIMP and nucleus to be a point-like interaction, the differential scattering cross-section, in this case, is given by [114, 115]:

$$\left(\frac{\mathrm{d}\sigma}{\mathrm{d}E_R}\right)_{\mathrm{SI}} = \frac{\sigma_0}{E_{R,max}(v)} F^2(E_R) \tag{3.6}$$

where σ_0 is the point-like scattering cross-section, $E_{R,max}$ is the maximum possible recoil energy for a WIMP of velocity v, and $F(E_R)$ is the nuclear form factor which will be described later. To figure out $E_{R,max}$, we can consider a scattering scenario of two particles in the non-relativistic limit and center-of-mass frame. The recoil energy as a function of scattering angle θ is given by:

$$E_R = \frac{\mu_N^2 v^2 (1 - \cos\theta)}{m_N} \tag{3.7}$$

Therefore, the maximum recoil energy transferred would be for $\cos\theta = -1$, which is

$$E_{R,max} = \frac{2v^2\mu_N^2}{m_N} \tag{3.8}$$

It also has to be considered that σ_0 contains the information about scattering with a particular target and thus cannot be compared between different experiments and approaches. Thus, σ_{WN} is used as the main quantity, which is the cross-section normalized to one nucleon, and it allows comparison between different experiments. It is given by [115]:

$$\sigma_{\mathrm{WN}} = \left(\frac{1 + m_\chi/m_N}{1 + m_\chi/m_p}\right)^2 \cdot \frac{\sigma_0}{A^2} \tag{3.9}$$

where m_p is the mass of a proton.

Thus, using Eq. 3.6, 3.8, 3.9 in Eq. 3.3, we get:

$$\frac{\mathrm{d}R}{\mathrm{d}E_R} = \frac{\rho_\chi}{2m_\chi\mu_p^2} A^2 \sigma_{\mathrm{WN}} F^2(E_R) \int_{v_{min}}^{v_{esc}} \mathrm{d}^3 v \frac{f(\vec{v})}{v} \tag{3.10}$$

where μ_p is the reduced mass of a WIMP and a proton.

The remaining quantities that need to be figured out are the velocity distribution of WIMPs in the Milky Way $f(\vec{v})$, the local dark matter density ρ_χ, which requires input from astrophysics, and the nuclear form factor $F(E_R)$, which needs input from nuclear physics. First, we focus on the astrophysical inputs and then on the form factor.

3.1.1 Velocity Distribution

To calculate the relative velocity of the WIMPs on Earth, the velocity of WIMPs in the galactic frame, the tangential movement of the sun around the galactic center, the annual movement of the Earth around the sun, and the rotation of Earth around its own axis need to be considered.

The dark matter halo is generally considered to follow an isotropic, spherical profile following the thermalization of the dark matter particles. In the galactic rest frame, the

simplest model that describes the velocity distribution for the given conditions is the Maxwell-Boltzmann distribution[115]:

$$f_G(\vec{v}_G) = \frac{1}{\mathcal{N}} \left(\frac{3}{2\pi w^2}\right)^{3/2} \exp\left(-\frac{3v_G^2}{2w^2}\right) \tag{3.11}$$

where w is the root-mean-square velocity given by $w = \sqrt{3/2}v_\odot$, $v_\odot$=220 km s^{-1} [116] denotes the velocity of the sun and $\mathcal{N}$ is the normalization factor which is given by:

$$\mathcal{N} = \text{erf}(z) - \frac{2}{\sqrt{\pi}} z \exp(-z^2) \tag{3.12}$$

for $z = v_{esc}/v_\odot$, and $v_{esc} = 544$ km s^{-1} [117] .

Now, since the detector is earth-bound and the earth is moving through the galactic halo along with the sun, a Galilean transformation has to be applied to the velocity distribution in Eq. 3.11. Earth's velocity in the galactic frame ($v_\oplus$) is given by [118]:

$$v_\oplus(t) = 220 \cdot \left[1.05 + 0.07\cos\left(\frac{2\pi(t-t_0)}{1\text{ yr}}\right)\right] \text{km s}^{-1} \tag{3.13}$$

where 220 km s^{-1} is the velocity of the tangential velocity of the sun around the galactic center [116], and t_0 represents the time of the year when the velocity of the earth is maximum with respect to the WIMP wind which happens at June 2nd. The factor 1.05 comes by taking the average velocity of the sun throughout the year and a factor of 0.07 comes by taking the component of velocity of the earth around the sun against the direction of the WIMPs. The Earth goes around the sun at $v_{\text{earth}} = 30$ km s^{-1} and rotates at an angle of 60^o w.r.t. the WIMP wind ($\frac{30}{220}$.cos 60^o $\sim$ 0.07). Thus, the final WIMP velocity w.r.t. the Earth would be v_G+$v_\oplus$. In principle, the daily modulation due to the earth's rotation on its own axis should also be taken into account, but we ignore that as the effect would be very small and cannot be probed given the sensitivities of the current experiments.

Now, it can be seen that the annual variation in velocity is of small magnitude ($\mathcal{O}(10\,\%)$), and as a typical CRESST run lasts more than a year, this value is averaged throughout the year. Therefore, applying this Galilean transformation to the velocity distribution, the velocity integral in Eq. 3.10 can thus be calculated, and its analytical form can be found in Ref. [115]. It has to be noted that the rate change due to this annual modulation can still be probed with the sensitivities of the current experiments if a signal above the backgrounds is observed and depending on the threshold of the detector, modulation of the rate much more than $\mathcal{O}(10\%)$ can be seen. Its observation with a correct phase would be considered as *smoking gun evidence* of the existence of WIMPs. However, this has to be confirmed by different experiments, and other possible effects that could cause an annual modulation (E.g., seasonal effects, stability of the detector, etc.) have to be cross-checked as well.

It could also be possible that the WIMP halo in the Milky Way has a net angular momentum, and thus can have a co-rotation or counter-rotation with the galactic disk. The effect of this rotation on the velocity distribution and the dark matter results has been studied and can be found in Ref. [115].

3.1.2 The Form Factor

The last ingredient left to be figured out is the input from nuclear physics about the form factor. In the case of a WIMP-nucleus interaction, that takes place with a high amount of momentum transfer, the structure of the nucleus also has to be taken into account and cannot be seen as a point-like interaction anymore. The form factor provides information about the internal structure of the nucleus, and it can be seen as a Fourier transform of the nuclear density.

The dark matter community most commonly uses the description put forth by Helm [119], which was investigated for SI and SD WIMP-nucleus interactions by Engel [120]. In this description, the nucleus is defined as a sphere of a constant density that drops at the edges with a Gaussian distribution with a defined *skin length (s)*. Taking the Fourier transformation of this density leads to the form factor given by:

$$F(q) = 3\frac{j_1(qR_0)}{qR_0}\exp\left(\frac{1}{2}q^2s^2\right) \tag{3.14}$$

where j_1 is the first spherical Bessel function, q is the transferred momentum during the scattering, and is given by:

$$q = \sqrt{2m_N E_R} \tag{3.15}$$

For R_0, the parametrization given by Lewin and Smith [121] can be used for various nuclei:

$$R_0 = \sqrt{c^2 + \frac{7}{3}\pi^2a^2 - 5s^2} \tag{3.16}$$

for,

$$a = 0.52 \text{ fm}, \quad c = 1.23A^{1/3} - 0.6 \text{ fm}, \quad s = 0.9 \text{ fm} \tag{3.17}$$

For the calculations and results shown in this work, the model-independent form factors were used for light nuclei, and the Wood-Saxon form factor [122] was used for Tungsten as described in Ref. [123]. Details of this approach can be found in Ref. [123]. It has to be noted that for low-mass dark matter interactions, the momentum transfer is low, and thus, the form factor factor does not play a very crucial role.

3.1.3 Differential Recoil Rate for different Nuclei

Having figured out all the different functions required to calculate the expected nuclear recoil spectra for WIMP-nucleus spin-independent interaction, we can go ahead and plot

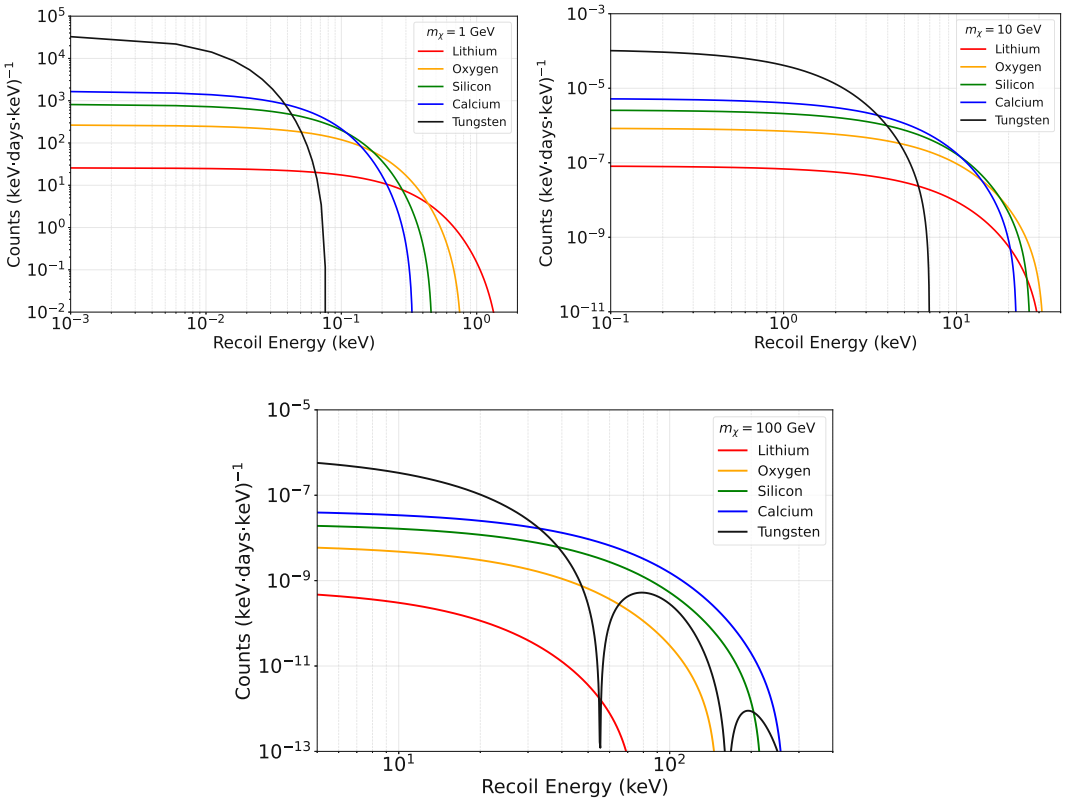

Figure 3.1: Expected nuclear recoil spectrum for elastic WIMP-nucleus spin-independent interaction for various nuclei and WIMP masses as shown in the figure. The interaction cross-section is taken to be 10^{-39}, 10^{-46} and 10^{-47} cm^2 for $m_\chi = 1$, 10 and 100 GeV/c^2 respectively.

the spectra for different target nuclei, for different potential WIMP masses. The value of the local WIMP density ρ_χ can also be extracted from astrophysics, and typically $\rho_\chi = 0.3$ GeV c^{-2} cm^{-3} [124] is used by the direct detection community although recently a slightly higher value ($\sim 0.4 - 0.6$ GeV c^{-2} cm^{-3}) has been proposed [125]. Although for the sake of comparison between different experiments, the calculations performed in this thesis are done with $\rho_\chi = 0.3$ GeV c^{-2} cm^{-3}. As ρ_χ scales the spectrum linearly, uncertainties on its value do not have an impact on the results.

For demonstration purposes, the spectra are calculated for three different WIMP masses of $m_\chi = 1$, 10, and 100 GeV/c^2 with the interaction cross-section $\sigma_{\mathrm{WN}} = 10^{-39}$, 10^{-46}, and 10^{-47} cm^2, respectively. These particular cross-sections are chosen as they lie just below the region in the parameter space, which has been excluded by different experiments for their respective masses (Fig. 2.7). Fig. 3.1 shows the spectra calculated for lithium, oxygen, silicon, calcium, and tungsten. These nuclei are chosen for calculation as these are the ones that are employed in the latest run of CRESST-III, along with Aluminium. The spectrum for aluminium looks very similar to the one for silicon as their mass numbers are close to each other; thus, they are not shown separately. The reasons for using these

particular choices of nuclei have been discussed in Chapter 5.

These spectra yield insights into the reasons why various experiments exhibit different sensitivities across distinct dark matter mass scales:

1. For higher WIMP masses, the expected rate is seen to be very low, and it decreases with using a lighter nucleus to probe the interaction. Thus, in order to detect a signal, it is useful to employ heavy nucleus targets and, more importantly, to scale the exposure to a very high order of magnitude rather than a few kg-days. Hence, we can understand why liquid noble gas experiments aim toward tonne-year exposures in order to reach a detectable count rate.

2. For lower WIMP masses, it can be seen that the exposure does not play as a critical role as the target nuclei and the detection threshold does, so a few kg-days of exposure is enough to see a signal if the interaction cross-sections are just below the current excluded limits. Even though using a heavy mass number target gives a higher count rate, the number of counts falls much more rapidly as we increase the mass number and can go to zero below the detection threshold. Thus, for probing low-mass WIMP interactions, it is useful to use lighter nuclei and also decrease the detection thresholds in order to see a detectable signal. The high sensitivity of CRESST for sub-GeV WIMPs can thus be understood as it has been using $CaWO_4$, Si, and Al_2O_3 containing these light nuclei and it is also able to achieve thresholds way below the keV range[89, 126, 127].

3.1.4 Detector Effects on Spectrum

The plots shown in Fig. 3.1 represent the recoil spectra for an ideal detector, i.e., a detector with zero resolution and threshold containing only one type of nucleus in the material. In the real world, however, detector effects come into play and have to be considered when deriving the sensitivities (or discovery claims). This is done by utilizing details regarding the finite resolution and threshold characteristics of the detector. If the detector material comprises multiple nuclei, their individual spectra, along with their mass fractions, are incorporated into the anticipated spectrum. Additionally, another crucial factor comes into play, stemming from the requirement to obtain a clear and accurate measured spectrum. Consequently, various analysis cuts are applied to eliminate evident noise and artifacts. While applying these cuts, there is a probability of removing valid events, which also has to be considered and is typically known as the survival probability. The procedure of selecting these analysis cuts and calculation of the survival probability is discussed in detail in Chapter 4.

Including these factors in the expected spectrum, the observed spectrum takes the form [128]:

$$\left(\frac{\mathrm{d}R}{\mathrm{d}E_R}\right)_{obs} = \Theta(E - E_{R,thr}) \cdot \epsilon(E_R) \cdot \int_0^\infty \left(\frac{\mathrm{d}R}{\mathrm{d}E}\right)_{exp} \cdot \mathcal{N}(E_R - E, \sigma_d^2(E_R))\mathrm{d}E \quad (3.18)$$

where E_{thr} is the detector threshold; $\epsilon(E_R)$ is the survival probability; $\mathcal{N}$ is the normal distribution with σ_d being the energy-dependent detector resolution to convolute the spectrum in order to account for the finite energy resolution.

3.2 Experimental setup

CRESST (**C**ryogenic **R**are **E**vent **S**earches with **S**uperconducting **T**hermometers) is an experiment that aims to probe the direct interaction of dark matter particles in the solar neighborhood with the nuclei of the target crystals using the phonon signals. The experiment began its efforts in 1995, producing its first results using Al_2O_3 crystals in 2002 in its first phase [129], known as CRESST-I. In CRESST-I, only the phonon signals were read out, giving no background discrimination power. In the experiment's second phase (CRESST-II), a second channel readout was introduced to measure the scintillation light along with the phonon signals, using the $CaWO_4$ crystals. Along with the additional background discrimination capability, thresholds were also reduced in this phase, and reach to even lower mass WIMPs was achieved [130–132]. The experiment currently runs in its third phase, known as CRESST-III, where it employs a smaller target size that is optimized to reach thresholds below 100 eV and probe sub-GeV dark matter masses [89, 126].

The experiment is located in the underground facility of the *Laboratori Nazionali del Gran Sasso* (LNGS) in order to shield it from the background cosmic radiations. The facility is under a 1400 m rock overburden, providing 3800 water equivalent shielding [133]. This leads to a reduction of the muon flux by about six orders of magnitude compared to the surface. This is important as, being a rare event search experiment, maximum mitigation of the backgrounds is necessary. In the following, different components and shieldings of the experiment have been briefly explained.

3.2.1 Dilution Refrigerator

In order to detect a recoil signature, CRESST uses TES sensors (Sec: 3.3.2) that have operation temperatures of around 15 mK. Hence, continuous operation at these temperatures is required to ensure smooth and optimized running conditions. Moreover, running at low temperatures also reduces the thermal noise. The cooling down is achieved by using a dilution refrigerator. The device uses the heat mixing of liquid ^{3}He and liquid ^{4}He to reach the mK temperatures. Below 870 mK, a spontaneous phase-separation of liquid Helium occurs where a concentrated ^{3}He phase (practically 100% ^{3}He) and a dilute ^{3}He phase (6.6% ^{3}He and 93.4% ^{4}He) are formed. In the dilute phase, ^{3}He drifts through the super-fluid ^{4}He and goes via the heat exchangers to the *still*, where it is vaporized by maintaining a pressure of about 0.1 mBar using pumps at room temperature. The ^{3}He vapors are then pre-cooled using liquid nitrogen (77 K) and liquid helium (4.2 K) and compressed to a few 100 mBar pressure. It is further cooled down to 1-1.5 K temperature using a 1K bath (containing depressurized liquid helium), and ^{3}He condenses as a result. Then, the ^{3}He passes through two heat exchangers, cooling down further before entering

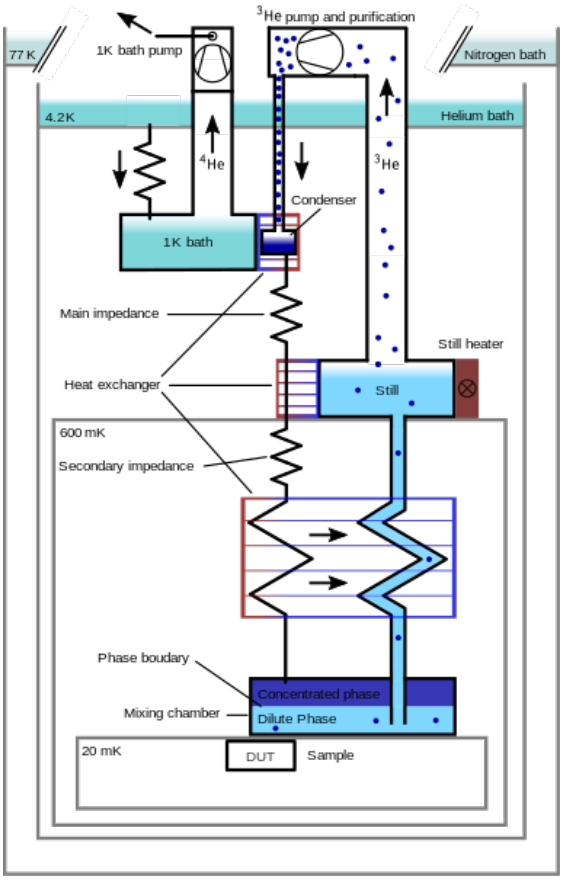

Figure 3.2: Schematic diagram of a wet dilution refrigerator. Image taken from Ref. [134].

the mixing chamber. Inside the mixing chamber, it crosses the phase boundary between the dilute and concentrated phases, which is an endothermic process and drives heat from the system. This is the primary process that achieves the desired low temperatures. A schematic of the dilution refrigerators is shown in Fig. 3.2.

The mixing chamber is connected to the housing that holds the detector modules, also known as the carousel, via a *cold finger*(1.5 m Copper rod), which also provides the thermal coupling. The helium inside the 1K bath is filled from the 4.2 K bath through a capillary. In CRESST, this liquid helium, as well as the liquid nitrogen, needs to be refilled thrice a week in order to ensure smooth operation. This refilling causes a downtime of the experiment of around 10-15 hours per week. Nowadays, however, this is majorly being replaced by the concept of "dry" cryostat, which uses a mechanical pump in a pulse tube, in order to achieve the pre-cooling of ^{3}He, which does not need the 1K bath discussed above. The main downside of this design is the mechanical oscillation produced as a result, which decreases the sensitivity of the experiment at these temperatures, although different de-coupling mechanisms can be used to mitigate these vibrations.

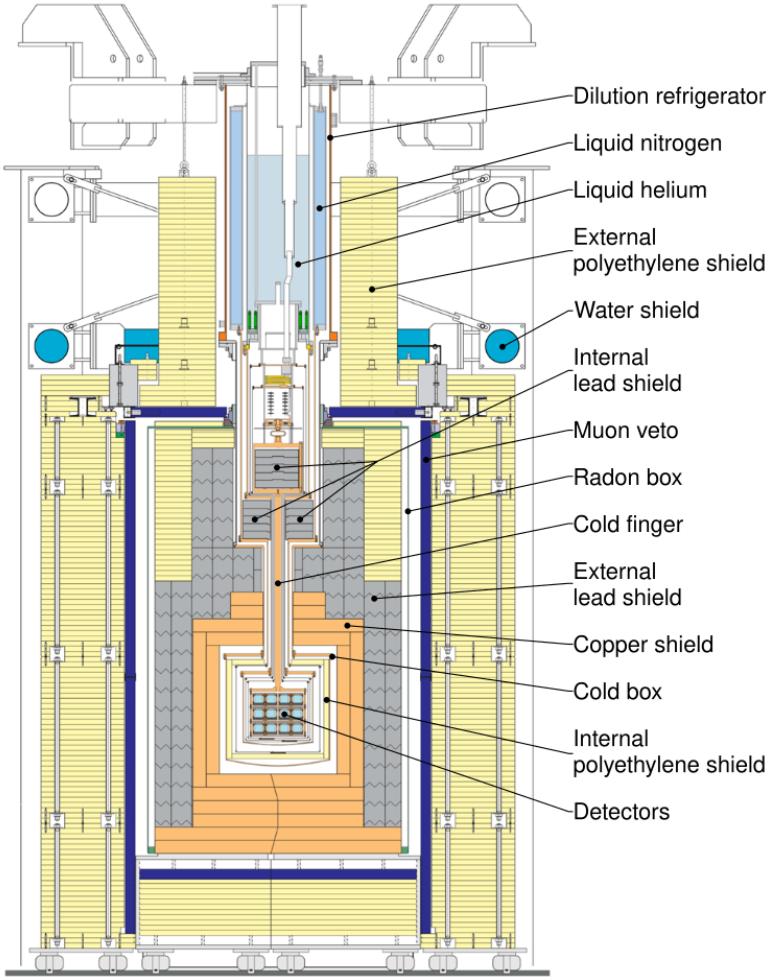

Figure 3.3: Schematic diagram of a CRESST cryostat with detector housing and detector shieldings. Image taken from Ref. [135].

3.2.2 Detector Shieldings

The carousel in which the detector modules are mounted is placed below the Dilution refrigerator unit and is centered between different layers of shieldings in order to mitigate particle backgrounds. A schematic of the CRESST cryostat can be seen in Fig. 3.3, a design that has been in use since the second phase of CRESST-II. Materials and the purpose of these shielding from outside towards the carousel are given below:

1. **External polyethylene:** A 45 cm thick shield of polyethylene surrounds the Radon box (see Fig. 3.3) in order to mitigate the neutron background, which poses the most dangerous threat to the experiment as neutrons give a similar recoil signature as a dark matter particle, i.e., a nuclear recoil. Neutrons lose more energy

upon an interaction with light nuclei due to kinematic reasons. Thus, the high number of hydrogen atoms in polyethylene makes it a perfect shielding material to moderate the incoming rate.

2. **Muon veto:** Even though setting the experiment underground reduces the cosmic muon flux by around six orders of magnitude, there are still some muons that make it to the detectors, as muons have a very low interaction rate. These remaining muons are not directly a background for CRESST, although they can create secondary particles upon interacting with the detector surroundings. Thus, the events associated with these secondary particles need to be identified and tagged. This is performed by using the muon veto system, that is, 20 plastic scintillator panels surrounding the radon box, each equipped with photomultipliers. In total, these panels cover 98.6% geometric volume of the detector, including the hole on top (Fig. 3.3).

3. **Radon box:** This is an air-tight steel container (not a shielding) that is filled with nitrogen gas in order to avoid radon deposition on the internal material surface.

4. **External Lead Shield:** The rock surrounding the experiment has natural background radioactivity coming from ^{40}K and from different isotopes formed in the decay chains of ^{238}U and ^{232}Th. This introduces a sufficient γ background, which is mitigated using 20 cm of low-background lead as it has a high mass number and thus provides excellent stopping power against γ's.

5. **Copper shield:** Even though low-background lead is used, it still has traces of ^{210}Pb, which decays to the stable ^{206}Pb via α, β, and γ decay. Thus, a 14 cm thick copper shield is used inside of the lead shield as it is possible to produce copper with low intrinsic radioactivity.

6. **Internal polyethylene shield:** Finally, an internal polyethylene shield is added in order to mitigate neutrons that could be produced in other shielding materials or from the outside.

3.3 Detectors

Having laid out the design and the shielding of the CRESST cryostat, this section will focus on the design and the physics of the detectors and their detection principle.

3.3.1 Detection Concept

CRESST uses its detectors as *cryogenic calorimeters*, which detect the heat, or phonons created upon a particle interaction using a highly sensitive thermometer known as a *Transition Edge Sensor*, or TES (next subsection 3.3.2). The phonons signal gives an estimate of the total energy deposited in the crystal upon interaction, although a tiny percentage of the energy is taken by scintillation light if a scintillating crystal is used for

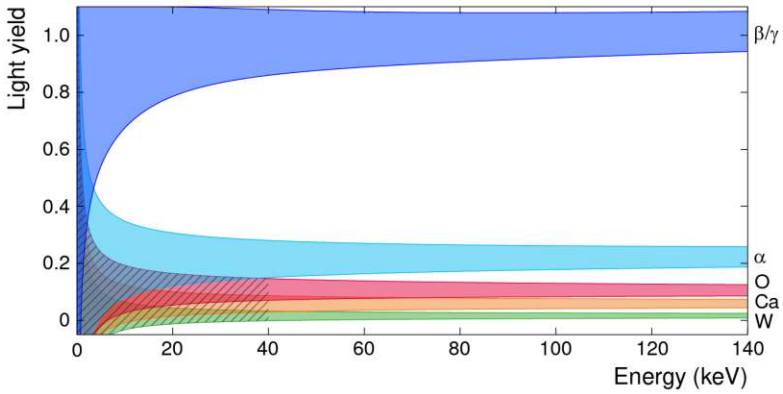

Figure 3.4: Typical Light yield plane used for particle discrimination in CRESST. The nuclear recoil bands are drawn for recoils off a $CaWO_4$ target. The hatched region is the main region of interest for WIMP searches in CRESST. Image taken from Ref. [135].

detection. The emitted scintillation light is also detected in CRESST using another TES. Thus, inside every detector module, there are two TES sensors, which are referred to as Phonon and Light detectors.

The light detectors are made of silicon-on-sapphire (SOS), which has high absorption for the blue scintillation light produced by various crystals used in CRESST ($CaWO_4$, Al_2O_3, $LiAlO_2$, etc.). The detector itself is basically a thin wafer of sapphire coated with an ultra-thin layer of silicon (as the name suggests), as the sapphire itself is transparent. Upon absorption of a scintillation photon by silicon, phonons are created, which are read out by the TES sensor. Thus, in theory, the light detector in CRESST is basically also a phonon detector, with the difference that it measures the scintillation light produced as a result of particle interaction in the main crystal and not the interaction itself. Hence, it is classified in CRESST as a light detector, and the main detector is known as the phonon detector.

The amount of scintillation light produced upon a particle interaction depends on the type of particle that interacts. An electron or a gamma interaction gives the most energetic light, followed by an alpha interaction and then a nuclear recoil. The reason for this is that electrons or gamma interact with the electron system of the molecules electromagnetically, producing more light than the recoil on the nucleus. This information is the useful aspect that allows for active background discrimination in CRESST. A parameter is defined which quantifies this and is called as the *Light Yield* (LY), which is given by:

$$\mathrm{LY} = \frac{E_l}{E_p} \tag{3.19}$$

where E_l and E_p are the energies measured by the light and the phonon detector, respectively. The energies here are given in electron equivalent units, which simply means

that an electron of energy E, would impart $E_l = E$ in the light channel and $E_p = E$ in the phonon channel. Hence, by definition itself, the electron recoils in CRESST are centered around $LY = 1$, as can be seen in Fig 3.4. However, using this definition assumes that a certain fraction of the energy goes into scintillation. Thus, the E_p for an event with a $LY > 1 (< 1)$ would be underestimated (overestimated). However, this can be corrected as the measurement is performed on both channels. Assuming η to be the scintillation efficiency (which falls around 6-7% for $CaWO_4$ [123]), the total energy of an event is given by:

$$E = \eta E_l + (1 - \eta)E_p = [1 - \eta(1 - LY)]E_p \tag{3.20}$$

Scintillation efficiency η can also be calculated by measuring the energy of direct hits on the light channel in absolute energy units and comparing them with the scintillation energy of the same event in the phonon channel in electron equivalent units. This is done using a calibration source like ^{55}Fe.

As was briefly described in the previous chapter, the amount of scintillation light produced by a nuclear recoil depends on the type of nucleus and is quantified by the *Quenching factor* (QF_X). It is given as:

$$\mathrm{QF}_X = \frac{\text{Scintillation light produced by particle } X \text{ for } E \text{ deposited energy}}{\text{Scintillation light produced by electron of energy } E} \tag{3.21}$$

It can be seen from Fig. 3.4 that lighter nuclei have higher QF than heavier ones. Although, the values of QFs for different nuclei from other measurements are available and can be used [136], having a neutron calibration source to irradiate the crystals also allows for in-situ measurement of the QFs with this technology in CRESST. As the dark matter recoils are expected to lie in the nuclear recoil band, a region-of-interest (ROI) in the nuclear recoil bands can subsequently be defined to look for candidate events.

3.3.2 Formation of a Pulse

The energy deposited in a crystal upon a recoil causes an increase in the temperature of the crystal depending on its heat capacity. They related in the following way:

$$\delta T = \frac{\delta E}{C} \tag{3.22}$$

where C is the heat capacity of the crystal. Thus, in order to increase the sensitivity of the experiment, low heat capacity is desired in order to measure the $\mathcal{O}$(eV) energy depositions. It is also known that the heat capacity scales with the temperature of the crystal as $\sim (T/\Theta_D)^3$. Running at cryogenic temperatures of a few mK, the heat capacity is already reduced by 13 orders of magnitude compared to room temperature. It can

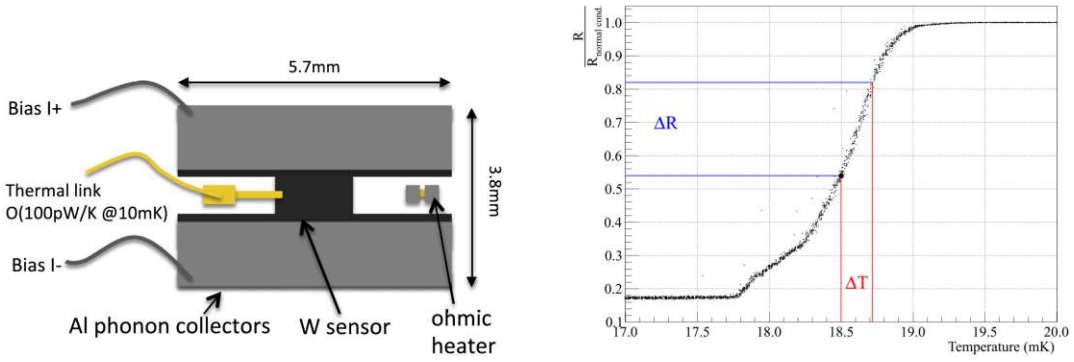

(a) (b)

Figure 3.5: (a) Schematic view of a TES with an Al-phonon collector used in CRESST-III. Image taken from Ref. [137]. (b) The transition curve of a transition edge sensor operating between superconducting and normal conducting state. The resistance on the y-axis is normalized to the resistance in the normal conducting state. Image taken from Ref. [138].

be further reduced by using smaller crystals with small masses, as heat capacity is an extensive property and scales with the mass of the material.

The small rise in the temperature is read by the Transition Edge Sensors which are basically Tungsten films operating between its super-conducting and normal conducting state. The Tungsten film is evaporated directly on the crystals and is sandwiched between two aluminium phonon collectors(Fig. 3.5). Tungsten has a transition temperature of around 15 mK to a superconducting state; below that, its electrical resistance falls practically to zero. Temperature is adjusted such that the films are operated in the transition region between the superconducting and normal conducting state, which typically happens within 1-2 mK (Fig. 3.5). Since the resistance change is quite sharp in the transition region, a small increase in the temperature ($\mathcal{O}(\mu\text{K})$) of the film causes a detectable change in the resistance of the film.

A very well-modeled parametric description of the phonons produced upon interactions in cryogenic detectors using TES readout is given in Ref. [139], which also works with CRESST detectors. Upon an interaction, a large population of very high-frequency phonons ($\mathcal{O}(\text{THz})$) are created, which have typical energies of meV. Since their energies are far above the thermal energy of the lattice at mK temperatures, these phonons are known as *athermal* phonons. Due to anharmonicities present in the crystal lattice, they quickly decay to lower frequency phonons, and the decay is strongly proportional to the frequency (ν^5_{phonon}). Thus, they decay to phonons of typical frequency of around 100 GHz in around 100μs, and these lower-frequency phonons are still known as *athermal* phonons as the energy of 100 GHz phonons is still too high compared to the thermal regime of the lattice. However, these phonons are relatively more stable compared to the response time of the thermometer and can thus be absorbed by the free electrons in the W-film after a few surface reflections in the crystal, heating up the film. The heated film is then brought

back to the base temperature as the heat escapes through the thermal coupling to the heat bath. This leads to the first (fast) component seen in the output, which is known as the *athermal* component. It is also possible for the *athermal* phonons to thermalize inside the crystal before being absorbed in the thermometer. These thermalized phonons eventually also reach the thermometer and form the second (slow) component known as the *thermal* component. For a detailed and quantitative description of this process, the reader is referred to [139].

3.3.3 Detector Module Design

As it was discussed in the previous subsection, using smaller mass crystals is useful for increasing the sensitivity of the experiment. With the aim of reaching the energy threshold of $\mathcal{O}(10\text{ eV})$, CRESST-III employs crystals of around 24 g each with $(2 \times 2 \times 1)$ cm^3 dimensions and a wafer light detector of $(2 \times 2 \times 0.04)$ cm^3 dimensions [89, 126, 140]. The phonon detector crystals are held in place using either instrumented/non-instrumented $CaWO_4$ sticks or Bronze clamps. The TES is deposited on the crystal and the wafer, for phonon and light detection, respectively. The detector housing is made up of highly radio-pure copper and is usually covered internally with a scintillating and reflecting 3M Vikuiti Enhanced Specular Reflector foil in order to increase the light detection efficiency. Fig. 3.6 shows the image and the schematic of a typical CRESST-III detector module.

Figure 3.6: (a) Schematic of a typical detector module in CRESST-III as shown in Ref. [89]. The blue parts are $CaWO_4$ crystals but could also be other materials employed in CRESST-III. Dimensions of the various parts are written in the text. The schematic shows the crystal being held by the instrumented sticks (iSticks), although this is not a general design in CRESST-III. (b) Image of the detector module used for calculating the dark matter results in Ref. [89].

3.4 Data Acquisition

In order to measure the resistance change in the TES, the detector electronics have to be designed sensitive enough to measure the change and also ensure that the TES is working in stable conditions. The detector electronics in CRESST that is able to perform these tasks is briefly described in this section.

3.4.1 SQUID Readout

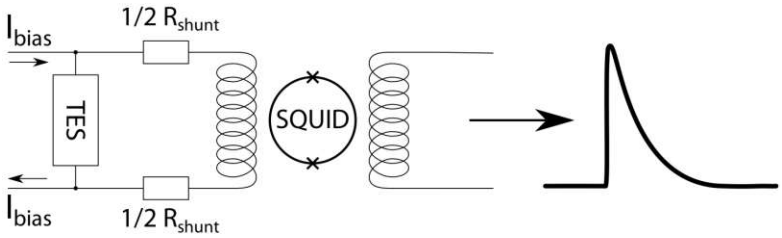

Figure 3.7: The SQUID readout circuit with the TES. Image taken from Ref. [138]

The TES sensor is connected in parallel to shunt resistors R_s, and a constant, optimized bias current I_B of a few μA is sent across the two. As soon as the temperature rises in the TES and causes a change in its resistance, the current distribution across the two loads changes. This change in current induces a magnetic field in the input coil (Fig. 3.7). This tiny change in the magnetic field is read using Superconducting QUantum Interference Devices (SQUIDs). The SQUIDs output a voltage proportional to the change in the magnetic field, thereby being proportional to the change in resistance of the TES, which occurs due to a change in temperature that is the result of the deposited energy in the crystal. The readout circuit of the SQUID is shown in Fig. 3.7.

3.4.2 Pulse and Data Recording

The schematic block diagram of the whole readout electronics is shown in Fig. 3.9. The voltage output from the SQUID electronics is further divided into three parts. Two of these parts are used for recording the data when a pulse is seen above a pre-defined voltage threshold. This stored data in CRESST-III is called the hardware-triggered data. One of these two parts goes to a transient digitizer. This digitizer uses a ring-buffer to record the incoming signal with 25 kHz frequency and 16-bit precision. Once the ring buffer completes a cycle and is full, the next cycle is overwritten from the beginning of the previous one. The second part of the output goes through a series of devices where the signal is filtered, amplified, and shaped. It then goes through a trigger gate where the signal is only recorded if the voltage crosses the pre-defined trigger threshold. If the trigger happens, a small window of the *post-trigger region* is recorded by the Data acquisition (DAQ), along with some samples of the *pre-trigger region*. Thereby, a pulse is stored with both the *pre-trigger* and the *post-trigger region*. In CRESST, the first 1/4th of the recorded pulse window contains the *pre-trigger region*, and the last 3/4th is the

post-trigger region. The third part of the voltage output is taken to another set of two transient digitizers that continuously records the whole data for 16 detector channels, with the same 25 kHz frequency and 16-bit precision. As one of the digitizers is read out, the other one records the data, and then they are switched. This was recently implemented only in CRESST-III as it gives the ability to trigger the data later on with a desired trigger value offline. This recorded data is referred to as the continuous data in CRESST. This part of the electronics is shown in blue in the block diagram in Fig. 3.9.

3.4.3 Heater Pulses and Stability

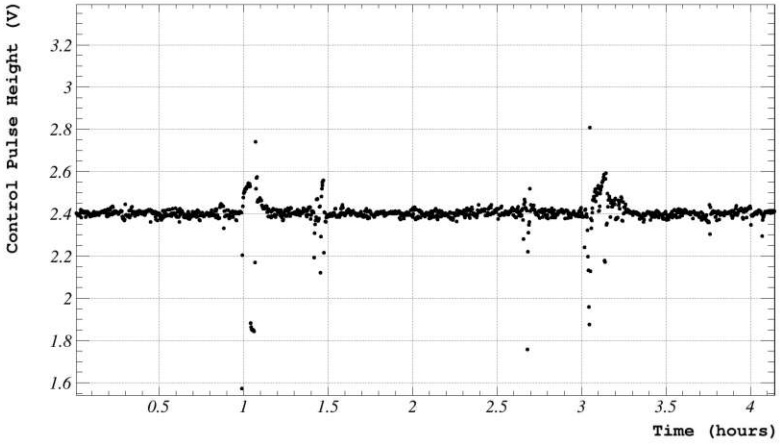

Figure 3.8: Recorded control pulse heights measured by SQUIDs output. The pulses are sent every 10 seconds. The saturating voltage of the TES is 2.4 V in this case.

It is possible that the temperature of the carousel might not be completely stable over a long period, and small variations could occur, which could result in a change of the working point of the TES. These changes can be corrected if the new working point of the TES is inferred, and the temperature is regulated accordingly to send the TES back to the previous working point. This is achieved by sending two different heating currents to the TES. One contribution comes from a DAC (digital-to-analog) that supplies a steady current to keep the TES at the wanted operating point. The second contribution comes from an artificial pulse form generator that sends the heater pulses at regular intervals to monitor the operating point of the TES. The signals are then added, passed through a square rooter, and converted to heater current by pairs of resistors. This part of the circuit is shown in red in Fig. 3.9.

The heater pulses used for stability, which are also known as the control pulses, regulate the operating point of the TES in the following way: these pulses heat the TES to the normal conducting state, and the output pulse height of the control pulse is thus a good indicator of where the TES is in the transition curve (Fig. 3.8). If the TES is too low in temperature and closer to the superconducting state, the saturation takes a longer time, and hence, a larger heater pulse than a normal one is seen in the SQUID output (points

above 2.4 V in Fig. 3.8). In this case, the quasi-constant heating has to be increased. On the other hand, if the operating point is close to the normal conducting state, a smaller temperature rise is required to thoroughly saturate it, thereby giving a smaller pulse in the SQUID output (points below 2.4 V in Fig. 3.8). In this case, the heating has to be decreased to get the TES back to the desired operating point. These functions are performed by an algorithm known as the Proportional-Integral-Differential (PID) loop. A more detailed description of the detector electronics can be found in Ref. [141].

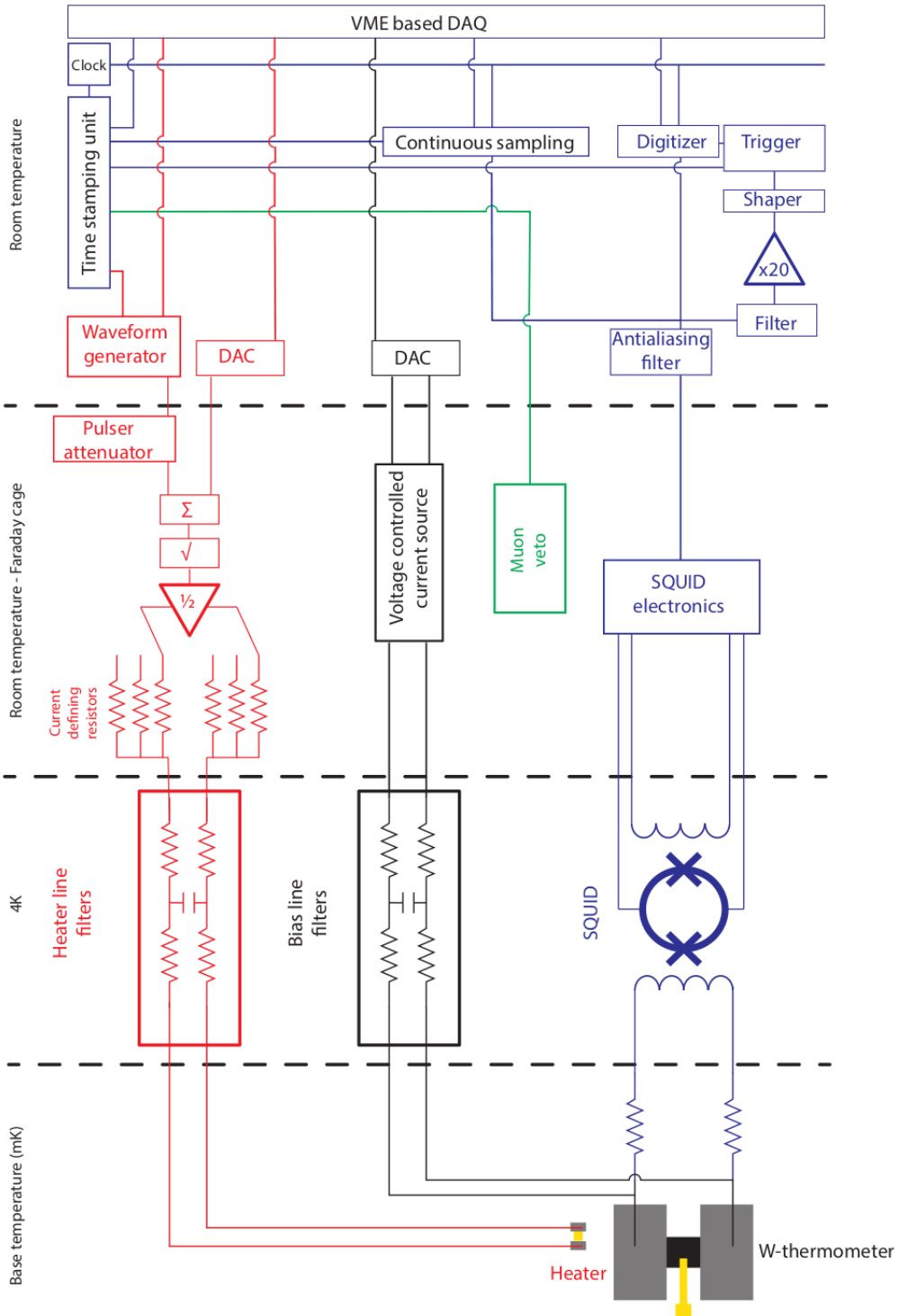

Figure 3.9: The block diagram of the electronics used in CRESST-III [141].

CHAPTER 4

Data Analysis chain in CRESST-III

As has been described in the previous chapter, the latest stage of CRESST, called CRESST-III, has been optimized for probing dark matter masses going down to the sub-GeV range. This has been achieved by using even smaller detector modules (Sec. 3.3.3) and triggering at optimized thresholds using offline triggering (Sec. 3.4.2). The continuous data acquisition in CRESST allows storing the data as a time series of voltage values, which can further be triggered and analyzed for extracting the physics results. This chapter focuses on the data analysis chain used in CRESST-III, beginning from the finding of the optimized trigger threshold to the extraction of the dark matter exclusion limits.

4.1 Triggering Mechanism

In the previous CRESST stages, only hardware-triggered data was stored and analyzed for physics results, whereas the rest of the stream was discarded. Given that multiple detector modules were run in a single CRESST run, one would expect that noise conditions would not be similar for all of them. Hence, the trigger values set for the hardware trigger algorithm could not be optimized for the signal shape and noise conditions of each individual detector. The changes were made in the third stage of CRESST in order to overcome this issue and reach lower thresholds by saving the whole time series of data as well [141]. Although the hardware-triggered data was still saved as hardware DAQ allows to keep the detectors stable in their operating point. The advantage of saving the whole raw data stream along with the hardware-triggered data is that one can gather information about the noise conditions and the pulse shape seen for every detector module and find an optimized trigger threshold, which can be used on the continuous stream to reach low energies. This optimization is done by filtering the stream using a filter known

as the *Optimum Matched Filter*, which incorporates the same information and gives a better signal-to-noise ratio. Then, the triggering could be performed on the raw stream, and the trigger threshold could be decided based on any desired benchmark factor. This factor is chosen to be allowed noise triggers per kg-day of data in CRESST. The following sections describe the principle of the Optimum filter and then the calculation of the trigger threshold based on the allowed noise triggers.

4.1.1 Optimum Filter

The concept of the optimum filter is based on the work done by E. Gatti and P.F. Manfredi in Ref. [142] for maximizing the signal-to-noise (SNR) ratio in particle detectors. The filter provides a much better energy resolution than the raw stream and can also be used for amplitude estimation, which gives a much more precise estimation of the energy deposition in the crystal.

A segment of raw time series of data containing a pulse can be represented as an addition of two components given by:

$$s(t) = A \cdot p(t) + n(t) \tag{4.1}$$

where $p(t)$ represents the normalized pulse shape of a detector, which is scaled with the amplitude A, and $n(t)$ is the stochastic term containing the various noise contributions such as 1/f noise, electrical noise, thermodynamic noise, etc. A detailed description of noise contributions in TESs can be found in Ref. [143].

Now, a transfer function could be written in the frequency domain, $H(\omega)$, that maximizes the SNR at the time of measurement t_m as [141, 142]:

$$H(\omega) = K\frac{\hat{p}^*(\omega)}{N(\omega)}e^{-i\omega t_m} \tag{4.2}$$

where $\hat{p}^*(\omega)$ represents the complex conjugate of the Fourier-transformed pulse function, $N(\omega)$ represents the Noise Power Spectrum (NPS), and K is the normalization constant. $H(\omega)$ can then be used to weigh the Fourier-transformed pulse function, and then the weighted pulse function is back-transformed in the time domain as:

$$p_F(t) = \frac{Q}{\sqrt{2\pi}}\int_{-\infty}^{+\infty} H(\omega)\hat{p}(\omega)e^{i\omega t}d\omega \tag{4.3}$$

where $p_F(t)$ is the filtered pulse shape, and Q is also another normalization constant. For the application to a particular detector module, the following is performed:

1. A NPS is created by obtaining information about the noise conditions of the detector. This is done by collecting a large sample of empty record windows containing only the noise without any pulse. In CRESST, these are known as *Empty Baselines*

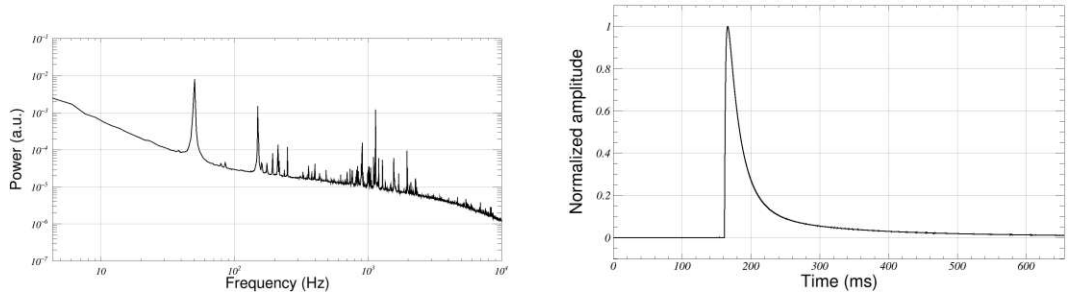

(a) (b)

Figure 4.1: Examples of (a) a NPS and (b) a SEV in a record window.

or EBLs. The hardware trigger algorithm triggers and saves a random sample within every few minutes (typically 2-3 minutes). As being in a low background environment, it is very unlikely for a randomly triggered sample to contain a pulse and should only contain the baseline noise. The few EBL samples that do have a pulse in them are removed. Then, each of the EBL, $n_i(t)$ is discretely fourier transformed to $\hat{n_i}(\omega_k)$, and the NPS is calculated as the ensemble average $\langle \hat{n_i}(\omega_k)\hat{n_i}^*(\omega_k)\rangle_i$ of all the empty baselines. An example of the NPS, with a vibrant 50 Hz electrical frequency, can be seen in Fig. 4.1(a).

2. An averaged particle pulse shape seen by the detector module is obtained from a large sample of particle pulses. Those pulses are used that fall within the linear range of the TES (i.e. do not suffer from saturation effect near the normal conducting phase of the TES) as it is seen that across the linear range, the pulse shape stays constant. All the pulses are then normalized and averaged in order to reduce the noise. The averaged clean pulse is typically known as the Standard Event (SEV) in CRESST (Fig. 4.1(b)). The SEV is then Fourier transformed to obtain $\hat{p}(\omega)$.

3. The transfer function can thus be calculated using the NPS and fourier-transformed SEV (Fig. 4.2(a)) and is then applied to the whole Fourier-transformed data stream. The stream is then back-transformed to the time domain in order to obtain the filtered time series of data. Both the raw stream and the filtered stream can be seen in the example shown in Fig. 4.2(b).

From Fig. 4.2(b), the improvement to the SNR provided by the optimum filter can be clearly seen, and thus, triggering on the filtered stream allows it to go to even lower thresholds compared to the raw stream. The dependence of the filter on the pulse shape can also be seen in the same plot. The noise fluctuation in the raw stream at around 350 ms goes above the pulse maximum, but the filter, being sensitive to the shape of the pulse, suppresses these artifacts. However, it has to be noted that being sensitive to the shape of the pulse, the filter performs well only for the pulses that are similar to the SEV that was used to create the filter. If the filter is applied to pulses from the non-linear, or

saturated region of the TES, the filter fails to give a good amplitude estimation, and other methods have to be used, which will be discussed later.

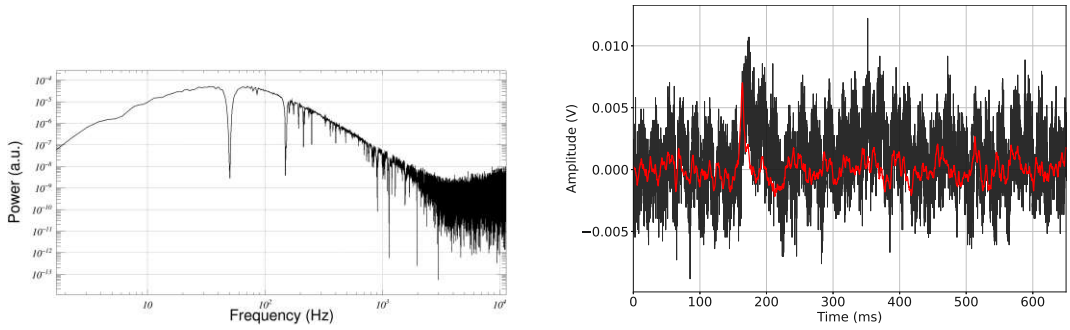

(a) (b)

Figure 4.2: (a) The transfer function of the optimum filter created using the NPS and SEV shown in Fig. 4.1. (b) A sample of raw (in black) and the same filtered (in red) stream compared together.

4.1.2 Calculating Trigger Threshold

Having obtained the filtered triggered stream, a trigger threshold has to be defined in volt units. If, at any time, the filtered stream goes above this value, that particular event (in a record window) is saved. Just like the hardware-triggered data, 1/4th of the record window is the pre-trigger region, i.e., before the pulse onset, in order to get the information about the baseline before the trigger, and the remaining 3/4th of the window is the post-trigger region, i.e., after the pulse onset. The trigger threshold has to be chosen so that it is low enough to increase the sensitivity of the module but not so low that it triggers in the noise region. Hence, the threshold has to be calculated based on a benchmark factor that considers the noise conditions as well. This factor is chosen to be the allowed number of noise triggers per kg-day of data and is typically kept at 1 noise trigger/kg-day in CRESST, but a higher value could be chosen as well.

The analytical description for this threshold calculation used in CRESST is based on the work done in Ref. [144]. First, a probability distribution function for the amplitude of the filtered noise baseline is defined as $P(x)$. And then, based on this function, another probability function $P_d(x_{\max})$ is calculated, which corresponds to the probability of finding the maxima of the samples as $x_{\max}$ for d statistically independent samples in the trigger window. It is seen that $P(x)$ usually follows a Gaussian distribution (Fig. 4.3(a)) given by:

$$P(x) = \frac{1}{\sqrt{2\pi}\sigma} e^{-\left(\frac{x}{\sqrt{2}\sigma}\right)^2} \tag{4.4}$$

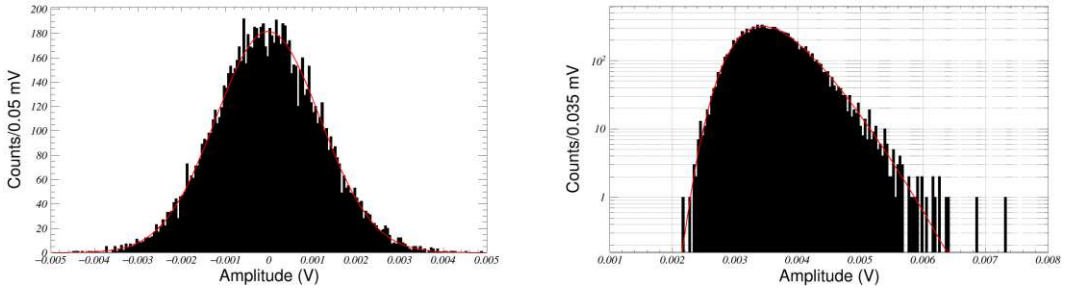

(a) (b)

Figure 4.3: (a) Distribution of the filtered EBLs along with the fitted Gaussian function in red. (b) The distribution of the maxima of the same EBLs with the fit in red to Eq. 4.6.

where σ is the resolution of the distribution. Thus, the joint probability of a sample to be $x_{\max}$ and the rest to be smaller than $x_{\max}$ can be given using the binomial distribution as:

$$P_d(x_{\max}) = \frac{d!}{1!(d-1)!} \cdot P(x_{\max}) \cdot \left(\int_{-\infty}^{x_{\max}} P(x)dx \right)^{d-1} \tag{4.5}$$

Hence, using the Gaussian error function as the integral of the distribution, $P_d(x_{\max})$ becomes:

$$P_d(x_{\max}) = \frac{d}{\sqrt{2\pi}\sigma} \cdot e^{-\left(\frac{x_{\max}}{\sqrt{2}\sigma}\right)^2} \cdot \left(\frac{1}{2} + \frac{\mathrm{erf}(x_{\max}/\sqrt{2}\sigma)}{2} \right)^{d-1} \tag{4.6}$$

And given $P_d(x_{\max})$, the expected noise trigger rate (NTR) could thus be calculated for a threshold value of x_{th} per kg-days as:

$$\mathrm{NTR}(x_{\mathrm{th}}) = \frac{1}{t_{win} \cdot m_{det}} \int_{x_{\mathrm{th}}}^{\infty} P_d(x_{\max})dx_{\max} \tag{4.7}$$

where t_{win} is the recorded time of all the EBLs in days and m_{det} is the detector mass in kg. Then the value of x_{th} can be solved for, that gives NTR as 1 $\mathrm{kg}^{-1}\mathrm{day}^{-1}$(Fig. 4.4).

In order to do this, typically, the same EBL samples are taken are used to create the NPS (Sec. 4.1.1). The samples are individually filtered, and the distribution of its maximas are fitted with Eq. 4.6 (Fig. 4.3(b)). Then, the NTR is calculated as a function of x_{th} for the fitted $P_d(x_{\max})$. In CRESST, a typical record window contains 16384 samples, and given the 25 kHz recording frequency, each sample is 40 μs long. Hence, NTR is calculated with $t_{win} = n \times 16384 \times (40 \times 10^{-6})/(24 \times 3600)$ days, where n is the total number of EBLs used, and the mass of the detectors is $m_{det} \approx 0.024$ kg. The value of x_{th}, in the end, is chosen such that it gives NTR = 1 trigger $\mathrm{kg}^{-1}\mathrm{day}^{-1}$ (Fig. 4.4).

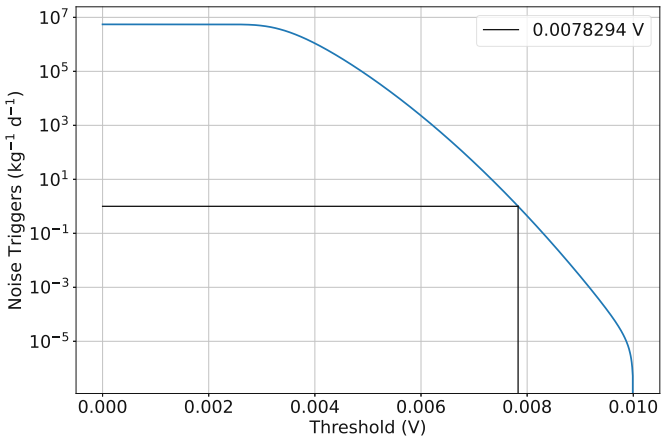

Figure 4.4: Noise trigger rate as a function of threshold. The drawn black line indicates the threshold that gives 1 NTR kg^{-1}day^{-1}, and its value is shown in the legend.

4.2 Pulse Parameters

After the data have been triggered with the desired threshold, the triggered events (also called Particle events) are saved in record windows as a time series of voltage values containing 16384 voltage points in each record window. This amounts to around 655.36 ms for each event in a record window. The timestamp of every triggered event is also saved along with it. The analysis is then divided into two parts, namely a low-level or raw data analysis, which is followed by a high-level or physics analysis. The high-level analysis consists of calculating the physics results (typically the dark matter exclusion limits) with the given data under a particular model. It has to be made sure that the data used to calculate the physics results in the high-level analysis consists of actual particle recoils and not artifacts, as it is possible that the changing noise conditions could trigger some events that are basically noise artifacts and not "real" particle events. The most common artifacts seen in CRESST are discussed in Sec. 4.3. Thus, all the events that are triggered have to be cleaned from these artifacts, and this is what is principally done in the low-level analysis.

Since a typical CRESST run lasts for months to years, the total number of events seen for a well-performing detector after triggering is in the order of $\mathcal{O}(10^4)$. Thus, it is not practical to go through the samples on an event-by-event basis in order to clean them. The cleaning is then performed in the following way: some parameters are defined for an event, and these parameters are calculated for every event. These are known as *Pulse parameters*. Different criteria are then established for the pulse parameters that should hold true for the "real" particle events and false for the noise artifacts. These criteria are commonly known as the analysis cuts, and these cuts are then applied to the whole list of events. As a result, the "real" particle events are then accepted, and the artifacts are rejected up to a high efficiency (which can be calculated and is discussed in Sec. 4.5). The common analysis cuts used for data cleaning are described in the next section 4.3.

In CRESST, some other classes of events are also saved along with the particle events, and the pulse parameters are also calculated for them. These events are:

1. **Empty Baselines (EBLs)**: As already defined above (Sec. 4.1.1), a fraction of EBLs are also saved by triggering randomly at different points, and given the low background environment, the random triggers usually contain only noise. They are usually saved in order to assess the noise conditions at different times. However, one can choose not to trigger them as well and only use the EBLs from the hardware-triggered data, if needed.

2. **Control Pulses**: Also known as heater pulses, and are used to ensure the stability of the detector module (as discussed in Sec. 3.4.3). These pulses are sent every 10 seconds with a maximal input voltage of 10 V, in order to saturate the TES.

3. **Test Pulses**: These pulses are used for time-dependent energy calibration of the detector, the details of which are discussed in Sec. 4.4. These pulses are sent every 20 seconds with increasing input voltages ranging from (0.1 - 10.0) V. After the 10.0 V input, the 0.1 V pulse is sent again, and the cycle repeats.

The different pulse parameters defined for all the classes of events and used for the analysis are given below.

4.2.1 Main Parameters

These parameters are calculated directly from the record window as a first step (Fig. 4.5). The main parameters contain:

1. **Baseline offset & slope**: In the pre-trigger region, a linear model is fitted in order to extract the information about the baseline. The y-intercept of the fit corresponds is the Baseline offset, which is around -3.75 V in the example in Fig. 4.5. This offset is subtracted from the whole pulse to get the baseline to zero. The baseline offset is not constant during the data taking due to discrete baseline levels of the SQUID. The slope of this fit corresponds to the Baseline slope.

2. **Baseline RMS**: This is the root mean square value calculated from the linear fit to the data.

3. **Baseline difference**: This is the difference between the average of the last 50 samples of the window and the first 50 samples in the window. This is also known as the right-minus-left baseline parameter in CRESST.

4. **Pulse Height**: After the baseline offset correction, a running average of 50 samples is calculated for the whole stream, and the maximum of those running averages corresponds to the Pulse Height. This provides the first approximation of the pulse amplitude. In the given example, this is around 1.5 V.

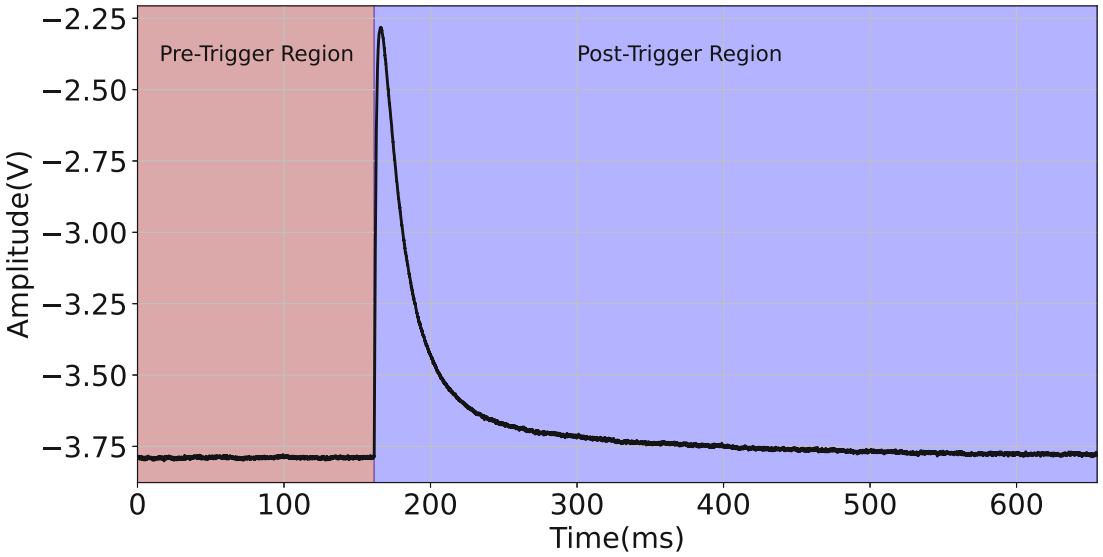

Figure 4.5: Example of a standard pulse in CRESST, along with pre and post-trigger regions.

5. **Peak Position**: This is the averaged x-position of the calculated Pulse Height. It is around 166 ms in the given example.

6. **Onset**: The time of the start of the pulse in ms. This is taken to be the time at which the data reaches three times the baseline RMS in the rising part of the pulse. It is around 161.5 ms in the given example.

7. **Rise & Decay time**: These are defined as the time it takes from 10% to 90% of the pulse height & 90% to 10%, respectively.

8. **Maximum & Minimum Derivative**: As the name suggests, this is the maximum or minimum derivative calculated between adjacent samples for the whole record window. The positions of the maximum and minimum derivatives are also saved along with their value.

4.2.2 Optimum Filter Parameters

The optimum filter is again applied to every event for a better amplitude estimation at low energies, as it is quite sensitive to the shape of the pulse. This also gives an advantage in cleaning the events. The filtered events are then fitted with the filtered SEV (Fig. 4.6), and the following parameters of the fit are saved:

1. **Filter Amplitude**: This corresponds to the scaling parameter used to fit the filtered SEV with the data. This is later used for better amplitude estimation at low energies. In the example shown in Fig. 4.6, this is around 17.5 mV.

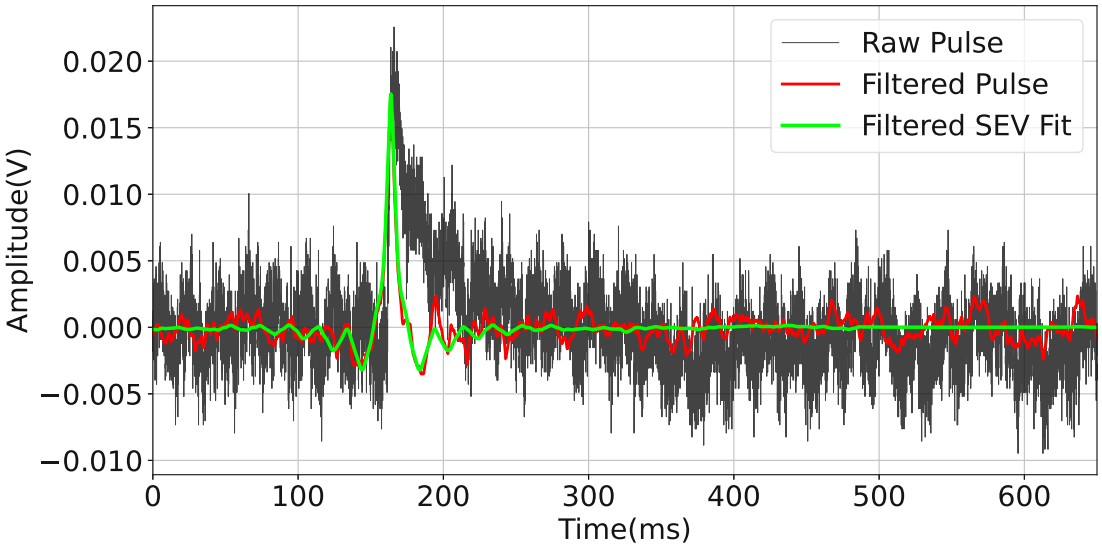

Figure 4.6: Example of a raw pulse (black) along with the filtered pulse (red). The filtered pulse is fitted with the filtered SEV (green).

2. **Filter RMS**: This is the root mean square of the fit.

3. **Peak RMS**: This is also the root mean square of the fit but calculated in the region around the pulse maximum.

4. **Maximum Position**: Corresponds to the position of the maximum of the filtered pulse. It is around 164 ms in the example shown.

4.2.3 Template Fit Parameters

Before the application of the optimum filter, the amplitude estimation was typically done with a *Template Fit* in CRESST [123, 138]. In order to do this, the pulse SEV is fitted, along with a polynomial, to the different events individually. The polynomial is fitted to model the baseline, and for this work, a second-degree polynomial has been used. The fit is performed by shifting the SEV to the onset of the pulse and then scaling the amplitude of the SEV to the pulse. A typical SEV template fit is shown in Fig. 4.7(a). Although the template fit does not give a better performance than the optimum filter at low energies, it has an advantage for application to higher energy pulses that heat the TES beyond its linear regime. These pulses are known as *Saturated Pulses*, as they result from a recoil that saturates the TES. These pulses have a different pulse shape than the ones in the linear region of the TES, and hence, the optimum filter can not be used with these pulses for amplitude estimation. However, allowing the template fit to use the data points only in the linear regime of the pulse, i.e., the whole pre-trigger region and the decaying pulse in the post-trigger region, the amplitude estimation can be done to a good

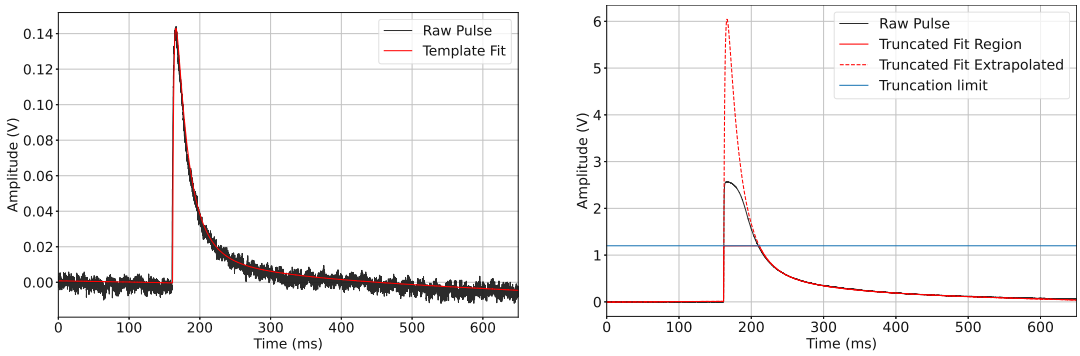

(a) (b)

Figure 4.7: (a) An example of a template fit and (b) a truncated fit with 1.2 V as the truncation limit (horizontal line in blue). The data are shown in black, and the fit is in red for both plots.

approximation. This method of fitting is called a *Truncated Fit*, and the limit below which the data points are used for fitting is called the *Truncation limit.* An example of the truncated fit can be seen in Fig. 4.7(b). As a result of the template or the truncated fit, different fit parameters are extracted, and the main parameters of these are:

1. **Fit Amplitude**: This is the scaling applied to the amplitude for template fit (around 0.14 V for the example in Fig. 4.7(a)) and the extrapolated amplitude as a result of the truncated fit (around 6 V for the example in Fig. 4.7(b)).
2. **Fit RMS**: This is the root mean square of the fit in both cases.

4.3 Analysis Cuts

The raw data analysis consists of three major parts, namely, cleaning the data using the analysis cuts to make sure only "real" particle pulses survive this chain, reconstructing the recoil energy of the cleaned data, and estimating the efficiency of the analysis to incorporate for the probability of a correct signal to survive the analysis chain. In this section, the analysis cuts typically used for data cleaning will be described.

It is possible that while designing the analysis cuts, the analyst could (sub-consciously) create a selection bias in order to get the best results. To avoid this from happening, a common technique used in the particle physics and dark matter community is to design the analysis cuts on a subset of the whole data, called the *training set*[145]. The cuts can be optimized on the training set to get the best viable results. These cuts are then saved and applied without any change to the rest of the data, which is known as the *blind data*, and the analysis is known as the *blind analysis*. The training set is not used for the calculation of the final physics results in order to remove any selection bias whatsoever. The whole process of applying the cuts to the blind data and checking the final results is

known as *Unblinding*. This blinding scheme is also followed in CRESST, and typically, the training set contains around 10% of the whole data.

The collected data in CRESST are further divided into different segments. After the start of a run, data is collected with a ^{57}Co source that has prominent gamma peaks at 122.1 keV and 136.5 keV. The source is put outside the cryostat as these energies are high enough to penetrate copper layers. This data is used for the energy calibration and calibration of the γ-band (Fig. 3.4) and is called *Cobalt calibration data* or the *cal* data. Another data set is also collected with an AmBe neutron source in order to calibrate the nuclear recoil bands of the detector (Fig. 3.4) and is known as the *Neutron calibration data* or the *ncal* data. This source is placed inside the outer neutron shielding of the cryostat to make sure enough neutrons reach the detector. Between the *cal* and the *ncal* data, the main data set for the physics results is taken without any source. This is known as the *Background data* or *bck* data, as in this segment, the data are only collected from the background. The training set is a subset of this data and usually consists of a few data files from throughout the whole segment, rather than just the beginning or the end of the *bck* data. This is done in order to account for any time-dependent variation in the training data so that the cuts can be tuned accordingly. The cuts defined below are optimized for the training set. However, the same cuts can also be used for *ncal* or *cal* data if the conditions of the detector do not change too much. However, since *ncal* or *cal* data do not have to follow the blinding scheme, the cuts can be optimized specifically for them as well.

4.3.1 Muon Veto and Coincidence Cut

It is possible that the event registered could have originated due to a muon-induced neutrons, and in order to exclude these events for calculating the final results, the coincidence information from the muon veto panels is used. The timestamp of every recorded event is compared to the closest muon event seen in any of the muon panels. If the difference between the timestamp of the event seen in the detector and the timestamp of the closest activated muon panel is positive, this means that the muon panel activated before the event was seen and vice-versa. A decision can be made on this time difference in order to avoid the coincidences between the two detections. This is known as the *Muon Veto Cut*. It has to be noted that in the underground lab, the muon flux is significantly reduced so the majority of events in the muon panels are due to the ambient electromagnetic background. A study on the probability distribution of muons at the LNGS can be found in Ref. [146]. Since the pulse onset in CRESST detectors is in the order of 1-3 ms, a window of $\pm$ 5 ms around the muon event is used to veto the cryogenic events. For the latest run of CRESST, it is seen that this window removed 4-5% of the registered events.

Another coincidence cut is performed based on the fact that a dark matter particle is highly unlikely to have multiple scatters inside the detector housing with multiple detectors and is supposed to create only a single recoil in only one detector module at a time (multiplicity = 1). If an event is seen in multiple detectors (high multiplicity), it is

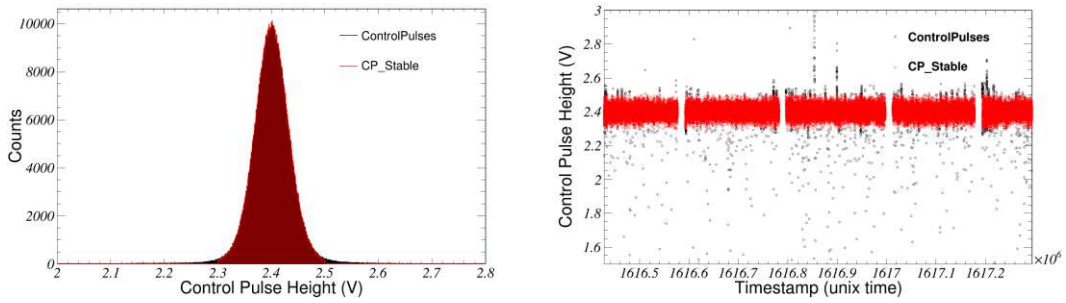

(a) (b)

Figure 4.8: (a) Histogram of Control pulse heights and (b) Control pulse height as a function of timestamps. In black are all the control pulses, and in red are the stable ones that survive the stability cut. The cut criterion is written in the text.

likely to have originated from a known background. This is removed by accounting for coincidences between events registered in different detector modules with a coincidence window of ±10 ms. This cut is known as the *Cryogenic Coincidence cut*. And since the rate is so low, there are not many accidental coincidences between multiple detectors. Hence, this cut removes a very tiny fraction of events ($< 1\%$).

4.3.2 Stability Cut

As it was already discussed in Sec. 3.4.3, in order to ensure the stability of the operating point of the TES, control pulses are sent every 10 seconds, and the PID controller monitors and corrects the temperature to keep the detector at a stable operating point. Since this correction also sometimes heats the detector out of transition, there are periods in the data taking when the control pulses are far away from the operating point, and these periods are defined as *unstable* periods. If a particle event is registered in these periods, it cannot be used as it would lead to wrong amplitude reconstruction. Thus, events in these periods have to be cut. This is done by performing the *Stability cut*. A histogram of the pulse heights of control pulses sent throughout the run is plotted and fitted with a Gaussian distribution. Then, the control pulses that are more than 3σ away from the Gaussian mean are marked as unstable. The stability of the triggered events is defined based on the two control pulses, between which is event is registered. If either of the control pulses is defined as unstable, then the registered event is also marked as unstable. The histogram of control pulse heights and their time series can be seen in Fig. 4.8.

4.3.3 Rate Cut

Being in an underground lab, the background rate of events is roughly constant with time. The hypothesized dark matter signal is also predicted to be roughly constant in time (with small variations due to annual modulation). Thus, if the detector suddenly

sees a huge increase in the count rate of events, then those events are likely to be invalid. Fig. 4.9 shows an example of this "burst" of events that can happen over a constant background rate. The cut used to remove the events occurring in these time windows is called as the *Rate cut*. The length of the time window to be used for the rate cut can be tuned depending on the bursts seen in the training set, but usually, a 10-minute window is used. An average rate per 10 min is calculated, and if the rate is suddenly more than 3σ from the average, those time windows, along with the two adjacent ones, are rejected.

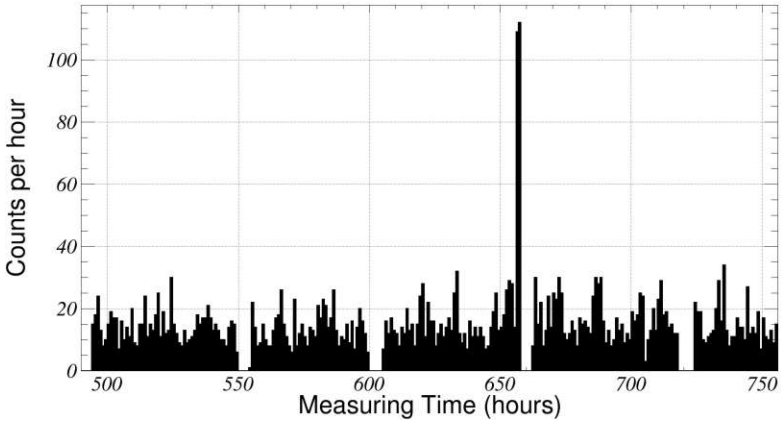

Figure 4.9: Example of a burst of events above a constant count rate as a function of time. The gaps after every $\sim$ 50 hours are due to refilling (Sec. 3.2.1)

.

4.3.4 Trigger Cut

With a multiple-channel read-out, it is necessary to know the pulse information in the second channel along with the first channel which triggered. Hence, whenever a pulse is seen in the phonon channel, the light channel is also triggered and saved in order to get information about the event type. The opposite happens as well, where phonon channel information is saved if the event directly happens on the light channel (also known as the direct hits). Since, in CRESST, the light channel is principally used only for the event discrimination and the phonon channel is used for the energy reconstruction, the direct hits on the light channel are rejected for the physics analysis. These are also known as *Light-only* events. This is done with the help of the *Trigger cut*. As soon as an event is triggered offline, the information about the filtered amplitude is saved along with the triggered timestamp. In the case when only the light channel is triggered and the phonon channel is not, and only saved because of light channel triggering, the filter amplitude of -10 V is saved for it. By making a cut to allow only the events where the triggered filter amplitude is above the trigger threshold, only the "true" triggered events are saved, and the light-only events are removed.

4.3.5 Data Quality Cuts

Having accepted data only in the stable and proper working conditions of the detector, the next set of cuts applied is based on the pulse shape of the events in the record window to make sure that the triggered events are valid recoils and no noise artifacts are triggered. Since the cuts depend on the quality of the triggered events, these are called *Data quality cuts*. In Ref. [147], another approach toward automated data cleaning has been proposed using artificial neural networks and has been shown to work with high accuracy with CRESST data. This approach would be highly useful for the upcoming CRESST upgrade with a large number of detector modules. However, for this work, the classical data-cleaning technique has been explained. The different types of noise artifacts and the data quality cuts applied in order to remove them are explained in the following.

4.3.5.1 Right-minus-left Cut

The two major kinds of artifacts that are present in the data are SQUID jumps (Fig. 4.10(a)) and the decaying baselines (Fig. 4.10(b)). The former is due to the fact that the SQUID does not always run with a constant baseline and can jump between different states (or baselines) if the deposited energy is too high, and the SQUID electronics cannot follow the fast rise time of the pulse. These are also known as *Flux quantum loss*. The latter occurs if a high-energy pulse hasn't had enough time in the record window to come back to the initial baseline. This causes a falling baseline to be seen in the next record window, and being above the constant baseline, it is also triggered.

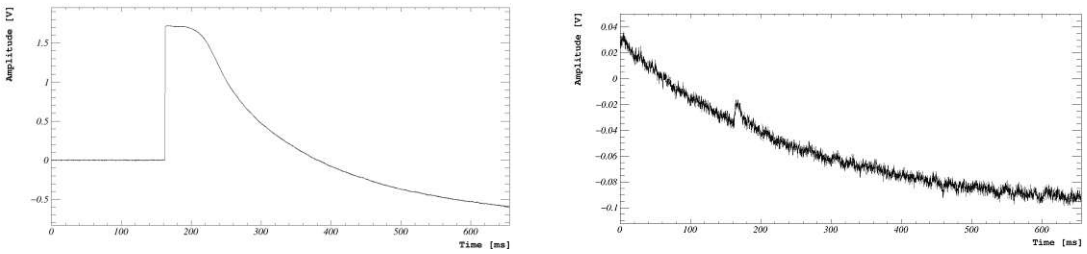

(a) (b)

Figure 4.10: Example of (a) Flux quantum loss and (b) Decaying baseline with a small pulse on top.

A very efficient cut that helps in removing both of these artifacts is the Right-minus-left cut, which is performed on the Baseline difference parameter (Sec. 4.2.1). Allowing the difference between the averages of the last 50 samples and the first 50 samples to be above a certain value, many of these artifacts can be efficiently removed. Typically, a value of baseline difference above -0.02 V is seen to work well with these noise events. The cut can be visualized in Fig. 4.11. In principle, a fluctuation above the baseline is also possible, and applying the cut on the positive value of the baseline difference should clean them. However, this would also remove the high-energy saturated pulses

that haven't had enough time to fall back to the baseline within the record window and have a much higher running average at the end of the record than at the beginning of the window. If the focus of the analysis is only on the low-energy region, a cut on the absolute value of baseline difference is more optimal.

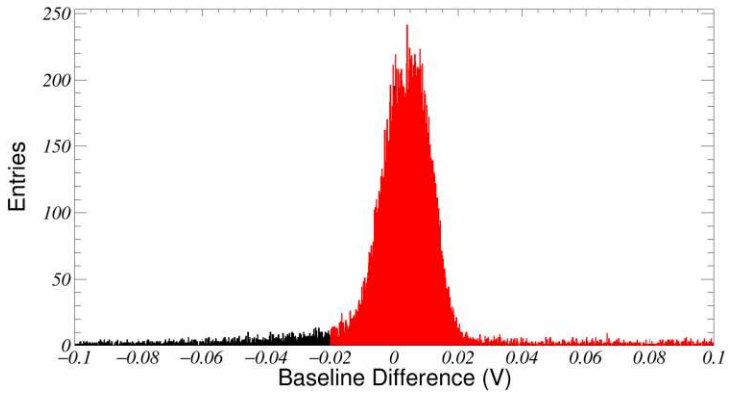

Figure 4.11: The typical cut applied on the baseline difference in order to remove the two artifacts in Fig. 4.10. The black histogram contains all the events, whereas the ones in red are the events surviving the cut.

4.3.5.2 Delta Voltage Cut

The readout electronics can sometimes cause a very low-voltage sample spike to be saved that has no particle origin. Such fluctuations of the baseline have to be removed as they could lead to a wrong energy reconstruction. An example of such a voltage spike can be seen in Fig. 4.12(a). A useful cut that helps in order to remove these spikes is using a combination of the minimum derivative and the baseline RMS parameters. As these spikes are quite instantaneous, their derivative is very high. Diving the minimum derivative with the baseline RMS gives a quantity that has information about the sharp fluctuation beyond the baseline of the record window. Thus, allowing the events only above a certain value of Minimum Derivative/Baseline RMS removes these jumps effectively. Since the cut depends on the baseline of the detector, its value changes from one detector to another. In the example shown in Fig. 4.12(b), a value above -300 s^{-1} is chosen.

4.3.5.3 Filter RMS Cut

After fitting all the individual filtered triggered pulses with the filtered SEV, the RMS obtained from the fit has the information on which events look like a pulse and which do not. Applying a cut on the filter RMS helps in getting rid of these events, which do not look like a typical pulse in a record window. These events could have multiple origins, such as unstable electronics, multiple events seen in the same record window (pile-up events), etc. These different events are visualized in Fig. 4.13. In the case where high-energy saturated events are also required to be saved, filter RMS cut is only applied for the pulses below the truncation limit of the detector, as the saturated pulses will

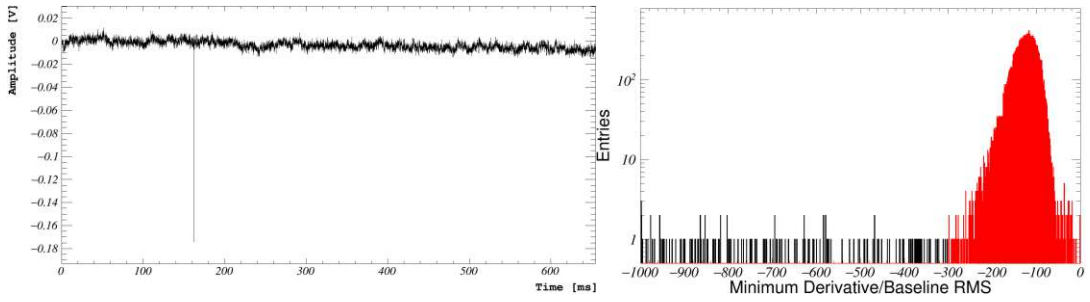

(a) (b)

Figure 4.12: (a) Example of voltage spike and (b) A delta voltage cut applied in order to remove them. The red histogram shows the surviving events, and the black one shows all the events.

obviously have a high RMS and will be otherwise cut out. In the case where the interest is only in the low-energy region, the filter RMS cut can be applied to the whole energy range.

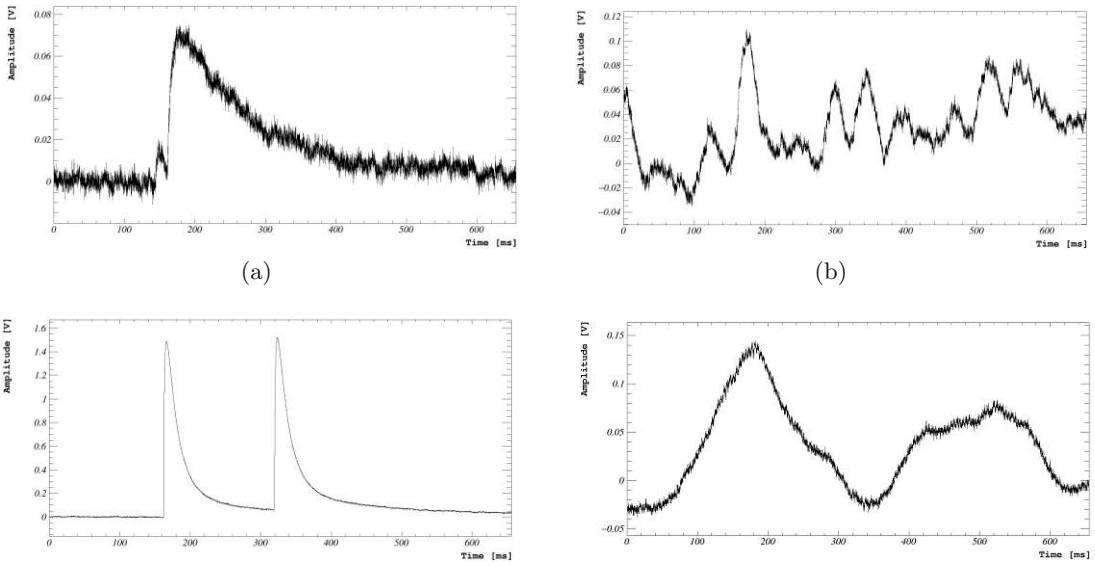

(a) (b)

(c) (d)

Figure 4.13: Examples of different noise artifacts removed by the filter RMS cut.

4.3.5.4 Template Fit RMS Cut

Similar to the filter RMS cut, this cut uses the RMS value evaluated from the template fit. As it has already been discussed, where the filter RMS value is useful for the low-energy events below the truncation limits of the detector, the template fit RMS is mainly used to clean high-energy pulses and artifacts. As the RMS is calculated only from the region

below the truncation limit of the detector, even for very high energy pulses, it serves as a good data quality parameter.

4.3.5.5 Jumps Cut

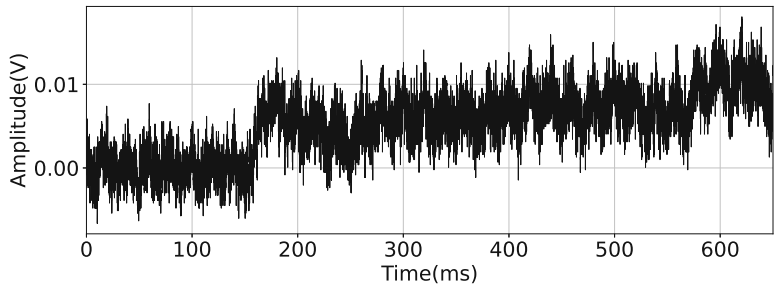

(a)

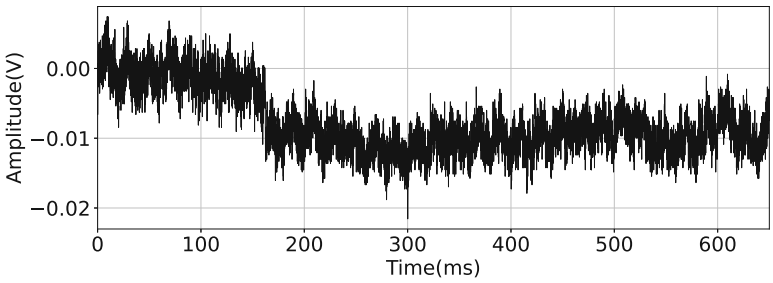

(b)

Figure 4.14: (a) Example of jump event and (b) the jump event is seen in the inverted stream, which is seen as jump down in the original stream.

Another class of events seen in some modules in the latest run of CRESST was the jumping noise baseline events. Ever so often, the baseline was seen to jump to a slightly higher value. Having the whole raw continuous data also allowed to trigger the inverted stream, and it was seen in the inverted seen that the jump events went back to the original baseline after some time (longer than the record window length). The jump events in the original stream and the inverted stream (or technically events reverting back to the baseline in the original stream) can be seen in Fig. 4.14. If not removed, these events formed a huge population close to the threshold. An efficient technique applied to remove them was to create a template from the jump events (or Jump SEV) and fit all the pulses with this template. For a normal pulse, one would expect a smaller RMS when fitted with a pulse SEV than a jump SEV. Similarly, for a jump event, the jump SEV would give a better fit and would have a smaller RMS than the pulse SEV. Allowing only the events where the difference between the Jump SEV fit RMS and template fit RMS was positive, was seen to work effectively against these events. This is known as the *Jumps cut*, and it can be seen in Fig. 4.15.

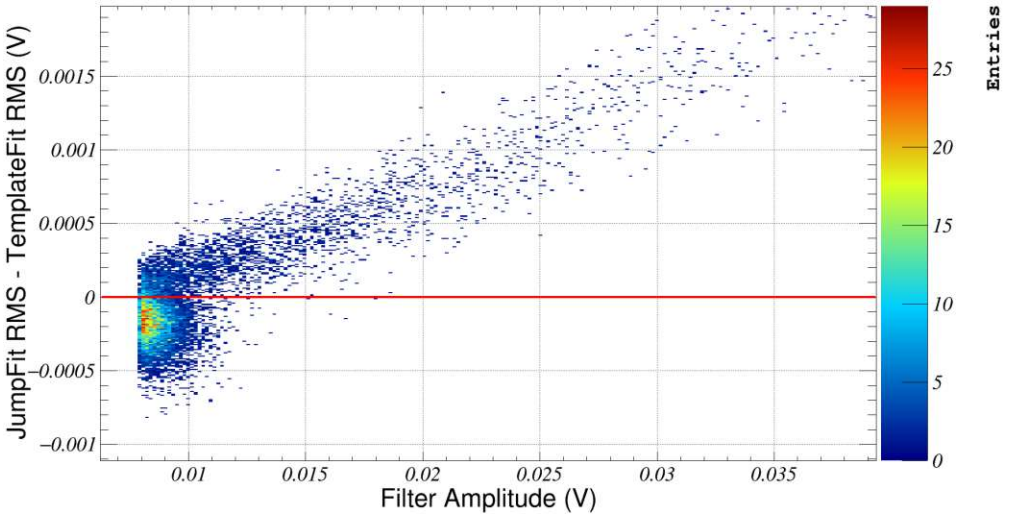

Figure 4.15: The cut applied to remove the jump events. Events above the line are accepted events.

4.4 Energy Calibration

After removing all the possible artifacts from the data and collecting the clean particle recoils, the energy reconstruction of the events is required in order to get the final spectrum. Since CRESST is a dual-channel readout experiment, the calibration process involves calibrating both the relevant parameters used for setting the dark matter region of interest (Fig. 3.4), i.e., the deposited energy in the crystal and the light yield of every event in order to get the information about the incoming particle. This section focuses on extracting the recoil energy and the light yield of events from the recorded voltage values.

4.4.1 Recoil Energy Estimation

4.4.1.1 Test Pulse Response

Even though the stability cut (Sec. 4.3.2) removes the periods of high instability, small variations of the detector response are still possible with the allowed deviation of 3σ. As a result, a linear conversion of the recorded voltage values directly to energy could lead to errors in the energy estimation, which is a concern at the low energies where CRESST aims to measure. Thus, a method is required in order to incorporate the time-dependent variation of the operating point and calibrate the detector accordingly. This is done by measuring the response of the heater pulses sent over time. For the estimation of the output amplitude seen by the SQUIDs for a given input amplitude at the TES, the artificial test pulses are sent by the waveform generator every 20 sec with increasing amplitudes starting from 0.1 V to 10.0 V. These are also known as the *Test Pulse Amplitudes* (TPAs) and can be visualized in Fig. 4.16(a) for a segment of

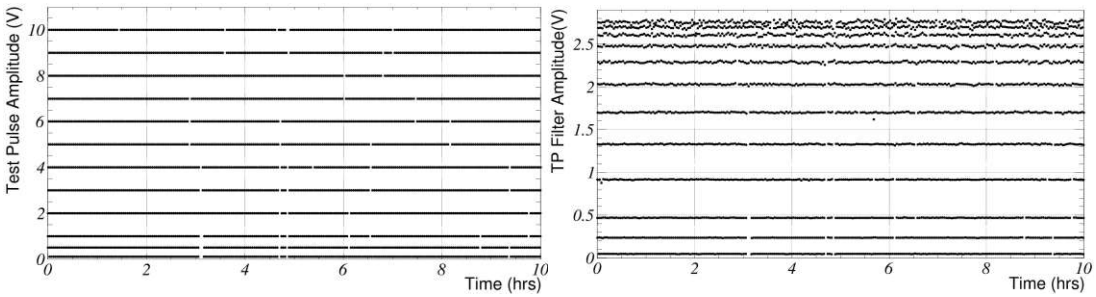

(a) (b)

Figure 4.16: (a) Injected test pulse amplitudes(TPAs) as a function of time for a segment of measurement. (b) The filter amplitude of the test pulses as a function of time from the same segment.

measurement.

For the estimation of the output amplitude of the test pulses, a SEV is created from the test pulses and is used to create an optimum filter for the test pulse with the same NPS. The optimum filter used for triggering cannot be used for the test pulses due to the different pulse shapes of the two. Then, all the test pulses are filtered with this test pulse optimum filter and fitted with the filtered test pulse SEV (just like it is done for particle pulses as discussed in Sec. 4.2.2). The extracted filter amplitude gives a precise estimate of the output amplitude. This filter amplitude as a function of time can be seen in Fig. 4.16(b), for the same segment shown in Fig. 4.16(a). High-voltage test pulses are seen close to each other as they start saturating the TES beyond its linear range. The same procedure can also be followed with the truncated fit of the test pulses, where the saturation effect of the high-voltage test pulses could be avoided.

In order to monitor the input-to-output response of the detector at any given time, the following technique is used: For every TPA, a Gaussian kernel smoothing is performed on the filtered output amplitude against time with a smoothing parameter. The parameter is typically chosen as 0.5 h. For any desired time when the response needs to be known, an *amplitude transfer function* is created, which relates the injected TPA with the reconstructed filter amplitude from the smoothing kernel. The two are fitted with a third-degree polynomial function (Fig. 4.17). Thus, this function allows the conversion of any reconstructed amplitude to the injected amplitude at any particular time of the detection.

Thus, assuming the response of the particle pulses is similar to that of the test pulses, for any output reconstructed amplitude, the input amplitude at the TES can be inferred. For every particle recoil, the timestamp is noted, and the amplitude transfer function is created for the region around that timestamp. In the example shown in Fig. 4.17, a transfer function is created when a particle recoil with a reconstructed filter amplitude of 1.5 V is recorded. Then, as per the transfer function, this would correspond to a 2.7 V injected amplitude. This calculated injected amplitude is typically called Test Pulse

Equivalent Amplitude (TPE Amplitude) as it represents the TPA needed to reproduce the given reconstructed amplitude.

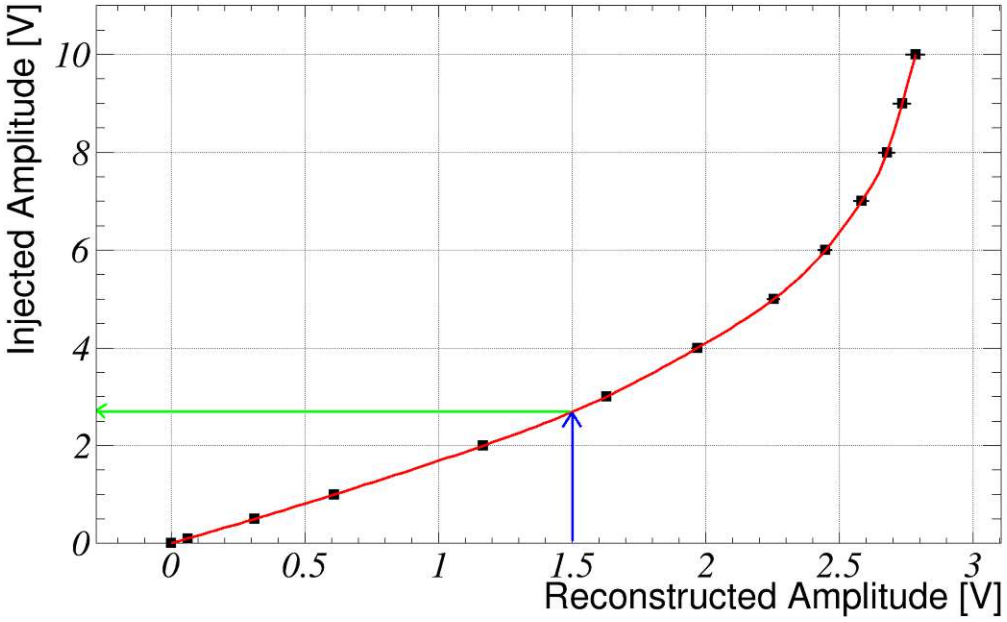

Figure 4.17: Example of a typical amplitude transfer function calculated at a time when a particle recoil with a Filter Amplitude of 1.5 V occurred. The given function gives approximately 2.7 V injected amplitude.

4.4.1.2 CPE Factor

Since the TPE amplitude contains information about the time-dependent variations of the detector response, the next step would be the direct conversion of the TPE amplitude to the energy units. In CRESST, this is typically done using the Cobalt calibration data that has 122.1 keV and 136.5 keV gamma lines originating from a ^{57}Co source. However, for the latest run of CRESST, the focus was more on the low-energy region (< 1 keV). Hence, a calibration source was required, which had significant peaks in the low-energy region, so that the energy scales could be trusted. For this reason, every module in the latest CRESST run was equipped with an ^{55}Fe screw. The ^{55}Fe nucleus decays with an electron capture to a ^{55}Mn nucleus that has significant K_α and K_β lines at 5.89 keV and 6.49 keV, respectively. These two peaks can be seen in the TPE Amplitude spectrum in Fig. 4.18. Fitting them with two Gaussians, extracting the means of both the peaks, and diving the means with the corresponding energy gives the conversion factor from TPE amplitude to energy. This factor is called the *Convert Pulse Height to Energy factor*(or CPE factor). Then, the whole spectrum is multiplied by the CPE factor in order to get the recoil energy spectrum.

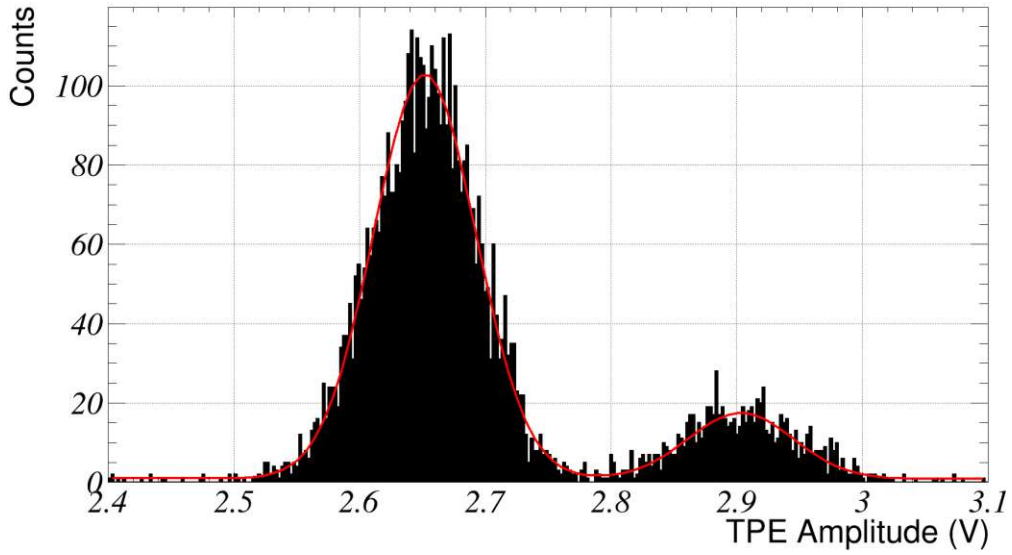

Figure 4.18: The iron lines seen in the TPE Amplitude spectrum (in black), fitted with two Gaussian and a constant background(in red).

4.4.2 Event Type Discrimination

The procedure followed in order to calibrate the phonon detector is also done for the light detector, with the only difference being that the light detector is not calibrated with the direct hits on the detector but rather the scintillation light produced by the phonon detector. Hence, the signal seen in the light detector for every ^{55}Fe hit on the phonon detector is also fitted with a Gaussian with a mean energy of the iron lines, but in electron equivalent units (as defined in Sec. 3.3.1). In this way, the scintillation energy output of all the events in the phonon detector is calculated in keV$_{ee}$ units.

The two most relevant recoils seen in the CRESST detectors are the nuclear recoils that result from interaction with neutrons or potentially dark matter particles and the electron or gamma interaction that amounts to the background. In order to increase the sensitivity of the experiment, proper calibration and discrimination of both types of events in the light yield vs recoil energy plane is necessary. Where calibration of the electron/gamma events is straightforward due to the presence of a calibration source, neutron calibration is tough due to multiple shielding layers preventing any background neutrons from making it to the detector. Hence, as already discussed in Sec. 4.3, after collecting the relevant data for the dark matter analysis (or the *bck* data), neutron calibration (ncal) data are collected by placing an AmBe source inside the neutron shielding. The similar analysis procedure described for the training set above is also applied to the whole neutron calibration data, and the recoil energies, along with the scintillation energy output, are calculated. This analysis does not need to be a blind analysis as no dark matter results are directly extracted from this data, and the data is only used for calibration purposes. After extracting the relevant quantities, the events are plotted in the light yield plane and

fitted with the relevant bands. A detailed analytical description of the band parameters can be found in Ref. [148] and [138]. The bandfit of the neutron calibration data for the last CRESST run can be seen in Fig. 4.19. The band information is then saved and overlaid with the *bck* data, and the dark matter region of interest is defined in the nuclear recoil bands, allowing tremendous reduction of the electron/gamma background.

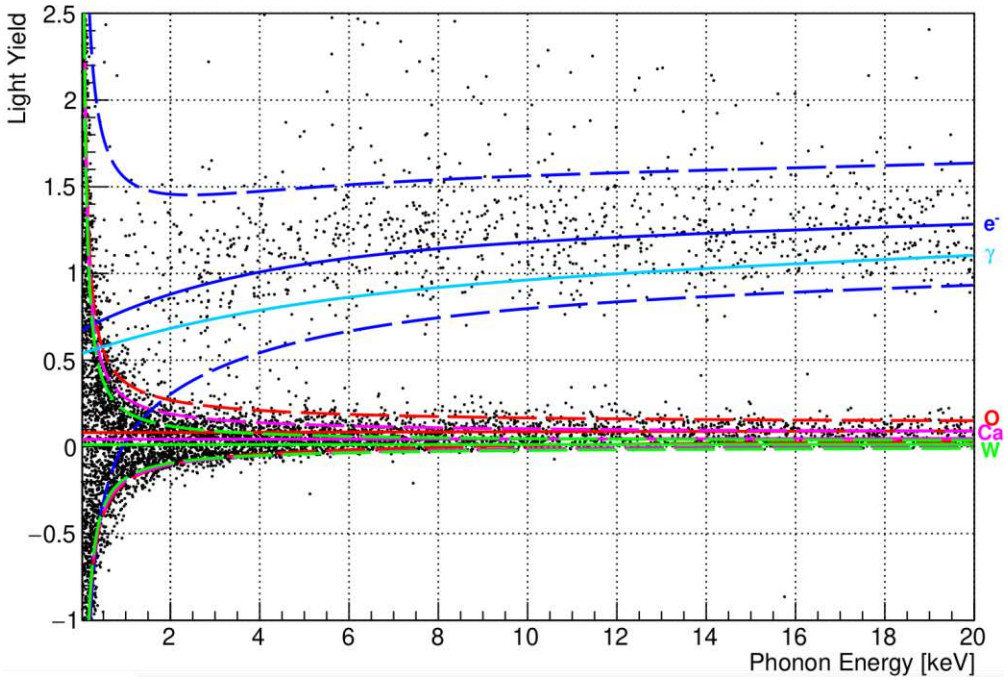

Figure 4.19: Bandfit with the neutron calibration data of the detector module used for first dark matter results with CRESST-III [89]. The electron band is shown in dark blue, the gamma band in light blue, the oxygen band in red, the calcium band in pink, and the tungsten band in green. The mean lines of the bands are shown with solid lines, and the standard deviations are with dashed lines. The image is taken from Ref. [149].

4.5 Efficiency Calculation

After extracting the recoil energy spectra, the last step of the low-level data analysis is the calculation of the efficiency of the analysis chain. This is essentially done in order to estimate the probability of the dark matter events surviving the triggering and the data-cleaning process. The basic approach of this calculation is to simulate a very large number of events throughout the energy region of interest and pass all these events through the whole analysis chain. In the end, the number of events that survive the chain is compared to the simulated ones, and this gives a good estimation of the efficiency. Simulation of a huge number of events is vital as it increases the statistical significance of the calculation. This section focuses on the approach used for the simulation of these events and the extraction of the efficiencies.

4.5.1 Simulation Approach

If the efficiency of a dark matter-like event has to be calculated, the simulated events should give a nuclear recoil-like signature as well. Thus, the most basic approach would be to simulate the nuclear recoil-like pulses on the stream. Another application of the continuous DAQ is the availability of the whole raw stream, on which this simulation can be performed and then analyzed in the same way as it is done of the *bck* data. Since the experiment is running in a very low-background environment, most of the stream is essentially empty and provides a possibility to simulate a huge number of events.

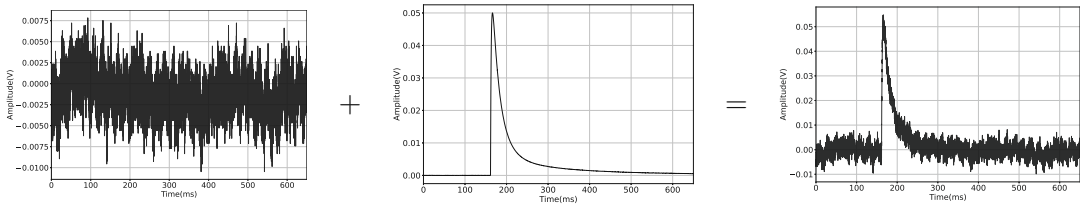

Figure 4.20: The process of simulation where a region in the raw stream is added with a scaled standard event of 0.05 V in order to give a simulated pulse of 0.05 V.

The simulation is performed essentially by adding the particle recoil SEV on the stream as shown in Fig. 4.20 for an event of around 0.05 V amplitude. The amplitude of the superimposed SEV is scaled with the required simulated amplitude. Since the baseline on which the pulse is superimposed contains the standard noise, the simulated event is a good representation of an actual recoil on the stream. This can be seen in the example shown in Fig. 4.21, where the simulated pulse shown in Fig. 4.20 is compared with an actual pulse of the same amplitude.

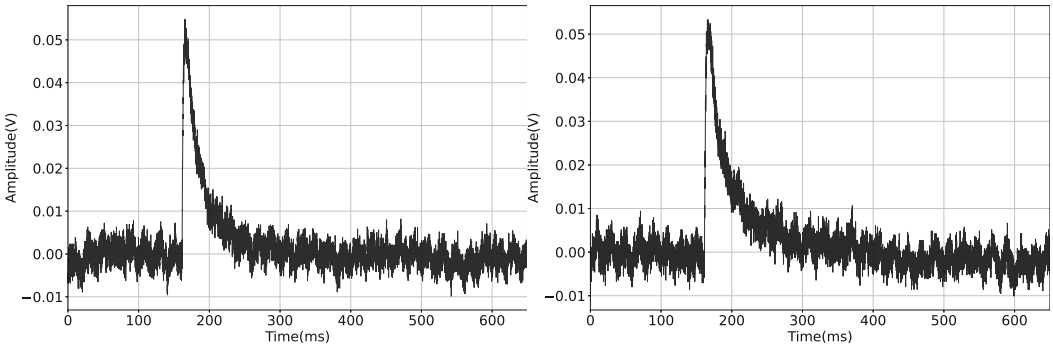

Figure 4.21: Comparison of the (a) Simulated pulse as shown in Fig. 4.20 with (b) an actual pulse of the same amplitude.

In order to perform this simulation, the following quantities need to be known and defined:

1. **Simulation rate:** This quantity sets the number of simulated pulses that are superimposed throughout the whole stream. This is usually given in average events per second and is typically chosen to be around 0.2-0.3 s^{-1}. This, on average, translates to a simulated pulse every 3-5 seconds in the stream. The precise location of the pulses is chosen randomly within the stream. If more pulses are required in the stream, then the simulation rate can be increased as well.

2. **Correlation index:** For a module with a dual channel readout, the light channel also needs to be simulated along with the phonon channel. Typically, electron events with LY=1 are simulated. As the majority of the analysis cuts are performed on the phonon channel, simulating electron events instead of nuclear recoils does not make a huge difference. Thus, the simulated energies are the same in both channels and are also at the same timestamps, with an additional buffer of a few samples. The additional buffer is added because a small shift in the maximum position of the optimum filter of the light channel is often seen when compared to the phonon channel. The correlation index decides which channel is treated as the principle simulation channel, which is essentially the phonon channel, but the light channel can be chosen as well if needed.

3. **Energy range for simulation:** The energy region required for simulation also needs to be defined. Typically, events are simulated equally within this energy region, but a logarithmic distribution could also be simulated where more events are simulated at lower energies for better statistics compared to the higher energy region. The choice of the energy range is kept within the linear range of the detector as the described simulation procedure cannot represent the behavior of the saturated pulses.

4. **CPE factor and amplitude transfer function:** After a random recoil energy is chosen in keV units for simulating an event, the energy has to be translated into the simulated amplitude on the stream in volt units. For this, the reverse calibration procedure needs to be applied. The event is first divided with the CPE factor of the particular detector in order to get the simulated TPE amplitude of that event. Then, with the information of the random timestamp of the event, the amplitude transfer function is created as described in Sec. 4.4.1.1. Now, using this function, the simulated TPE amplitude is converted to the simulated filter amplitude, and the standard event is scaled with this amplitude and superimposed on the stream at the same random timestamp. This amplitude is called *Simulated Amplitude*, and the energy from which it is extracted is called *Simulated Energy*. Therefore, within the statistical fluctuation, the reconstruction of this event, after following the standard energy calibration process, should match with the simulated energy of the event.

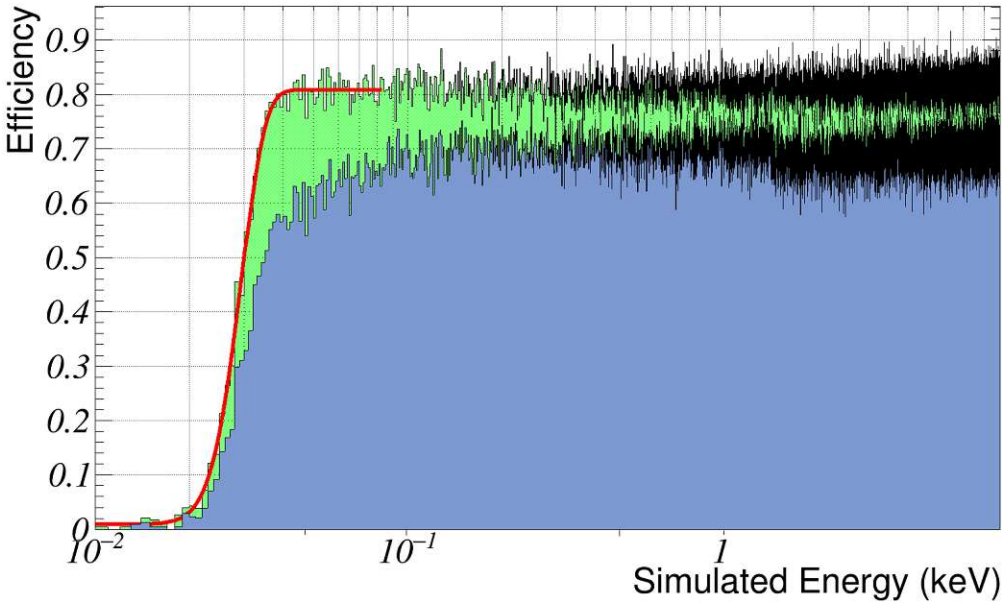

Figure 4.22: Example of trigger(green) and cut(blue) efficiency taken by diving the triggered and events surviving the cuts with the reference list of events. The triggered efficiency is fitted with an error function (in red).

4.5.2 Trigger and Cut Efficiency

Now, the large samples of events can be simulated directly on the stream depending on the choice of the parameters described above. The stream is then treated in the same way as the *bck* data and is passed through the triggering mechanism, where the triggered filter amplitude of every event is saved. Before applying the analysis cuts, the reference list of events needs to be defined, which passes through the rest of the analysis chain, and the final surviving list of events is compared with. This reference list is chosen to be all the events with the multiplicity of one, i.e., all the events where only one simulated pulse is present in a record window. This is chosen due to the fact that it is very unlikely that two dark matter particles would recoil with the detector within the same record window. If a higher multiplicity events are kept inside the reference list, then all those events would not survive the data quality cuts and hence would give an unrealistically low survival probability of a dark matter event.

Then, as a first step, the trigger cut is applied with the criteria that: 1) The triggered filter amplitude has to be greater than the trigger threshold, and 2) The event should not have a coincidence with test or control pulses. Where the first criterion is straightforward, the second criterion takes care of the fact that it is possible for a dark matter recoil to occur when a test or control pulse is passed. And as that valid recoil is not treated as a particle event, it will not show up in the final spectrum and has to be considered in the efficiency. Since test pulses are sent every 20 seconds, and the control pulses every 10 seconds, the trigger cut removes the largest share of the simulated events. This can be

seen in Fig. 4.22 as the trigger cut removed about 20% of the events in the whole energy range. In the region close to the trigger threshold, the trigger efficiency is fitted with a Gaussian convoluted error function to extract the trigger threshold. The convolution is done with the resolution of the detector. The functional form is given by:

$$f(E_{sim}) = \frac{1-c_1}{2} \cdot \left(1 + \mathrm{erf}\left(\frac{E_{sim} - E_{thr}}{\sqrt{2}\sigma}\right)\right) + c_2 \tag{4.8}$$

where c_1 and c_2 denote the flat part of the efficiency after and before the step, respectively. The fitted value of E_{thr} is reported as the official threshold value of the detector, as this value is extracted by simulating on the whole stream. Thus, it averages the time variations of the detector response over time. In the shown example in Fig. 4.22, this corresponds to 28.7 eV.

After the trigger cut has been applied, the simulated events are passed through the rest of the analysis cuts with the same selection criteria as the *bck* data, and the final list of events is compared with the reference list. This causes further reduction of the efficiency, and this can also be seen in Fig. 4.22 with the cut efficiency flatting at around 67% in the high-energy region. This final cut efficiency is used along with the recoil energy spectrum in order to do the high-level analysis.

4.6 High-level Analysis

The last step of the analysis chain is to calculate the dark matter physics results using the final recoil spectrum and the cut efficiency. In the case where a potential signal above the known background is seen in the data, the statistical significance of the detection has to be calculated in order to claim a discovery. In the case where no signal could be seen in the data, constraints on the interaction of the dark matter particles could be placed depending on the data. The focus of this section is the calculation of the detection significance in the presence of a signal and the exclusion limits in the presence of only a background (known or unknown). The framework explained here follows from Ref. [138, 148].

4.6.1 Positive Analysis

4.6.1.1 Likelihood Formalism

The approach used for the calculation of the significance of a process is the profile likelihood ratio test. The test is basically a comparison of the signal model with a background-only model and no signal (null hypothesis). Thus, it relies on the model that parameterizes the contributions from both the background and the signal, and this is essentially done by defining a *Likelihood function*, $\mathcal{L}(\theta|O)$, for the set of parameters θ and the observed data O. The function is basically the plausibility of the given θ set of parameters, for the observed data O. Thus, by fitting the data O with a model under θ

parameters, a better fit would give a larger likelihood value, giving higher plausibility. Mathematically, the likelihood function is the inverse of the probability of observing the data O, given θ as the parameters, in the sense:

$$\mathcal{L}(\theta|O) = \mathcal{P}(O|\theta) \tag{4.9}$$

The likelihood function is constructed using the probability density function (PDF) and is evaluated at each individual data point O_i. It is given by [148]:

$$\mathcal{L}(\theta|O) = \prod_{i=1}^{N} \rho(O_i|\theta) \tag{4.10}$$

where $\rho(O_i|\theta)$ defines the two-dimensional probability function of the dark matter signal and the background, given by [138]:

$$\rho(O|\theta) = \rho(O|\theta_\chi) + \rho(O|\theta_b) \tag{4.11}$$

where the first term on the left-hand side represents the PDF of the dark matter signal, with θ_χ as the dark matter parameters of interest, which for our case, are the cross-section and mass, i.e. $\theta_\chi = \sigma_\chi, m_\chi$. In principle, other properties of dark matter that impact the PDF could also probed using this formalism, e.g., coupling strengths, etc. The second term describes the contribution from the background.

Now, since the number of data points observed, N is also a free parameter and thus can also have a deviation from its expected value. The deviation is subject to Poissonian fluctuations. Thus, given that N is a random number described by a Poissonian distribution with a mean ν, this information is included in the likelihood function in the following way:

$$\mathcal{L}(\theta|O) = e^{-\nu} \prod_{i=1}^{N} \rho(O_i|\theta) \tag{4.12}$$

This formalism is known as the *extended maximum likelihood* method. It has to be noted that with the given form of the likelihood function in Eq. 4.12, small errors in the density estimation could lead to huge errors upon multiplication, and it would also lead to dealing with huge numbers and would be computationally expensive. For this reason, the logarithm of the likelihood function is generally dealt with instead, as logarithm is a continuously increasing function. Thus, the extended log-likelihood function would take the form:

$$\ln[\mathcal{L}(\theta|O)] = -\nu + \sum_{i=1}^{N} \ln[\rho(O_i|\theta)] \tag{4.13}$$

4.6.1.2 Discovery Calculation

The profile likelihood test for the significance of a signal introduced previously can now be formulated for the dark matter signal as:

$$\lambda(0) = \frac{\mathcal{L}(0, \hat{\hat{\theta}}_b|O)}{\mathcal{L}(\hat{\theta}_\chi, \hat{\theta}_b|O)} \tag{4.14}$$

where $\lambda(0)$ is the likelihood ratio that compares the model under a null hypothesis in the numerator with the model under a signal hypothesis in the denominator. The numerator shows the maximum likelihood function in the presence of no signal. The values of the background parameters that maximize the likelihood function are labeled with double hats as $\hat{\hat{\theta}}_b$. The denominator gives the maximum likelihood value under the signal hypothesis, and the values that maximize the likelihood function are shown in single hats as $\hat{\theta}_\chi$ and $\hat{\theta}_b$. Looking at the form of the likelihood ratio, one can see that in the presence of a significant signal, the discrepancy between the null hypothesis and signal hypothesis would increase, and thus $\lambda(0)$ would be small. In the case where no signal (or no significant signal) is present in the data, the numerator and the denominator would come close to each other, and thus the value of $\lambda(0)$ would be close to one. The significance decreases as the likelihood ratio increases, and its value is bound as $0 \leq \lambda(0) \leq 1$.

In order to convert the likelihood ratio to the statistical significance of the signal, a test statistic is commonly defined in the following way:

$$q_0 = -2 \ln (\lambda(0)) \tag{4.15}$$

where q_0 takes a value close to zero for $\lambda(0) \to 1$ and increases as $\lambda(0)$ decreases, thus directly signifies the agreement between the data and the signal hypothesis. Now, we can define a quantity known as p-value, P_0, which quantifies a statistical fluctuation to fake a signal and is given by:

$$p_0 = \int_{q_0,obs}^{\infty} f(q_0|0) dq_0 \tag{4.16}$$

where $f(q_0|0)$ is the pdf of q_0, under null hypothesis. Note that a smaller value of P_0 thus gives a lower probability of a fluctuation to mimic a signal, giving a higher significance of the presence of an actual signal. The significance Z, which is given as the number of standard deviations away from the mean, can thus be translated from the p-value as:

$$Z = \Phi^{-1}(1 - P_0) = \sqrt{2}\ \mathrm{erf}^{-1}(2P_0 - 1) \tag{4.17}$$

with $\Phi(x)$ as the first quantile of the normal distribution. Now, Wilk's theorem states that for a large sample N, the probability density function $f(q_0|0)$ follows a χ^2-distribution with n degree of freedom, where n is the number of free parameters of interest, which for our case is only the cross-section σ_χ, so n=1. Thus, applying Wilk's theorem, the significance can be written simply as [150]:

$$Z = \sqrt{q_{0,obs}} \tag{4.18}$$

For claiming a discovery, the particle physics community requires a significance of $Z \geq 5$ as mandatory. The recent discovery of the Higgs boson by the ATLAS and CMS collaboration showed a significance of signal at $Z = 5.9$ [151, 152].

4.6.2 Calculating Exclusion Limits

If no evidence of signal above the known (or unknown) background is seen in the data, some information about the interaction of dark matter particles can still be extracted. In such a situation, constraints on the interaction cross-section are placed, which defines the sensitivity of the experiment and is used to compare different experiments. The calculation is performed separately for different dark matter masses, starting from the lowest mass that the detector can probe given its threshold. This is calculated using Eq. 3.8 with $E_{R,max}$ as the threshold, and v as the galactic escape velocity. For a compound nucleus, the mass of the lightest nuclei is taken. After fixing the mass m_χ, the upper limits on σ_χ are calculated with a chosen confidence level. Typically, a confidence level of 90% is used as a standard one. Finding upper limits for different masses, the final exclusion limit is set as an interpolation of all (m_χ, σ_χ) points. Two standard methods used for the calculation of upper limits are the Likelihood approach and Yellin's method, which are described here.

4.6.2.1 Likelihood Approach

For setting an upper limit on the cross-section using the likelihood framework, the formalism is very similar to the one in the discovery case explained above, except that now the significance is set on the cross-section σ_χ that can be excluded to be compatible with the given data and the model. The likelihood ratio in this case becomes:

$$\lambda(\sigma_\chi) = \frac{\mathcal{L}(\sigma_{\chi,excl}, \theta_b|O)}{\mathcal{L}(\sigma_{\chi,best}, \theta_b|O)} = \frac{\mathcal{L}_{excl}}{\mathcal{L}_{best}} \tag{4.19}$$

where the denominator doesn't change compared to the Eq. 4.14 and represents the maximum likelihood obtained, leaving σ_χ as a free parameter. However, the numerator is now calculated by setting a fixed σ_χ that leads to the desired significance. The test statistic, consequently, also changes and is given by:

$$q_{\sigma_\chi} = \begin{cases} -2 \ln \lambda(\sigma_\chi), & \text{for } \sigma_{\chi,best} > 0 \\ 0, & \text{for } \sigma_{\chi,best} < 0 \end{cases} \tag{4.20}$$

and the significance becomes:

$$Z = \sqrt{q_{\sigma_\chi}} = \sqrt{-2(\ln\mathcal{L}_{excl} - \ln\mathcal{L}_{best})} \tag{4.21}$$

For a 90% confidence level, $Z = 1.282$. Thus, in order to calculate the exclusion limit, first, the data is fit, leaving σ_χ free to obtain $\mathcal{L}_{best}$. And then $\sigma_{\chi,excl}$ is found by solving the Eq. 4.21.

4.6.2.2 Yellin's Methods

Where the likelihood framework allows handling the background information into the limit calculation, there could also be cases where there is a background of unknown origin.

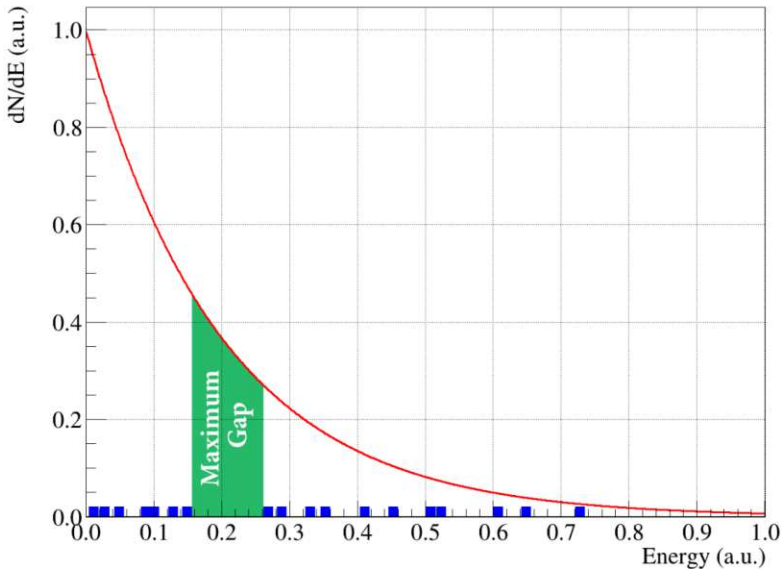

Figure 4.23: Demonstration of the maximum gap(green-shaded region) for the expected spectrum (in red) and the observed data points (in blue). The image is taken from Ref. [138].

The work done by S. Yellin [153, 154] allows the setting of an upper limit in these cases where no information about the background is needed. In this framework, all the events are treated as signal candidate events, and the limit is set based on their distribution. As one can expect, without the background information, the limit set by Yellin's methods is more conservative than the likelihood limits. Moreover, Yellin's method can only be used to set an upper limit and cannot be used for discovery calculation in the case when evidence of a signal is seen.

Maximum Gap Method: This method uses the "maximum gap" in the observed data set to set the limit on the cross-section. A gap x_i, in this case, is defined as the integral of the expected energy spectrum between the two observed data points at E_i and E_{i+1}. That is:

$$x_i = \int_{E_i}^{E_{i+1}} \frac{dN}{dE} dE \tag{4.22}$$

Thus, a maximum gap is found in the whole energy range, which corresponds to the maximum discrepancy between the number of expected events in the gap and the absence of any event. This is illustrated in Fig. 4.23.

Now, as one would expect, the number of expected events found in the maximum gap would increase as we increase the interaction cross-section. Thus, we aim to set a limit on the cross-section, which can be excluded with a 90% confidence level. That is to say that if the same experiment is performed multiple times, in 90% of the cases, the maximum gap would be smaller than the one we have found. It has been analytically shown in Ref. [153] that the probability of finding a gap smaller than x, for the expected number of events μ in that gap, is given by:

$$C_0(x,\mu) = \sum_{k=0}^{m} \frac{(kx-\mu)^k \exp(-kx)}{k!} \left(1 + \frac{k}{\mu - kx}\right) \tag{4.23}$$

with m is the greatest integer function of μ/x. Thus, this calculation is performed by increasing σ_χ and stopping at the point where $C_0 = 0.9$, in order to extract the upper limit with a 90% confidence level. As one can see, the method can only be used in order to set the limit on a parameter that linearly scales the expected recoil spectrum and cannot be utilized if the parameter creates a shape dependence. For such cases, a likelihood formalism must be used instead.

Optimum Interval method: In a situation where the number of observed data points is large, it is useful to extend the formalism of the maximum gap method to include more points in the gap. The optimum interval method, in contrast to the maximum gap method, calculates the probability $C_n(x,\mu)$, which corresponds to the probability of finding an interval of smaller size than x, containing n number of data points, where n could range from zero (which is the maximum gap method) to the total number of observed events N. Thus, we would then have N values of the probability calculated for each $n \in 0...N$. Thus, that value of n is chosen that gives the best exclusion limit on the cross-section, which is the largest value of all C_n's:

$$C_{max} = \max_{n \in 0...N} C_n(x,\mu) \tag{4.24}$$

Now, compensation has to be accounted for the freedom allowed to choose the optimum value of n. This is done by defining a function $\bar{C}_{max}(0.9,\mu)$, that is, the probability of a random experiment with μ observed events to give for $C_{max} \leq \bar{C}_{max}(0.9,\mu)$, for 90% confidence level. Thus, the limit is set by finding the value where $C_{max} = \bar{C}_{max}(0.9,\mu)$[154]. A detailed study of $\bar{C}_{max}$ as a function of μ can be found in Ref. [138].

CHAPTER 5

CRESST-III Run36 - Objectives and Results

The aim of the third stage of CRESST was to increase the sensitivity to sub-GeV dark matter particle masses. In the first phase of the CRESST-III, the most stringent exclusion limits were obtained for the dark matter masses ranging from 0.16 - 1.8 GeV/c^2, with the module design described in Sec. 3.3.3 and data collected in the data-taking campaign between October 2016 and January 2018 [89]. In this measurement, a roughly exponential increase of events in the low energy region (below $\sim$ 200 eV) of unknown origin was seen (Fig. 5.1), which limits the sensitivity to dark matter particles below the mass of 7 GeV/c^2. The observed events were seen across different modules with different spectral shapes, and thus, no common origin to this background could be asserted [149].

A similar rise of events was also seen in other experiments running at thresholds below 1 keV such as EDELWEISS [87, 155], MINER [156], NUCLEUS [157], SuperCDMS-HVeV [88, 158], SuperCDMS-CPD [103], DAMIC [159, 160], SENSEI [161], NEWS-G [101] etc. The finding of these excesses by various experiments led to a collaborative effort in the form of a workshop aimed at trying to understand its origin. An extensive summary of these various experiments with the observed excesses can be found in the report of this *EXCESS* Workshop in Ref. [162].

The aim of the latest run of CRESST (called Run36) was mainly to understand the nature and origin of this low energy excess (LEE) in order to mitigate or model it so that sensitivity could be increased to even lower dark matter particle masses and cross-sections. Thus, an accurate calibration at these low energies is necessary. For this reason, an ^{55}Fe source was placed with every detector module operated in this run, as it has two major gamma lines at 5.89 keV and 6.49 keV, and the calibration can be done even with small measuring time due to the fast activity of the ^{55}Fe source. One possible way of studying the LEE is its dependence on the type of material. Hence, four different

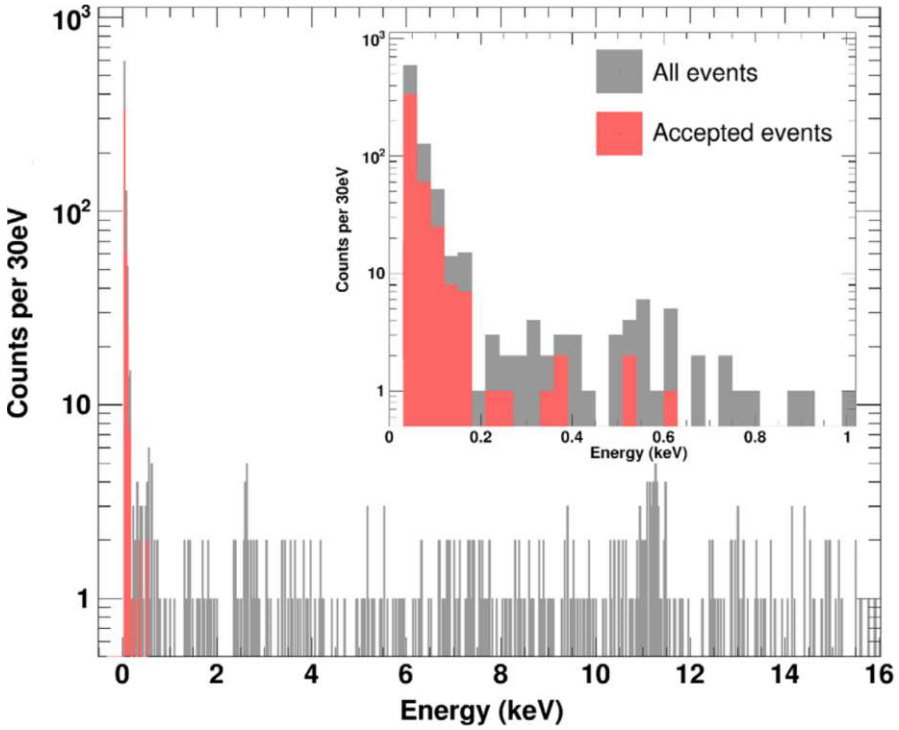

Figure 5.1: The observed spectrum of the results from CRESST-III Phase one [89]. The gray histogram corresponds to all the events observed, and the red histogram corresponds to the events inside the acceptance region. The inset histogram shows the spectrum in the low energy region with exponentially rising events of unknown origin.

types of materials were employed in Run36, namely the traditional calcium tungstate ($CaWO_4$) and sapphire (Al_2O_3), along with lithium aluminate ($LiAlO_2$) and Silicon (Si). In addition to studying the material dependence, time-dependent studies of the LEE were also performed in order to see how it evolves in time and if that can hint towards a possible origin.

In this chapter, the details and results of Run36 of CRESST have been described. In Sec. 5.1, the design and details of the operated modules have been described, followed by the studies performed on the LEE in Sec. 5.2. In Sec. 5.3, the data collected during the neutron calibration period have been discussed, where a new recoil peak at very low energies was seen, which could be used for further accurate calibration at low energies. Although the focus of this run was not to improve on the previous CRESST-III dark matter results, as the presence of the iron source increases the background events in the low-energy region, a significant improvement on the spin-dependent limits was seen with the lithium aluminate targets. In the last Sec. 5.4, these dark matter results will be discussed.

5.1 Description of the Modules

All the absorber modules operated in this run were standard CRESST-III size of ($20 \times 20 \times 10$) mm^3 operated with W-TES and were held by three sticks (except one, which was held with clamps). The modules were accompanied by a thin light detector module with ($20 \times 20 \times 0.4$) mm^3 dimensions, made of Silicon-on-Sapphire (SOS).

After the observation of the LEE in the phase one results, two major origins of the excess were hypothesized, and modifications in the detector module design were applied accordingly to study these hypotheses. These hypotheses will be described in the following, along with the description of the modification applied in order to study it:

1. **Holding structure:** It is possible that the mechanical stress coming from the holding structure on the crystal surface inside the copper housing of the module is the origin of the LEE. In order to test this, two different holding designs were

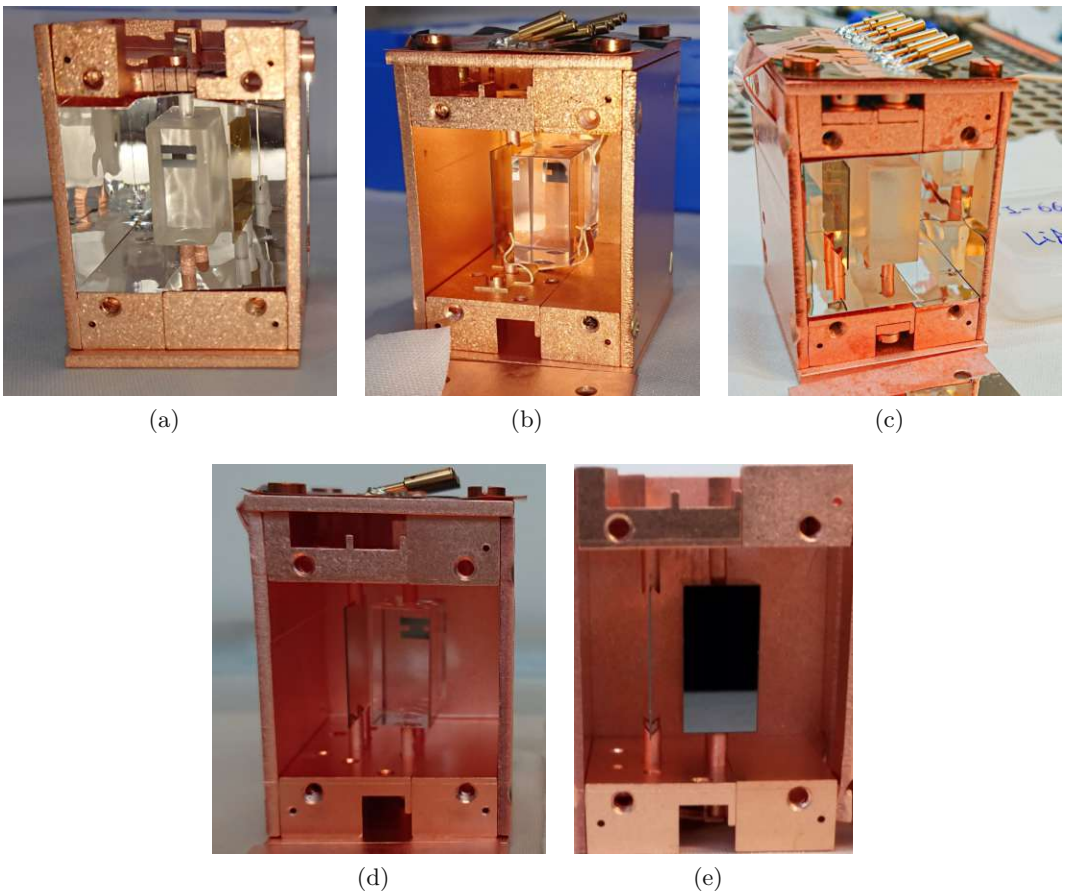

(a) (b) (c) (d) (e)

Figure 5.2: Various detector modules used in Run36. Their description is summarized in Tab. 5.1. (a) TUM93 (b) Comm2 (c) Li1 (d) Sapp2 (e) Si2.

used in Run36. One of these designs is similar to the one used in the previous run, i.e., using the sticks. For Si, Al_2O_3, and $LiAlO_2$ modules, non-instrumented copper sticks were used instead of $CaWO_4$ i-sticks. However, one i-stick was still used for one of the $CaWO_4$ modules for comparison purposes. The other holding design was using bronze clamps to hold the crystals, which was used for another $CaWO_4$ module. As bronze clamps have a larger contact area with the crystal than the sticks, a comparison between the excess could be used to quantify the effect of the holding structure.

2. **Scintillating foil:** In order to study if the excess (or a part of it) was coming from the scintillating and reflecting foil, which could not be seen by the light detector, the foil was removed from the Al_2O_3 modules and one of the $CaWO_4$ modules. Also, since silicon is non-scintillating, any effect of scintillation on the excess could be studied by its comparison with other modules.

The different modules operated in the Run36 can be seen in Fig. 5.2, and their details have been summarized in the table below:

Module	Target	Holding	Foil	Mass(g)	Threshold(eV)
Si2	Si	Cu	No	0.35	10
Sapp1	Al_2O_3	Cu	No	16	157
Sapp2	Al_2O_3	Cu	No	16	52
Li1	$LiAlO_2$	Cu	Yes	10.46	83.4
TUM93A	$CaWO_4$	2 Cu + 1 $CaWO_4$	Yes	24	54
Comm2	$CaWO_4$	Bronze Clamps	No	24	29

Table 5.1: Summary of various well-operating modules operated in Run36. The table is adapted from Ref. [163].

5.2 Observation and Studies of the Low Energy Excess

The analysis procedure described in Chapter 4 was applied to all these various modules, and the cut efficiencies were also calculated for each of them individually. The studies on the LEE were only done on the data where no additional calibration source was present. Thus, *cal* and *ncal* data were not analyzed for studying the LEE. In addition to the *bck* data, two more data sets were used, namely *postcal*, which is the data taken after the neutron calibration source was removed, and the *awu*, or the after warm-up data. The *awu* data correspond to all the data taken after warming the cryostat up to 60 K. This warm-up was done in order to study the temperature dependence of the excess, and hence, after the 60 K warm-up, many other further warm-ups to different temperatures were performed. In addition to them, a snowstorm outside the LNGS facility caused several power outages, which led to an unplanned warm-up to 600 mK (Sec. 5.2.2.2). A timeline of the Run36 can be seen in Fig. 5.3. In the following subsection, the particular analysis cuts applied for the *Comm2* module in order to extract the results are described,

although a similar procedure is applied for all the other modules. The observations have been discussed after that in Sec. 5.2.2 with the results from other modules as well.

Figure 5.3: The timeline of the Run36 of CRESST-III. The data used for studying the low energy excess are drawn in orange bars, the calibration data are shown in blue bars, and the warm-ups are shown as blue lines.

5.2.1 Analysis Cuts Applied

It was observed in the hardware-triggered data that the noise conditions were changed after the 60 K warm-up. Hence, the threshold value in mV units had to be calculated again for the *awu* data. The procedure followed to calculate the threshold is similar to what has been described in Sec. 4.1.2, which gave a threshold value of 7.9 mV for *bck* & *postcal* data and 5.5 mV for *awu* data. The comparison of the noise conditions for these three different periods can be seen in Fig. 5.4.

As a result of these varying noise conditions, the analysis cuts had to be tuned differently for the *awu* data. Further small changes in the cuts were also made in the *postcal* data as the interest for this data was only the low-energy region, and the high-energy saturated pulses could be cut out. However, for the *bck* period, information on the high-energy pulses was saved in order to model the background with the GEANT4-simulations [164]. The different analysis cuts applied, and its values are:

1. **Muon Veto Cut**: This was applied only for the *bck* data as it was seen that no real coincidences of muon events were observed. Events with a ±5 ms window of a muon veto trigger were removed.

2. **Stability Cut:** Events in the periods where control pulse height was outside of 3σ from its overall distribution were removed for all three datasets.

3. **Trigger Cut:** The events with trigger threshold below 7.9 mV for *bck* & *postcal* and 5.5 mV for *awu* data were removed.

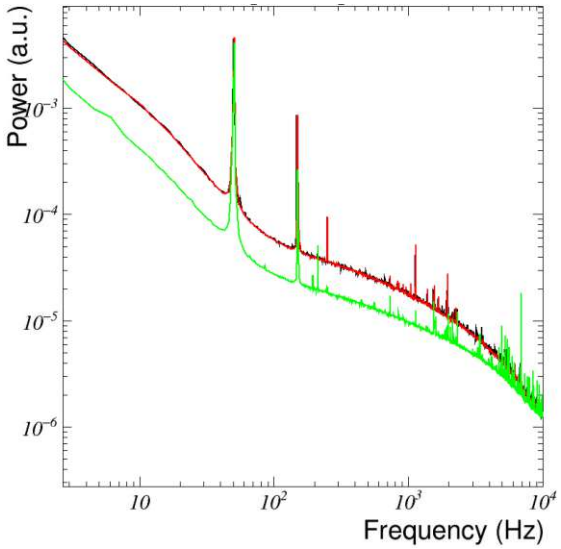

Figure 5.4: Comparison of the noise power spectrum between *bck*(black), *postcal*(red) and *awu*(green) data for *Comm2* detector module.

4. **Right-minus-left Cut:** For the *postcal* and *awu* data, events with Baseline difference below -0.02 V and above 0.02 V were removed, whereas for the *bck* data, only events below -0.02 V were removed. Many of the events above 0.02 V correspond to high-energy saturated pulses that haven't had enough time to fall back to the baseline and hence, were not removed.

5. **Delta Voltage Cut:** Only the events with Minimum Derivative/Baseline RMS above -300 s^{-1} were kept for *bck* and *postcal* data and above -250 s^{-1} were kept for the *awu* data.

6. **Filter RMS Cut:** For the *bck* data events with Filter RMS above 0.02 V and filter amplitude below 1 V were removed. For *postcal* and *awu* data, events with Filter RMS above 0.003 V and 0.025 V were removed, respectively.

7. **Template Fit Cut:** This was applied only for the *bck* data for cleaning the high-energy pulses. Events with fit RMS above 0.03 V were removed.

8. **Jumps Cut:** The jump events described in Sec. 4.3.5.5 were seen in huge amount in *Comm2* module. Thus, applying this as described in Sec. 4.3.5.5 helps in removing all the jump events.

After performing energy calibration on the surviving events, for both the phonon and the light channel, only the events with a light yield value below 10 are saved as the events with a very high light yield value are likely to be direct hits on the light channel which we are not interested in. This final cut is typically known as the *Light yield cut* and is performed for all the detector modules. For the calculation of the cut efficiency, events

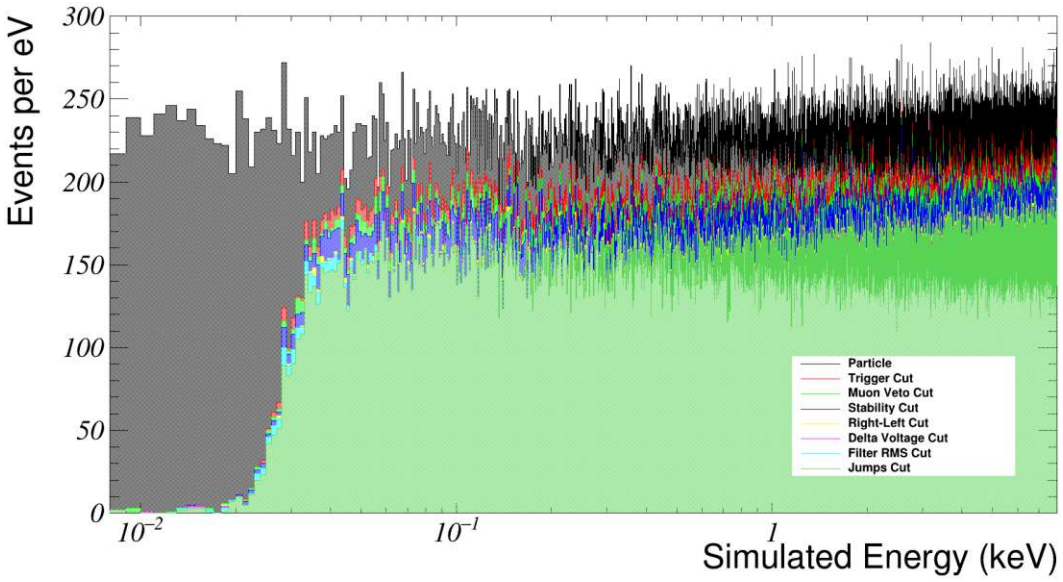

Figure 5.5: A comparison between histograms of the simulated spectrum after applying various analysis cuts for *bck* data of *Comm2* module.

were simulated on the continuous stream for all the data sets with 0.25 Hz frequency between 0-8 keV. Following the procedure described in Sec. 4.5, the cut efficiencies are calculated, and one example showing the effect of the different cuts on all the simulated events has been shown in Fig. 5.5 for the *bck* data.

5.2.2 Observations

5.2.2.1 Energy Spectra

After applying the analysis cuts and calculating the cut efficiencies, the spectrum of the particular module can be plotted. The spectrum for the *bck* data of the *Comm2* module extracted after correcting with the cut efficiency can be seen in Fig. 5.6. The two broad lines correspond to the ^{55}Fe K_α and K_β X-ray lines, which were used for energy calibration. The presence of the LEE can be clearly seen in the spectrum.

The spectrum can thus be compared with the spectra from other detector modules, and they have been shown in Fig. 5.7 [163]. The presence of the LEE was confirmed in all the detector modules below a few hundred eV. The comparison is shown between two different rates, one which is scaled with the mass of the detector, known as the specific rate, and the other being the absolute rate where the mass scaling is not used. As it was already confirmed from the results of the CRESST-III phase one, the LEE was seen to have different rates in different $CaWO_4$ modules [149], this is seen in Run36 results as well, where the rate is different for different materials also. The difference is seen to be up to an order of magnitude in the absolute rate between 60-120 keV, and up to two orders of magnitude in the specific rate. This observation can safely discard the excess coming

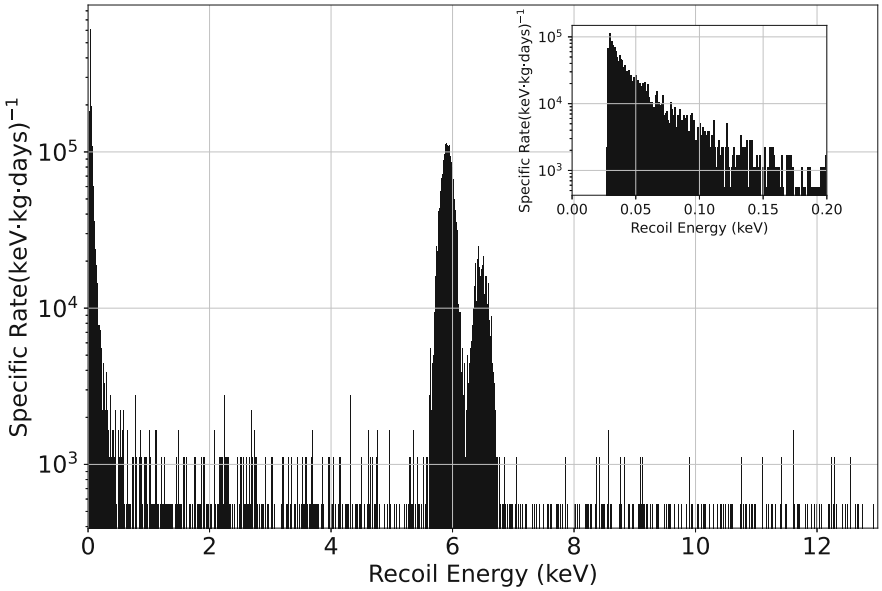

Figure 5.6: Spectrum of the *Comm2* module after cleaning the data with any artifacts. The spectrum is corrected with the exposure and the cut efficiency. The inset plot shows the same spectra zoomed in the low-energy region where a clear presence of the LEE can be seen.

from a particle origin as one would expect it to scale with the mass of the detector as *Si2* is seen to have the smallest excess in the absolute rate and largest when scaled with the mass.

In order to confirm that the events comprising the LEE were not coming out of artifacts or noise fluctuations, but were actual pulses looking similar to a particle recoil, a template was built from the events between threshold and energies below twice the resolution (i.e. $\sim$ 4.5 eV for *Comm2*) above the threshold and was compared with the particle template of the module. A comparison between the two can be seen in Fig. 5.8 for the *Comm2*

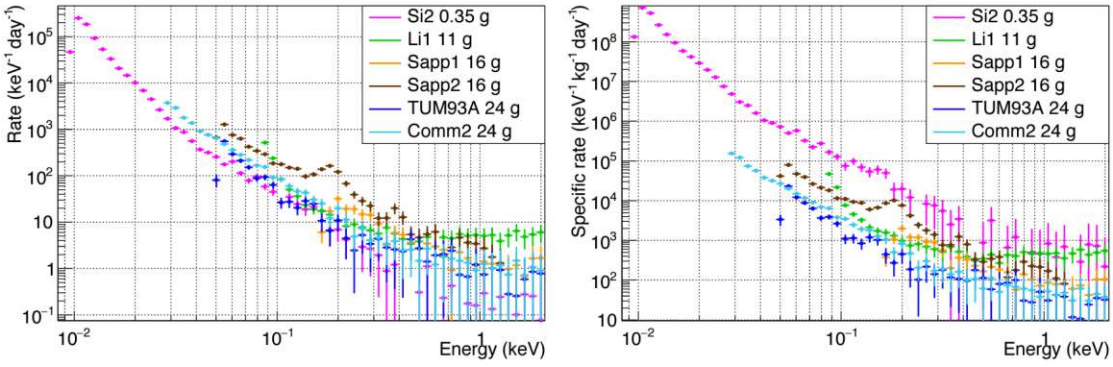

Figure 5.7: Comparison of the LEE rate(left) and specific rate(right) between different modules in Run36. The image is adapted from Ref. [163].

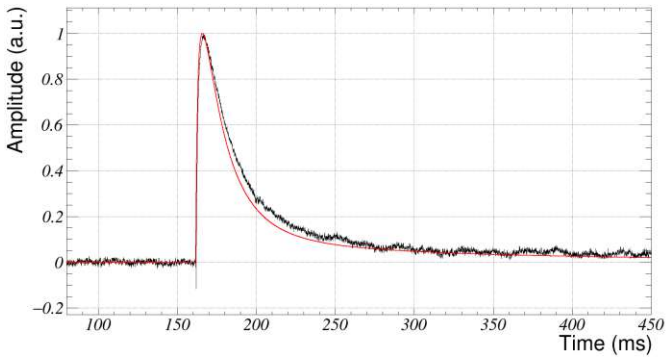

Figure 5.8: Comparison of the LEE template(black) created with the pulses between 29-38 eV and the particle template(red) used for creating the optimum filter and performing the template fit for the *Comm2* module.

module. It has to be noted that it is possible for a very small percentage of noise events very close to the threshold to survive the analysis cuts. The small spike down at the onset in the LEE template could have originated from these few noise artifacts that survived the data cleaning process. For the comparison of the templates of the other modules, the reader is referred to Ref. [165]. The LEE template is seen to be more noisy than the particle template, but this is expected as the low-energy pulses used to build this template have a relatively small signal-to-noise ratio. It can be seen that the LEE template has a very identical pulse shape compared to the particle template; hence, the origin from any noise artifacts can also be discarded.

5.2.2.2 Time Dependence

Upon checking the evolution of the rate of the LEE, it was seen that the excess decays over a long period of time in the *bck* data. The study of the decay rates was performed for various detectors, and the weekly evolution of the rate of events occurring between 60 eV to 120 eV is shown in Fig. 5.9 fitted with an exponential. The detectors with a bit higher threshold have not been in these plots, namely the *Li1* and *Sapp1*. For the *Comm2* module, the data points start at 150 days after the first cool-down as the detector faced changes in the operating point in between and became stable only afterwards.

After the neutron calibration was performed, *postcal* data was taken in order to check if neutrons had an impact on the rate of the LEE, and no significant impact was seen in the data for any detector. It was observed by the EDELWEISS collaboration that the excess observed in their detectors also decays with time, and more importantly, it was seen that the excess rate was "recharged" after warming up the detector [166]. In order to study this effect, a dedicated set of warm-up tests were performed in CRESST to various different temperatures to replicate this. In the first warm-up, the cryostat was warmed up to $\sim$ 60 K temperature and then cooled down again back to the operating temperature. In the data collected after this warm-up (*awu*), the "recharge" of this rate was indeed seen in all of the detectors. This "recharged" rate was then seen to be decaying

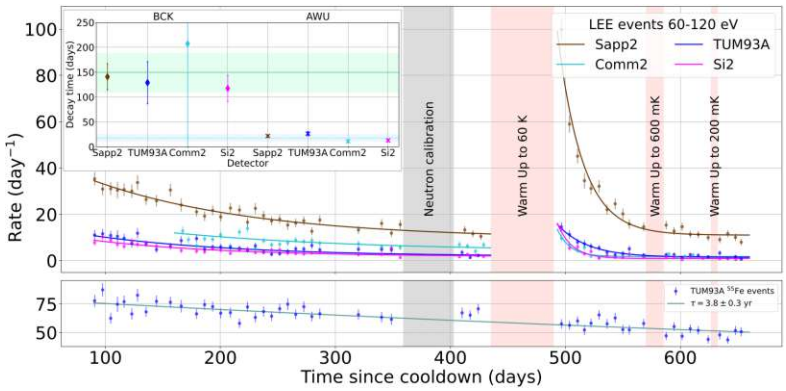

Figure 5.9: Time evolution of the LEE for *Sapp2* (brown), *Comm2* (light blue), *TUM93A* (blue) and *Si2* (pink) detector modules. The rate is shown for the events occurring between 60-120 eV for all the modules. The solid lines represent the fit of the rate to the function $R(t) = A \cdot e^{-t/\tau} + C$, where τ is the time constant of the decay. The fit is performed separately for periods before the 60 K warm-up (*bck*) and the periods after (*awu*). The inset plot shows the result of the fit plotting the decay times for both periods separately. The bottom plot shows the decay of the ^{55}Fe lines for the TUM93A module, which matches the literature value. The image is taken from Ref. [163].

faster, with an average of (18 ± 7) days for all the modules, than the rate in the *bck* data, which is seen to be decaying with an average of (149 ± 40) days [163]. Both the decaying constants for various modules can be seen in Fig. 5.9 as well. After this fast decay, the rate went back to the slowly decaying tail for all of the detectors.

In order to assess the temperature point at which the rate resets to a higher value as it did after the 60 K warm-up, many other controlled warm-up tests were performed where the cryostat was warmed up to 200 mK, 3.5 K, 11 K, and 30 K. In addition to those, a warm-up to 600 mK also happened as a result of the power failure at the underground site due to a snowstorm. The evolution of the excess rate for *Sapp2*, *Si2*, and *Comm2*, after these various warm-up periods can be seen in Fig. 5.10, 5.11 and 5.12, respectively. It can be seen from these figures that the excess rate resets again after the 30 K for the *Sapp2* and *Si2* modules. The amount of increase in the rate is also seen to be proportional to the warm-up temperature. An analytical relation between the amplitude of the "recharged" rate and the warm-up temperature for various modules in Run36 can be found in Ref. [167]. For the 11 K warm-up, a very slight increase in the rate could be seen for the *Sapp2* and *Si2* modules as well. In Ref. [167], it was shown that *TUM93A* module also shows a reset of the excess rate after the 30 K warm-up but no significant reset after the 11 K warm-up. However, for the *Comm2* module, no reset of the excess rate was seen for any temperature other than 60 K. The reason for this is not yet confirmed, although some speculations suggest that it could be due to the difference in the thermal expansion coefficient between the crystal and the SiO_2 layer, that is present between the TES and the crystal [167]. The direction of the expansion depends on the orientation of the lattice, and it is possible that the discrepancy of the

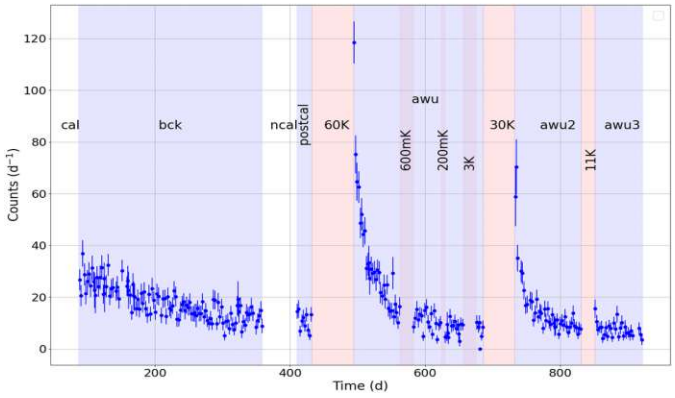

Figure 5.10: Time evolution of the LEE rate for *Sapp2* module (65-130 eV). The periods when the warm-ups were performed are shown in red, and the collected data periods are shown in blue. Image is taken from [167].

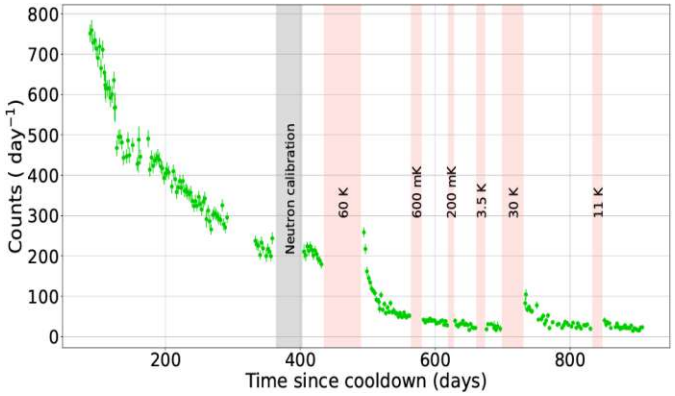

Figure 5.11: Time evolution of the LEE rate for *Si2* module (12-200 eV). The periods when the warm-ups were performed are shown in red. Image is taken from [167].

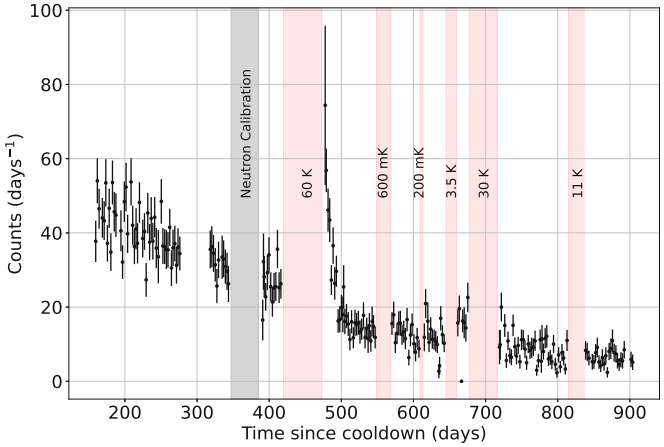

Figure 5.12: Time evolution of the LEE rate for *Comm2* module (29-200 eV). The periods when the warm-ups were performed are shown in red.

30 K reset between the *TUM93A* and the *Comm2* module, even though they are the same material, could be due to the difference in the lattice orientation compared to the deposited SiO_2 layer, although this has not yet been confirmed.

5.2.3 Conclusions

Based on the given observations and the tests performed, the following conclusion can be made about the LEE:

1. The excess is seen across all different modules operated in the Run36 of CRESST, irrespective of the detector material
2. The rate of the excess does not scale with the mass of the detectors.
3. The particle origin or the external radioactivity can be disregarded as the possible origin as the spectral shape is different across different detectors. Also, the rate of the excess increases after warming up the detector, which is not expected from an external radioactive background.
4. The pulse shape of the excess matches the pulse shape of a particle recoil, and thus, the contribution of noise artifacts to the excess can also be rejected.
5. The excess rate is seen to be decaying over time with two different decaying constants. The "recharged" excess rate after warming up seems to decay an order of magnitude faster than the slower component.
6. The spectral shape and the rate are seen to be similar for different holding structures. Hence, not a huge contribution is coming from the holding structure. However, it was shown in the recent work by the SPICE/HeRALD collaboration that the excess rate increases in a high-stress holding structure, compared to a low-stress one [168].
7. The excess does not originate from the scintillating parts of the module, as the excess was also seen in a fully non-scintillating module.
8. Upon heating the detector to temperatures of 11 K and 30 K, the surplus rate returns to an elevated level for the *Sapp2* and *Si2* modules, but not for the *Comm2* module. This gives very strong speculations that the increased rate may be linked to the interface between SiO_2 and the crystal, as the thermal expansion coefficients of SiO_2 differ from those of the detector materials

The impact of a lower amount of excess can be seen if the dark matter results are calculated and compared between the *bck* data and the end of *awu* data as the excess decays significantly afterwards, and this has been shown in App. A.2. The current efforts of the CRESST collaboration aim at understanding the origin of this excess, and the R&D involves testing crystals with even lower holding stress and measuring crystals with

multiple TES sensors on the same crystal. The latter is done in order to understand the contribution of the excess that originates from the crystal-TES interface and compare it to the one that originates inside the crystal mass [169].

5.3 Neutron Calibration

Traditionally, energy calibration for the sub-keV threshold detectors involves utilizing the complete photo-absorption of X-rays with known energy, such as those emitted during the ^{55}Fe decay. This process results in a peak in the observed energy spectrum at a few keV. However, in order to understand the origin of LEE, or increase the sensitivity to low-mass dark matter, these calibration peaks may still be too high to trust the calibration at the energy region of interest that is typically below a few hundred eVs. Moreover, the calibration peak results from an electromagnetic interaction rather than a nuclear recoil, which is the interaction of interest. As it is explained in Sec. 3.3.1, electromagnetic interactions result in a more energetic scintillation signal than a nuclear recoil. Thus, the amount of energy registered as a phonon signal is lesser for an electromagnetic interaction compared to a nuclear recoil, for the same total input energy. Thus, using electromagnetic interactions for energy calibration could result in a slight overestimation of the input energy, depending on the scintillation efficiency of the crystal.

It was recently shown in the collaborative work by the NUCLEUS [157] and CRAB [170] collaborations that it is possible to use nuclear recoil peaks that originate upon a radiative capture of a thermal neutron. As the thermal neutrons are captured by the nucleus, the nucleus is excited to a higher energy state from which it deexcites via a γ-emission. Due to the conservation of momentum, the emitted γ-ray results in a transfer of kinetic energy to the nucleus and imparts a nuclear recoil signature. If the deexcitation happens only via a single γ-emission, then the signature nuclear recoil is also monoenergetic. In a measurement performed by irradiating neutrons from a ^{252}Cf source on a 0.75 g $CaWO_4$ prototype detector, such a peak was observed at the predicted energy of 112 eV [171]. Since a dedicated neutron calibration is also performed in CRESST-III using an AmBe source, such a peak is also predicted in the CRESST $CaWO_4$ crystals, as the high energy neutrons from the AmBe source are slowed down and thermalized due to interactions in the shielding material before reaching the detector. The Q-values of the neutron capture occurring on different isotopes of tungsten, along with their natural abundances, imparted recoil energy and branching ratios ($BR_{1\gamma}$) for single γ emission and the thermal neutron capture cross-sections ($\sigma_{n,\gamma}$) are summarized in Table 5.2.

The value that determines the strength of the final nuclear recoil peaks is given in the last row of Table 5.2, which corresponds to the multiplication of the branching ratios, thermal capture cross-sections, and the natural abundances for different nuclei. This value is named the Figure of Merit (FOM) for the resulting nuclear recoil peak. It can be seen that the most prominent peak expected from this calculation comes from the ^{182}W isotope, which gives a nuclear recoil at 112.4 eV, followed by the peak at 160.2 eV from ^{183}W, which is expected to be about 90% less intense than the former peak.

	^{182}W	^{183}W	^{184}W	^{186}W
Q(keV) [172]	6190.7	7411.2	5794.1	5467.0
Recoil Energy(eV)	112.4	160.2	96.1	85.8
Abundance (%) [172]	26.50	14.31	30.64	28.42
$\sigma_{n,\gamma}$(barn) [173]	20.31	9.87	1.63	37.88
BR$_{1\gamma}$ [172]	13.936	5.829	1.477	0.263
FOM [171]	7500.6	823.3	73.8	283.1

Table 5.2: Different properties of the thermal neutron capturing processing on different isotopes of tungsten that determine the strength of the possible nuclear recoil peak. Table is adapted from Ref. [171].

In order to estimate the amount of neutrons that originate from the AmBe source in CRESST, pass through the detector shieldings, and make it to the detector modules to impart a nuclear recoil signature, simulation studies were performed using Monte Carlo simulations with ImpCRESST code [175] based on GEANT4 10.6.3 [176–178]. The details of the simulation and extensive study on the neutron background and the impact of the neutron calibration in CRESST-III can be found in Ref. [146]. The spectrum simulated for *DetA* operated in CRESST-III phase-one has been shown in Fig. 5.13 up to 500 eV, after convolving the spectrum with the detector resolution and correcting it for the signal survival probability. It is seen in the simulated spectrum that corresponding nuclear recoil peaks have very high intensity for peak originating from ^{186}W nucleus at a mean value of around 85 eV, which is in contrast to what we expect from Table 5.2. This is a limitation

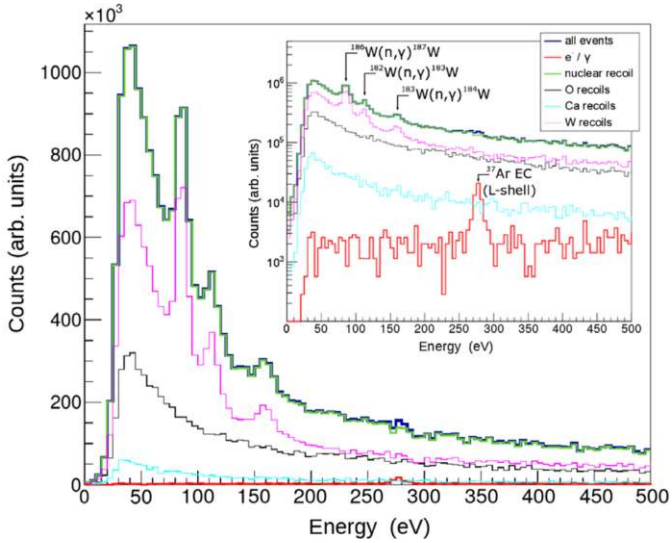

Figure 5.13: Simulated spectrum of the neutron calibration data for *DetA* extracted using the ImpCRESST code. The spectrum is convolved with the detector resolution and corrected for the signal survival probability. The inset shows the same plot in logarithmic y-scale. The image is taken from Ref. [174].

of GEANT4, as the corresponding branching ratios cannot be applied in the software, and only a single γ-emission is taken as the principle process for the deexcitation. In the original data, the highest peak is expected at around 112.4 eV, followed by the peak at 160.2 eV, based on the FOM calculation shown in Table 5.2. Another peak is seen in the e^-/γ background at around 270 eV that originates from electron capture decay of ^{37}Ar, although with negligible intensity. The ^{37}Ar is produced in the crystal due to (n,α) reactions on ^{40}Ca.

In this section, the data obtained with neutron calibration measurement in Run36 have been described for the *Comm2* module along with the bandfit performed in order to separate e^-/γ background and nuclear recoils. Then, the results for this low-energy nuclear recoil peak have also been shown combined with the results from other $CaWO_4$ modules operated in CRESST-III that have been described in the Ref. [174].

5.3.1 Spectrum and Bandfits

The neutron calibration in the Run36 was performed between August - September 2021 with an active measuring time of around 39.2 days using an AmBe source with an activity of $\sim$ 35.5 MBq. This active measuring time amounts to an exposure of around 0.94 kg-days for the *Comm2* module. The source was placed between the muon veto and the radon box in order to provide a strong neutron flux at the position of the detectors. For a schematic of the 2-D position of the source in Run36 and Run34 (CRESST-III phase one), the reader is referred to Ref. [174].

A similar triggering algorithm was applied for the collected *ncal* data, as was with the *bck* data, with a triggering threshold value of 29.8 eV. As the noise conditions did not change during the *ncal* measurement, the analysis cuts with similar parameters were applied to this measurement as were to the *bck* data (Sec. 5.2.1). Like the *bck* data, the stream simulation was also performed with the *ncal* data in order to calculate the cut efficiency

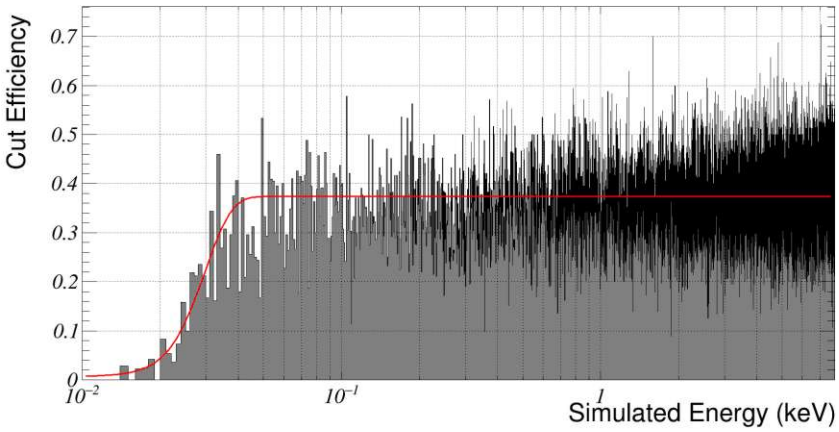

Figure 5.14: Cut efficiency for neutron calibration analysis for *Comm2* module fitted with an error function (in red).

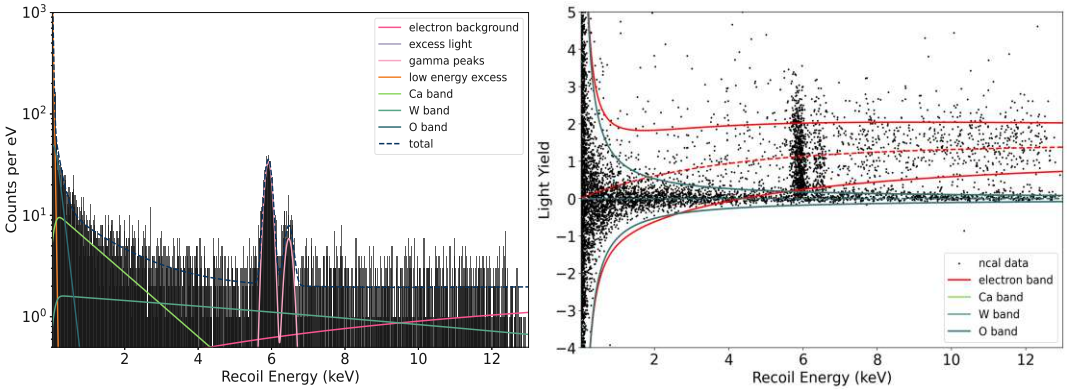

(a) (b)

Figure 5.15: (a) Spectrum of the neutron calibration data along with the spectral fits. (b) Scatter plot of neutron calibration data in the Light Yield vs Energy plane along with fitted electron and nuclear recoil bands.

of the analysis cuts, and the energy-dependent cut efficiency for this measurement has been shown in Fig. 5.14 with a fit of an error function.

The efficiency flattens at a value of around 37% at higher energies compared to 67% for the *bck* data. The decrease in efficiency in this measurement is due to a huge amount of pile-ups as a result of the high neutron rate. The final resulting recoil energy spectrum can be seen in Figs. 5.15(a) and 5.15(b), as a 1D energy histogram and scatter in the light-yield plane, respectively. Spectral and band fits have also been performed on both spectra in order to separate the e^-/γ background from the nuclear recoils. The presence of the nuclear recoil bands can be clearly seen in Fig. 5.15(b), along with the prominent ^{55}Fe lines in the electron band. In Fig. 5.15(a), along with the contributions from the nuclear recoil bands, electron band, and gamma peaks, the presence of the LEE can also be clearly identified, which is fitted with an exponential function. The 1D and 2D analytical description of these various bands can be found in detail in Refs. [123, 138, 148].

5.3.2 Observation of Low-energy Nuclear Recoil Peak

The zoomed version of the plots in Fig. 5.15, in the low-energy region, can be seen in Fig. 5.16. The presence of the peak at around 110 eV can be seen prominently in both plots. In Fig. 5.16(b), the line of the peak is seen to be centered around the nuclear recoil band, which is expected. The spectrum of the same module for the *bck* data can be seen in Fig. 5.6, where no peak is seen at the given value. Hence, it can be asserted that the peak seen only in the *ncal* data originates due to the thermal neutron capture by the ^{182}W isotope. Another line is seen at around 160 eV, although it is more likely a statistical fluctuation rather than the peak from the radiative capture on ^{183}W, as that peak is expected to be of 90% lesser intensity than the first peak. Also, this peak is seen to be

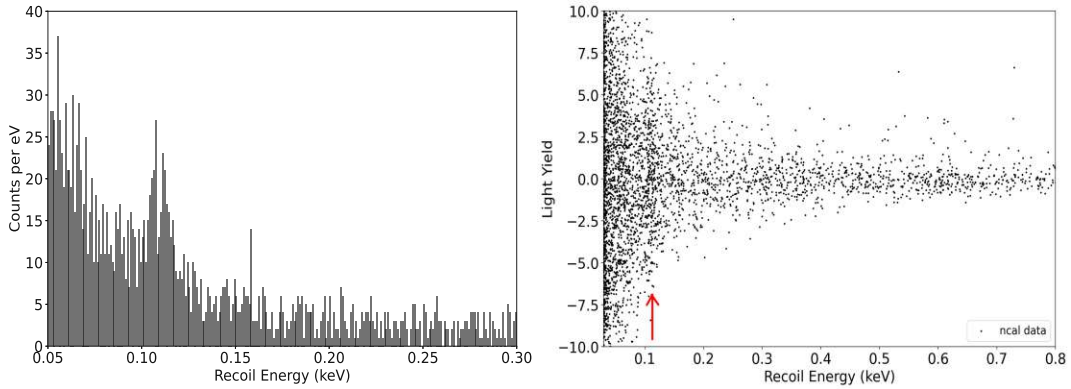

(a) (b)

Figure 5.16: Zoomed in version of the plots in Fig. 5.15. The presence of the radiative neutron capture by ^{182}W at ∼110 eV can be seen as a peak in (a) and as a line in (b) pointed by the red arrow.

quite sharp with a very low width, which is not expected in a non-ideal (or real-world) detector.

In order to find the mean energy of the given peak in the data and also compare the rate of events in the peak with the one seen in other $CaWO_4$ modules in CRESST-III, the 1D recoil energy spectrum of the data is fitted with the following function in the low-energy region:

$$f(E) = N_{sig} \cdot \mathcal{G}(E; \mu, \sigma) + N_{exp} \cdot \exp(-E/E_0) + N_{flat} \tag{5.1}$$

The given function models three different contributions to the recoil energy spectrum. One contribution comes from the nuclear recoils of the incoming neutrons, which is modeled by an exponential function with a decay constant of E_0 and has N_{exp} number of expected events. This exponential sits on a flat background with an expected value of N_{flat}. The last contribution is from the nuclear recoil peak that is modeled by a Gaussian function with a mean value, resolution, and expected number of events as μ, σ, and N_{sig}, respectively.

The spectrum is first corrected for the energy-dependent cut efficiency shown in Fig. 5.14 and then is fitted with the Eq. 5.1. The fitting is performed with unbinned extended maximum likelihood using the ZFIT package [179], between 60 and 500 eV. The fitted value of the number of expected events from each contribution can be converted to the event rate per day R, by dividing the expected events by the measurement time, i.e., ∼ 39.2 days. The values of the fit are shown in Table 5.3, along with the value obtained from other $CaWO_4$ modules operated in CRESST-III [174]. The fitted spectrum with the data is shown in Fig. 5.17. The fitted spectrum from other modules can be found in Ref. [174].

Detector	R_{sig}(1/d)	μ(eV)	σ(eV)	R_{exp}(1/d)	E_0(eV)	R_{flat}(1/d)
Comm2	7.4(1.2)	110.0(0.9)	4.9(0.7)	66.0(2.9)	50.4(3.7)	47.6(2.6)
Det-A	1.6(0.6)	113.3(1.4)	3.5(0.8)	25.1(2.6)	52.0(9.3)	36.8(2.4)
TUM93A	5.5(1.2)	106.2(1.8)	7.0(1.4)	38.0(2.4)	60.4(5.3)	34.6(2.0)

Table 5.3: The fit parameters for the *ncal* data of the $CaWO_4$ modules operated in Run34 and Run36 of CRESST-III. The values for *Comm2* are extracted from the data and the fit shown in Fig. 5.17, whereas the values for *Det-A* and *TUM93A* are taken from Ref. [174]. The statistical errors of the fits are shown in the brackets with the values.

The fit results reveal that the anticipated nuclear recoil peak manifests at a mean value of 110 eV, closely aligning with its expected value of 112.4 eV. The minor deviation at this energy level is attributed to the marginal error introduced during energy calibration using iron peaks, situated at relatively higher energies and the interaction is electromagnetic, which slightly overestimates the energy scales as already discussed. The rate of events in the Gaussian peak is statistically compatible between *Comm2* and *TUM93A* modules as they were both operated in the same run, were calibrated using the same neutron source, and also have the same material and geometry. These rates are significantly different from that of *DetA* as it was operated in a different run with a different source activity and position. Furthermore, the decay parameter of the exponential background is observed to be similar across all modules, aligning with expectations given their similar material composition.

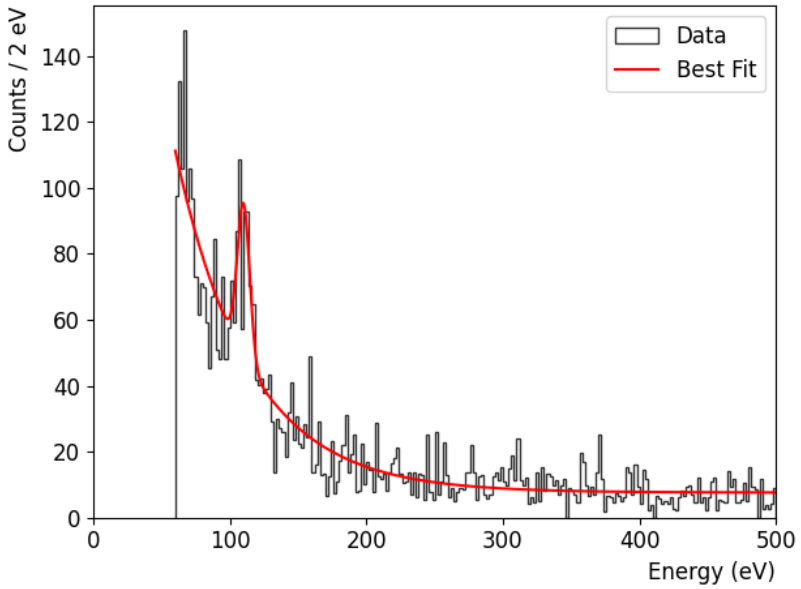

Figure 5.17: The spectrum for the *ncal* data of *Comm2* module between 60 and 500 eV. The data is fitted with a model described in Eq. 5.1, which is shown in red.

Hence, from this measurement, the expected peak that results from the deexcitation of ^{182}W isotope upon a thermal neutron capture is seen clearly in the data taken for different $CaWO_4$ modules in CRESST-III, confirming the observation made by the NUCLEUS and CRAB collaborations [171]. Similar nuclear recoil peaks are also expected for detector modules made from other materials as well. One such observation is also made for the Saphhire modules operated in this run of CRESST, and the details of this observation can be found in Ref. [146, 165]. It is also shown in this measurement that the intensity of the peak is also high enough, which allows for a more accurate calibration of the nuclear recoil spectrum at such low energies, compared to conventional X-ray sources used.

5.4 Spin-dependent Dark Matter Results with Lithium Aluminate Targets

As it has been discussed previously in this chapter, the focus of the Run36 of CRESST was to try to understand the origin of the LEE, which is why different detector materials and holding designs were employed. Along with these changes, an ^{55}Fe source was also placed with each detector module to allow for faster calibration. However, because of the presence of the iron source, the background levels at lower energies were also increased, but this was not a huge concern given the objective of the run was not to set stronger dark matter limits, but to understand the LEE. Despite this, the exclusion limits were calculated for different detector modules, and it was seen that employing $LiAlO_2$ as a detector material provided huge improvements on the current spin-dependent dark matter-nucleus exclusion limits. Minor improvements were also seen in the spin-independent exclusion limits, and sensitivity to even lower dark matter masses was achieved using Silicon wafer targets. In this section, the analysis and the dark matter results for the $LiAlO_2$ detector module have been discussed in detail. The results obtained with the Silicon wafer module have been briefly shown in App A.1. The results shown in this section have been published and can be found in Ref. [140].

$LiAlO_2$ was used as a target material for this run as lithium is the lightest element that can be used in a CRESST-like detector, and using a lighter element provides advantages for probing the light mass dark matter particles (Sec. 3.1). In order to probe spin-dependent interaction with protons or neutrons, it is necessary to have an unpaired number of protons or neutrons in the detector element, respectively. As lithium occurs as ^{7}Li and ^{6}Li in $LiAlO_2$ with natural abundances of 92.41% and 7.49% [180], it allows for probing both spin-dependent proton and neutron interactions due to an unpaired number of protons in both ^{7}Li and ^{6}Li and an unpaired number of neutrons in ^{6}Li. The potential of $LiAlO_2$ to probe spin-dependent dark matter interactions was already shown in an above-ground measurement by CRESST [181].

In Run36, two different detector modules made from $LiAlO_2$ were used and were called *Li1* and *Li2*. The geometry and the detector design of both modules were identical, and the main absorber crystals were provided by the Leibnitz-Intitut für Kristallzüchtung. As mentioned previously, the dimensions of the absorber crystals were the standard

CRESST-III size of $(2 \times 2 \times 1)$ cm^3, operated along with a silicon-on-sapphire (SOS) substrate light detector with $(2 \times 2 \times 0.04)$ cm^3 dimensions. Given the mass density of 2.62 g/cm^3 of $LiAlO_2$, the absorber crystals had a weight of 10.46 g. Both the light and the phonon detector were held in place using three copper sticks inside the copper housing. The copper housing of both the detector modules was covered with a 3M Vikuiti^{TM} Enhanced Specular Reflector scintillating and reflective foil to maximize the scintillation light collection efficiency, as $LiAlO_2$ is a scintillating crystal that has an emission maximum wavelength of 340 nm [182]. Unfortunately, no transition was seen for the TES sensor on top of the *Li2* light detector, and only the phonon channel could be operated, whereas for the *Li1* module, both the detectors worked adequately. For this reason, the analysis of *Li1* was used as the main analysis to calculate the dark matter results as it was capable of suppressing electromagnetic background due to a dual channel readout. The *Li2* analysis was used as a cross-check analysis to verify the results and compare the impact of the dual channel readout on the final results. The analysis described below is performed on the *Li1* module and compared in the end with the results from *Li2* module. An image of the *Li1* detector module can be seen in Fig. 5.2(c).

5.4.1 Analysis cuts applied

For the calculation of dark matter exclusion limits, the *bck* data were used that were collected between February and August 2021, with an active measuring time for the blind data set of around 2757 h. This amounts to an exposure of 1.202 kg-days. The analysis was designed on the training set with an exposure of 0.152 kg-days and applied to the blind data. Using the similar triggering scheme described in Sec. 4.1.1, the continuous data was triggered with a threshold of 5.68 mV for the phonon channel and 13.31 mV for the light channel. Different analysis cuts applied thereon are described below. The complete description of these analysis cuts has been described in detail in Sec. 4.3.

1. **Trigger Cut:** If the triggered threshold of the event was below 5.68 mV in the phonon channel, then the event was removed.
2. **Muon Veto Cut:** All the events within a ± 5 ms of a muon veto trigger were removed.
3. **Stability Cut:** Events registered when the control pulse height was more than 3σ away from its mean value were removed.
4. **Right-minus-left Cut:** Events with a Baseline Difference below -0.02 V and above 0.02 V were removed. This cut also removed all the saturated pulses. Hence, no truncated fit was required, and thus, no fit RMS cut was applied.
5. **Delta Voltage Cut:** All the events having Minimum Derivative/Baseline RMS below -500 s^{-1} were removed.

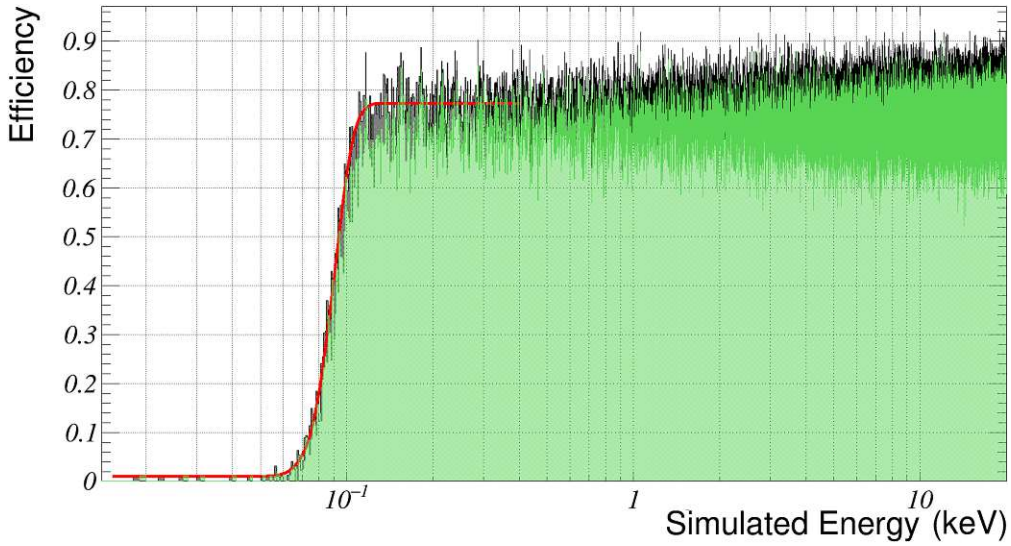

Figure 5.18: Energy-dependent trigger(gray) and cut efficiency(green) of the analysis chain applied on the *Li1* module for the *bck* data. The trigger efficiency is fit with an error function(red line) between 10-400 eV. The particular values of the cuts applied can be found in the text.

6. **Filter RMS Cut:** Only the events with an optimum filter fit RMS value below 5 mV were kept.

7. **Light yield Cut:** Events with a light yield above 10 are removed as they likely correspond to direct hits of the light detector.

In order to calculate the analysis efficiency, a correlated stream simulation was performed in the same way as described in Sec. 4.5 with a simulation rate of 0.25 Hz between 0-20 keV, which simulated a total of around 1.81×10^6 events. The energy-dependent trigger and cut efficiency of the analysis chain can be seen in Fig. 5.18. After fitting the trigger efficiency with an error function, the fit gives a threshold value of (88.9±5.6) eV with the constant efficiency of (77.3±3.0)% at energies above the threshold. The value of resolution of the detector, extracted from the fit, is (12.4±0.6) eV. The corresponding values for *Li2* can be found in Ref. [140].

5.4.2 Spectrum and Bandfits

The recoil energy spectrum obtained after applying the analysis cuts and correcting for the exposure and cut efficiency can be seen in Fig. 5.19 in grey. The obtained spectrum exhibits three major features. First, the lines at 5.89 keV and 6.49 keV originating from the ^{55}Fe source, that are used for the energy calibration. Second, the presence of the LEE can be seen in the inset plot. Since the origin of the LEE is not known, these are considered as the particle recoils as well. The third feature in the spectrum is seen to be the presence of events that extend out to around 17 keV. This contribution comes from

the beta spectrum of tritium that is present in the absorber crystal due to high cross section for the ^{6}Li(n,α) ^{3}He reaction:

$$^{6}\mathrm{Li} + \mathrm{n} \rightarrow \alpha + ^{3}\mathrm{H} + 4.78\ \mathrm{MeV} \tag{5.2}$$

As the crystal was manufactured above ground and brought later on to the LNGS facility, the crystal was exposed to the cosmogenic neutrons, and the above reaction took place to leave traces of ^{3}H.

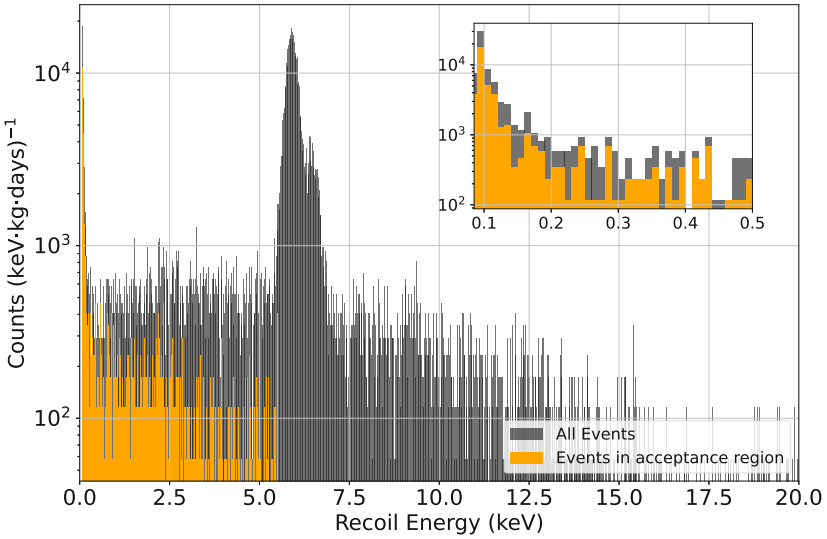

Figure 5.19: Recoil energy spectrum of the dark matter dataset for *Li1* module after correcting for exposure and cut efficiency. The grey histogram shows all the events surviving the analysis cuts, and the orange histogram shows the events in the acceptance region. The inset shows the same plot in the low-energy region, showing the presence of the LEE.

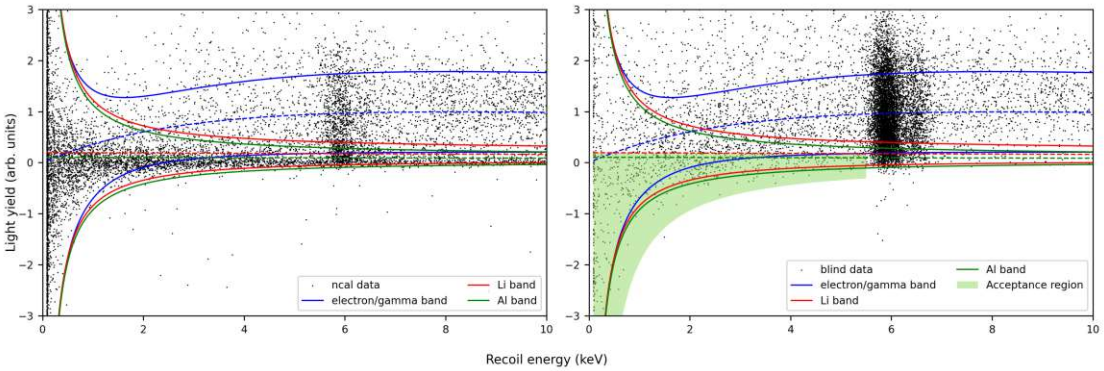

Figure 5.20: Scatter plot showing the *ncal*(left) and the *bck*(right) data along with the bandfits showing the e^{-}/γ and ^{7}Li and ^{27}Al nuclear recoils bands. The green shaded region in the *bck* data shows the dark matter recoil region of interest that has been described in the text.

In order to separate the nuclear recoils from the electromagnetic background and also define the acceptance region (or the region of interest) for the potential dark matter recoil candidate events, a bandfit is performed on the neutron calibration data collected with the same AmBe source as was used to get the results in Sec. 5.3. The scatter plot showing the events collected for the *bck* and the *ncal* data, along with the bandfits in the light yield vs. recoil energy plane, can be seen in Fig. 5.20. It can be seen from the width of the e^-/γ band that the scintillation efficiency of $LiAlO_2$ is relatively low as the band is not able to efficiently distinguish between electromagnetic and nuclear recoil events at low energies. A clear leakage of the events from the ^{55}Fe source into the nuclear recoil bands can also be seen. The nuclear recoil bands are only shown for ^{7}Li and ^{27}Al as the oxygen band is expected to lie between the two and the ^{6}Li, having an almost identical quenching factor as ^{7}Li, is expected to have a similar band as ^{7}Li. The dark matter region of interest (ROI) is defined as the lower half of the lithium nuclear recoil band. The ROI starts at the detector threshold and ends at 5.5 keV. Events above 5.5 keV are not kept in the ROI because of the leakage of events from the iron lines. Nevertheless, no significant signal is expected above this energy range from the sub-GeV dark matter masses. The histogram of the events inside the ROI is also shown in Fig. 5.19(orange).

5.4.3 Dark Matter Results

The calculation of the exclusion limits on spin-dependent dark matter-nucleus interaction rate is done in the limit of zero momentum transfer, and thus, the form factors are neglected. The expected different recoil spectrum for proton/neutron-only spin-dependent interaction takes the form:

$$\frac{dR}{dE_R} = \frac{2\rho_0}{m_\chi}\sigma^{SD}_{p/n}\sum_{i,T} f_{i,T}\left(\frac{J_{i,T}+1}{3J_{i,T}}\right)\left(\frac{\langle S_{p/n,i,T}\rangle^2}{\mu^2_{p/n}}\right)\eta(v_{min}) \tag{5.3}$$

where E_R is the recoil energy; ρ_0 is the local dark matter density in the solar neighborhood; m_χ is the mass of the dark matter particle; $\sigma^{SD}_{p/n}$ is the reference dark matter-proton/neutron spin-dependent cross-section; $f_{i,T}$ represents the fraction of each element in the nucleus of the target, scaled by its mass which is given by:

$$f_{i,T} = \frac{n_T \zeta^i m^i_T}{\sum_{i,T'} n_{T'}\zeta^i m^i_{T'}}, \tag{5.4}$$

where n_T is the multiplicity of the element T, ζ^i is the natural abundance of the isotope i, and m^i_T is its mass; $J_{i,T}$ represents the nuclear ground state angular momentum of the isotope i of element T; $\langle S_{p/n,i,T}\rangle$ is the expected value of the proton/neutron spins in the target isotope i of the element T; $\mu_{p/n}$ is the reduced mass of the dark matter and proton/neutron; and $\eta(v_{min})$ is the mean inverse velocity of the standard halo model [183] with v_{min} being the minimum velocity required to impart a nuclear recoil of energy E_R.

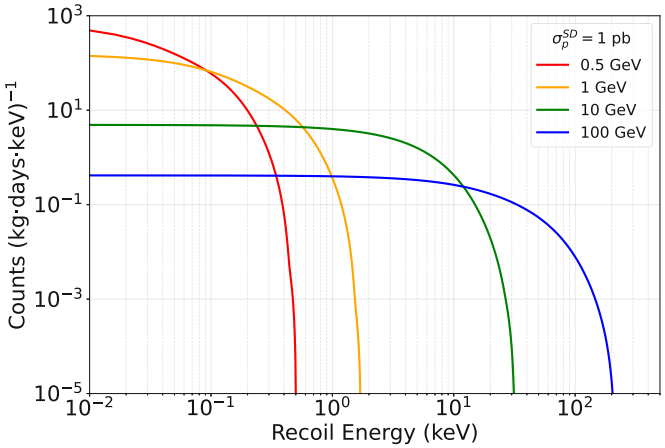

Figure 5.21: Expected recoil energy spectrum for spin-dependent dark matter-proton interaction on $LiAlO_2$ for 0.5, 1, 10 and 100 GeV dark matter particles with the reference cross-section $\sigma_p^{SD} = 1$ pb.

The standard dark matter halo model has been used in the following calculations, having a Maxwellian velocity distribution with a local dark matter density of $\rho_0 = 0.3$ GeV/c^2/cm^3 [124], having an escape velocity of $v_{esc} = 544$ km/s [117] and the radial velocity of sun in the galactic frame of $v_\odot = 220$ km/s [116]. The spin expectation values are taken as $\langle S_n \rangle = \langle S_p \rangle = 0.472$ for ^{6}Li [184], $\langle S_p \rangle = 0.497$ for ^{7}Li [185] and $\langle S_n \rangle = 0.0296$, $\langle S_p \rangle = 0.343$ for ^{27}Al [186]. The value for f_{Oxygen} is taken to be zero as only ^{17}O is sensitive to spin-dependent neutron-only interaction and also has a very low natural abundance of 0.0367%, and thus it has a negligible impact on the results. The expected recoil spectrum for different dark matter masses on $LiAlO_2$ can be seen in Fig. 5.21.

For the calculation of the following exclusion limits, it needs to be understood how the spectrum of a potential dark matter signal would look like in the given detector. A different approach has been used for these results, rather than using the analytical description of the detector effects described in Sec. 3.1.4. Here, all the simulated events are used in order to understand the effect of the analysis chain on a potential signal, rather than using just the binned cut efficiency. The flat simulated spectrum of the injected energy of all the 1.81×10^6 events is re-weighed in order to resemble the potential dark matter signal for a given dark matter mass. Then, the spectrum after triggering, applying the analysis cuts, and doing the energy reconstruction is obtained. Thus, in this way, we collect an *observed spectrum* in the detector, for a given *input dark matter spectrum*. This already accounts for all the detector effects, including the detector resolution and threshold. The *observed simulated* spectrum is then compared to the actual recoil spectrum in order to calculate the exclusion limits. A comparison of the results obtained with this method and using the analytical description of detector effects as described in Sec. 3.1.4 can be seen in Ref. [128] for the results obtained with the *DetA* module.

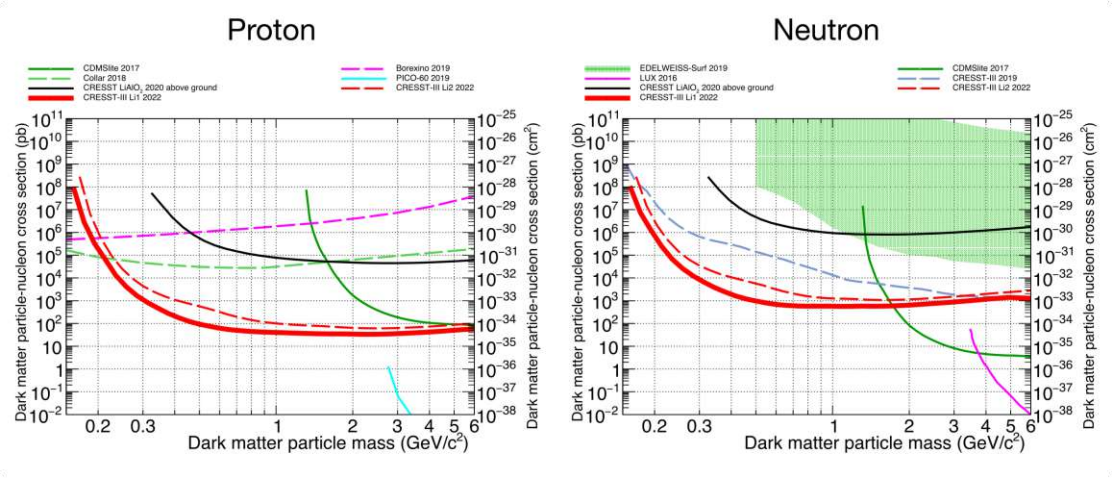

Figure 5.22: The spin-dependent dark matter-nucleon exclusion limits from proton-only (left) and neutron-only (right) interactions for various experiments compared to the results obtained with the two lithium modules employed in the Run36 of CRESST-III. The results for the *Li1* module are shown as a solid red line, and the ones from the *Li2* module are shown as the dashed red line. The results exclusion limits are only shown between 0.16-6.0 GeV/c^2. The results obtained with the same detector material operated in an above-ground measurement from CRESST-III are shown in black [181]. Also, the neutron-only results from CRESST-III phase one are shown in light blue (right) using ^{17}O in a $CaWO_4$ detector (*DetA*). The exclusion limits from various other experiments are also shown: EDELWEISS [155] and CDMSlite [88] using ^{73}Ge, PICO [86] using ^{19}F, LUX [187] using ^{129}Xe + ^{131}Xe, J.I. Collar with ^{1}H [188] and the constraints derived by Borexino [189].

Yellin's optimum interval method [153, 154] was used in order to extract the exclusion limits using the events in the ROI described above. For the calculation of proton-only interactions, recoils on all ^{6}Li, ^{7}Li and ^{27}Al were used, and for neutron-only interactions, ^{6}Li and ^{27}Al were used. With a detector threshold of 88.9 eV and using a 2σ shuffling, the sensitivity to recoils on lithium nucleus of dark matter masses as low as 0.16 GeV/c^2 was achieved with this measurement. The upper limits on the interaction cross-section are calculated with a 90% confidence interval between 0.16 GeV/c^2 up to 6 GeV/c^2 and are shown in Fig. 5.22 (red solid line). These results are shown along with the results from *Li2* module (red dashed line) and are compared to the exclusion limits from other experiments for the standard scenario. It can be seen that the strongest exclusion limits are set with these results between $(0.25 - 2.5)$ GeV/c^2 for proton-only and $(0.16 - 1.5)$ GeV/c^2 for neutron-only interactions. The results show an improvement by around 3-4 orders of magnitude in the whole probed mass range compared to the results obtained in the above-ground measurement using the same detector material, with a higher threshold and low exposure [181]. The advantage of using a module with a dual channel readout can also be seen when the results are compared with the ones from *Li2* module as the sensitivity of *Li1* module is from twice to 10 times better than *Li2* results through the whole mass range. More than an order of magnitude improvement in

the neutron-only exclusion limits from the previous results obtained with *DetA* using ^{17}O [89] can also be seen. At lower masses, the limit is seen to get worse, which can be attributed to the presence of the LEE, which also limits the lowering of the threshold and probing even lower masses. In the upcoming runs of CRESST, further modifications in the detector design are planned in order to understand the LEE so that the sensitivity of the experiment can be increased to even lower masses and cross-sections.

CHAPTER 6

Study of Universal Bound States with CRESST-III

The success of the Self-Interacting Dark Matter (SIDM) in its ability to explain the shortcomings of ΛCDM was already discussed in Sec. 1.4.2 and a detailed review can also be found in Ref. [41]. Defining $\sigma_{\chi-\chi}$ to be the self-interaction cross-section between the two dark matter particles (represented by χ), it is seen that the preferred value of the self-interactions required to solve the small-scale crisis (Sec. 1.4.1) falls within $\sigma_{\chi-\chi}/m_\chi \sim 1 - 50$ cm^2/g at the particular scale [55], whereas the observations on the cluster scales constraint the value to be less than $\sim 0.1 - 1.25$ cm^2/g [19, 190, 191]. As the velocities range on the small-scale structures falls in the $\mathcal{O}(10)$ km/s and that on the cluster scales in the $\mathcal{O}(1000)$ km/s, a model that allows for velocity dependence in these self-interactions could accommodate the observation on both the scales. This has led to the construction of several particle physics models where velocity-dependent self-interactions are incorporated [41], where the astrophysical and cosmological observations constrain the value of $\sigma_{\chi-\chi}/m_\chi$.

It has been shown that if the interaction between the dark matter particles happens via a light mediator particle, which results in a Yukawa potential, the elastic self-interactions can be boosted by Sommerfeld enhancement by a factor of $1/v$ [192]. Similar other enhancements could also be possible where the relative velocities of the dark matter particles would play a crucial role. For example, in Resonance enhancement, interaction is boosted by a factor of $1/v^2$ from a bound state of two dark matter particles that are sufficiently near the scattering threshold [64], a factor of $1/v^4$ could be provided by the Breit-Wagner enhancement from an elementary particle near the scattering threshold [193].

Braaten & Hammer have shown in Ref. [64] that provided a resonance is in the S-wave channel, all the above-mentioned resonances are equivalent and can be constrained by

universal two-body physics. Given that the resonance is near the scattering threshold, the universal properties depend mainly on the large scattering length rather than the enhancement mechanism. In the case where the resonance is below the scattering threshold, the two dark matter particles form a bound state whose binding energy and lifetime are also dependent on the scattering length. Thus, these bound states provide a very well-motivated possibility of the internal structure of dark matter, just like in the Standard Model. This resonant self-interacting dark matter has been explored extensively, and inverse velocity dependence of the cross-section is shown to exist in a model-independent way that is also independent of the internal structure of the bound states [194, 195].

Laha & Braaten [65] have explored the impact of these bound states on the expected signature in direct detection experiments. They argue that in the low-energy region, where the self-interactions between the dark matter particles come close to saturating the S-wave unitarity bound, the universal scattering properties of these states are dependent only on the scattering length. The scattering of these bound states with the nucleus in the direct detection experiments would also depend on the same parameter. This would change the expected recoil spectrum in the direct detection experiments compared to the scattering of a single dark matter particle. This can be seen as an impact due to the extended structure of the dark matter, which transmits into the recoil-energy spectrum as an additional form factor. In the case where the scattering with the nucleus results in the breaking of the bound state, the recoil-energy spectrum can again be expected to be different.

In this chapter, the presence of these bound states is investigated by studying their impact on the expected spectrum seen with the CRESST-III detectors, and the first attempt to set the lower bounds on the self-interacting cross-section of these bound states from the direct detection window is made. The sensitivity of CRESST concerning the scenario of elastic and inelastic scattering of these bound states is also explored. In Sec. 6.1 and 6.2, the properties of these bound states and their expected recoil spectrum for different scattering scenarios, as shown in Ref. [65] are communicated respectively. In the following Sec. 6.3, the same recoil spectra for different CRESST-III nuclei and crystals are calculated, along with the exclusion limits on dark matter-nucleus scattering cross-section under these different scattering scenarios. Then, the approach used to set the exclusion limits on the self-interaction cross-section of these states is explained in Sec 6.4 followed by the results and conclusions.

6.1 Universal Properties

Observations from the cluster mergers and the ΛCDM simulations have shown that limited self-interaction between dark matter particles can take place at relativistic velocities. Whereas at non-relativistic velocities a strong self-interaction can solve the discrepancies on the small-scale structures. Thus, an assumption is made that there exists a region in the velocity space, where the self-interactions come close to saturating the S-wave

unitarity bound. This region could be called as the *scaling region*, where the scattering cross-section of the particles has inverse proportionality with their relative velocity v. For example, it could be proportional to $1/v^2$. As it is already argued in Ref. [64], all the scattering properties in this region depend on the large scattering length, which is denoted by a. If a has a small negative imaginary part, then we could also expect the existence of some annihilation channels. The condition for the existence of the scaling region is $|a| \gg r_0$, where r_0 is the range of interaction of the dark matter particles.

Similarly, a *universal region* could also be defined where the corresponding energies are in and below the scaling region. *Universality* is context means that all the low-energy scattering properties of dark matter particles is determined only by the large S-wave scattering length. Thus, in the universal region, the elastic and inelastic (annihilation) cross-section for identical bosonic dark matter particles can be given by[64]:

$$\sigma_{el} = \frac{8\pi}{|-ik-\gamma|^2}, \tag{6.1}$$

and,

$$\sigma_{ann} = \frac{8\pi \mathrm{Im}(\gamma)}{k|-ik-\gamma|^2}, \tag{6.2}$$

where k is the relative momentum between the two particles and is given by $k = m_\chi v/2$, with m_χ being the mass of each individual particle and v being the magnitude of their relative velocities; and $\gamma = 1/a$ is the inverse scattering length. The above equations have to be multiplied by a factor of $1/2$ if the particles are not identical. The $-ik$ term in the above equations is the effect of re-scattering of these particles, and it becomes essential if the resonance is very close to the threshold.

In the given universal region, resonance forms a bound state of dark matter particles if $\mathrm{Re}(\gamma > 0)$. This bound state can be called *Darkonium* (also represented by D from here on) and can be seen as a dark copy of the deuteron if the bound state is of two dark matter particles. Like other properties, the binding energy and the decay width of this darkonium would also depend on the scattering length and is given by:

$$E_B = \frac{\mathrm{Re}(\gamma)^2 - \mathrm{Im}(\gamma)^2}{m_\chi}, \tag{6.3}$$

and

$$\Gamma = \frac{4\mathrm{Re}(\gamma)\mathrm{Im}(\gamma)}{m_\chi} \tag{6.4}$$

Now, we are interested in the bound states that have survived cosmic evolution and thus have a very long lifetime. It can be proclaimed that this is not a very wild assumption as

the deuteron is also a weakly bound state of a proton and a neutron and has successfully survived cosmic evolution, which is evident from the theory of Big Bang Nucleosynthesis. Therefore, from the above equations, we require that $\mathrm{Im}(\gamma) \to 0$, and as a result, the annihilation cross-section can be seen to vanish.

In the given limit, the elastic self-interaction cross-section of individual dark matter particles changes to:

$$\sigma_{el} = \sigma_{\chi-\chi} = \frac{8\pi}{k^2 + \gamma^2}, \tag{6.5}$$

and the binding energy would be,

$$E_B = \frac{\gamma^2}{m_\chi}. \tag{6.6}$$

Thus, from Eq. 6.5, if the scattering length of the dark matter particles could somehow be inferred, the self-interacting elastic scattering cross-section could be figured out, and vice-versa. The inverse velocity dependence of the self-interacting cross-section is also evident. γ can thus be figured out from the same equation as:

$$\gamma = \sqrt{\frac{8\pi}{m_\chi}\left(\frac{\sigma_{\chi-\chi}}{m_\chi}\right)^{-1} - \left(\frac{1}{2}m_\chi v\right)^2} \tag{6.7}$$

With the definition of γ set in place, we could assess the mass range of dark matter particles (order of magnitude estimate) at different scales, which would be required for

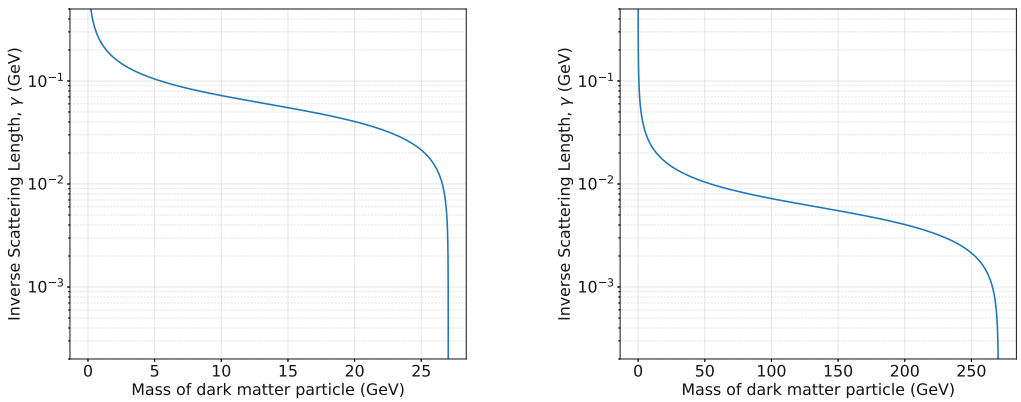

(a) (b)

Figure 6.1: Inverse scattering length as a function of the dark matter particle mass for (a) $\sigma_{\chi-\chi}/m_\chi = 0.1$ cm^2/g & $v = 1000$ km/s and (b) $\sigma_{\chi-\chi}/m_\chi = 1$ cm^2/g & $v = 10$ km/s

saturating the S-wave unitarity bound. At the cluster scales, typical collisional velocities of halos are estimated to be around $v \sim 1000$ km/s [196], and the upper bound on the self-interaction cross-section is $\sigma_{\chi-\chi}/m_\chi \sim 0.1$ cm^2/g. Similarly, to solve the small-scale structure problem, the self-interaction required is in the order of $\sigma_{\chi-\chi}/m_\chi \sim 1$ cm^2/g with the typical velocities around $v \sim 10$ km/s [196]. Thus, the inverse scattering length for different dark matter masses is plotted in Fig. 6.1.

Hence, it can be seen that the required mass for the dark matter particles that saturates the S-wave unitarity bound on cluster scales is around 27 GeV and that on the small scales is around 270 GeV, where the scattering length increases significantly. Above this mass range, γ becomes imaginary and contradicts our requirement for the bound state to have a very long lifetime (Eq. 6.4). Although this is an order of magnitude estimate, it gives us the region of mass range where the scattering of the dark matter particles forms bound states at different velocity scales. The region beyond this mass scale falls above the scaling region, and thus the formation of the bound states is not possible, although it can be accommodated if the scaling region is above the given velocity scale. Interestingly, this order of magnitude estimate gives the resulting mass range aligning with the pertinent regime for ongoing direct detection experiments.

It is also possible for the darkonium particles to have self-interactions, and in that case, the scattering is again determined by the inverse scattering length. In the case when the scattering is inelastic, different final state configurations are possible. Such as four individual dark matter particles, one darkonium and two individual dark matter particles, a dark matter particle along with a bound state of three dark matter particles, or a bound state of four dark matter particles. However, the formation of higher-order bound states can be avoided by imposing symmetry conditions just like in the visible sector. The elastic self-scattering scenario of darkonium, on the other hand, is a non-trivial 4-body problem, and hence for further calculations, we focus only on the self-interactions between the dark matter particles that result in the formation of darkonium and not the self-interaction between darkonium. However, it is argued in Ref. [65] that the low-energy elastic scattering cross-section is in the same order of magnitude as it is for the dark matter particles, i.e., $1/\gamma^2$. In the high-energy scattering case, the total scattering cross-section also has the same order of magnitude as for the dark matter scattering case, i.e., $1/k^2$. Although the elastic scattering scenario has an extra suppression factor of $(\gamma/k)^4$ as the momentum should transfer to all the individual constituent particles.

The probability of darkonium interacting with each and their breakup can also be calculated and is also shown in Ref. [65]. It is estimated that assuming $\sigma_{\chi-\chi}/m_\chi = 1$ cm^2/g, the mean free path of the darkonium in the cosmological (galactic) dark matter background density of 1.26×10^{-6} GeV/cm^3 (0.1 GeV/cm^3) is 150 Gpc (2 Mpc). Hence, the possibility of its survival from this order of magnitude estimate is quite high unless the darkonium passes through a very dense region of dark matter.

6.2 Scattering Scenarios and Energy Spectrum

The expected signal for direct detection experiments will be shown in this section as it is demonstrated in Ref. [65]. The focus is only on the case where the bound state is composed of two dark matter particles or the Darkonium. The interaction of the dark sector with the nuclei is considered to be isospin-conserving, momentum-independent, and spin-independent. The total expected number of events measured for an incident flux of dark matter, in the units of events per unit target mass per unit time and per unit recoil energy, is given by (similar to what is already shown in Eq. 3.3):

$$\frac{dR}{dE_R} = N_T n_\chi \int d^3\boldsymbol{v} f(\boldsymbol{v}+\boldsymbol{v}_E) \times \frac{d(\sigma v)}{dE_R}, \tag{6.8}$$

where N_T is the number of target nuclei; n_χ is the number density of dark matter i.e. $n_\chi = \rho_\chi/m_\chi$ for $\rho_\chi = 0.3$ GeV/c^2/cm^3 being the local dark matter density [124] and m being the mass of incoming dark matter particle. It has to be noted that $n_\chi = \rho_\chi/2m_\chi$ for the case where it is assumed that the solar neighborhood is composed of purely darkonium, which has a mass of $2m_\chi$; $\boldsymbol{v}$ is the incoming dark matter velocity; $\boldsymbol{v}_E$ is the average velocity of the Earth; $d(\sigma v)/dE_R$ is the differential scattering rate which is calculated in the following subsections; and $f(x)$ is the velocity distribution of dark matter particles. The truncated Maxwell-Boltzmann distribution [121] is considered for further calculation:

$$f(\boldsymbol{v}+\boldsymbol{v}_E) = Ne^{(\boldsymbol{v}+\boldsymbol{v}_E)^2/2v_\odot^2}\Theta(v_{esc}-v), \tag{6.9}$$

with $v_E = 232$ km/s, the asymptotic velocity $v_\odot = 220$ km/s [116] and the galactic escape velocity $v_{esc} = 544$ km/s [117].

Now, the differential scattering rate will be given for three main cases that we focus on. The first case would be the scattering of a dark matter particle with the nucleus, where the physics is similar to what has already been established in Sec. 3.1, but it is stated for the sake of completeness. The second case would be the scattering of Darkonium with the nucleus, where the scattering happens elastically, and darkonium remains in a bound state. The last case would be the scattering of darkonium with the nucleus, where it breaks apart as a result of this scattering. The details of the derivations can be found in the Appendix of Ref. [65].

6.2.1 Dark Matter Scattering with the Nucleus

The Feynman diagram of this interaction can be seen in Fig. 6.2. The differential scatter rate for this interaction can be given by:

$$\left(\frac{d(\sigma v)}{dE_R}\right)_{A+1} = \frac{m_A}{2\pi v}\,|G_A(q)|^2\,\Theta(v-q/2\mu), \tag{6.10}$$

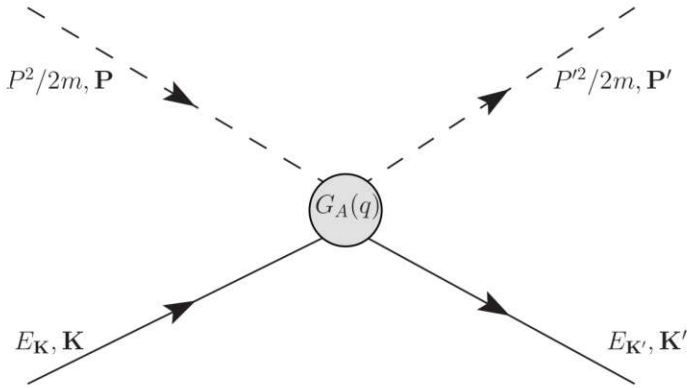

Figure 6.2: Feynman diagram for the scattering of a dark matter particle with mass m, incoming momentum $\mathbf{P}$ and outgoing momentum $\mathbf{P}'$ (dashed lines), with the nucleus of mass m_A for the atomic number A, incoming momentum $\mathbf{K}$ and outgoing momentum $\mathbf{K}'$ (solid line). The vertex factor of the given interaction is given by the grey circle and has a value of $G_A(q)$, where q is the exchange momentum. Image is taken from Ref. [65].

where v is the velocity of the incoming dark matter particle; m_A is the mass of the target nucleus with the mass number A. The $\Theta(x)$ represents the Heaviside step function as there is a minimum velocity required for the dark matter particle to produce a recoil, which is $v > q/2\mu$, where q is the exchange momentum in the interaction and μ is the reduced mass of the dark matter-nucleus system. $G_A(q)$ is the vertex factor of the interaction, and under our assumptions of spin-independent interaction, it is given by:

$$|G_A(a)|^2 = \frac{\pi\sigma_{\mathrm{SI}} A^2 F_N^2(q)}{\mu_n^2} \tag{6.11}$$

where σ_{SI} is the spin-independent dark matter-nucleon cross-section; $F_N(q)$ is the nuclear Helm form factor [119]; and μ_n is the reduced mass of the dark matter particle and the nucleon. It can easily be shown that using the given differential scattering rate, the final total scattering rate in Eq. 6.8 is analogous to what has already been derived in Sec. 3.1.

6.2.2 Darkonium Elastic Scattering with the Nucleus

As it can be seen from the Feynman diagram in Fig. 6.3, upon approaching the target nucleus, the darkonium splits up where one of the constituents scatters with the nucleus and then recombines with the other constituent. The calculation of the phase space of the given Feynman diagram can be found in the Appendix of Ref. [65]. The differential scattering rate for this case is given by:

$$\left(\frac{d(\sigma v)}{dE_R}\right)_{A+2} = \frac{2m_A}{\pi v} \, |G_A(q)|^2 \, |F(q)|^2 \, \Theta(v - q/2\mu_2), \tag{6.12}$$

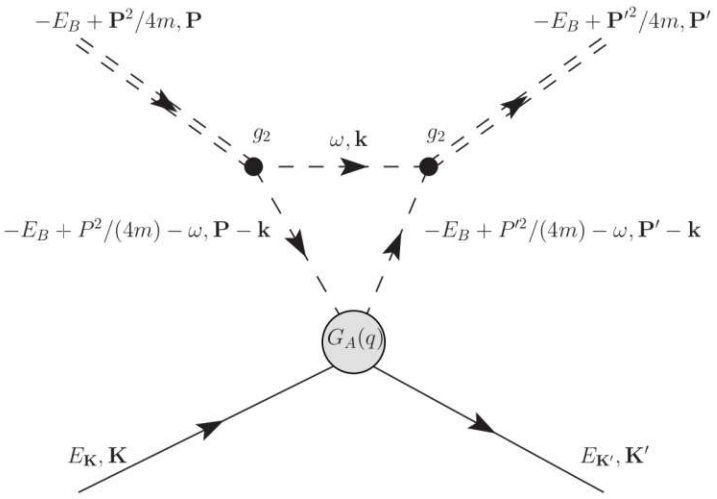

Figure 6.3: Feynman diagram for elastic scattering of a darkonium with mass $2m$, binding energy E_B, incoming momentum $\mathbf{P}$ and outgoing momentum $\mathbf{P}'$ (dashed lines), with the nucleus of mass m_A for the atomic number A, incoming momentum $\mathbf{K}$ and outgoing momentum $\mathbf{K}'$ (solid line). The vertex where the darkonium splits is given by g_2, where one of the particles has energy ω and momentum $\mathbf{k}$. Image is taken from Ref. [65].

When we compare this to the differential scattering rate of a dark matter particle in Eq. 6.10, it can be seen that the two cases differ by a factor of 4, which comes as a result of the coherence effect of two dark matter particles scattering with the nucleus (2^2), a different Theta function as now the minimum velocity required to produce a recoil correlates with the reduced mass of darkonium and the nucleus, μ_2 (rather than the dark matter particle and the nucleus as in the previous case), and the influence of the internal structure of the incoming particle imparts itself in the form of a darkonium form factor $F(q)$, which is given by:

$$F(q) = \frac{4\gamma}{q}\tan^{-1}\left(\frac{q}{4\gamma}\right), \tag{6.13}$$

where $\gamma = 1/a$ is the inverse scattering length of the darkonium. Its form comes from the scattering phase space calculation, which can be found in Ref. [65]. It is assumed here that both darkonium and the dark matter particle scatter with the nucleus with the same amplitude of $G_A(q)$.

6.2.3 Darkonium Breakup after Scattering with the Nucleus

For this scenario, the Feynman diagrams are shown in Fig. 6.4. In the first diagram, darkonium breaks up, and one of the constituents scatters with the nucleus. In the second diagram, the two constituents re-scatter thereon and break up after that. The second diagram needs to be included as the interaction is associated with a large scattering

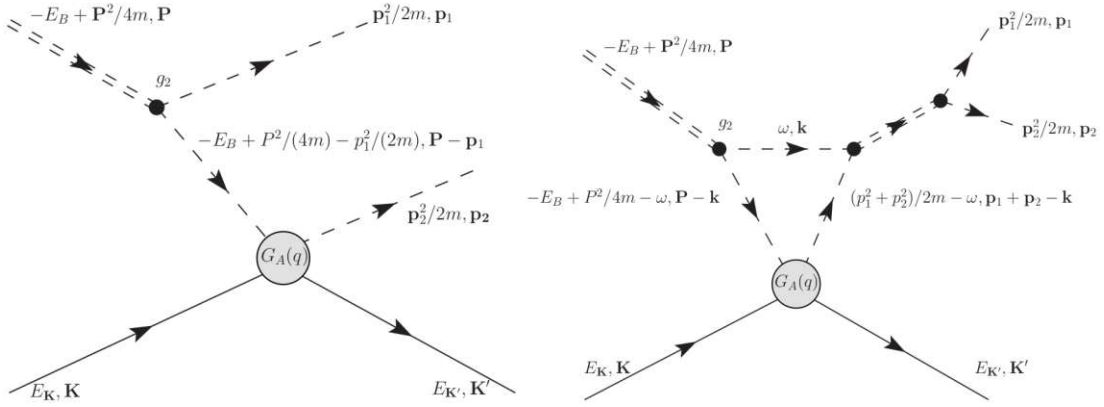

Figure 6.4: Feynman diagrams for the breakup of a darkonium upon scattering with the nucleus. The incoming darkonium has a mass $2m$, binding energy E_B, and incoming momentum $\mathbf{P}$. The outgoing particles have mass m, momentum p_1, and p_2, respectively. The vertex where the darkonium splits in the second diagram is given by g_2, where one of the particles has energy ω and momentum $\mathbf{k}$. Image is taken from Ref. [65].

length and is thus non-perturbative. The differential scattering rate of the breakup scenario is given by:

$$\left(\frac{d(\sigma v)}{dE_R}\right)_{A+1+1} = 128\gamma \frac{m_A}{v}|G_A(q)|^2 \times \int \frac{d^3\mathbf{r}}{(2\pi)^3}\left|\frac{1}{4\gamma^2+(2\mathbf{r}-\mathbf{q})^2}+\frac{1}{4\gamma^2+(2\mathbf{r}+\mathbf{q})^2}-\frac{i}{2q(\gamma+ir)}\ln\frac{4r^2+(2\gamma-iq)^2}{4\gamma^2+(2r-q)^2}\right|^2 \times \Theta\left(v-\left(\frac{q}{2\mu_2}+\frac{\gamma^2}{mq}\right)\right) \quad (6.14)$$

All the symbols in the given term have their usual meanings. The first two terms in the given equation correspond to the first diagram in Fig. 6.4, and the third term corresponds to the second diagram. The integral over the magnitude of $\boldsymbol{r}$ ranges from $0 < r < R$, where R is given by:

$$R^2 = mq\left(v-\left(\frac{q}{2\mu_2}+\frac{\gamma^2}{m_\chi q}\right)\right). \quad (6.15)$$

In this particular scenario, the minimum velocity required to impart a recoil is given by $q/2\mu_2 + \gamma^2/mq$. Only those recoil energies are valid in this scenario where $q/2 \ll 1/r_0$ and $R \ll 1/r_0$, where r_0 is the range of interaction of dark matter particles. Similar to previous scenarios, the calculation of the Feynman diagrams in this scenario can also be found in the Appendix of Ref. [65].

6.3 Results for CRESST-III

Having established the differential recoil rate for different scenarios, the total recoil spectra could now be calculated using Eq. 6.8 for different nuclei used in the CRESST-III Run36. The expected spectra are calculated for ^{7}Li, ^{16}O, ^{28}Si, ^{40}Ca and ^{183}W. The spectrum is not calculated for ^{27}Al as it is very similar to the spectrum of ^{28}Si, since their mass numbers are very close to each other.

6.3.1 Expected Recoil Energy Spectrum

Since the starting motivation of this model was the requirement of large cross-sections on small scales in order to solve the problems in λCDM, the inverse scattering length γ is determined using Eq. 6.7 by considering the self-interacting cross-section $\sigma_{\chi-\chi}/m_{\chi} = 1$ cm^2/g at the relative velocity of $v = 10$ km/s between the dark matter particles [196]. It can be seen from Eq. 6.5 and 6.6 that the corresponding darkonium binding energies for 10 GeV dark matter particles would be ~ 54 keV and for 100 GeV dark matter particles would be ~ 0.5 keV. For this calculation, the normalizing reference spin-independent(SI) cross-section, $\sigma_{\mathrm{SI}} = 10^{-46}$ cm^2 is used for $m_{\chi} = 100$ GeV and $\sigma_{\mathrm{SI}} = 10^{-45}$ cm^2 is used for $m_{\chi} = 10$ GeV. These particular values are motivated as they fall just around the region which is excluded by the latest data from LUX-ZEPLIN(LZ)[81] and XENON1T[105] experiments.

In Fig. 6.5 and 6.6, the expected recoil spectra are shown for the various nuclei used in CRESST-III detector modules for all different scattering scenarios that have been considered. For both dark matter masses, we see that the elastic scattering of darkonium is almost double the dark matter particle scattering rate at lower energies. This can be seen easily as an effect that comes due to two different reasons. An enhancement of four is provided by the coherence effect of two dark matter particles in a darkonium that scatter with the nucleus, and a reduction of half is taken due to the fact that the elusive matter's number density (n_{χ}) in the solar neighborhood decreases as the darkonium mass is twice the dark matter particle mass. The shape of the spectrum is also seen to be different than the normal case, and this effect comes due to the participation of the darkonium form factor in the scattering process. It can be noted that the darkonium form factor is nearly one at lower energies due to very small momentum transfer compared to the assumed inverse scattering length.

For the case where $m_{\chi} = 100$ GeV, the spectra of the breakup scenario could also be seen in Fig. 6.5. The spectra are seen to rise slowly, peak, and then fall off slower than the darkonium elastic scattering or the particle scattering case. The peak is seen to be reached at the energy that depends on the mass of the scattering nucleus. The fall off of the spectrum at low energies could be understood as at very low recoil energies, the exchanged momentum is not enough to break apart the bound state. It is also noted that the breakup scenario is suppressed for low-mass nuclei as in the case of ^{7}Li, hardly any contribution of breakup scattering could be seen in the energy spectra until 25 keV.

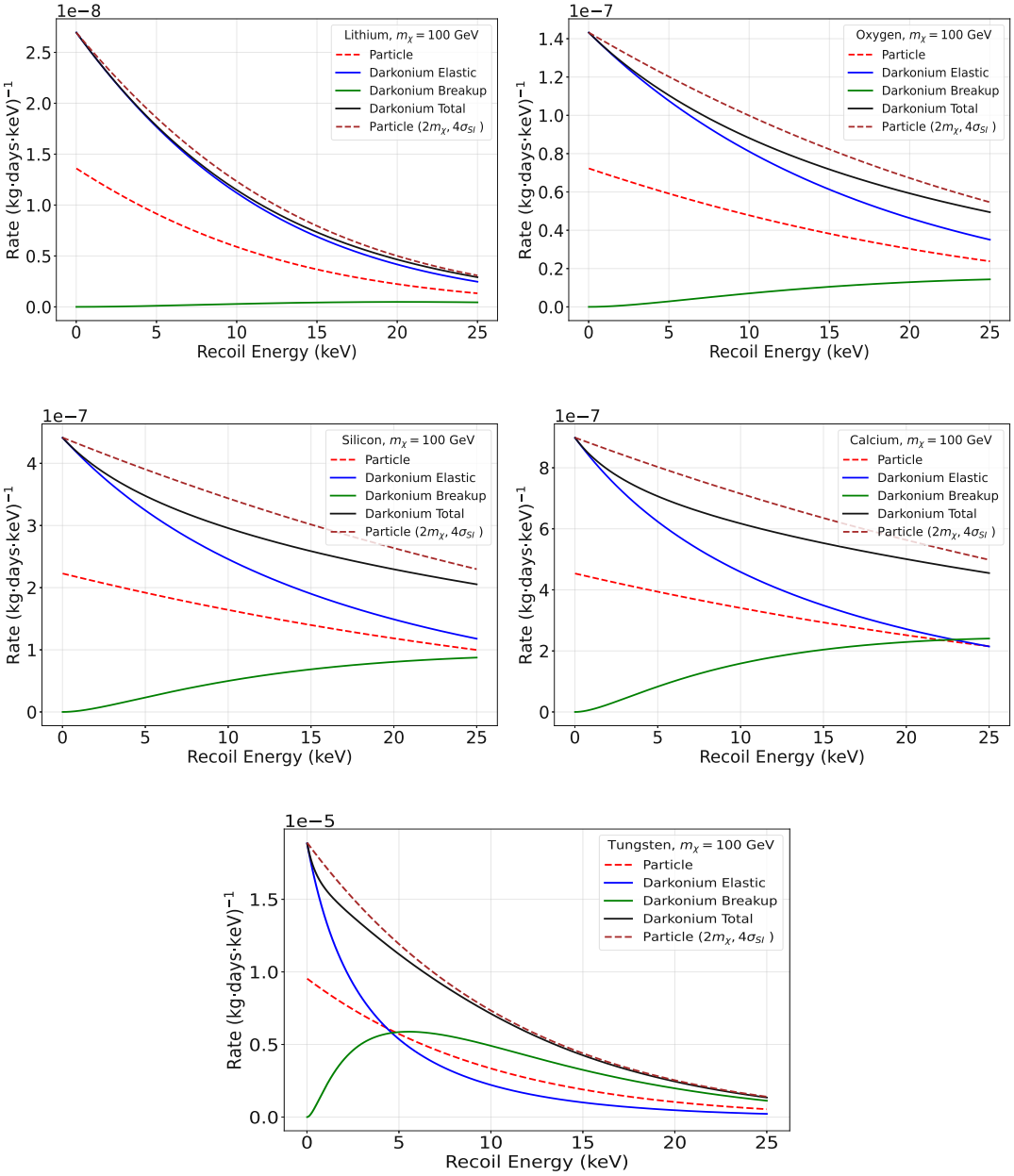

Figure 6.5: Expected recoil spectrum per kg/day/keV for $m_\chi = 100$ GeV dark matter particle with the nuclei present in the CRESST-III detector modules. The normalizing reference cross-section $\sigma_{\mathrm{SI}} = 10^{-46}$ cm^2. The spectra are shown for the recoil of a dark matter particle (red dashed line), darkonium scattering elastically (blue line), darkonium inelastic scattering or break up (green line), and a sum of both elastic and inelastic darkonium scattering (dark blue line), with the nucleus. A case in which the scattering happens with a particle of twice the mass and 4 times the cross-section is also shown (brown dashed line). The particular scattering nucleus is shown on top of each plot.

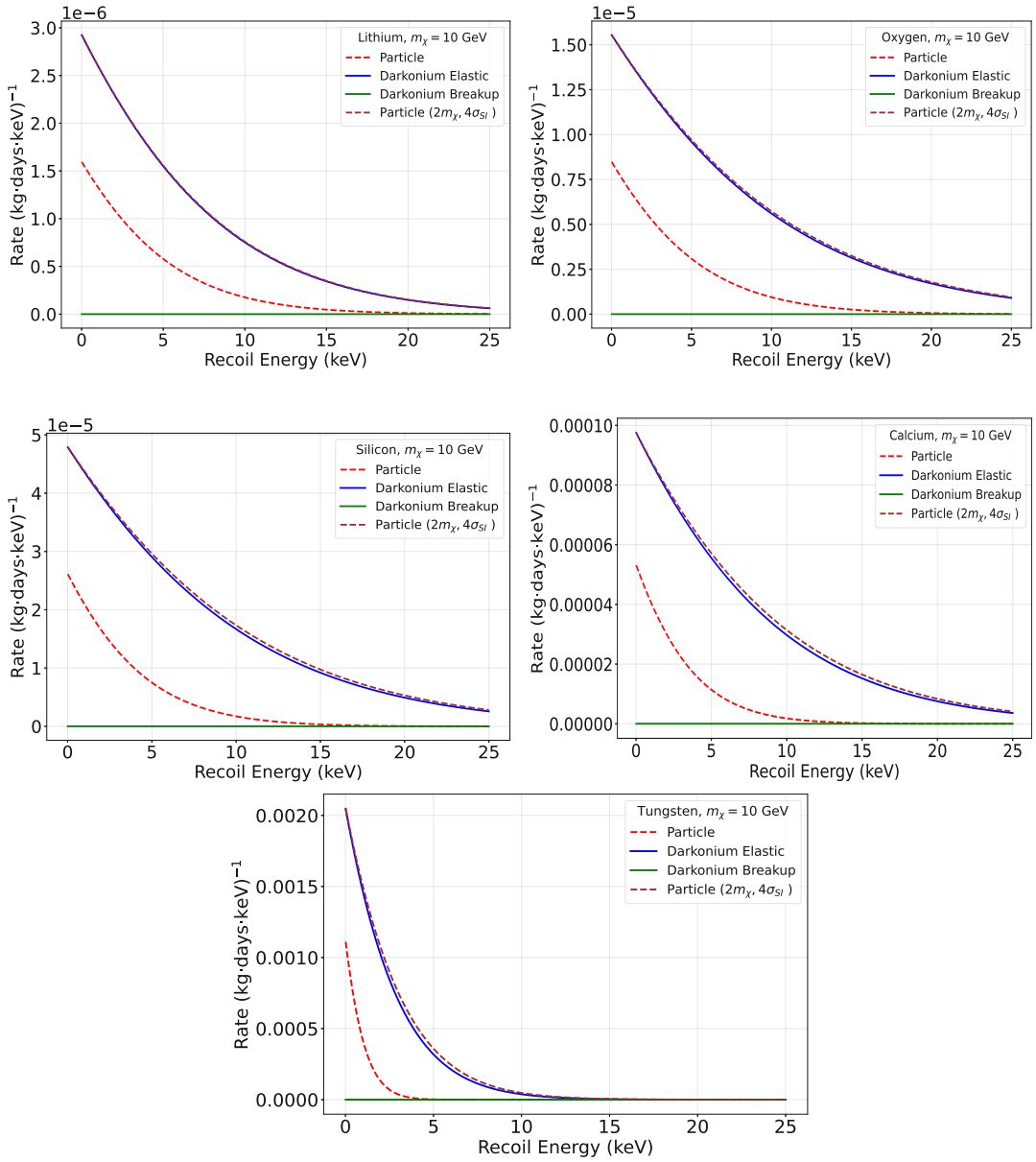

Figure 6.6: Expected recoil spectrum per kg/day/keV for $m_\chi = 10$ GeV dark matter particle with the nuclei present in the CRESST-III detector modules. The normalizing reference cross-section is taken as $\sigma_{\mathrm{SI}} = 10^{-45}$ cm^2. The spectra are shown for the recoil of a dark matter particle (red dashed line), darkonium scattering elastically (blue line), and darkonium inelastic scattering or break up (green line), with the nucleus. It can be seen that the breakup scenario is suppressed for this mass. A case in which the scattering happens with a particle of twice the mass and 4 times the cross-section is also shown (brown dashed line). The particular scattering nucleus is shown on top of each plot.

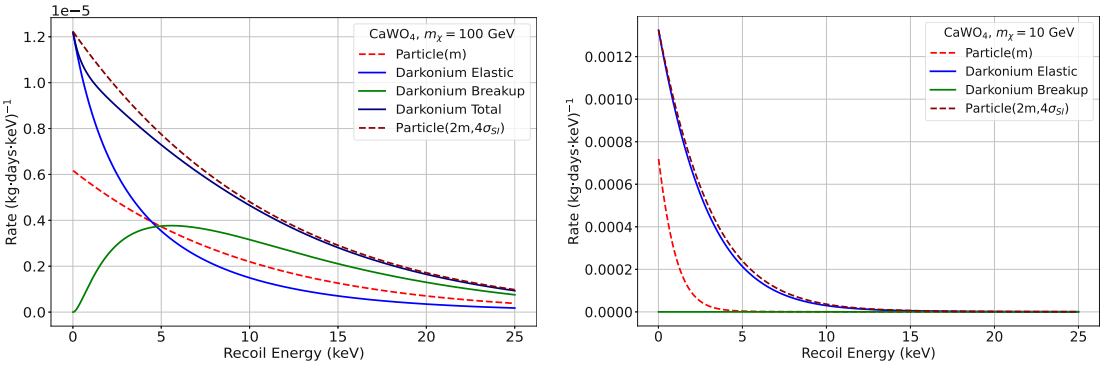

(a) (b)

Figure 6.7: Expected recoil spectrum per kg/day/keV for the $CaWO_4$ modules. The normalizing reference cross-section is taken as $\sigma_{SI} = 10^{-46}$ cm^2 for $m_\chi = 100$ GeV(left) and $\sigma_{SI} = 10^{-45}$ cm^2 for $m =_\chi 10$ GeV(right). The spectra are shown for the recoil of a dark matter particle (red dashed line), darkonium scattering elastically(blue line), and darkonium inelastic scattering or break up (green line), with the nucleus. It can be seen that the breakup scenario is suppressed for this mass. A case in which the scattering happens with a particle of twice the mass and 4 times the cross-section is also shown (brown dashed line).

For $m_\chi = 10$ GeV (Fig. 6.6), only the darkonium elastic scattering rate could be seen, and the breakup scenario is not visible. The breakup scenario is extremely suppressed for low-mass dark matter particles. This is forbidden kinematically and could be the effect of the large binding energy of the low-mass darkonium. The elastic scattering spectra are seen to decay rather slowly than the dark matter particle scattering case, as the effect of the form factor is relatively tiny at higher recoil energies.

Another interesting feature was noted in both cases. For the 100 GeV case, it is seen that upon adding the spectra for elastic scattering and inelastic scattering, the total spectra are very similar to the spectra for the scattering of an elementary particle with twice the mass ($2m_\chi$) and 4 times the cross-section ($4\sigma_{SI}$). Similarly, for the 10 GeV case, the spectra for elastic scattering are very similar to that of the $2m_\chi$ and $4\sigma_{SI}$ case. Thus, if the dark matter particle's mass could somehow be inferred from other detection methods, this degeneracy (if seen in the direct detection experiments) could be broken.

Now, having calculated the expected recoil spectrum for each nucleus in CRESST-III, the focus is mainly on $CaWO_4$ as the material contains light, medium, and heavy nuclei within. The total expected spectrum for a $CaWO_4$ module could now be calculated by weighing the spectra of each individual nuclei by their mass fraction in the material. Again, the spectra have been calculated for $m_\chi = 100$ GeV, $\sigma_{SI} = 10^{-46}$ cm^2 and for $m_\chi = 10$ GeV, $\sigma_{SI} = 10^{-45}$ cm^2. These can be seen in Fig. 6.7.

6.3.2 Darkonium-Nucleus Cross-Section Exclusion Limits

For calculating the exclusion limits on the darkonium-nucleus scattering cross-section for all the scenarios described above, the data taken with *DetA* from CRESST-III phase one has been used. This particular dataset is chosen as it was used to set the most stringent exclusion limits on the spin-independent dark matter-nucleus scattering cross-section between 0.16-1.8 GeV/c^2 dark matter masses [89]. The recoil energy spectrum and the recorded events in the light yield vs recoil energy plane can be seen in Fig. 6.8. The data acquisition, triggering, data cleaning, and energy reconstruction are done in the same way as it is described in Chapter 4. The data is calibrated using the two X-ray lines at 2.60 keV and 11.27 keV. These arise from the L_1 and M_1 shells of ^{179}Hf, generated through the decay chain following the cosmogenic activation of ^{182}W. The position of different bands Fig. 6.8(b) is fitted using the neutron calibration data, and the dark matter region of interest (ROI) is defined as the upper 50% boundary of the oxygen recoil band (red) and the lower 99.5% boundary of the tungsten recoil band (green). The histogram of the events falling in the ROI is shown in red in Fig. 6.8(a). The energy range for the ROI starts at the threshold of 30.1 eV and ends at 16.0 keV, with an active exposure of 5.6 kg-days. For the cut efficiency and other details of the measurement, the reader is referred to [89].

To extract the 95% upper limits on the darkonium-nucleus scattering cross-section, profile likelihood ratio (PLR) has been used as described in Sec. 4.6.2.1, with σ_{SI} (Eq. 6.11), or more precisely $\sigma_{\text{D-SM}}$, being the parameter of interest, where D stands for the Darkonium and SM implies the Standard Model. The value of γ is calculated using Eq. 6.7 using

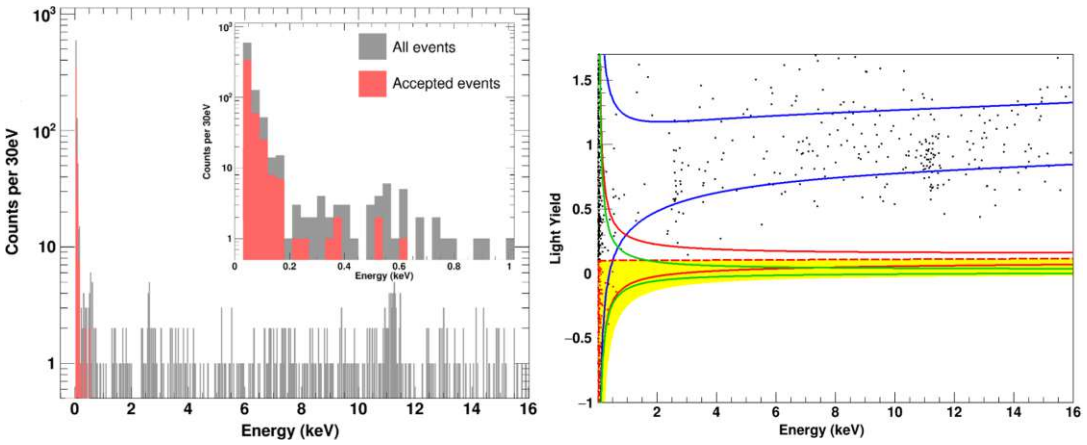

Figure 6.8: (a) Recoil energy spectrum for the CRESST-III phase one dark matter dataset. The grey histogram shows all the recorded events, and the red histogram shows the events in the dark matter ROI. (b) Scatter plot of recorded events in the light yield vs recoil energy plane. The blue band shows the upper and lower 90% boundaries of the e^-/γ band, and the red and green band shows the same boundaries for the nuclear recoil bands for oxygen and tungsten nuclei, respectively. The yellow region is defined as the dark matter ROI (see text). Both the plots are reprinted from Ref. [89].

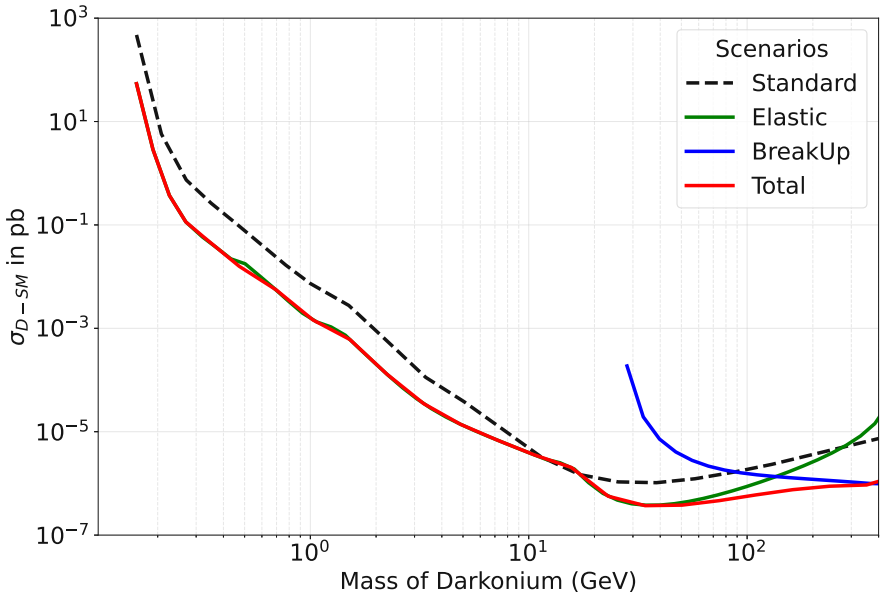

Figure 6.9: 95% C.I. darkonium-nucleus scattering exclusion limits for elastic scattering scenario (green), break-up scenario (green) and total scattering scenario (red). The 95% C.I. exclusion limits for standard dark matter particle-nucleus elastic scattering cross-section have also been plotted for reference.

the self-interacting parameters described in Sec. 6.3.1. The astrophysical parameters used for the calculation are shown in Sec. 6.2. The exclusion limits are calculated as a function of darkonium mass ($2m_\chi$) and are shown in Fig. 6.9. For reference, the limits are plotted along with the limits from the standard scenario of a single particle scattering on the nucleus and should not be compared one-to-one with the other limits, as these are from a different physics model and describe the scattering of darkonium and not individual dark matter particles. No significant difference is seen between the limits from the elastic scattering and the total scattering in the lower masses. This is expected as there is the break-up scenario is suppressed for lower masses, and hence, the contribution to the total scattering comes solely from the elastic scattering. The breakup scattering scenario starts showing an impact on the recoil spectrum at around 30 GeV darkonium mass, after which we see a separation between the elastic and total scattering limits. As expected, we see that the exclusion limits for low masses are lower than the standard scenario, as the expected recoil rate is higher for the darkonium scattering because of the resonant scattering of the two particles as already discussed in Sec. 6.3.1. As the mass increases, the total scattering limit stays lower than the standard scenario, but the elastic scenario limit starts getting worse. This is due to the impact of the form factor on the elastic scattering rate as it decays faster than the standard scenario for higher masses, resulting in a lower number of expected events and hence worse limit.

Thus, assuming the dark matter self-interaction cross-section of $\sigma_{\chi-\chi}/m_\chi = 1.0$ cm^2/g at the relative velocity of $v = 10$ km/s, which falls in the range required to solve the small-

scale crisis of ΛCDM, the first exclusion limits on the darkonium-nucleus spin-independent scattering cross-section have been extracted. The exclusion limits are calculated with the dataset collected with *DetA* from CRESST-III phase one, as the detector already has the most stringent exclusion limits in the standard scenario for sub-GeV dark matter masses. The limits have been calculated for three different scattering scenarios, including the elastic scattering of darkonium with the nucleus, the breakup of darkonium upon scattering with the nucleus, and a scenario where the contribution to the recoil energy spectrum comes from both elastic and the breakup scenario.

6.4 Probing Self-interacting Cross-Section

As it has been already described in Sec. 6.1, the scattering properties of dark matter particles, in the presence of a S-wave resonance very close to the scattering threshold, depends on the scattering length a, or equally, on the inverse scattering length γ. Thus, in order to study the self-interactions between the dark matter particles in the given scenario, an approach has to be established that allows to estimate γ from the recoil spectrum at the direct detection experiments. This section studies the influence of varying γ on the expected recoil spectrum in CRESST-III and uses it to estimate the self-interacting cross-section of the dark matter particles in this bound state.

6.4.1 Impact of γ on Recoil Energy Spectrum

To examine how varying the value of γ influences the recoil energy spectrum, other variables that determine the shape and scaling of the spectrum have to be fixed. In order to understand it, we focus on the simplest scattering case, i.e., the elastic scattering of darkonium on the target nucleus, although the same calculation is also performed for the total scattering scenario. The differential elastic scattering rate and the form factor are given in Eq. 6.12 and 6.13. The spectrum is calculated for the dark matter particle mass $m_\chi = 10$ GeV, or the darkonium mass $m_\mathrm{D} = 20$ GeV. The value of the darkonium-nucleus scattering cross-section $\sigma_{\text{D-SM}} = 10^{-5}$ pb, which is just above the lowest that can be probed for the given mass by CRESST-III (Fig. 6.9). The spectra are calculated for four values of γ as shown in Fig. 6.10.

The influence of γ through the darkonium form factor is evident in this context. When γ is small, the spectrum exhibits a nearly linear scaling with γ across all recoil energies. This aligns with expectations, given the functional form of the darkonium form factor as $|x \cdot \tan^{-1}(1/x)|^2$ (Eq. 6.13), which is a linearly increasing function for small values of x, x being $4\gamma/q$. However, the influence diminishes as γ increases and approaches the MeV range, becoming comparable to the exchange momentum q. This reduction occurs as the form factor asymptotically approaches its maximum value of 1, particularly at low recoil energies. Consequently, while γ can enhance the spectrum up to a certain point, further increases in γ have a diminishing impact as the darkonium form factor converges to 1. A similar influence of γ is observed in the total scattering scenario for a 100 GeV dark matter particle mass (with a 200 GeV darkonium mass) as illustrated in Fig. 6.11.

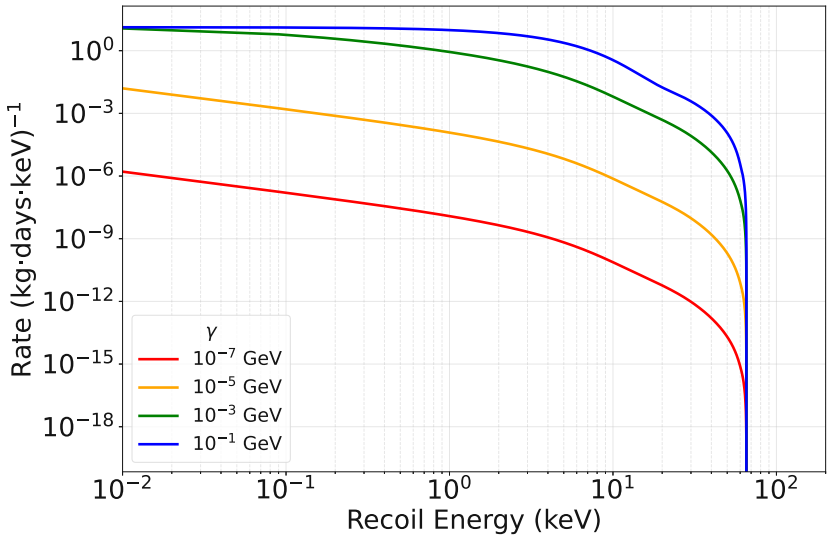

Figure 6.10: Expected nuclear recoil spectra for Elastic scattering of darkonium with $CaWO_4$ target for a 10 GeV dark matter particle or a 20 GeV darkonium particle with a darkonium-nucleus scattering cross-section of $\sigma_{D-SM} = 10^{-5}$ pb, and for $\gamma = 10^{-7}$ GeV(red), 10^{-5} GeV(yellow), 10^{-3} GeV(green) and 10^{-1} GeV.

Additionally, the tungsten nuclear form factor exhibits an impact for this mass as the spectra are seen to have quivering features at high recoil energies.

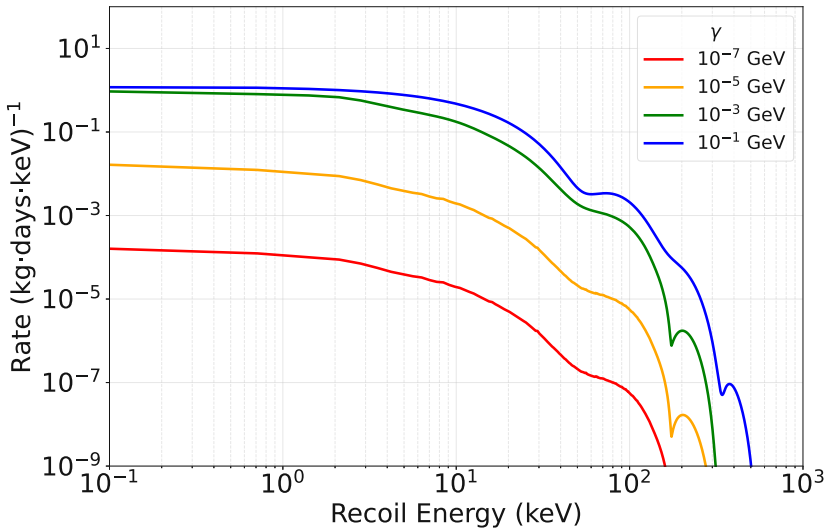

Figure 6.11: Expected nuclear recoil spectra for Elastic scattering of darkonium with $CaWO_4$ target for a 100 GeV dark matter particle or a 200 GeV darkonium particle with a darkonium-nucleus scattering cross-section of $\sigma_{D-SM} = 10^{-5}$ pb, and for $\gamma = 10^{-7}$ GeV(red), 10^{-5} GeV(yellow), 10^{-3} GeV(green) and 10^{-1} GeV.

Therefore, it is evident that γ possesses the capability to proportionally adjust the spectrum, either upward or downward, particularly for extremely small values. However, as γ increases and approaches the magnitude of q, its influence on the spectrum diminishes, aligning with the darkonium form factor's asymptotic approach to 1. Achieving a further enhancement in the spectrum requires an increased value of the darkonium-nucleus cross-section.

6.4.2 Likelihood Ratio and Test Statistic

In the standard scenario of the dark matter particle scattering on the detector nucleus, the scattering rate depends on two unknown dark matter parameters, i.e., the dark matter mass (m) and the scattering cross-section with the detector nucleus ($\sigma_{\text{D-SM}}$). The functional form of the expected recoil spectrum of the darkonium scattering shows that the spectrum depends on another unknown parameter that decides the self-interaction cross-section between the dark matter particles, i.e., the inverse scattering length (γ). In total, there are three unknown parameters for this scenario, and these three parameters are shown in red, green, and blue for the elastic scattering scenario in Eq. 6.16, respectively.

$$\left(\frac{d(\sigma v)}{dE_R}\right)_{A+2} = \frac{2m_A}{\pi v} \cdot \frac{\pi \sigma_{\text{D-SM}} A^2 F_N^2(q)}{\mu_n^2} \cdot \left|\frac{4\gamma}{q}\tan^{-1}\left(\frac{q}{4\gamma}\right)\right|^2 \Theta(v - q/2\mu_2), \tag{6.16}$$

In order to calculate the exclusion limits in the standard scenario for different dark matter masses using the profile likelihood framework explained in Sec. 4.6.2.1, the dark matter mass is fixed and the best fit to the parameter of interest (POI), i.e., the interaction cross-section is found. This is then compared to the fit of the POI that gives the desired confidence level, using the likelihood ratio and the defined test statistic. However, this approach cannot directly be used in the darkonium scattering scenario as we have another POI. An extension of this method, nonetheless, can be used where the likelihood fit is performed, keeping two free POIs. Applying Wilk's theorem [197] defined in Sec. 4.6.1.2, the probability distribution of the test statistic then follows a χ^2-distribution with 2 degrees of freedom. Following this approach would give a set of values of POIs for a fixed mass, that gives the desired exclusion limits. These set of values of POIs are then calculated for each different mass point to give exclusion limits in a 3D space of mass, and the two POIs (which in the given case would be $\sigma_{\text{D-SM}}$ and γ). However, a different method is used here to simplify and easily visualize the results. The dark matter mass m is initially fixed to a particular value so that we are again left with two POIs. Now, a similar calculation can be performed by probing in the σ_{D-SM} space and fitting the spectrum for the values of γ. The likelihood ratio in this approach takes the form:

$$\lambda(\gamma) = \frac{\mathcal{L}(\gamma_{excl}, \theta_b|O)}{\mathcal{L}(\gamma_{best}, \theta_b|O)} = \frac{\mathcal{L}_{excl}}{\mathcal{L}_{best}} \tag{6.17}$$

where θ_b describes all the nuisance parameters of the background for the probed σ_{D-SM} (with a fixed m). Following this approach gives the exclusion limits in the σ_{D-SM} vs γ

plane for that particular fixed mass m. This calculation can then be performed for various masses, and exclusion limits can be extracted for each m. It has to be noted that Yellin's methods [153, 154] cannot be used for extraction of exclusion limits in this physics case, as the Yellin's method can only be applied for setting exclusion limits on a parameter that scales the spectrum linearly in the whole parameter space, which is not the case for γ.

6.4.3 Results on Self-Interaction Cross-Section

To perform the exclusion calculation described above, two prerequisites are needed. The masses of dark particles are needed for which the calculation should be performed, and the probing region for $\sigma_{\text{D-SM}}$'s for each mass needs to be known for which the exclusion limits on γ can be set. To cover different ranges, the calculation is performed for four different dark matter particle masses, i.e., 0.5 GeV, 1 GeV, 10 GeV, and 100 GeV. For each mass, we select the minimum value of $\sigma_{\text{D-SM}}$ that can be excluded at a 95% confidence level in the elastic scattering scenario for the given mass (see Fig. 6.12). This is a conservative choice and is motivated by the findings in Sec. 6.4.1, where it is observed that beyond a certain threshold value of γ, increasing its value no longer amplifies the recoil spectrum, and its impact diminishes. Consequently, beyond this threshold, only $\sigma_{\text{D-SM}}$ has the capacity to scale up the spectrum to align with the observed data. As the excluded $\sigma_{\text{D-SM}}$ represents the minimum value that can be excluded by the data, the detector exhibits insensitivity to $\sigma_{\text{D-SM}}$'s below this value, irrespective of how much γ is increased.

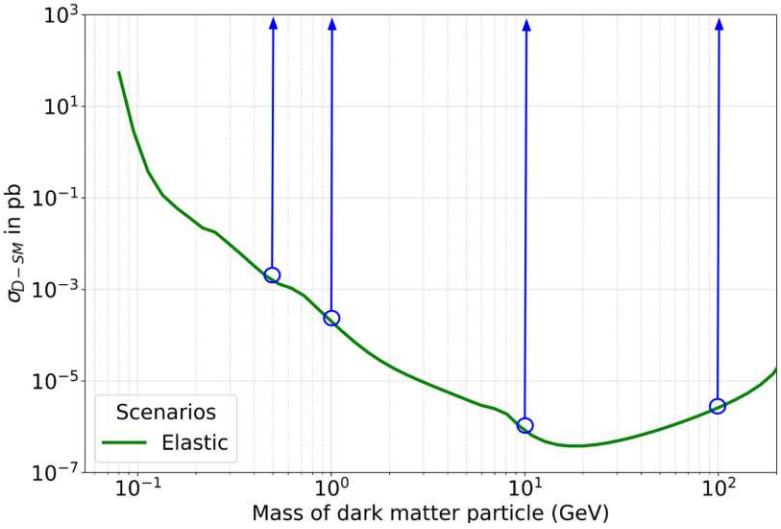

Figure 6.12: The probing range (blue arrows) of $\sigma_{\text{D-SM}}$ for setting the exclusion limits on γ for m_χ = 0.5, 1.0, 10.0 and 100.0 GeV. Blue circles show the smallest probed value, which lies on the 95% exclusion limits (green solid) for the elastic scattering scenario from *DetA*.

The 95% confidence level upper limits on γ can be seen in Fig. 6.13 plotted for 4 different dark matter particle masses. It can be seen that the limits decrease with the

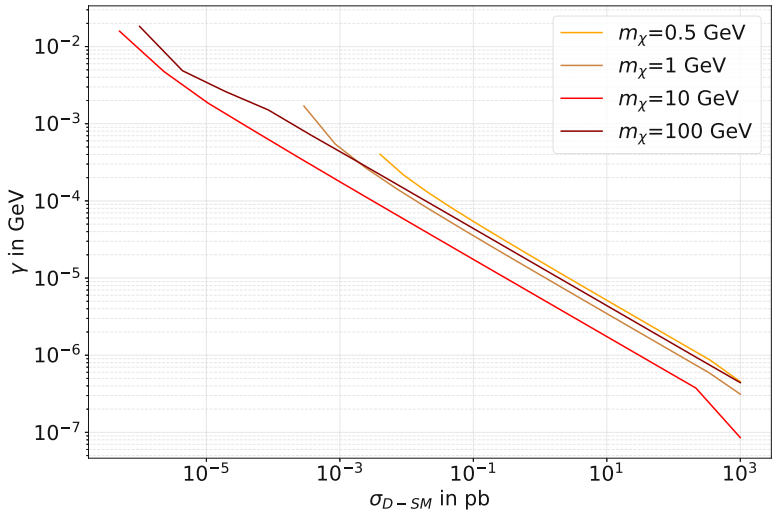

Figure 6.13: The 95% exclusion limits on the value of inverse scattering length γ with respect to the daronium-nucleus scattering cross-section, $\sigma_{\text{D-SM}}$ for $m_\chi = 0.5$, 1.0, 10.0 and 100.0 GeV set using the *DetA* data.

increasing value of $\sigma_{\text{D-SM}}$ as lowering γ scales down the spectrum. Thus, increased $\sigma_{\text{D-SM}}$ is accommodated by lowering γ to fit the observed spectrum.

Now, the exclusion limits on the value of γ can be converted into the self-interaction cross-section between dark matter particles using Eq. 6.5. Since the constraints from astrophysics and N-body simulations are formed on the value of $\sigma_{\chi-\chi}/m_\chi$, the exclusion limits are translated to $\sigma_{\chi-\chi}/m_\chi$ as:

$$\frac{\sigma_{\chi-\chi}}{m_\chi} = \frac{8\pi/m_\chi}{\gamma^2 + \left(\frac{1}{2}m_\chi v\right)^2} \tag{6.18}$$

As it can seen, the value of $\sigma_{\chi-\chi}/m_\chi$ depends not only on γ but also on the relative momentum between the dark matter particles. This allows us an advantage of comparing the exclusion to astrophysical observations at both the small-scales, with the typical velocities of $\mathcal{O}(10)$ km/s, and the cluster scales, with the typical velocities of $\mathcal{O}(1000)$ km/s. This velocity v in Eq. 6.18 should not be confused with the velocity in Eq. 6.8. The former represents the relative velocity between the dark matter particles when the bound state is formed, whereas the latter represents the velocity of the bound states in the Milky Way with respect to the Earth.

The exclusion limits are calculated only for the elastic scattering scenario, as for lower masses, the break-up scenario does not play a role. For $m_\chi = 100$ GeV, the calculation is only shown as a proof-of-principle and, in principle, can be done for the total scattering scenario also. The exclusion limits are calculated for $v = 30$ km/s to compare them with the current constraints on the small-scale structures from the astrophysical observations

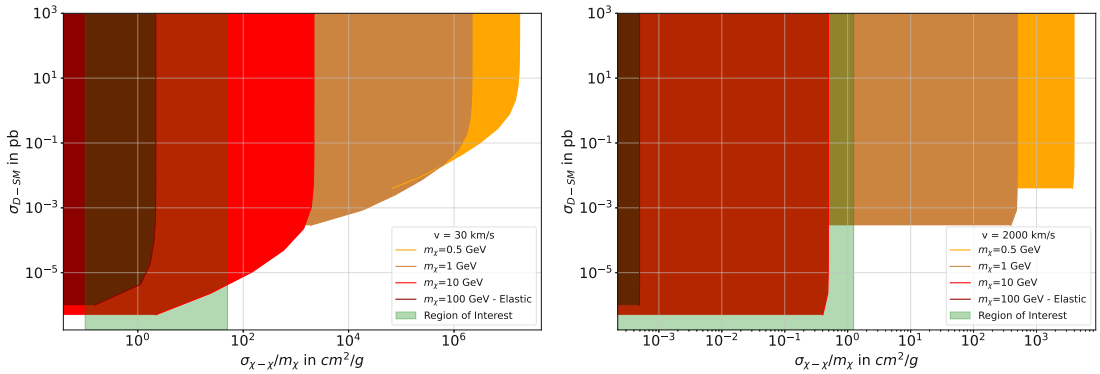

Figure 6.14: 95% exclusion limits on the self-interaction cross-section of dark matter particles in a bound state for different dark matter-nucleus scattering cross-sections calculated with the *DetA* data from CRESST-III compared with the region of interest (ROI) that comes from the constraints from astrophysics and N-body simulation(green band) at small-scales with $v = 30$ km/s (left) [198, 199] and at cluster scales with $v = 2000$ km/s (right) [19, 190, 191, 196]. The exclusion limits are calculated for $m_\chi = 0.5$, 1.0, 10.0, and 100.0 GeV dark matter particles and the excluded region is shaded for each particular.

requiring $\sigma_{\chi-\chi}/m_\chi = (0.1 - 50)$ cm^2/g [198, 199]. For comparison with the current constraints from the cluster mergers that demand $\sigma_{\chi-\chi}/m_\chi < 1.25$ cm^2/g, the exclusion limits are calculated at $v = 2000$ km/s [19, 196]. As these constraints show the value of $\sigma_{\chi-\chi}/m_\chi$ required to match the observations and simulations on both the scales, we call this range as the region of interest (ROI) for $\sigma_{\chi-\chi}/m_\chi$. The exclusion limits for both the velocity scales are shown in Fig. 6.14, and the excluded region falls below the exclusion limit for the given masses (shaded region).

To comprehend these exclusion limits, let's concentrate on the constraints established for a dark matter particle mass of $m_\chi = 10$ GeV, specifically for self-interactions occurring at small-scale velocities. Assuming that each dark matter particle in the bound state has a mass of m_χ =10 GeV, a scattering cross-section with the target nucleus of $\sigma_{\text{D-SM}} = 10^{-5}$ pb, and is distributed in these bound states within the Milky Way halo, the illustrated exclusion limits, as depicted in Fig. 6.14(left), reveal that, in this particular scenario, the self-interaction cross-section $\sigma_{\chi-\chi}/m_\chi$ below approximately 100 cm^2/g can be ruled out with a 95% confidence level based on the available data and exposure under the given model. In order to exclude lower self-interaction cross-sections, the sensitivity of the experiment has to be increased to lower darkonium-nucleus or equivalently dark matter-nucleus cross-sections for a given mass.

It is seen that if the mass of dark matter particle is lighter (for $m_\chi = 0.5$ and 1 GeV), the $\sigma_{\chi-\chi}/m_\chi$ ROI is completely excluded with the $\sigma_{\text{D-SM}}$ that can be probed with the given data at both the velocity scales (the yellow and the brown shaded region). Thus, it can be asserted that if the dark matter exists in the form of darkonium, has $\sigma_{\chi-\chi}/m_\chi$ in the ROI and has a mass below 10 GeV, then the impact of the internal structure of darkonium on the recoil energy spectrum at the direct detection experiments can only be

seen if lower $\sigma_{\text{D-SM}}$ can be probed for the given mass. It can also be seen that there exists an upper limit to the sensitivity of $\sigma_{\chi-\chi}/m_\chi$ for any given mass as the exclusion limits remain constant at higher $\sigma_{\text{D-SM}}$ values. For example at 100 GeV, $\sigma_{\chi-\chi}/m_\chi > 2.2$ cm^2/g cannot be probed at $v = 30$ km/s. This occurs as increasing the darkonium-nucleus cross-section decreases the value of γ (Fig. 6.13), and for very small values of γ where $\gamma \ll (m_\chi v/2)$, $\sigma_{\chi-\chi}/m_\chi$ depends only on m_χ and v (Eq. 6.18), which is taken to be constant. For cluster scale velocities, the limits are seen to be constant for all the $\sigma_{\text{D-SM}}$ probed due to the large value of v, whereas at small-scale velocities, this is seen only for high $\sigma_{\text{D-SM}}$ where γ is small enough. Thus, probing higher $\sigma_{\text{D-SM}}$ cross-sections does not help us gain any sensitivity, and only going to lower $\sigma_{\text{D-SM}}$ will allow us to probe more parameter space.

The exclusion limits shown for $m_\chi = 0.5$ and 1.0 GeV are probed with the detector that has the strongest sensitivity in the given mass range. However, for $m_\chi = 10.0$ and 100.0 GeV, liquid noble gas experiments take the lead in the sensitivity and 3-4 order of magnitude lower $\sigma_{\text{D-SM}}$ can be probed (Fig. 2.7), where including the effect of break-up scenario for masses above few tens of GeV would also become important.

6.4.4 Summary and Conclusions

In this study, we establish the inaugural 95% confidence level direct detection exclusion limits on the self-interaction cross-section of asymmetric dark matter particles in the universal bound states as suggested by Laha and Braaten in Ref. [65]. The limits are calculated only for the elastic scattering of darkonium from the detector nucleus, for four different dark matter masses of $m_\chi = 0.5$, 1.0, 10.0, 100.0 GeV/c^2. The exclusion limits are formulated in terms of the inverse scattering length and are subsequently converted to the self-interaction cross-section using Eq. 6.18, which also depends on the relative momentum between the dark matter particles. This methodology facilitates comparisons of self-interactions across various velocity scales and, thus, can be directly juxtaposed with astrophysical and N-body simulation constraints on the self-interaction.

The work is done in the assumption that the dark mater exists in the Milky Way halo purely in the form of these bound states. For low-mass dark matter particles, the findings exclude the necessary self-interaction cross-sections required to address small-scale crises and the allowed limit from cluster merger observations. This occurs within the scope of current dark matter-nucleus scattering cross-sections that are probeable, and exploring lower cross-sections could potentially unveil the required self-interacting cross-sections. For the whole mass range, there exists an upper bound on the self-interaction cross-sections that can be probed, which is independent of the darkonium-nucleus scattering cross-section, and the upper bound decreases with increasing mass. This points towards the fact that very heavy mass dark matter particles can be excluded to have significant self-interactions required to solve the small-scale crisis, under the assumptions of the given model. Our limits are scrutinized at the minimum dark matter-nucleus scattering cross-section for low masses achievable with the current experimental technology using CRESST-III data. However, for relatively higher masses, lower cross-sections can still be

explored using results from liquid noble gas experiments such as XENONnT [80], LZ [81], PandaX [82], and others.

CHAPTER 7

Conclusions and Outlook

Dark matter has been one of the biggest questions in modern-day physics and has remained an unsolved mystery for about a century. From the astrophysical observations, it has been shown that this non-luminescent matter comprises around 25% of the energy density and about 85% of the matter density of the universe. It is seen to be ubiquitous across various astrophysical scales, ranging from dwarf satellite galaxies to clusters of galaxies. Vast amounts of effort have gone into understanding its nature, origin, and properties. Different models have tried to explain the universe with significant dark matter, and the most prevalent one is known as the ΛCDM model of the universe. The model has three main ingredients, i.e., Λ that describes the negative pressure that results in the accelerated expansion of the universe, CDM that represents the Cold non-relativistic Dark Matter, and the visible matter. The latter two exhibit gravitational interactions that provides the potential well to form structures in the universe. Various N-body simulations of the universe have been performed under the ΛCDM paradigm, and tremendous agreement has been reported between the outcome of the simulations and observations of the universe at very large scales. However, the pictures seem different at small scales as various discrepancies are observed, which are reported in Sec. 1.4.1. Introducing strong self-interaction between dark matter particles at low velocities provides a remarkable solution to these discrepancies, keeping the agreement on large scales intact. This has motivated various particle physics models that introduce self-interactions between dark matter particles.

In order to explain the nature of dark matter, various models and explanations have been proposed, and the most prominent ones assume it to be composed of particles, just like visible matter, but beyond the Standard Model (SM) of particle physics. The interaction of these particles with the SM particles has been used as the primary probe to hunt for the elusive stuff. The main efforts have gone into three principle approaches, namely its production in the particle accelerators using the collisions between the SM particles (production), astrophysical observation of the possible SM particles that result from the

annihilation of dark matter particles (indirect detection), and studying the signatures of their scattering with the SM particles in the earthbound detectors (direct detection). However, no confirmed signal has yet been observed via any of these approaches. In the absence of a signal, the sensitivity of an experiment is defined using the exclusion limits on the interaction cross-section of the dark matter particles with the Standard Model that the experiment can draw. These various efforts have been described in Chapter 2, focusing mainly on direct detection experiments.

CRESST stands as one of the most sensitive direct detection experiments in the sub-GeV dark matter mass regime and can achieve this by employing scintillating calorimeters operated at cryogenic temperatures. The third stage of CRESST, called CRESST-III, employs small targets with a mass of around 25 g and has reached the detection threshold of $\mathcal{O}(10)$ eV. The details of the expected dark matter signature, detector shielding, detector concept, and data acquisition in CRESST-III are discussed in detail in Chapter 3 and the data analysis chain applied to clean the data of any artifacts, calibrate it and extract the dark matter results have been described in Chapter 4.

In the first run of the CRESST-III, known as phase one, an almost exponential unknown background of events was seen at recoil energies below around 200 eV in various detectors. This excess background is called as the Low Energy Excess (LEE). This background limits the experiment's sensitivity to probe even lower mass dark matter particles and interaction cross-sections. A few hypotheses were put in place in order to explain the origin of this excess, which are explained in Sec. 5.1. In the latest run of CRESST, known as *Run36*, modifications were made in order to study these hypotheses, and all the various results obtained in this run are described in Chapter 5.

It was observed that the LEE was present in all of the detector modules operated in this run with different strengths and spectral shapes. The observations excluded the origin of the LEE coming from any dark matter interaction, external or intrinsic radioactivity, noise triggers, and scintillation light. It could also be asserted that no considerable contribution to the excess comes from the holding structure's stress. During the run, it was also observed that the excess is decaying slowly over time with $\mathcal{O}(100)$ days decay time. In order to study the effect of increasing the temperature of the crystal on the LEE, various warm-ups of the cryostat were performed at 200 mK, 3.5 K, 11 K, 30 K, and 60 K. The rate of the LEE was seen to be increased in the 60 K warm-up for all of the detectors. After 30 K and 11 K warm-up, the rate increased in all but one detector module. This "recharged" rate is seen to decay relatively quickly with $\mathcal{O}(10)$ days decay time, and the rate goes back to the long decaying tail afterward. This strongly points towards the origin coming from the interface between the crystal and the TES film, as the relative difference between the expansion coefficients of the two are different for different crystals. In the upcoming run of CRESST, other modifications are being performed in order to further narrow down the possible origins of the excess and either mitigate or model it to increase the sensitivity of the experiment.

The *Run36* modules analyzed principally for this thesis were *Comm2* and *Li1*, and various results were also obtained with both of these modules. With *Comm2*, a new

way of calibrating nuclear recoil events at very low energies was observed with a peak originating upon a radiative capture of a thermal neutron on the ^{182}W nucleus, using an AmBe neutron source. The peak is seen upon deexcitation of a single photon at around 110 eV. This process was first observed by the NUCLEUS-CRAB collaborations [171] and now was also confirmed in CRESST using various $CaWO_4$ crystals [174]. The same process was also observed for the radiative capture on ^{27}Al with the sapphire module of the same run [165]. With the *Li1* module, the exclusion limits on spin-dependent dark matter-nucleus scattering cross-sections were extracted for both *proton-only* interactions with ^{6}Li, ^{7}Li and ^{27}Al and *neutron-only* interactions with ^{6}Li and ^{27}Al. With the detection threshold of 88.9 eV, sensitivity was increased down to dark matter masses of 0.16 MeV/c^2, increasing the sensitivity by up to three orders of magnitude compared to the above-ground results using the same detector material. The results exhibit the best sensitivity in the 0.25-2.5 GeV/c^2 dark matter mass range for the *proton-only* and in the 0.16-1.5 GeV/c^2 dark matter mass range for the *neutron-only* interactions.

Lastly, Chapter 6 focuses on studying the dark matter particles in the universal bound states suggested by Laha and Brateen [65] with CRESST-III. As has already been discussed, self-interactions between dark matter particles at non-relativistic velocities are required to explain the observations of small-scale structures. Assuming there is an energy region where the self-interaction cross-section between the dark matter particles comes close to saturating the S-wave unitarity bound, the low-energy scattering properties are dependent solely on the large scattering length, including the self-interacting scattering cross-section $\sigma_{\chi-\chi}$. This assumption needs the existence of an S-wave resonance very close to the scattering threshold. If the resonance is just below the scattering threshold, the scattering can result in forming a bound state called the Darkonium. The presence of these bound states results in a different recoil energy spectrum than the standard case, where the spectral shape is determined by the inverse scattering length γ. Thus, estimating γ from direct detection experiments allows us to study the $\sigma_{\chi-\chi}$ in the given model. As no positive signal is observed in CRESST, the exclusion limits are drawn on the value of γ based on the collected data. The calculation has been performed for four different dark matter masses of 0.5, 1.0, 10.0, and 100.0 GeV/c^2, and for each mass, the exclusion limits are drawn on γ for varying darkonium-nucleus scattering cross-sections. The exclusion limits on γ are then subsequently converted to exclusion limits on $\sigma_{\chi-\chi}/m_\chi$, which also depends on the relative momentum between the dark matter particles. This procedure allows us to compare the drawn exclusion limits with the constraints on different astrophysical scales. The results show that there exists an upper limit to the $\sigma_{\chi-\chi}/m_\chi$ that can be probed for each mass. The results also show that for very heavy masses, the required $\sigma_{\chi-\chi}/m_\chi$ cannot form bound states at the small-scale velocities. For low-mass particles, the $\sigma_{\chi-\chi}/m_\chi$ required to solve the small-scale problem is completely excluded with the current darkonium-nucleus scattering cross-section that can be probed. However, with increased sensitivity in the future, lower darkonium-nucleus scattering cross-sections can be probed for studying the self-interactions.

APPENDIX A

Spin-Independent Dark Matter Results

The results obtained with the *Run36* of CRESST-III have already been described in Chapter 5. As it was already discussed several times in this thesis, the aim of this run was to understand the origin of the LEE and study its nature. This was done as LEE forms an irreducible background and restricts the sensitivity of the experiment to probe lower dark matter-nucleus scattering cross-sections. Along with the studies performed on the LEE and the spin-dependent dark matter results with $LiAlO_2$, standard spin-independent results were also obtained. Here, the spin-independent results obtained in this run are described along with the comparison of the exclusion limits extracted with two different LEE levels to illustrate its impact on the results.

A.1 Results with Silicon Wafer Module

The *Si2* module consisted of two Silicon crystals. One of them was the bulk crystal having the standard dimensions of $(20 \times 20 \times 10)$ mm^3, whereas the other crystal was the wafer module having the dimensions of a typical CRESST-III light detector of $(20 \times 20 \times 0.4)$ mm^3. The analysis was performed on the wafer module due to its better performance compared to the bulk one, and the results were published in [126]. The detector module had a mass of 0.35 g. The dark matter dataset was collected between November 2020 to August 2021, with 157.3 days of the active measuring time of the blind dataset. This amounts to a total exposure of 55.06 g-days. With the similar methodology described in Chapter 4, a threshold value extracted from the stream simulation was $E_{\text{thr}} = (10.0 \pm 0.2)$ eV with the baseline resolution of $\sigma_{\text{BL}} = (1.36 \pm 0.05)$ eV. This is already a large improvement compared to the previous CRESST detector threshold and resolution of 30.1 eV and 4.6 eV, respectively. The spectrum obtained after applying the analysis cuts described in Sec. 4.3 is shown in Fig. A.1. On top of the standard analysis

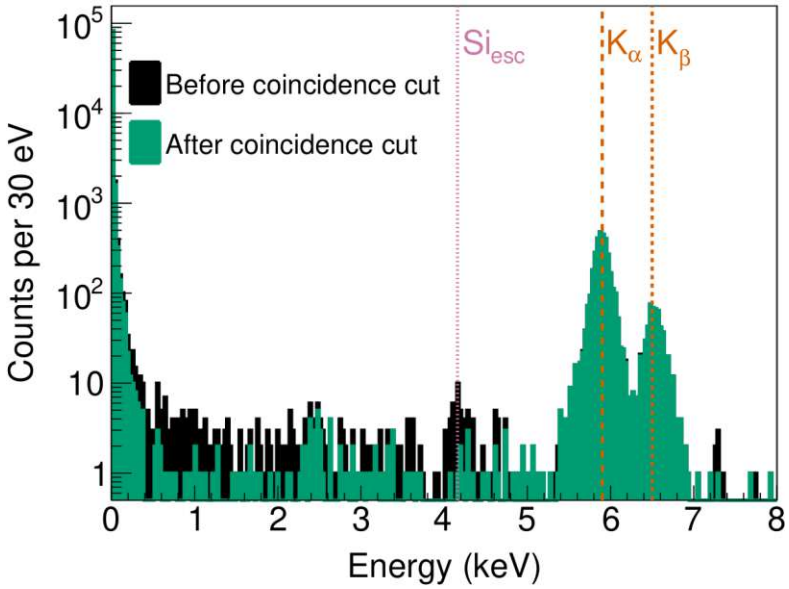

Figure A.1: The recoil spectrum obtained with the Si wafer module with 55.06 g-days of exposure. The histogram shown in black is all the events surviving the standard analysis cuts, and the histogram in green shows the events after applying the coincidence cut with the bulk module. The iron peaks used for calibration are shown with the orange dashed line, and the silicon escape peak from the K_α X-ray at 4.16 keV is shown with dotted pink line [126].

cuts used to clean the data, another cut was applied to remove the events that were in coincidence between the wafer and the bulk module. This is done as the extremely rare dark matter event is not expected to simultaneously have multiple scatters in both modules.

As the linear range of the detector is below 300 eV, larger pulses get saturated, and the amplitude estimation is done using a truncated fit. Since the saturated pulses beyond the linear range cannot to simulated on the stream, the survival probability calculation beyond this range becomes difficult. Thus, the energy region of interest for the dark matter results was taken from the threshold of 10.0 eV to the maximum of the linear range of 300 eV.

The standard halo model was used to calculate the exclusion limits using the same parameters as were used in obtaining the results with the $LiAlO_2$ modules (Sec. 5.4). As the crystal is non-scintillating, the electromagnetic background cannot be identified, and all the events in the region of interest are taken as potential dark matter candidates, including the events in the LEE.

The 90% confidence level exclusion limits are calculated using Yellin's optimum interval method [153, 154] and are shown in Fig. A.2. The exclusion limits are calculated for the dark matter masses between 0.115 GeV/c^2 and 0.5 GeV/c^2, thus allowing to probe the lowest dark matter mass that CRESST can measure. This measurement improves on

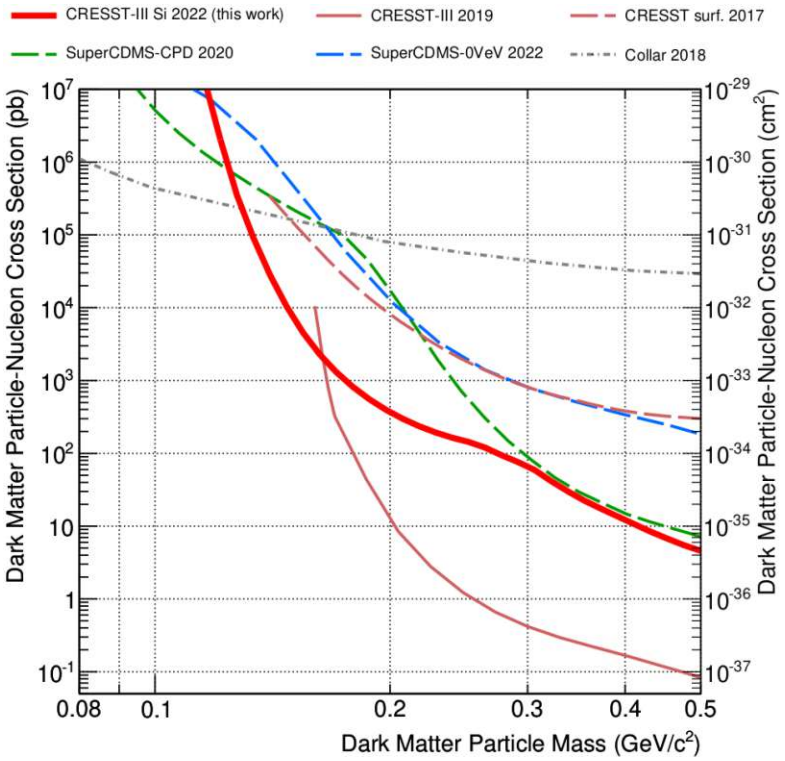

Figure A.2: The 90% C.L. spin-independent dark matter-nucleus scattering cross-section exclusion limits obtained with Si wafer module in the *Run36* of CRESST-III. The exclusion limits are compared with the ones from previous CRESST measurements and other experiments in a similar parameter space. The image is taken from Ref. [126].

the existing exclusion limits between 0.13 GeV/c^2 and 0.165 GeV/c^2. An improvement factor of 20 is seen in this range compared to the previous exclusion limits. Due to the presence of the LEE and the inability to distinguish electromagnetic background, the limits get worse for lower masses.

A.2 Comparison of the Limits with Lower Excess

It was described in Sec. 5.2.2 that the rate of the LEE decreases with time with two decaying constants. The long component decays with a decay time of $\mathcal{O}(100)$ days, while the short one is seen only after warming up the detector, with a decay time of $\mathcal{O}(10)$ days. Thus, after a very long measuring time, when the detector has significantly reduced LEE, exclusion limits can be calculated again, and results can be improved. In order to illustrate the impact of a lower LEE rate on the dark matter exclusion limits, the blind analysis is performed on the data taken after the 11 K warm-up (red in Fig. A.3) and the results are compared with the one from the *bck* data (black in Fig. A.3) for the *Comm2* module.

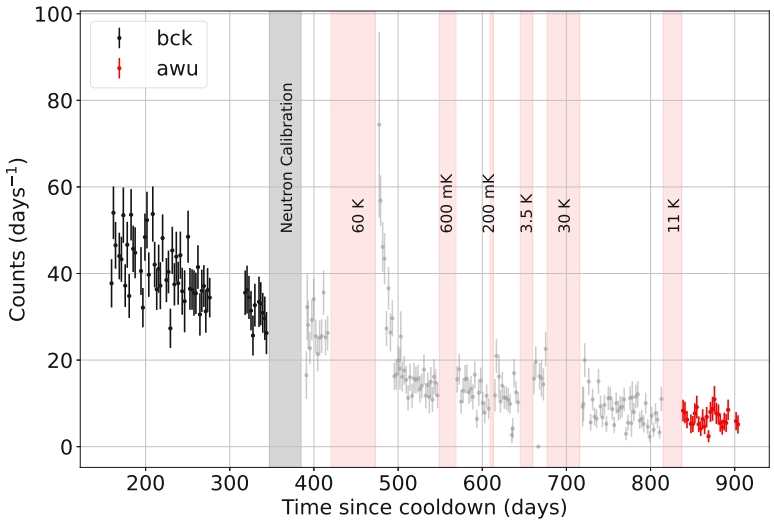

Figure A.3: The evolution of the LEE rate for the *Comm2* module including the periods of various warm ups. The *bck* data is shown in black, the blind *awu* data is shown in red, and the rest of the data points are shown in grey.

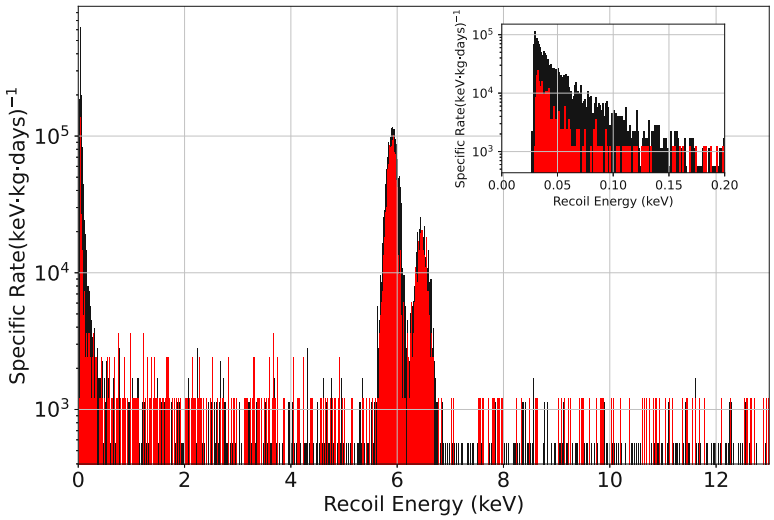

Figure A.4: The recoil energy spectrum of *Comm2* module for *bck* data (black) and *awu* blind data (red) taken after the 11 K warm up. both the spectra are corrected for the exposure and cut efficiency. The inset plot shows the same plot in the low-energy region close to the threshold.

The analysis cuts applied to both datasets are already discussed in Sec. 5.2.1. The detection threshold for both the periods remained similar at $E_{\text{thr}} = (29.0 \pm 0.7)$ eV with a resolution of $\sigma_{\text{BL}} = (4.5 \pm 0.3)$ eV. The spectra of both periods are compared in Fig. A.4. The active measuring time for the *bck* and *awu* data is 2757 hours and 1130 hours, respectively. Given the mass of the detector module of 24.5 g, this amounts to an

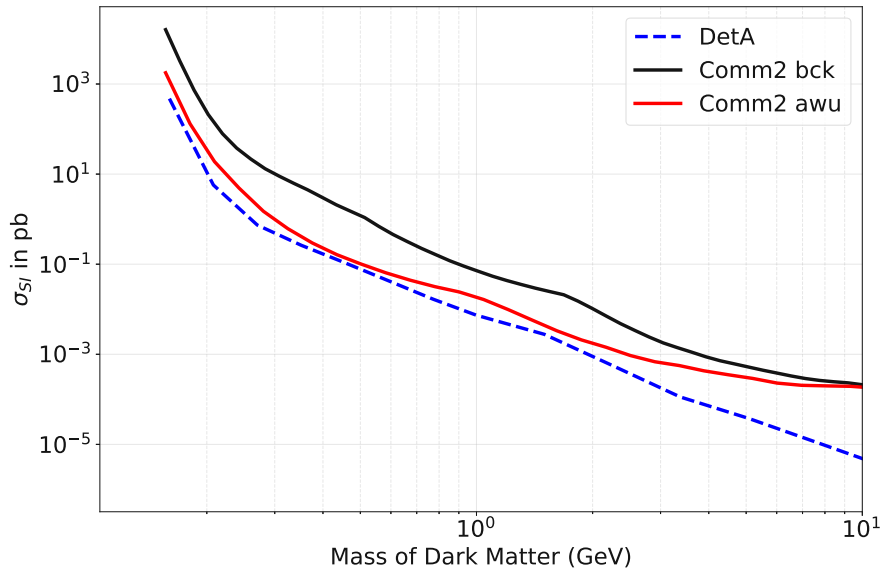

Figure A.5: The 90% confidence level exclusion limits for the spin-independent dark matter-nucleus scattering cross-section with the *Comm2* detector module. The exclusion limits for the *bck* data are shown in black, and for the *awu* data are shown in red. The limits from *DetA* [89] are also shown shown for comparison.

exposure of 2.81 kg-days and 1.15 kg-days. It can be clearly seen that the LEE in the *awu* spectrum is significantly reduced compared to the *bck* data, as one would expect looking at the evolution of LEE. A small reduction of the events in the iron peaks is also seen. This is expected given the decay time of the ^{55}Fe electron capture is 2.737 years [200].

Given the detection threshold and allowing for $2\sigma_{\mathrm{BL}}$ fluctuation, the lowest probable dark matter mass remains similar to the one achievable with *DetA*. The band fit is performed, and the upper boundary of the acceptance region is chosen to be 50% of the oxygen band, and the lower boundary is taken to be the lower 99.5% tungsten band. The energy region of interest is taken to be all the events below 8 keV as the detector exhibits a saturation effect beyond this energy range. The 90% confidence level exclusion limits are calculated using Yellin's optimum interval method [153, 154] and are shown in Fig. A.5. It can be seen that in the low mass regime, almost an order of magnitude improvement in the exclusion limits is seen with the reduced LEE in the *awu* data in spite of having lower exposure compared to the *bck* data. The *awu* limits become almost equal to the best limits obtained in the given mass region with *DetA* in spite of having almost 5 times lower exposure. The limits start becoming worse for heavier masses, where the larger exposure of the other two starts having a significant impact. Therefore, it can be confidently said that reducing the excess even further would allow us to probe even lower cross-sections, which is the aim of the CRESST experiment in the upcoming years.

Bibliography

[1] A. Secchi. *L'Astronomia in Roma nel pontificato di Pio IX: memoria*. Tipografia della Pace, 1877.

[2] Gianfranco Bertone and Dan Hooper. „History of dark matter". In: *Rev. Mod. Phys.* 90 (4 2018), p. 045002. DOI: 10.1103/RevModPhys.90.045002.

[3] William Thomson Baron Kelvin. *Baltimore Lectures on Molecular Dynamics and the Wave Theory of Light*. Cambridge Library Collection - Physical Sciences. Cambridge University Press, 2010. DOI: 10.1017/CBO9780511694523.

[4] Fritz Zwicky. „Die rotverschiebung von extragalaktischen nebeln". In: *Helvetica Physica Acta, Vol. 6, p. 110-127* 6 (1933), pp. 110–127.

[5] F. Zwicky. „On the Masses of Nebulae and of Clusters of Nebulae". In: *The Astrophysical Journal* 86 (1937), p. 217. DOI: 10.1086/143864.

[6] M. Schwarzschild. „Mass distribution and mass-luminosity ratio in galaxies". In: *The Astronomical Journal* 59 (1954), p. 273. DOI: 10.1086/107013.

[7] Vera C. Rubin and W. Kent Ford Jr. „Rotation of the Andromeda Nebula from a Spectroscopic Survey of Emission Regions". In: *Astrophys. J.* 159 (1970), pp. 379–403. DOI: 10.1086/150317.

[8] Vera C. Rubin, W. Kent Ford Jr., and Norbert Thonnard. „Extended rotation curves of high-luminosity spiral galaxies. IV. Systematic dynamical properties, Sa through Sc". In: *Astrophys. J. Lett.* 225 (1978), pp. L107–L111. DOI: 10.1086/182804.

[9] V. C. Rubin, N. Thonnard, and W. K. Ford Jr. „Rotational properties of 21 SC galaxies with a large range of luminosities and radii, from NGC 4605 R = 4kpc to UGC 2885 R = 122 kpc". In: *Astrophys. J.* 238 (1980), p. 471. DOI: 10.1086/158003.

[10] Edvige Corbelli and Paolo Salucci. „The extended rotation curve and the dark matter halo of M33". In: *Monthly Notices of the Royal Astronomical Society* 311.2 (Jan. 2000), pp. 441–447. DOI: 10.1046/j.1365-8711.2000.03075.x. eprint: https://academic.oup.com/mnras/article-pdf/311/2/441/2881340/311-2-441.pdf.

[11] *Wikipaedia: Galaxy rotation curve*. https://commons.wikimedia.org/wiki/File:Rotation_curve_of_spiral_galaxy_Messier_33_(Triangulum).png. (visited in May 2023). 2023.

[12] A. A. Penzias and R. W. Wilson. „A Measurement of Excess Antenna Temperature at 4080 Mc/s.“ In: *The Astrophysical Journal* 142 (July 1965), pp. 419–421. DOI: 10.1086/148307.

[13] J.C. Mather, E. S. Cheng, Jr. Eplee R. E., et al. „A Preliminary Measurement of the Cosmic Microwave Background Spectrum by the Cosmic Background Explorer (COBE) Satellite“. In: *The Astrophysical Journal Letters* 354 (May 1990), p. L37. DOI: 10.1086/185717.

[14] *The european space agency: Planck CMB*. https://www.esa.int/ESA_Multimedia/Images/2013/03/Planck_CMB. (visited in May 2023). 2013.

[15] Planck Collaboration, Ade, P. A. R., Aghanim, N., et al. „Planck 2013 results. XVI. Cosmological parameters“. In: *A&A* 571 (2014), A16. DOI: 10.1051/0004-6361/201321591.

[16] Planck Collaboration, Aghanim, N., Akrami, Y., et al. „Planck 2018 results - VI. Cosmological parameters“. In: *A&A* 641 (2020), A6. DOI: 10.1051/0004-6361/201833910.

[17] Philippe Brax. „What makes the Universe accelerate? A review on what dark energy could be and how to test it“. In: *Reports on Progress in Physics* 81.1 (2017), p. 016902. DOI: 10.1088/1361-6633/aa8e64.

[18] Douglas Clowe, Maruša Bradač, Anthony H. Gonzalez, et al. „A Direct Empirical Proof of the Existence of Dark Matter*“. In: *The Astrophysical Journal* 648.2 (Aug. 2006), p. L109. DOI: 10.1086/508162.

[19] Scott W. Randall, Maxim Markevitch, Douglas Clowe, et al. „Constraints on the Self-Interaction Cross Section of Dark Matter from Numerical Simulations of the Merging Galaxy Cluster 1E 0657–56“. In: *The Astrophysical Journal* 679.2 (2008), p. 1173. DOI: 10.1086/587859.

[20] Edwin Hubble. „A Relation between Distance and Radial Velocity among Extra-Galactic Nebulae“. In: *Proceedings of the National Academy of Science* 15.3 (Mar. 1929), pp. 168–173. DOI: 10.1073/pnas.15.3.168.

[21] T. Lasserre and EROS Collaboration. *Not enough stellar Mass Machos in the Galactic Halo*. 2000. arXiv: astro-ph/0002253 [astro-ph].

[22] Pablo Villanueva-Domingo, Olga Mena, and Sergio Palomares-Ruiz. „A Brief Review on Primordial Black Holes as Dark Matter“. In: *Frontiers in Astronomy and Space Sciences* 8 (2021). DOI: 10.3389/fspas.2021.681084.

[23] M. Milgrom. „A modification of the Newtonian dynamics as a possible alternative to the hidden mass hypothesis.“ In: *The Astrophysical Journal* 270 (July 1983), pp. 365–370. DOI: 10.1086/161130.

[24] Jacob D. Bekenstein. „Relativistic gravitation theory for the modified Newtonian dynamics paradigm“. In: *Phys. Rev. D* 70 (8 Oct. 2004), p. 083509. DOI: 10.1103/PhysRevD.70.083509.

[25] S. D. M. White, C. S. Frenk, and M. Davis. „Clustering in a neutrino-dominated universe“. In: *The Astrophysical Journal* 274 (Nov. 1983), pp. L1–L5. DOI: 10.1086/184139.

[26] M. Davis, J. Huchra, D. W. Latham, et al. „A survey of galaxy redshifts. II. The large scale space distribution.“ In: *The Astrophysical Journal* 253 (Feb. 1982), pp. 423–445. DOI: 10.1086/159646.

[27] C. A. Baker, D. D. Doyle, P. Geltenbort, et al. „Improved Experimental Limit on the Electric Dipole Moment of the Neutron“. In: *Phys. Rev. Lett.* 97 (13 Sept. 2006), p. 131801. DOI: 10.1103/PhysRevLett.97.131801.

[28] R. D. Peccei and Helen R. Quinn. „CP Conservation in the Presence of Pseudoparticles“. In: *Phys. Rev. Lett.* 38 (25 June 1977), pp. 1440–1443. DOI: 10.1103/PhysRevLett.38.1440.

[29] R. D. Peccei and Helen R. Quinn. „Constraints imposed by CP conservation in the presence of pseudoparticles“. In: *Phys. Rev. D* 16 (6 Sept. 1977), pp. 1791–1797. DOI: 10.1103/PhysRevD.16.1791.

[30] N. Du, N. Force, R. Khatiwada, et al. „Search for Invisible Axion Dark Matter with the Axion Dark Matter Experiment“. In: *Phys. Rev. Lett.* 120 (15 Apr. 2018), p. 151301. DOI: 10.1103/PhysRevLett.120.151301.

[31] V. Anastassopoulos et al. „New CAST limit on the axion–photon interaction“. In: *Nature Physics* 13.6 (2017), pp. 584–590. DOI: 10.1038/nphys4109.

[32] Kalliopi Petraki and Raymond R. Volkas. „Reviw of Asymmteric Dark Matter“. In: *International Journal of Modern Physics A* 28.19 (2013), p. 1330028. DOI: 10.1142/S0217751X13300287.

[33] Jonathan L. Feng. „Dark Matter Candidates from Particle Physics and Methods of Detection“. In: *Annual Review of Astronomy and Astrophysics* 48.1 (2010), pp. 495–545. DOI: 10.1146/annurev-astro-082708-101659. eprint: https://doi.org/10.1146/annurev-astro-082708-101659.

[34] Benjamin W. Lee and Steven Weinberg. „Cosmological Lower Bound on Heavy-Neutrino Masses“. In: *Phys. Rev. Lett.* 39 (4 1977), pp. 165–168. DOI: 10.1103/PhysRevLett.39.165.

[35] Max Tegmark, Michael R. Blanton, Michael A. Strauss, et al. „The Three-Dimensional Power Spectrum of Galaxies from the Sloan Digital Sky Survey“. In: *The Astrophysical Journal* 606.2 (2004), p. 702. DOI: 10.1086/382125.

[36] Max Tegmark, Michael A. Strauss, Michael R. Blanton, et al. „Cosmological parameters from SDSS and WMAP“. In: *Phys. Rev. D* 69 (10 2004), p. 103501. DOI: 10.1103/PhysRevD.69.103501.

[37] Julio F. Navarro, Carlos S. Frenk, and Simon D. M. White. „The Structure of Cold Dark Matter Halos“. In: *the Astrophysical Journal* 462 (May 1996), p. 563. DOI: 10.1086/177173. arXiv: astro-ph/9508025 [astro-ph].

[38] John Dubinski and R. G. Carlberg. „The Structure of Cold Dark Matter Halos“. In: *The Astrophysical Journal* 378 (1991), p. 496. DOI: 10.1086/170451.

[39] Ben Moore. „Evidence against dissipation-less dark matter from observations of galaxy haloes“. In: *Nature* 370.6491 (Aug. 1994), pp. 629–631. DOI: 10.1038/370629a0.

[40] Se-Heon Oh, Deidre A. Hunter, Elias Brinks, et al. „High-resolution Mass Model of Dwarf Galaxies from LITTLE THINGS“. In: *The Astronomical Journal* 149.6 (2015), p. 180. DOI: 10.1088/0004-6256/149/6/180.

[41] Sean Tulin and Hai-Bo Yu. „Dark matter self-interactions and small scale structure“. In: *Physics Reports* 730 (2018), pp. 1–57. DOI: https://doi.org/10.1016/j.physrep.2017.11.004.

[42] Ben Moore, Sebastiano Ghigna, Fabio Governato, et al. „Dark Matter Substructure within Galactic Halos“. In: *The Astrophysical Journal* 524.1 (1999), p. L19. DOI: 10.1086/312287.

[43] Alyson M. Brooks, Michael Kuhlen, Adi Zolotov, et al. „A Baryonic Solution to the Missing Satellites Problem“. In: *The Astrophysical Journal* 765.1 (2013), p. 22. DOI: 10.1088/0004-637X/765/1/22.

[44] Andrew R. Wetzel, Philip F. Hopkins, Ji hoon Kim, et al. „Reconciling Dwarf Galaxies with LCDM Cosmology: Simulating a Realistic Population of Satellites around a Milky Way–Mass Galaxy“. In: *The Astrophysical Journal Letters* 827.2 (2016), p. L23. DOI: 10.3847/2041-8205/827/2/L23.

[45] Stacy Y. Kim, Annika H. G. Peter, and Jonathan R. Hargis. „Missing Satellites Problem: Completeness Corrections to the Number of Satellite Galaxies in the Milky Way are Consistent with Cold Dark Matter Predictions“. In: *Phys. Rev. Lett.* 121 (21 2018), p. 211302. DOI: 10.1103/PhysRevLett.121.211302.

[46] Anatoly Klypin, Andrey V. Kravtsov, Octavio Valenzuela, et al. „Where Are the Missing Galactic Satellites?“ In: *The Astrophysical Journal* 522.1 (1999), p. 82. DOI: 10.1086/307643.

[47] Michael Boylan-Kolchin, James S. Bullock, and Manoj Kaplinghat. „The Milky Way's bright satellites as an apparent failure of LCDM“. In: *Monthly Notices of the Royal Astronomical Society* 422.2 (2012), pp. 1203–1218. DOI: 10.1111/j.1365-2966.2012.20695.x.

[48] F. Governato, C. Brook, L. Mayer, et al. „Bulgeless dwarf galaxies and dark matter cores from supernova-driven outflows“. In: *Nature* 463.7278 (2010), pp. 203–206. DOI: 10.1038/nature08640. eprint: 0911.2237.

[49] Se-Heon Oh, Chris Brook, Fabio Governato, et al. „The Central Slope of Dark Matter Cores in Dwarf Galaxies: Simulations versus THINGS“. In: *The Astronomical Journal* 142.1 (2011), p. 24. DOI: 10.1088/0004-6256/142/1/24.

[50] Arianna Di Cintio, Chris B. Brook, Andrea V. Macciò, et al. „The dependence of dark matter profiles on the stellar-to-halo mass ratio: a prediction for cusps versus cores“. In: *Monthly Notices of the Royal Astronomical Society* 437.1 (2013), pp. 415–423. DOI: 10.1093/mnras/stt1891.

[51] Till Sawala, Carlos S. Frenk, Azadeh Fattahi, et al. „The APOSTLE simulations: solutions to the Local Group's cosmic puzzles“. In: *Monthly Notices of the Royal Astronomical Society* 457.2 (2016), pp. 1931–1943. DOI: 10.1093/mnras/stw145.

[52] Papastergis, E. and Shankar, F. „An assessment of the "too big to fail" problem for field dwarf galaxies in view of baryonic feedback effects“. In: *Astronomy & Astrophysics* 591 (2016), A58. DOI: 10.1051/0004-6361/201527854.

[53] Kyle A. Oman, Julio F. Navarro, Azadeh Fattahi, et al. „The unexpected diversity of dwarf galaxy rotation curves“. In: *Monthly Notices of the Royal Astronomical Society* 452.4 (2015), pp. 3650–3665. DOI: 10.1093/mnras/stv1504.

[54] Pedro Colín, Vladimir Avila-Reese, Octavio Valenzuela, et al. „Structure and Subhalo Population of Halos in a Self-interacting Dark Matter Cosmology“. In: *The Astrophysical Journal* 581.2 (2002), p. 777. DOI: 10.1086/344259.

[55] Oliver D. Elbert, James S. Bullock, Shea Garrison-Kimmel, et al. „Core formation in dwarf haloes with self-interacting dark matter: no fine-tuning necessary“. In: *Monthly Notices of the Royal Astronomical Society* 453.1 (2015), pp. 29–37. DOI: 10.1093/mnras/stv1470.

[56] Mark Vogelsberger, Jesus Zavala, and Abraham Loeb. „Subhaloes in self-interacting galactic dark matter haloes“. In: *Monthly Notices of the Royal Astronomical Society* 423.4 (2012), pp. 3740–3752. DOI: 10.1111/j.1365-2966.2012.21182.x.

[57] Felipe Menanteau, John P. Hughes, Cristóbal Sifón, et al. „The Atacama Cosmology Telescope: ACT CL J0102 4915 'El Gordo', a Massive Merging Cluster at Redshift 0.87“. In: *The Astrophysical Journal* 748.1 (2012), p. 7. DOI: 10.1088/0004-637X/748/1/7.

[58] J. Merten, D. Coe, R. Dupke, et al. „Creation of cosmic structure in the complex galaxy cluster merger Abell 2744“. In: *Monthly Notices of the Royal Astronomical Society* 417.1 (2011), pp. 333–347. DOI: 10.1111/j.1365-2966.2011.19266.x.

[59] Liliya L. R. Williams and Prasenjit Saha. „Light mass offsets in the lensing cluster Abell 3827: evidence for collisional dark matter?“ In: *Monthly Notices of the Royal Astronomical Society* 415.1 (2011), pp. 448–460. DOI: 10.1111/j.1365-2966.2011.18716.x.

[60] M. C. Bento, O. Bertolami, R. Rosenfeld, et al. „Self-interacting dark matter and the Higgs boson“. In: *Phys. Rev. D* 62 (4 2000), p. 041302. DOI: 10.1103/PhysRevD.62.041302.

[61] John McDonald. „Thermally Generated Gauge Singlet Scalars as Self-Interacting Dark Matter“. In: *Phys. Rev. Lett.* 88 (9 2002), p. 091304. DOI: 10.1103/PhysRevLett.88.091304.

[62] Jonathan L. Feng, Manoj Kaplinghat, and Hai-Bo Yu. „Halo-Shape and Relic-Density Exclusions of Sommerfeld-Enhanced Dark Matter Explanations of Cosmic Ray Excesses“. In: *Phys. Rev. Lett.* 104 (15 2010), p. 151301. DOI: 10.1103/PhysRevLett.104.151301.

[63] Sean Tulin, Hai-Bo Yu, and Kathryn M. Zurek. „Beyond collisionless dark matter: Particle physics dynamics for dark matter halo structure“. In: *Phys. Rev. D* 87 (11 2013), p. 115007. DOI: 10.1103/PhysRevD.87.115007.

[64] Eric Braaten and H.-W. Hammer. „Universal two-body physics in dark matter near an S-wave resonance“. In: *Phys. Rev. D* 88 (6 2013), p. 063511. DOI: 10.1103/PhysRevD.88.063511.

[65] Ranjan Laha and Eric Braaten. „Direct detection of dark matter in universal bound states“. In: *Phys. Rev. D* 89 (10 2014), p. 103510. DOI: 10.1103/PhysRevD.89.103510.

[66] Timon Emken. *Dark Matter in the Earth and the Sun – Simulating Underground Scatterings for the Direct Detection of Low-Mass Dark Matter*. 2019. arXiv: 1906.07541 [hep-ph].

[67] Oliver Buchmueller, Caterina Doglioni, and Lian-Tao Wang. „Search for dark matter at colliders“. In: *Nature Physics* 13.3 (2017), pp. 217–223. DOI: 10.1038/nphys4054. eprint: 1912.12739 (hep-ex).

[68] Aram Hayrapetyan et al. „Search for inelastic dark matter in events with two displaced muons and missing transverse momentum in proton-proton collisions at $\sqrt{s} = 13$ TeV“. In: (2023). arXiv: 2305.11649 [hep-ex].

[69] *Dark matter summary plots for s-channel, 2HDM+a, Higgs portal and Dark Higgs models*. Tech. rep. Geneva: CERN, 2023.

[70] V.A. Acciari, S. Ansoldi, L.A. Antonelli, et al. „Combined searches for dark matter in dwarf spheroidal galaxies observed with the MAGIC telescopes, including new data from Coma Berenices and Draco“. In: *Physics of the Dark Universe* 35 (2022), p. 100912. DOI: https://doi.org/10.1016/j.dark.2021.100912.

[71] M. Ackermann, M. Ajello, A. Albert, et al. „The Fermi Galactic Center GeV Excess and Implications for Dark Matter“. In: *The Astrophysical Journal* 840.1 (2017), p. 43. DOI: 10.3847/1538-4357/aa6cab.

[72] Anuj Gautam, Roland M. Crocker, Lilia Ferrario, et al. „Millisecond pulsars from accretion-induced collapse as the origin of the Galactic Centre gamma-ray excess signal“. In: *Nature Astron.* 6.6 (2022), pp. 703–707. DOI: 10.1038/s41550-022-01658-3.

[73] III Johnson W. N., Jr. Harnden F. R., and R. C. Haymes. „The Spectrum of Low-Energy Gamma Radiation from the Galactic-Center Region.“ In: *The Astrophysical Journal* 172 (1972), p. L1. DOI: 10.1086/180878.

[74] Douglas P. Finkbeiner and Neal Weiner. „Exciting dark matter and the INTEGRAL/SPI 511 keV signal“. In: *Phys. Rev. D* 76 (8 2007), p. 083519. DOI: 10.1103/PhysRevD.76.083519.

[75] R. Abbasi, M. Ackermann, J. Adams, et al. „Search for GeV-scale dark matter annihilation in the Sun with IceCube DeepCore“. In: *Phys. Rev. D* 105 (6 2022), p. 062004. DOI: 10.1103/PhysRevD.105.062004.

[76] Jennifer M. Gaskins. „A review of indirect searches for particle dark matter“. In: *Contemporary Physics* 57.4 (2016), pp. 496–525. DOI: 10.1080/00107514.2016.1175160.

[77] Florian Reindl. „COSINUS: Direct dark matter search with cryogenic NaI detectors“. Talk at ICHEP. 2020.

[78] Julien Billard, Mark Boulay, Susana Cebrián, et al. „Direct detection of dark matter—APPEC committee report*“. In: *Reports on Progress in Physics* 85.5 (2022), p. 056201. DOI: 10.1088/1361-6633/ac5754.

[79] J Aalbers, S S AbdusSalam, K Abe, et al. „A next-generation liquid xenon observatory for dark matter and neutrino physics“. In: *Journal of Physics G: Nuclear and Particle Physics* 50.1 (2022), p. 013001. DOI: 10.1088/1361-6471/ac841a.

[80] E. Aprile, K. Abe, F. Agostini, et al. „First Dark Matter Search with Nuclear Recoils from the XENONnT Experiment“. In: *Phys. Rev. Lett.* 131 (4 2023), p. 041003. DOI: 10.1103/PhysRevLett.131.041003.

[81] J. Aalbers, D. S. Akerib, C. W. Akerlof, et al. „First Dark Matter Search Results from the LUX-ZEPLIN (LZ) Experiment“. In: *Phys. Rev. Lett.* 131 (4 2023), p. 041002. DOI: 10.1103/PhysRevLett.131.041002.

[82] Yue Meng, Zhou Wang, Yi Tao, et al. „Dark Matter Search Results from the PandaX-4T Commissioning Run“. In: *Phys. Rev. Lett.* 127 (26 2021), p. 261802. DOI: 10.1103/PhysRevLett.127.261802.

[83] P. Agnes, I. F. M. Albuquerque, T. Alexander, et al. „Low-Mass Dark Matter Search with the DarkSide-50 Experiment“. In: *Phys. Rev. Lett.* 121 (8 2018), p. 081307. DOI: 10.1103/PhysRevLett.121.081307.

[84] P.-A. Amaudruz, M. Baldwin, M. Batygov, et al. „First Results from the DEAP-3600 Dark Matter Search with Argon at SNOLAB“. In: *Phys. Rev. Lett.* 121 (7 2018), p. 071801. DOI: 10.1103/PhysRevLett.121.071801.

[85] F Aubin, M Auger, M-H Genest, et al. „Discrimination of nuclear recoils from alpha particles with superheated liquids“. In: *New Journal of Physics* 10.10 (2008), p. 103017. DOI: 10.1088/1367-2630/10/10/103017.

[86] C. Amole, M. Ardid, I. J. Arnquist, et al. „Dark matter search results from the complete exposure of the PICO-60 C_3F_8 bubble chamber“. In: *Phys. Rev. D* 100 (2 2019), p. 022001. DOI: 10.1103/PhysRevD.100.022001.

[87] Q. Arnaud, E. Armengaud, C. Augier, et al. „First Germanium-Based Constraints on Sub-MeV Dark Matter with the EDELWEISS Experiment“. In: *Phys. Rev. Lett.* 125 (14 2020), p. 141301. DOI: 10.1103/PhysRevLett.125.141301.

[88] R. Agnese, A. J. Anderson, T. Aralis, et al. „Low-mass dark matter search with CDMSlite“. In: *Phys. Rev. D* 97 (2 2018), p. 022002. DOI: 10.1103/PhysRevD.97.022002.

[89] A. H. Abdelhameed, G. Angloher, P. Bauer, et al. „First results from the CRESST-III low-mass dark matter program“. In: *Phys. Rev. D* 100 (10 2019), p. 102002. DOI: 10.1103/PhysRevD.100.102002.

[90] G. Angloher, P. Carniti, L. Cassina, et al. „Results from the first cryogenic NaI detector for the COSINUS project“. In: *Journal of Instrumentation* 12.11 (2017), P11007. DOI: 10.1088/1748-0221/12/11/P11007.

[91] R. Bernabei, P. Belli, A. Bussolotti, et al. „Further results from DAMA/LIBRA-phase2 and perspectives“. In: *Nuclear Physics and Atomic Energy* 22.4 (2021), pp. 329–342. DOI: 10.15407/jnpae2021.04.329.

[92] C. Savage, G. Gelmini, P. Gondolo, et al. „Compatibility of DAMA/LIBRA dark matter detection with other searches“. In: *Journal of Cosmology and Astroparticle Physics* 2009.04 (2009), p. 010. DOI: 10.1088/1475-7516/2009/04/010.

[93] R. Bernabei, P. Belli, R. Cerulli, et al. „Search for WIMP annual modulation signature: results from DAMA/NaI-3 and DAMA/NaI-4 and the global combined analysis“. In: *Physics Letters B* 480.1 (2000), pp. 23–31. DOI: https://doi.org/10.1016/S0370-2693(00)00405-6.

[94] G. Adhikari, E. Barbosa de Souza, N. Carlin, et al. „Three-year annual modulation search with COSINE-100“. In: *Phys. Rev. D* 106 (5 2022), p. 052005. DOI: 10.1103/PhysRevD.106.052005.

[95] Gyunho Yu. „Dark matter search using NaI(Tl) at the COSINE-100 experiment“. In: *PoS* ICRC2023 (2023), p. 1421. DOI: 10.22323/1.444.1421.

[96] J. Amaré, S. Cebrián, D. Cintas, et al. „Annual modulation results from three-year exposure of ANAIS-112“. In: *Phys. Rev. D* 103 (10 2021), p. 102005. DOI: 10.1103/PhysRevD.103.102005.

[97] M. Antonello, E. Barberio, T. Baroncelli, et al. „The SABRE project and the SABRE Proof-of-Principle“. In: *The European Physical Journal C* 79.4 (2019). DOI: 10.1140/epjc/s10052-019-6860-y.

[98] Masahiro Ibe, Wakutaka Nakano, Yutaro Shoji, et al. „Migdal effect in dark matter direct detection experiments“. In: *Journal of High Energy Physics* 2018.3 (2018), p. 194. DOI: 10.1007/JHEP03(2018)194.

[99] Arkady B. Migdal. *Qualitative Methods in Quantum Theory*. Vol. 48. 1977.

[100] SuperCDMS. *Dark Matter Limit Plotter*. https://supercdms.slac.stanford.edu/dark-matter-limit-plotter. Plots created in September 2023. 2023.

[101] Q. Arnaud, D. Asner, J.-P. Bard, et al. „First results from the NEWS-G direct dark matter search experiment at the LSM“. In: *Astroparticle Physics* 97 (2018), pp. 54–62. DOI: https://doi.org/10.1016/j.astropartphys.2017.10.009.

[102] A. Aguilar-Arevalo, D. Amidei, D. Baxter, et al. „Results on Low-Mass Weakly Interacting Massive Particles from an 11 kg d Target Exposure of DAMIC at SNOLAB“. In: *Phys. Rev. Lett.* 125 (24 2020), p. 241803. DOI: 10.1103/PhysRevLett.125.241803.

[103] I. Alkhatib, D. W. P. Amaral, T. Aralis, et al. „Light Dark Matter Search with a High-Resolution Athermal Phonon Detector Operated above Ground“. In: *Phys. Rev. Lett.* 127 (6 2021), p. 061801. DOI: 10.1103/PhysRevLett.127.061801.

[104] Ciaran A. J. O'Hare. „New Definition of the Neutrino Floor for Direct Dark Matter Searches“. In: *Phys. Rev. Lett.* 127 (25 2021), p. 251802. DOI: 10.1103/PhysRevLett.127.251802.

[105] E. Aprile, J. Aalbers, F. Agostini, et al. „Dark Matter Search Results from a One Ton-Year Exposure of XENON1T“. In: *Phys. Rev. Lett.* 121 (11 2018), p. 111302. DOI: 10.1103/PhysRevLett.121.111302.

[106] E. Aprile, J. Aalbers, F. Agostini, et al. „Search for Coherent Elastic Scattering of Solar ^{8}B Neutrinos in the XENON1T Dark Matter Experiment“. In: *Phys. Rev. Lett.* 126 (9 2021), p. 091301. DOI: 10.1103/PhysRevLett.126.091301.

[107] D. Franco et al. „Light dark matter search with DarkSide-50“. In: *57th Rencontres de Moriond on Electroweak Interactions and Unified Theories*. 2023. arXiv: 2306.12151 [hep-ex].

[108] R. Bernabei et al. „First results from DAMA/LIBRA and the combined results with DAMA/NaI“. In: *Eur. Phys. J. C* 56 (2008), pp. 333–355. DOI: 10.1140/epjc/s10052-008-0662-y.

[109] Govinda Adhikari, Estella B. de Souza, Nelson Carlin, et al. „Strong constraints from COSINE-100 on the DAMA dark matter results using the same sodium iodide target“. In: *Science Advances* 7.46 (2021), eabk2699. DOI: 10.1126/sciadv.abk2699.

[110] J. Aalbers, F. Agostini, M. Alfonsi, et al. „DARWIN: towards the ultimate dark matter detector“. In: *Journal of Cosmology and Astroparticle Physics* 2016.11 (2016), p. 017. DOI: 10.1088/1475-7516/2016/11/017.

[111] C. E. Aalseth et al. „DarkSide-20k: A 20 tonne two-phase LAr TPC for direct dark matter detection at LNGS“. In: *The European Physical Journal Plus* 133.3 (2018), p. 131. DOI: 10.1140/epjp/i2018-11973-4.

[112] The DarkSide 20k collaboration, P. Agnes, S. Albergo, et al. „Sensitivity of future liquid argon dark matter search experiments to core-collapse supernova neutrinos“. In: *Journal of Cosmology and Astroparticle Physics* 2021.03 (2021), p. 043. DOI: 10.1088/1475-7516/2021/03/043.

[113] Posti, Lorenzo and Helmi, Amina. „Mass and shape of the Milky Way´s dark matter halo with globular clusters from Gaia and Hubble“. In: *Astronomy and Astrophysics* 621 (2019), A56. DOI: 10.1051/0004-6361/201833355.

[114] Gianfranco Bertone, Dan Hooper, and Joseph Silk. „Particle dark matter: evidence, candidates and constraints“. In: *Physics Reports* 405.5 (2005), pp. 279–390. DOI: https://doi.org/10.1016/j.physrep.2004.08.031.

[115] F. Donato, N. Fornengo, and S. Scopel. „Effects of galactic dark halo rotation on WIMP direct detection“. In: *Astroparticle Physics* 9.3 (1998), pp. 247–260. DOI: https://doi.org/10.1016/S0927-6505(98)00025-5.

[116] F. J. Kerr and D. Lynden-Bell. „Review of galactic constants“. In: *Monthly Notices of the Royal Astronomical Society* 221.4 (1986), pp. 1023–1038. DOI: 10.1093/mnras/221.4.1023.

[117] Martin C. Smith, Gregory R. Ruchti, Amina Helmi, et al. „The RAVE survey: constraining the local Galactic escape speed“. In: *Monthly Notices of the Royal Astronomical Society* 379.2 (2007), pp. 755–772. DOI: 10.1111/j.1365-2966.2007.11964.x.

[118] Katherine Freese, Joshua Frieman, and Andrew Gould. „Signal modulation in cold-dark-matter detection“. In: *Phys. Rev. D* 37 (12 1988), pp. 3388–3405. DOI: 10.1103/PhysRevD.37.3388.

[119] Richard H. Helm. „Inelastic and Elastic Scattering of 187-Mev Electrons from Selected Even-Even Nuclei“. In: *Phys. Rev.* 104 (5 1956), pp. 1466–1475. DOI: 10.1103/PhysRev.104.1466.

[120] J. Engel. „Nuclear form factors for the scattering of weakly interacting massive particles“. In: *Physics Letters B* 264.1 (1991), pp. 114–119. DOI: https://doi.org/10.1016/0370-2693(91)90712-Y.

[121] J. D. Lewin and P. F. Smith. „Review of mathematics, numerical factors, and corrections for dark matter experiments based on elastic nuclear recoil“. In: *Astropart. Phys.* 6 (1996), pp. 87–112. DOI: 10.1016/S0927-6505(96)00047-3.

[122] Gintaras Dūda, Ann Kemper, and Paolo Gondolo. „Model-independent form factors for spin-independent neutralino–nucleon scattering from elastic electron scattering data“. In: *Journal of Cosmology and Astroparticle Physics* 2007.04 (2007), p. 012. DOI: 10.1088/1475-7516/2007/04/012.

[123] Jens Michael Schmaler. „The CRESST Dark Matter Search - New Analysis Methods and Recent Results“. PhD thesis. TU München, 2010.

[124] Salucci, P., Nesti, F., Gentile, G., et al. „The dark matter density at the Sun´s location“. In: *Astronomy & Astrophysics* 523 (2010), A83. DOI: 10.1051/0004-6361/201014385.

[125] Pablo F de Salas and A Widmark. „Dark matter local density determination: recent observations and future prospects“. In: *Reports on Progress in Physics* 84.10 (2021), p. 104901. DOI: 10.1088/1361-6633/ac24e7.

[126] G. Angloher, S. Banik, G. Benato, et al. „Results on sub-GeV dark matter from a 10 eV threshold CRESST-III silicon detector“. In: *Phys. Rev. D* 107 (12 2023), p. 122003. DOI: 10.1103/PhysRevD.107.122003.

[127] G. Angloher, P. Bauer, A. Bento, et al. „Results on MeV-scale dark matter from a gram-scale cryogenic calorimeter operated above ground“. In: *European Physical Journal C* 77.9, 637 (2017), p. 637. DOI: 10.1140/epjc/s10052-017-5223-9.

[128] A. H. Abdelhameed et al. „Description of CRESST-III Data“. In: (2019). arXiv: 1905.07335 [astro-ph.CO].

[129] G Angloher, M Bruckmayer, C Bucci, et al. „Limits on WIMP dark matter using sapphire cryogenic detectors“. In: *Astroparticle Physics* 18.1 (2002), pp. 43–55. DOI: https://doi.org/10.1016/S0927-6505(02)00111-1.

[130] G. Angloher et al. „Results from 730 kg days of the CRESST-II Dark Matter Search“. In: *Eur. Phys. J. C* 72 (2012), p. 1971. DOI: 10.1140/epjc/s10052-012-1971-8.

[131] G. Angloher et al. „Results on low mass WIMPs using an upgraded CRESST-II detector“. In: *Eur. Phys. J. C* 74.12 (2014), p. 3184. DOI: 10.1140/epjc/s10052-014-3184-9.

[132] G. Angloher et al. „Results on light dark matter particles with a low-threshold CRESST-II detector“. In: *Eur. Phys. J. C* 76.1 (2016), p. 25. DOI: 10.1140/epjc/s10052-016-3877-3.

[133] M. Ambrosio, R. Antolini, G. Auriemma, et al. „Vertical muon intensity measured with MACRO at the Gran Sasso laboratory“. In: *Phys. Rev. D* 52 (7 1995), pp. 3793–3802. DOI: 10.1103/PhysRevD.52.3793.

[134] *Wikipaedia: Dilution refrigerator*. https://en.wikipedia.org/wiki/Dilution_refrigerator. (visited in October 2023). 2023.

[135] A. H. Abdelhameed, G. Angloher, et al. „Geant4-based electromagnetic background model for the CRESST dark matter experiment“. In: *The European Physical Journal C* 79.10 (2019), p. 881. DOI: 10.1140/epjc/s10052-019-7385-0.

[136] I. Bavykina, P. Christ, P. Huff, et al. „Interpretation of light-quenching factor measurements“. In: *Astroparticle Physics* 28.4 (2007), pp. 489–493. DOI: https://doi.org/10.1016/j.astropartphys.2007.09.006.

[137] R. Strauss, G. Angloher, P. Bauer, et al. „A prototype detector for the CRESST-III low-mass dark matter search“. In: *Nuclear Instruments and Methods in Physics Research Section A: Accelerators, Spectrometers, Detectors and Associated Equipment* 845 (2017). Proceedings of the Vienna Conference on Instrumentation 2016, pp. 414–417. DOI: https://doi.org/10.1016/j.nima.2016.06.060.

[138] Florian Reindl. „Exploring Light Dark Matter With CRESST-II Low-Threshold Detectors“. en. PhD thesis. Technische Universität München, 2016, p. 206.

[139] F. Pröbst, M. Frank, S. Cooper, et al. „Model for cryogenic particle detectors with superconducting phase transition thermometers“. In: *Journal of Low Temperature Physics* 100.1-2 (1995), pp. 69–104. DOI: 10.1007/BF00753837.

[140] G. Angloher, S. Banik, G. Benato, et al. „Testing spin-dependent dark matter interactions with lithium aluminate targets in CRESST-III“. In: *Phys. Rev. D* 106 (9 2022), p. 092008. DOI: 10.1103/PhysRevD.106.092008.

[141] Nahuel Ferreiro Iachellini. „Increasing the sensitivity to low mass dark matter in CRESST-III“. en. PhD thesis. Ludwig-Maximilians-Universität München, 2019.

[142] E. Gatti and P. F. Manfredi. „Processing the Signals From Solid State Detectors in Elementary Particle Physics“. In: *Riv. Nuovo Cim.* 9N1 (1986), pp. 1–146. DOI: 10.1007/BF02822156.

[143] K.D. Irwin and G.C. Hilton. „Transition-Edge Sensors“. In: *Cryogenic Particle Detection*. Ed. by Christian Enss. Berlin, Heidelberg: Springer Berlin Heidelberg, 2005, pp. 63–150. DOI: 10.1007/10933596_3.

[144] M. Mancuso, A. Bento, N. Ferreiro Iachellini, et al. „A method to define the energy threshold depending on noise level for rare event searches“. In: *Nuclear Instruments and Methods in Physics Research Section A: Accelerators, Spectrometers, Detectors and Associated Equipment* 940 (2019), pp. 492–496. DOI: https://doi.org/10.1016/j.nima.2019.06.030.

[145] Baxter, D., Bloch, I. M., Bodnia, E., et al. „Recommended conventions for reporting results from direct dark matter searches“. In: *Eur. Phys. J. C* 81.10 (2021), p. 907. DOI: 10.1140/epjc/s10052-021-09655-y.

[146] Alexander Fuss. „Simulation based neutron background studies for the CRESST and COSINUS dark matter search experiments“. en. PhD thesis. Technische Universität Wien, 2022, p. 230. DOI: https://doi.org/10.34726/hss.2022.86617.

[147] G. Angloher, S. Banik, D. Bartolot, et al. „Towards an automated data cleaning with deep learning in CRESST“. In: *The European Physical Journal Plus* 138.1 (2023), p. 100. DOI: 10.1140/epjp/s13360-023-03674-2.

[148] Daniel Schmiedmayer. „Calculation of dark-matter exclusions-limits using a maximum Likelihood approach“. MA thesis. Technische Universität Wien, 2019. DOI: https://doi.org/10.34726/hss.2019.63441.

[149] Martin Stahlberg. „Probing low-mass dark matter with CRESST-III: data analysis and first results“. PhD thesis. Technische Universität Wien, 2020. DOI: https://doi.org/10.34726/hss.2021.45935.

[150] Glen Cowan, Kyle Cranmer, Eilam Gross, et al. „Asymptotic formulae for likelihood-based tests of new physics“. In: *The European Physical Journal C* 71.2 (2011), p. 1554. DOI: 10.1140/epjc/s10052-011-1554-0.

[151] G. Aad, T. Abajyan, B. Abbott, et al. „Observation of a new particle in the search for the Standard Model Higgs boson with the ATLAS detector at the LHC“. In: *Physics Letters B* 716.1 (2012), pp. 1–29. DOI: https://doi.org/10.1016/j.physletb.2012.08.020.

[152] S. Chatrchyan, V. Khachatryan, A.M. Sirunyan, et al. „Observation of a new boson at a mass of 125 GeV with the CMS experiment at the LHC“. In: *Physics Letters B* 716.1 (2012), pp. 30–61. DOI: https://doi.org/10.1016/j.physletb.2012.08.021.

[153] S. Yellin. „Finding an upper limit in the presence of an unknown background“. In: *Phys. Rev. D* 66 (3 2002), p. 032005. DOI: 10.1103/PhysRevD.66.032005.

[154] S. Yellin. „Extending the optimum interval method“. In: *arXiv e-prints*, arXiv:0709.2701 (2007). DOI: 10.48550/arXiv.0709.2701. arXiv: 0709.2701.

[155] E. Armengaud, C. Augier, A. Benoît, et al. „Searching for low-mass dark matter particles with a massive Ge bolometer operated above ground“. In: *Phys. Rev. D* 99 (8 2019), p. 082003. DOI: 10.1103/PhysRevD.99.082003.

[156] G. Agnolet, W. Baker, D. Barker, et al. „Background studies for the MINER Coherent Neutrino Scattering reactor experiment“. In: *Nuclear Instruments and Methods in Physics Research Section A: Accelerators, Spectrometers, Detectors and Associated Equipment* 853 (2017), pp. 53–60. DOI: https://doi.org/10.1016/j.nima.2017.02.024.

[157] R. Strauss, J. Rothe, G. Angloher, et al. „Gram-scale cryogenic calorimeters for rare-event searches“. In: *Phys. Rev. D* 96 (2 2017), p. 022009. DOI: 10.1103/PhysRevD.96.022009.

[158] D. W. Amaral, T. Aralis, T. Aramaki, et al. „Constraints on low-mass, relic dark matter candidates from a surface-operated SuperCDMS single-charge sensitive detector“. In: *Phys. Rev. D* 102 (9 2020), p. 091101. DOI: 10.1103/PhysRevD.102.091101.

[159] A. Aguilar-Arevalo, D. Amidei, I. Arnquist, et al. „Characterization of the background spectrum in DAMIC at SNOLAB“. In: *Phys. Rev. D* 105 (6 2022), p. 062003. DOI: 10.1103/PhysRevD.105.062003.

[160] A. Aguilar-Arevalo et al. „Confirmation of the spectral excess in DAMIC at SNOLAB with skipper CCDs“. In: (2023). arXiv: 2306.01717 [astro-ph.CO].

[161] Liron Barak, Itay M. Bloch, Mariano Cababie, et al. „SENSEI: Direct-Detection Results on sub-GeV Dark Matter from a New Skipper CCD“. In: *Phys. Rev. Lett.* 125 (17 2020), p. 171802. DOI: 10.1103/PhysRevLett.125.171802.

[162] P. Adari, A. Aguilar-Arevalo, D. Amidei, et al. „EXCESS workshop: Descriptions of rising low-energy spectra“. In: *SciPost Phys. Proc.* (2022), p. 001. DOI: 10.21468/SciPostPhysProc.9.001.

[163] G. Angloher, S. Banik, G. Benato, et al. „Latest observations on the low energy excess in CRESST-III“. In: *SciPost Phys. Proc.* (2023), p. 013. DOI: 10.21468/SciPostPhysProc.12.013.

[164] Sahil Arora. „Development of Electromagnetic background model for the CRESST-III dark matter experiment using likelihood fit normalisation“. MA thesis. Department of Physics and Photonics Science, National Institute of Technology Hamirpur, India, 2023.

[165] Dominik Raphael Fuchs. „New Analysis Methods for Enhanced Sensitivity to Light Dark Matter at CRESST-III and Studies of Discovery Potential for Next-Generation Cryogenic experiments“. en. PhD thesis. Technische Universität München, 2023, p. 232.

[166] Emeline Queguiner. „Analysis of the data of the EDELWEISS-LT experiment searching for low-mass WIMP“. PhD thesis. Université de Lyon, 2018.

[167] Dominik Fuchs. „The low energy excess in CRESST-III“. Talk at the EXCESS workshop in TAUP-2023. 2023.

[168] Robin Anthony-Petersen et al. „A Stress Induced Source of Phonon Bursts and Quasiparticle Poisoning“. In: (Aug. 2022). arXiv: 2208.02790 [physics.ins-det].

[169] Francesca Pucci. „Results of doubleTES detectors“. Talk at the EXCESS workshop in TAUP-2023. 2023.

[170] L. Thulliez, D. Lhuillier, F. Cappella, et al. „Calibration of nuclear recoils at the 100 eV scale using neutron capture“. In: *Journal of Instrumentation* 16.07 (2021), P07032. DOI: 10.1088/1748-0221/16/07/P07032.

[171] H. Abele, G. Angloher, A. Bento, et al. „Observation of a Nuclear Recoil Peak at the 100 eV Scale Induced by Neutron Capture“. In: *Phys. Rev. Lett.* 130 (21 2023), p. 211802. DOI: 10.1103/PhysRevLett.130.211802.

[172] R.B. Firestone, K. Abusaleem, M.S. Basunia, et al. „EGAF: Measurement and Analysis of Gamma-ray Cross Sections“. In: *Nuclear Data Sheets* 119 (2014), pp. 79–87. DOI: https://doi.org/10.1016/j.nds.2014.08.024.

[173] D.A. Brown, M.B. Chadwick, R. Capote, et al. „ENDF/B-VIII.0: The 8th Major Release of the Nuclear Reaction Data Library with CIELO-project Cross Sections, New Standards and Thermal Scattering Data“. In: *Nuclear Data Sheets* 148 (2018). Special Issue on Nuclear Reaction Data, pp. 1–142. DOI: https://doi.org/10.1016/j.nds.2018.02.001.

[174] G. Angloher, S. Banik, G. Benato, et al. „Observation of a low energy nuclear recoil peak in the neutron calibration data of the CRESST-III experiment“. In: *Phys. Rev. D* 108 (2 2023), p. 022005. DOI: 10.1103/PhysRevD.108.022005.

[175] A. H. Abdelhameed, G. Angloher, P. Bauer, et al. „Geant4-based electromagnetic background model for the CRESST dark matter experiment“. In: *The European Physical Journal C* 79.10 (2019), p. 881. DOI: 10.1140/epjc/s10052-019-7385-0.

[176] S. Agostinelli, J. Allison, K. Amako, et al. „Geant4—a simulation toolkit“. In: *Nuclear Instruments and Methods in Physics Research Section A: Accelerators, Spectrometers, Detectors and Associated Equipment* 506.3 (2003), pp. 250–303. DOI: https://doi.org/10.1016/S0168-9002(03)01368-8.

[177] J. Allison, K. Amako, J. Apostolakis, et al. „Geant4 developments and applications“. In: *IEEE Transactions on Nuclear Science* 53.1 (2006), pp. 270–278. DOI: 10.1109/TNS.2006.869826.

[178] J. Allison, K. Amako, J. Apostolakis, et al. „Recent developments in Geant4“. In: *Nuclear Instruments and Methods in Physics Research Section A: Accelerators, Spectrometers, Detectors and Associated Equipment* 835 (2016), pp. 186–225. DOI: https://doi.org/10.1016/j.nima.2016.06.125.

[179] Jonas Eschle, Albert Puig Navarro, Rafael Silva Coutinho, et al. „zfit: Scalable pythonic fitting“. In: *SoftwareX* 11 (2020), p. 100508. DOI: https://doi.org/10.1016/j.softx.2020.100508.

[180] Juris Meija, Tyler B. Coplen, Michael Berglund, et al. „Isotopic compositions of the elements 2013 (IUPAC Technical Report)“. In: *Pure and Applied Chemistry* 88.3 (2016), pp. 293–306. DOI: doi:10.1515/pac-2015-0503.

[181] G. Angloher et al. „Probing spin-dependent dark matter interactions with ^{6}Li: CRESST Collaboration“. In: *Eur. Phys. J. C* 82.3 (2022), p. 207. DOI: 10.1140/epjc/s10052-022-10140-3.

[182] Takayuki Yanagida, Yutaka Fujimoto, Masanori Koshimizu, et al. „Comparative studies of optical and scintillation properties between LiGaO2 and LiAlO2 crystals“. In: *Journal of the Physical Society of Japan* 86.9 (2017). DOI: 10.7566/JPSJ.86.094201.

[183] Katherine Freese, Mariangela Lisanti, and Christopher Savage. „Colloquium: Annual modulation of dark matter“. In: *Rev. Mod. Phys.* 85 (4 2013), pp. 1561–1581. DOI: 10.1103/RevModPhys.85.1561.

[184] A. Gnech, M. Viviani, and L. E. Marcucci. „Calculation of the ^{6}Li ground state within the hyperspherical harmonic basis“. In: *Phys. Rev. C* 102 (1 2020), p. 014001. DOI: 10.1103/PhysRevC.102.014001.

[185] A. F. Pacheco and D. Strottman. „Nuclear-structure corrections to estimates of the spin-dependent WIMP-nucleus cross section“. In: *Phys. Rev. D* 40 (6 1989), pp. 2131–2133. DOI: 10.1103/PhysRevD.40.2131.

[186] J. Engel, M. T. Ressell, I. S. Towner, et al. „Response of mica to weakly interacting massive particles“. In: *Phys. Rev. C* 52 (4 1995), pp. 2216–2221. DOI: 10.1103/PhysRevC.52.2216.

[187] D. S. Akerib, S. Alsum, H. M. Araújo, et al. „Limits on Spin-Dependent WIMP-Nucleon Cross Section Obtained from the Complete LUX Exposure“. In: *Phys. Rev. Lett.* 118 (25 2017), p. 251302. DOI: 10.1103/PhysRevLett.118.251302.

[188] J. I. Collar. „Search for a nonrelativistic component in the spectrum of cosmic rays at Earth“. In: *Phys. Rev. D* 98 (2 2018), p. 023005. DOI: 10.1103/PhysRevD.98.023005.

[189] Torsten Bringmann and Maxim Pospelov. „Novel Direct Detection Constraints on Light Dark Matter“. In: *Phys. Rev. Lett.* 122 (17 2019), p. 171801. DOI: 10.1103/PhysRevLett.122.171801.

[190] Naoki Yoshida, Volker Springel, Simon D. M. White, et al. „Weakly Self-interacting Dark Matter and the Structure of Dark Halos“. In: *The Astrophysical Journal* 544.2 (2000), p. L87. DOI: 10.1086/317306.

[191] Miguel Rocha, Annika H. G. Peter, James S. Bullock, et al. „Cosmological simulations with self-interacting dark matter – I. Constant-density cores and substructure“. In: *Monthly Notices of the Royal Astronomical Society* 430.1 (2013), pp. 81–104. DOI: 10.1093/mnras/sts514.

[192] Steen Hannestad and Thomas Tram. „Sommerfeld enhancement of DM annihilation: resonance structure, freeze-out and CMB spectral bound“. In: *Journal of Cosmology and Astroparticle Physics* 2011.01 (2011), p. 016. DOI: 10.1088/1475–7516/2011/01/016.

[193] Masahiro Ibe, Hitoshi Murayama, and T. T. Yanagida. „Breit-Wigner enhancement of dark matter annihilation“. In: *Phys. Rev. D* 79 (9 2009), p. 095009. DOI: 10.1103/PhysRevD.79.095009.

[194] Xiaoyong Chu, Camilo Garcia-Cely, and Hitoshi Murayama. „Velocity Dependence from Resonant Self-Interacting Dark Matter“. In: *Phys. Rev. Lett.* 122 (7 2019), p. 071103. DOI: 10.1103/PhysRevLett.122.071103.

[195] Xiaoyong Chu, Camilo Garcia-Cely, and Hitoshi Murayama. „Finite-Size Dark Matter and its Effect on Small-Scale Structure“. In: *Phys. Rev. Lett.* 124 (4 2020), p. 041101. DOI: 10.1103/PhysRevLett.124.041101.

[196] Manoj Kaplinghat, Sean Tulin, and Hai-Bo Yu. „Dark Matter Halos as Particle Colliders: Unified Solution to Small-Scale Structure Puzzles from Dwarfs to Clusters“. In: *Phys. Rev. Lett.* 116 (4 2016), p. 041302. DOI: 10.1103/PhysRevLett.116.041302.

[197] S. S. Wilks. „The Large-Sample Distribution of the Likelihood Ratio for Testing Composite Hypotheses“. In: *The Annals of Mathematical Statistics* 9.1 (1938), pp. 60 –62. DOI: 10.1214/aoms/1177732360.

[198] Felix Kahlhoefer, Manoj Kaplinghat, Tracy R. Slatyer, et al. „Diversity in density profiles of self-interacting dark matter satellite halos“. In: *Journal of Cosmology and Astroparticle Physics* 2019.12 (2019), p. 010. DOI: 10.1088/1475-7516/2019/12/010.

[199] Hiroya Nishikawa, Kimberly K. Boddy, and Manoj Kaplinghat. „Accelerated core collapse in tidally stripped self-interacting dark matter halos“. In: *Phys. Rev. D* 101 (6 2020), p. 063009. DOI: 10.1103/PhysRevD.101.063009.

[200] G. Audi, O. Bersillon, J. Blachot, et al. „The Nubase evaluation of nuclear and decay properties“. In: *Nuclear Physics A* 729.1 (2003). The 2003 NUBASE and Atomic Mass Evaluations, pp. 3–128. DOI: https://doi.org/10.1016/j.nuclphysa.2003.11.001.

Acknowledgements

The completion of this thesis would not have been possible without the support and encouragement of the people around me in my personal and professional life. I had heard that the period of Ph.D. is one of the most stressful times in a person's career, although because of the people around me, it was one of the most enjoyable and exciting periods of my life. I will always be thankful to each and everyone I stumbled across during these years and apologize to anyone whose name I could not include here.

First and foremost, I express my most profound appreciation and gratitude to my supervisor, Prof. Dr. Jochen Schieck. This thesis would not have gotten any results if it hadn't been your ideas and inspirations. All that I have learned from you in these past years, and not just the scientific knowledge, will stay with me for the rest of my life. You allowed me to take a break when I needed it the most so I could come back and be productive with a fresh mind. The support you have provided me from day one is inexpressible.

Understanding the details of the CRESST experiment, the data acquisition, the data analysis, and also the German culture would not have been possible for me without my second supervisor, Dr. Florian Reindl. Thank you so much for being immensely responsive whenever I had doubts about anything and also for proofreading my thesis. Especially starting a Ph.D. on a new topic during COVID times when I could not have in-person discussions to understand the concepts much more readily, your support really helped me dive into this new territory. And sorry, I could not keep my promise to clean the COSINUS tank. I got to visit LNGS regardless, also thanks to you.

Using this opportunity, I would also like to thank my HEPHY colleagues. I am utterly grateful for the perfect and healthy working environment created by all of you during this time, starting all the way from the coffee breaks during the COVID year. To my officemates, Dr. Samir Banik and Dr. Felix Wagner, thank you so much for all the scientific non-scientific discussions and clearing all the doubts that I ever had. I could not have asked for better people to share the office space with. Felix, let's ensure we keep Oktoberfest an annual thing now. To Daniel Schmiedmeyer, for taking the time out to teach me about the basics of data analysis in my very first months at HEPHY, especially when you agreed to commute 50 minutes to the office every day just to make sure that I had all the help I needed. To Leonie Einfalt, thank you for quickly fixing all the bugs I annoyed you within the Limitless software. Producing the final results would not have

been possible without your help. To Jens Burkhart, for not just being a colleague but a supporter, a motivator, and most importantly, a very close friend. To Rituparna Maji, for the discussions and collaborative efforts during all the courses (especially Stats) and schools. To Dr. Holgar Kluck, Dr. Valentyna Mokina, Dr. Alexander Fuss, Dr. Mariano Cababie, Dr. Vasile Ghete, and Philipp Schreiner, for all our fun conversations, which provided a perfect distraction during the stressful times. Mainly, also thanks again to Valentyna for taking care of my sweet tooth whenever I had it. And, a special thanks to Nathalie Fortin for being super nice and warm every morning I arrived at the institute and for all the musical discussions.

Without the support of the whole CRESST analysis team, I would not have been able to understand the intricacies of the process and solve the problems I had dealt with during the analysis. Thank you for the detailed discussions we had during the analysis meetings, which helped clear a lot of air and triggered new ideas as well. I am also grateful to Dr. Martin Stahlberg for guiding me in the initial stages of analysis when I was trying to understand the analysis software CAT and spammed him with a lot of issues and bugs. I also want to express my gratitude to the other members of the CRESST collaboration, including the on-site team, for keeping the experiment running smoothly during these years. Additionally, I would also like to thank Dr. Ranjan Laha for the discussions about his resonant DM theory on which this work is based, which helped clear a lot of theoretical doubts.

After work and during the weekends and trips, I got the opportunity to relax, travel, and explore, thanks to all the friends I made in these years. Linus, Manuel, Stefanie, Morgane, Florian, Nadine, Moomal, Dhanlakshmi, Aiswarya, Abhishek, Mahnoor, Dr. Diksha, Disha, Shivam, Sampriti, Marcel, Arushi and last but not the least Sourav, spending time with you all was highly delightful. You made the time in Vienna as great as it was. Particularly, I am exceedingly grateful to Swadheen Dubey, a friend I made through my time in Vienna and explored anything and everything with. From Himachal to Iceland, every conversation created an impact that is going to sustain. To the years of more of this to come !!

Finally, the most significant appreciation goes to my brothers Deepankur Gupta and Sidharth Gupta, my sisters Deepshikha Gupta, Deepika Gupta and Kamna Saini Gupta, and especially my parents, Mrs. Poonam Gupta and Dr. Jatinder Gupta, for providing the platform, the support, and the warmth throughout my studies and career since I was a kid. Thank you so much for having confidence in me and standing by my side through all the decisions I have made in my life. And to the one closest person I lost through this journey... Badi maa, I know you can't read this, but also I can't put into words the amount of love you gave me and how much I adore it and miss it now. This one is for you all equally.